# DC-DC CONVERTER FOR POWER COLLECTION IN WIND FARMS

SAMIR MILAD ALI ALAGAB

A thesis submitted in partial fulfilment of the requirement of Staffordshire University for the degree of Doctor of Philosophy

September 2019

# Declaration

I hereby declare that except where specific reference is made to the work of others, it has been composed by the author and has not been previously submitted for examination which has led to the award of any degree in this, or any other University. This dissertation is the result of my own work and includes nothing which is the outcome of work done in collaboration, except where specifically indicated in the text.



Samir Milad Ali Alagab
September 2019

# Dedication

*... to my wife, Fatima and my lovely kids: Fatima, Amera, Amany, Rawa, Mohamed and Raghad.*

# Acknowledgments

First of all, I am grateful to the Almighty Allah for establishing me to complete this thesis.

First and foremost, I would like to thank my thesis supervisor, Professor Sarath Tennakoon for his guidance and support throughout my studies. I am honoured to have had the opportunity to work with such a wise man of great knowledge and experience. He challenged me with his continuous flow of new research ideas and concepts. I have really enjoyed our discussions on research, politics and worldwide history during his daily visits in the research office.

I want to express my gratitude to Professor Abdel-Hamid Soliman for valuable advice and excellent guidance since the beginning of the project.

My sincere thanks to the Higher Institute for Science and Technology Al-khoms - Libya for supporting and funding my PhD project.

A special thanks to acknowledge faculty staff members and my good friends Hesham, Masum, Ghanim, Ernest, Philip and Manilka for their support.

Most importantly, I would like to thank my Family members; my mother, father, my brothers Khalid, Sami, Mohamed, Salem, Nabil, Mosbah, and my sisters for all the mental and physical support that they gave me, they all made my journey full of many unforgettable moments.

Last but not least, no words can describe how I feel towards my lovely wife Fatima, she gave away everything, and she had just to give me full support and worked day and night to make me feel comfortable; so, I can complete my studies on the highest possible standards. May God bless her and my beloved daughters Fatima, Amira, Amany, Rawa, Raghad and my Son, Mohamed and keep them by my side as long as I live.

# Abstract

Offshore wind farms have grown rapidly in number in recent years. Several large-scale offshore wind farms are planned to be built at further than 100 km from the United Kingdom coast. While high-voltage high-power installations have addressed the technical issues associated with reactive power flow in AC transmission, reactive power can be avoided by using High-Voltage Direct Current transmission (HVDC). Reactive power causes problems when transmission distances are long, therefore, HVDC transmission is now being considered for wind farm grid connection. However, as wind farms constitute weak systems Line Commutated Converter (LCC) based HVDC is not viable and newer Modular Multilevel Converter (MMC) based Voltage Source Converters (VSC) are needed for the AC-DC conversion. One of the key components in such systems is the DC-DC converter, which is required to act as the interface between the generation, transmission, and distribution voltage levels, and reduces the power conversion stages, avoiding transformers typically used in AC grid integration systems.

In addition, there is no high-power Medium-Voltage MV DC-DC converter available for offshore wind farm energy systems at present. The specification requirements of high-power MV DC-DC converters can be set once the output characteristics of the wind turbine generators have been reviewed. An offshore wind farm with MVDC-grid collection does not exist today, but it is a promising alternative, although specification analysis of high power MV DC-DC converters is necessary.

The work reported in this thesis aims to introduce two types of high power MV DC-DC converter topologies, for offshore wind farm energy systems, termed single-stage, and multi-stage converters. Ways of reducing losses by soft switching and reduction in the number of components are considered. Both topologies are based on the Marx principle where capacitors are charged in parallel and discharged in series to achieve the step-up voltage transformation. During doldrums, light and calm wind, and for maintenance work, it is necessary to supply the offshore wind farm with auxiliary power. This thesis proposes a

novel Bidirectional Modular DC-DC converter (BMDC) and evaluates its performance. The simulation results show that the proposed BMDC allows up to 5% of the wind farm's power rating to be drown from the onshore substation. This means that the proposed DC-DC converter is capable to provide bidirectional power flow.

For offshore wind farm application, BMDC can be inserted between the offshore wind farm and onshore substation. The studies, in this thesis, are based on an input DC collection at 6 kV with the DC to DC converter stepping up the voltage to 30 kV. The proposed system is integrated and simulated with the DC offshore wind farm and a Voltage Source Converter (VSC) in the onshore station.

The steady-state simulation results, to transmit the power between two different voltage levels, and the dynamic performance of the proposed converter were investigated. The advantages of the proposed converter include its simple design and that it does not require an AC transformer; hence can easily be implemented in an offshore wind farm since it requires less weight and size on the platform in the sea, which ultimately results in minimal cost. Furthermore, the proposed converter can ride through a fault which complies with the UK Grid code. However, in this case, it is necessary to provide protection systems such as a large chopper resistor for energy absorption or de-loading the wind turbine. Finally, the proposed integrated BMDC converter showed its suitability for offshore wind farms as well as improving their reliability.

# Table of Contents

## Chapter 6

## Chapter 7

# List of Figures

# List of Tables

# List of Acronyms

| | |
|---|---|
| AC | Alternating Current |
| BJT | Bipolar Junction Transistor |
| BMC | Bidirectional Modular Converter |
| CS | Collector System |
| DAB | Dual Active Bridge |
| DC | Direct Current |
| DFIG | Doubly Fed Induction Generator |
| EMI | Electromagnetic Interference |
| FBIC | Full Bridge Insulated Converter |
| FBR | Full Resonant Converter |
| FM | Forward Mode |
| FSWG | Fixed Speed Wind Turbine |
| GWEC | Global Wind Energy Council |
| GTO | Gate Turn Off |
| HVAC | High Voltage Alternating Current |
| HBIC | Half Bridge Insulated Converter |
| HVDC | High Voltage Direct Current |
| IGBT | Insulated Gate Bipolar Transistor |
| IG | Induction Generator |
| LCC | Line Commutated Converter |
| LSC | Line Side Converter |
| MC | Marx Converter |
| MI | Mass Impregnated |
| MV | Medium Voltage |
| MMC | Modular Multilevel Converter |
| MTDC | Multiterminal HVDC |
| MW | Megawatt |
| OWT | Offshore Wind Turbine |
| OWF | Offshore Wind Farm |
| PI | Proportional-integral |

| | |
|---|---|
| PMSG | Permanent Magnet Synchronous Generator |
| RM | Reverse Mode |
| PV | Photovoltaics |
| PWM | Pulse with modulation |
| RSC | Rotor Side Converter |
| SCFF | Self-Contained Fluid Filled |
| SM | Sub Module |
| TNO | Transmission System Operators |
| TSO | Transmission System Operation |
| VSC | Voltage Source Converter |
| XLPE | Crossed Linked Polyethylene |
| ZCS | Zero Current Switching |

# List of Symbols

| | |
|---|---|
| $\varphi$ | The phase shift angle |
| $\omega$ | The angular frequency |
| $\Delta VC$ | The desired peak-to-peak voltage ripple |
| $C_n$ | Number of capacitors in the middle converter |
| $C_{eq(p)}$ | Equivalent capacitance of parallel |
| $C_{eq(S)}$ | Equivalent capacitance of series |
| $C_{eq(FP)}$ | Forward equivalent capacitance of parallel |
| $C_{eq(RP)}$ | Reverse equivalent capacitance of parallel |
| $C_{eq(FS)}$ | Forward equivalent capacitance of Series |
| $C_{eq(RS)}$ | Reverse equivalent capacitance of Series |
| $C_{out}$ | Output capacitor |
| $d$ | Duty cycle |
| $D_n$ | Number of diodes |
| $F_s$ | Switching Frequency |
| $i^*_d$ | The current references |
| $i_{L1}$ | The current in the inductor $L_1$ |
| $I_{in}$ | Input current |
| $I_{out}$ | Output current |
| $K_{i\text{-}pll}$ | Integral gain |
| $K_{p\text{-}pll}$ | Proportional gain |
| $KHz$ | Kilo Hertz |
| $L_\sigma$ | The total leakage inductance of the transformer |
| $L_{in}$ | Input inductor |
| $N_{(boost\text{-}buck)}$ | The voltage conversion ratio |
| $N_C$ | The number of capacitor cells |
| $N_s$ | Secondary winding |
| $N_p$ | Primary winding |
| $P_{DAB}$ | Transferred power |
| $P_{rate}$ | Rating power |
| $R_{load}$ | Load resistance |

| | |
|---|---|
| $S_F$ | IGBT switch connected in Forward |
| $S_P$ | IGBT switch connected in Parallel |
| $S_R$ | IGBT switch connected in Reverse |
| $S_{valve}$ | IGBT switch valve |
| $t_{on}$ | Operating Time |
| $t_{off}$ | Turn-off Time |
| $T_s$ | Switching Time |
| $V_{cell}$ | Cell capacitor voltage |
| $V_{dc}$ | Voltage between the positive and negative poles |
| $V_{in}$ | Input voltage |
| $V_H$ | High Voltage |
| $V_L$ | Low Voltage |
| $V_{out}$ | Output voltage |

# Chapter 1

## Introduction

## 1.1 Background

Harnessing of wind energy; in particular, offshore wind energy is a keystone in the policy of several European countries for the large-scale use of renewable energy. The realisation and the grid connection of offshore wind farms is receiving much attention, in countries such as in Denmark, United Kingdom, Germany, Sweden, and the Netherlands [1].

Seas and oceans make ideal locations for wind farm turbines since wind energy sources are much stronger and more constant compared to onshore locations. The ocean's surface is not obstructed by hills, trees and houses, like the land, so winds over the water are faster because there is less friction to slow them down [2]. Thus, offshore wind farms offer more significant potential for renewable energy. The massive potential of the United Kingdom's shoreline makes it one of the most attractive places in the world to invest in offshore wind farm technology [2].

### 1.1.1 Current and Future Development in Europe Wind Farm

European countries were harnessing wind energy a long time ago; Denmark installed the first offshore wind farm in 1991, which was rated at a few kilowatts [3]. Since then in Europe, offshore wind farms have grown rapidly in number and capacity. In 2015, 12,800 MW of wind power capacity was installed and grid-connected in the European Union, 6.3% more than 2014. Figure 1.2 shows EU country market shares for new wind energy capacity installed during 2017. One can see that; the total wind energy capacity is 15.638 MW. 42% of all new Europe installation in 2017 took place in Germany, and the second largest percentage is the United Kingdom at 27.2% [3].

In the North Sea region, offshore wind generation is expected to reach about 70 TWh by the year 2035, further increasing to a capacity of 309 TWh by 2050 [4]. However, there is a strong case for implementing a Multi-Terminal Direct Current (MTDC) grid in the North Sea to interconnect offshore wind farms and onshore substations and to form so-called "European offshore super DC grid" as displayed in Figure 1.2.

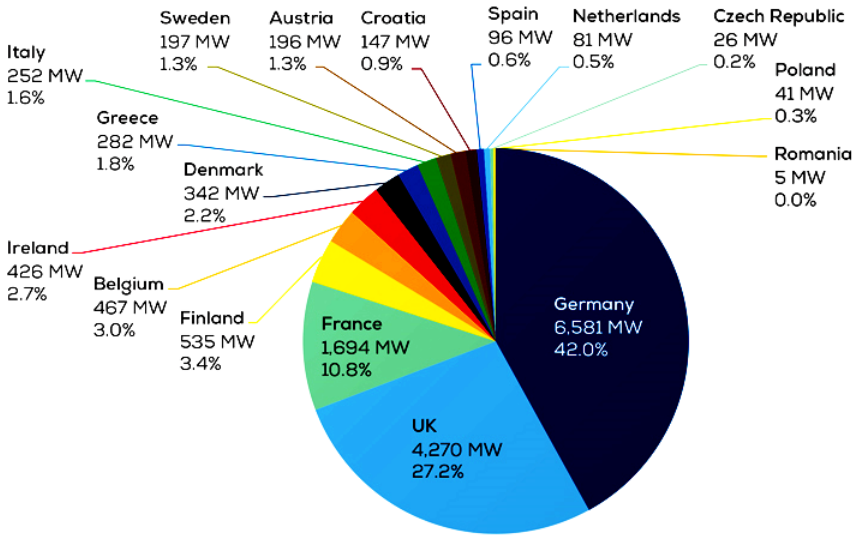


Figure 1.1: Europe shared new wind energy capacity installed during 2017 [3]

Figure 1.2: The European offshore super grid [4]

### 1.1.2 Research Motivation

Several offshore wind farms with a capacity around 1000 MW are planned to be built in Europe with expected distances of more than 100 km to onshore station [1], [2]. With such transmission distances, AC transmission is impractical due to the problems associated with reactive power flow. With DC transmission, reactive power issues are eliminated and therefore, DC transmission is being

considered for harnessing offshore wind power for grid integration, despite the additional cost of converter stations [1], [2]. A DC grid will naturally grow out of the interconnection of existing point-to-point transmission corridors [5]. This would require the interconnection of sections operating at different DC voltage levels through DC-to-DC converters as illustrated in Figure 1.3.

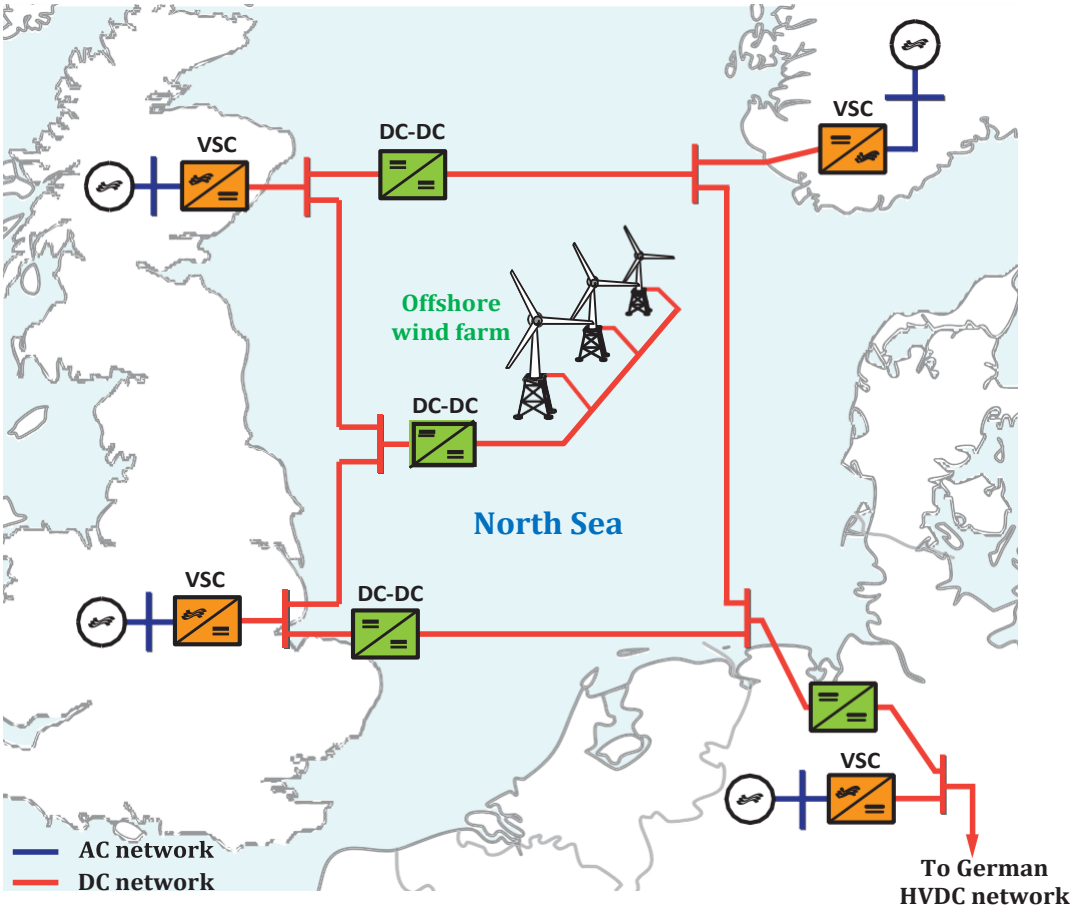


Figure 1.3: Possible application areas of DC-DC converters in the HVDC grid [5]

Generally, a DC-DC converter can be described as the DC equivalent of an AC transformer in the HVAC system. This research project is focused on contributing to the HVDC concept by providing a new bidirectional DC-DC converter for offshore wind farms.

## 1.2 Research Aim and Objectives

Considering the subject of "DC-DC converter for power collection in wind farms". The aim of the research is to develop and investigate a bidirectional DC-DC converter for power collection in wind farms. To achieve this aim, the following objectives are addressed in this thesis:

1. To carry out a comprehensive literature review and survey to gain a thorough understanding of state-of-the-art High Voltage Direct Current (HVDC). The topics include;
    i. Current offshore wind farm collection schemes.
    ii. Technologies used to implement high-power MV DC-DC converters for offshore wind farms and main challenges impeding their utilisation in high voltage and high-power applications.
    iii. Voltage source converter based HVDC transmission.

2. To investigate and determine the specifications and ratings of DC-DC converters in the electrical system for grid integration of offshore wind farms.

3. To propose, design and evaluate unidirectional DC-DC converter topologies to be applied for offshore wind farms, and to compare them steady-state performance of different converter topologies suitable for high-power MV.

4. To propose and design a novel bidirectional DC-DC converter to operate between two different voltage levels.

5. To validate and evaluate all the developed operating modes for the proposed DC-DC converter, control strategies, and topologies through the computer simulations in steady-state and dynamic-state operating conditions.

## 1.3 Thesis Structure and Content

In particular, the outcomes of this work are presented in seven chapters as follows:

**Chapter 1:** Introduces the thesis, includes a background on the development of current and future wind farms in Europe, research motivation and finally research aims and objectives.

**Chapter 2:** Comprises a literature review of previous work with the development of HVDC technology in an offshore wind farm, then an evaluation for the HVDC transmission compared to the traditional HVAC transmission system. The state of wind farms and their challenges are also described. Further, the Grid integration of offshore wind farms is explained, and several possible layouts of the internal collection grid are explained and the components in the offshore wind farms are presented. Different wind turbine concepts are described.

**Chapter 3:** Existing, and suitable DC-DC converter topologies used for high power collection are discussed and reviewed, followed by identifying the requirements for DC-DC converters that can realise such DC collection networks and the advantages and disadvantages of each of the converter topologies.

**Chapter 4:** Two DC-DC converter topologies, a single-stage and multi-stage converters are improved and developed. The analysis, steady-state and dynamic performance, and comparison of the steady-state performance of these converter topologies through computer simulation. A comparison of both topologies in terms of device rating count is made at the end of the chapter.

**Chapter 5:** Developed and designed of a new bidirectional DC-DC converter for offshore wind farm application. Full mathematical analysis leading to the design methodology to determine the component values and ratings including solid-state devices. In order to evaluate the

performance of the new bidirectional converter and control strategies in both power flow directions, simulation models are implemented. This chapter presents the results of this simulation and comments on the technical performance of each power flow direction.

**Chapter 6:** The new bidirectional converter presented in Chapter Five, is Implemented and integrated into the wind farm power collection. This chapter presents, in more detail, the control mechanisms of the system, and presents and discusses both steady state and dynamic state operation. Finally, validation through computer simulation is presented.

**Chapter 7:** Presents general conclusions, summary of contributions and recommendations for future research.

References and appendices are displayed at the end of this research thesis.

## 1.4 Author's Publications based on this Work

**Journal Publication**

- Alagab, Samir Milad, Sarath Tennakoon, and Chris Gould. *"Bidirectional Marx DC–DC converter for offshore wind farm application."* The Journal of Engineering, vol. 17, pp.3848-3854, IET 2019. [Published]

- Alagab, Samir Milad, Sarath Tennakoon, and Chris Gould. "*A Compact DC-DC Converter for Offshore Wind Farm Application*." Renew. Energy Power Qual. Journal, vol. 1, no. 15, pp. 529–533, 2017. [Published]

**Conference Publication**

- Alagab, Samir Milad, Sarath Tennakoon, and Chris Gould. "*Review of wind farm power collection schemes*." In Power Engineering Conference (UPEC), 50th International Universities, pp. 1-5. IEEE, 2015. [Published]

- Alagab, Samir Milad, Sarath Tennakoon, and Chris Gould. "*High voltage cascaded step-up DC-DC Marx converter for offshore wind energy systems"*. In Power Electronics and Applications (EPE'17 ECCE Europe), 19th European Conference on, pp. P-1. IEEE, 2017. [Published]

- Alagab, Samir Milad, Sarath Tennakoon, and Chris Gould. "*A novel bidirectional DC-DC converter for offshore DC collection grid"*. In Power Electronics and Applications (EPE'18 ECCE Europe), 20th European Conference on, pp. 1-10. IEEE, 2018. [Published]

- Alagab, Samir Milad, Sarath Tennakoon, and Chris Gould. "*Comparison of Single-stage and Multi-stage Marx DC-DC Converters for HVDC application*". 53rd International Universities Power Engineering Conference (UPEC 2018), pp. 1-6. IEEE, 2018. [Published]

**Co-authored Conference Publication:**

- Hosseini, Ehsan, Samir Milad Alagab, and Sarath B. Tennakoon. "*Voltage regulated interleaved Marx topology DC-DC converter*" In Universities Power Engineering Conference (UPEC), 2017 52nd International, pp. 1-5. IEEE, 2017. [Published]

- Tennakoon, Sarath B., and Samir M. Alagab. *"Converters for the grid integration of wind farms."* In Industrial and Information Systems (ICIIS), 2017 IEEE International Conference on, pp. 1-7. IEEE, 2017. [Published]

**Internal Conferences and Workshops:**

- Poster presentation in the second MEEPS workshop focusing on Future Trends & Applications in HVDC by the University of Manchester, 7th November 2014. Accessible online via: https://sites.google.com/site/ieeesbpeschapteruom/meeps

- Poster presentation at 8th Universities High Voltage Network Colloquium, jointly hosted by Staffordshire University and GE Grid Solutions, Staffordshire University, 14th–15th January 2015. Accessible online via http://www.uhvnet.org.uk/uhvnet2015.html

- Poster Presentation at the 9th Universities High Voltage Network Colloquium, Cardiff University 14th–15th January 2016. Presentation accessible online via http://www.uhvnet.org.uk/uhvnet2016.html

# Chapter 2

## Review of Wind Farm Grid Integration Technologies

## 2.1 Introduction

This chapter presents a brief literature review about the advent of Offshore Wind Farms and the concepts of suitable AC and DC collection grids. At first, the state of the art AC technology is reviewed, and basic concepts are presented. Subsequently, the focus is on the DC collection grid, and description of several high voltage DC collections. Basic principles and kinds of wind turbines are illustrated. To conclude, the chapter ends with an overview of the characteristics of DC collection grids and the challenges that need to be addressed.

## 2.2 Advent of Offshore Wind Farms

Wind power has emerged as one of the most dominant renewable sources of energy with immense growth potential across the globe [6], [7]. In fact, global wind energy capacity has increased rapidly and has become the fastest developing renewable energy technology. With the rapid development of wind energy, wind energy conversion systems have been developed by researchers and manufacturers [6], [8]. Figure 2.1, illustrates the cumulative wind power capacity from 1999 to 2020. World wind farm energy in 2013 reached 318 .6 GW, and increased in 2014, to reach 369.8 GW. In 2016, global wind farm installation reached 486.7 GW. From this data, wind power has grown rapidly, as shown the capacity in 2012 was only 283 GW and this is expected to achieve 760 GW in 2020.

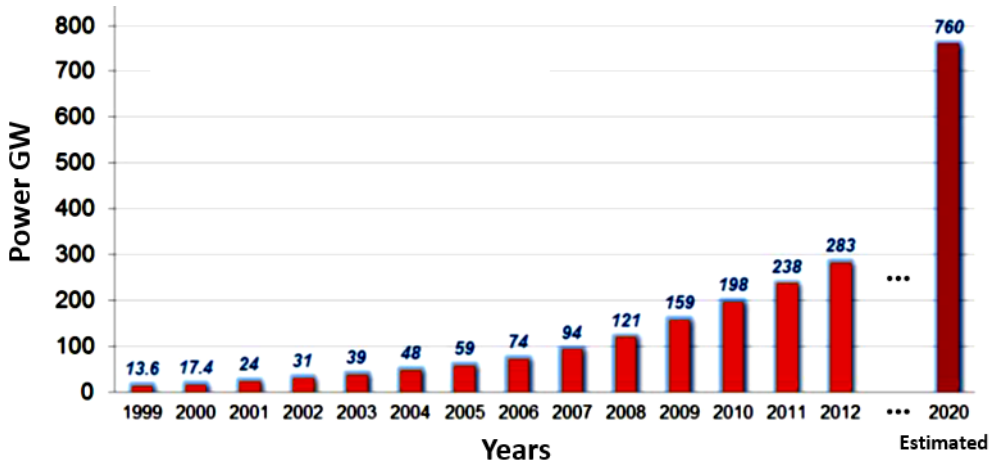


Figure 2.1: Global cumulative installed wind power capacity [9]

The Global Wind Energy Council's (GWEC) rolling five-year forecast sees almost 60 GW of new wind installations in 2017, rising to an annual market of about 75 GW by 2021, to bring the cumulative installed capacity of over 800 GW by the end of 2021 [10].

Offshore Wind Farms (OWF) exhibit many advantages over onshore wind farms. Some of those are; strong but less turbulent wind; the availability of large sea areas, and reduced visual and noise impact from offshore structures. These advantages lead to an increase in energy production and to a reduction of fatigue on the blades and structural components of the wind turbines.

This growth is expected mainly from the UK market and a faster deployment in France and the Netherlands, against a background of still recovering regulatory and financial stability as illustrated in Figure. 2.2 [8],[11], [12]. The development of the industry in the coming years is expected to create major growth opportunities for Europe if long-term visibility and stable regulatory frameworks are in place.

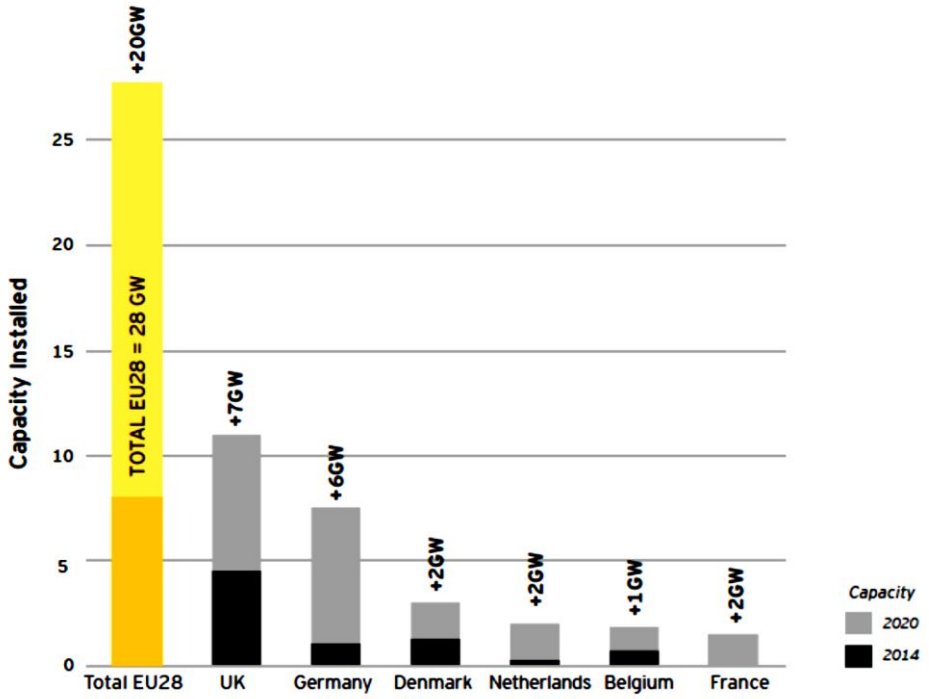


Figure 2.2: A breakdown of potential growth in 2020 [12]

According to [8], the UK has done more than any other country to support the development of a sustainable and ambitious offshore wind industry. The first offshore wind farm in the UK started operating in 2000, it is called Blyth Offshore Wind Farm, and its capacity is 4 MW. In 2001, the first phase of development (Round 1) was launched involving 18 sites in England and Wales, with a potential capacity of 1.5GW. Further offshore wind farms "Round 2" and "Round 3" were installed in 2003 and 2010 respectively [13]. Furthermore, the world's largest offshore wind farm, London Array, was opened in July 2013.

During 2013, the Government has been working in partnership with industry to develop the UK's offshore wind industry. It provides the tools necessary to support large-scale investment in the UK supply chain and raise awareness of the commercial opportunities in the UK and overseas. However, to deliver the innovation and competition required, the cost to consumers needed to be reduced [14], [15].

The UK transmission system for the 2030 Accelerated Growth Scenario is defined by the National Grid [15]. The Rounds 1 and 2 offshore wind projects mostly utilised High Voltage Alternating Current (HVAC) export cables which have a rated voltage of 132 – 150 kV. However, a few projects used 33 kV Medium Voltage Alternating Current (MVAC) export cables for transmission to shore. For Round 3 projects, at 150 km distance, wind farm arrays are aggregated using 500 MW HVAC hubs, and the intra-zonal connection between offshore HVAC transformer substations is achieved using HVAC cables. Furthermore, the power aggregated by two HVAC hubs is transmitted to shore via 1 GW and ±320 kV offshore converter platforms with 1 GW, 320 kV bipole cable circuits [15].

The offshore technology has a number of issues in terms of; modest efficiency, high weight and size of the offshore installation, cost of transportation, installation, and maintenance [16]. Presently, there are two solutions to integrate offshore electrical power transmission: HVAC and HVDC, mostly using Voltage Source Converters (VSC) [6], [17]. HVAC has the advantage of a simpler system structure and lower cost. However, transmission distances are getting longer, and the capacities of offshore wind farms are increasing, leading to the following problems with AC distribution and transmission [6], [18]:

- The stability of the AC system decreases with the increase in transmission distance
- Dynamic reactive power compensation must be provided, in particular under AC faults
- Cost increases with the increase of transmission distance

These problems can be overcome by using HVDC transmission with VSC for power conversion. Such a system has the following advantages:

+ Maximum capture of wind energy by frequency control
+ Black-start capability
+ Independent control of real and reactive power
+ No stability issues
+ No additional reactive power compensation equipment is needed

There are several issues in offshore wind farms, which need resolving. Those are; offshore wind turbines face greater potential for corrosion from exposure to seawater and should be designed more robustly with less maintenance required; in addition, the installation and maintenance of wind farms at sea are much more complex than on the land, and requires special equipment and good weather conditions [19], [20].

## 2.3 Wind Turbines

The energy from the wind has been harnessed by mankind for millennia to carry ships across oceans and later to pump water and grind grain. The conversion of wind kinetic energy to electrical energy started during 1887 with an automated wind turbine equipped with a 12-kW DC generator. To generate electricity from wind turbines more efficiently and reliably, and to compete against fossil fuel-based power plants, many improvements have been made in the design of wind turbine mechanical and electrical components. Wind turbine technology reached sufficient maturity by the 1980s, leading to the commissioning of the first 50-kW utility-scale wind turbines [20], [21], [22]. With large turbines, wind farms can capture higher wind power with lower installation and maintenance costs, when compared to a group of small turbines. Owing to this fact, the size of commercial wind turbines has exponentially increased over the past 30 years as

demonstrated in Figure 2.3. Turbine size has increased from 50 kW in 1980 to 7.5 MW in 2010 and up to 10 MW in 2018 [23].

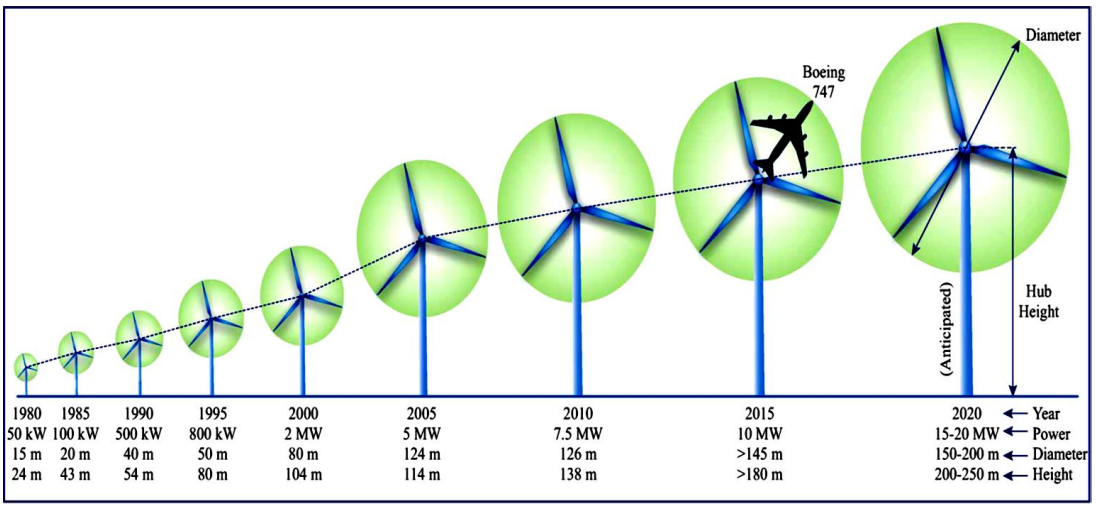


Figure 2.3: Evolution in the size of commercial wind turbines [23]

Types of wind turbine generator systems are described in more detail in [23], [24]. There are several different ways to convert the mechanical power from the rotor section of the wind farm to electrical energy. For offshore wind turbines connected to an AC grid, there are two basic types; a variable speed generator; and a fixed speed generator [24],[25],[26]. A gearbox is included in the generator assembly to increase the fairly slow speed of the wind turbine shaft to a higher speed suitable for the electrical generator.

### 2.3.1 Variable Speed Turbine with Doubly Fed Induction Generator (DFIG)

As shown in Figure 2.4, the stator of a DFIG is directly connected to the grid while the rotor winding is supplied through a power electronic converter. By varying the frequency and magnitude of the rotor voltage, the generated active and reactive power can be controlled independently of each other.

The Rotor Side Converter (RSC) usually provides active and reactive power control of the machine while the line-side converter (LSC) keeps the voltage of the DC-link constant. The converter only has to handle 20-30% of the total power and the losses in the converter can be reduced compared to the converter that has to handle the full power [27]. This system has a sufficient speed range to also smooth out incoming wind power variations. In addition, the power rating of the rotor-side converter is determined

by the range of slip required and is approximately proportional to the product of stator power and slip [28].

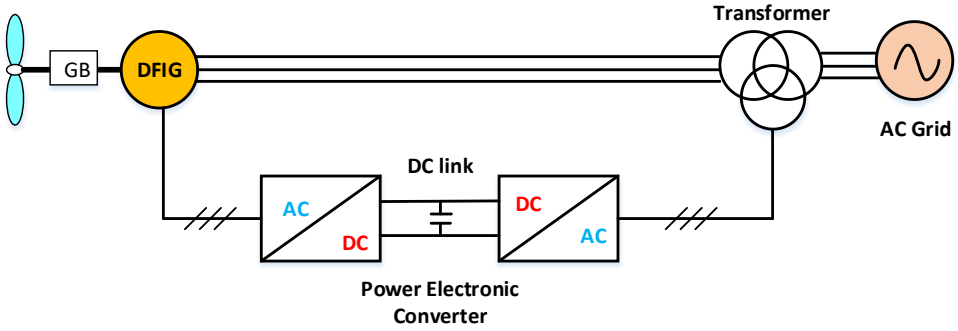


Figure 2.4: Variable speed wind turbine with a doubly fed induction generator [28]

### 2.3.2 Full Variable Speed Converter Machines (Synchronous Generator)

The generator can be either an induction generator or a synchronous generator. The arrangement with a synchronous generator is shown in Figure 2.5. The rotational speed of the wind turbine is controlled by the full power converter. In fact, if the generator is designed with multiple poles, the gearbox can be eliminated. In the full variable speed wind turbine, power fluctuations caused by varying wind speed can be absorbed by slightly changing the rotor side speed [24], [28].

The advantage of a synchronous generator is that it can be connected to a diode or thyristor rectifier. The low losses and the low price of the rectifier make the total cost much lower than that of the induction generator with a self-commutated rectifier [24]. When using a diode rectifier, the fundamental of the armature current has almost unity power factor. The induction generator needs a higher current rating because of the magnetization current. The disadvantage is that it is not possible to use the main frequency converter for the motor start of the turbine. If the turbine cannot start by itself, it is necessary to use auxiliary start equipment.

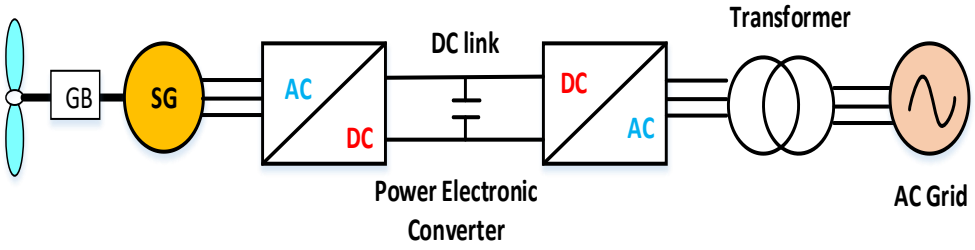


Figure 2.5: Full Variable speed wind turbine of an induction or synchronous generator [24]

### 2.3.3 Fixed Speed Wind Turbine

Fixed-speed wind turbine generator (FSWG) technology has an important presence in countries where wind energy started to be developed more than a decade ago. This kind of wind turbine generator consists of an Induction Generator (IG) which is connected directly to the grid as depicted in Figure 2.6. The speed of this turbine is fixed and determined by the grid frequency, gearbox and the pole-pair number of the generator.

Fixed speed is mechanically basic, stable, reliable and well-demonstrated. They incur lower cost for maintenance and electrical parts. However, they experience the ill effects of the inconvenience of mechanical stress, limited power quality control, and poor wind energy conversion efficiency [24], [28].

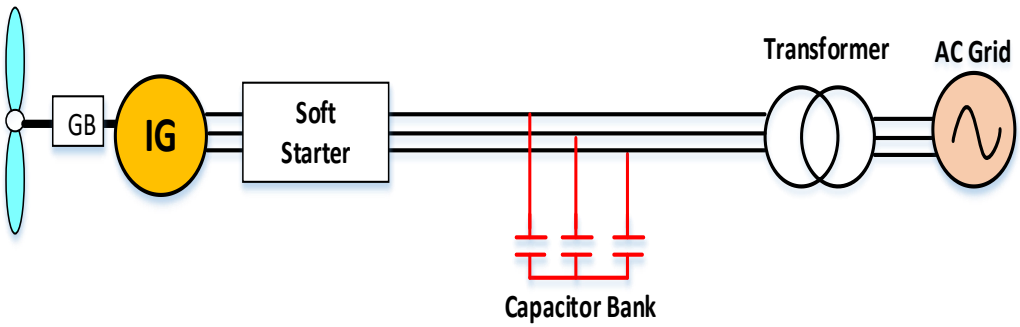


Figure 2.6: Fixed speed turbine with an induction generator [24]

## 2.4 Grid Integration of Offshore Wind Farms

Wind farm developers and the transmission system operators are facing a number of technical, economic, and environmental challenges in transmitting the bulk power developed at these offshore wind farms over long distances (up to 150 Km far from the coast) [29]. Some of these issues are explained in the following sections, emphasizing basic system requirements along with various options for transmission and grid integration.

The key factors to consider in offshore wind farm connection design are the trade-offs between the initial capital investment, power losses, availability due to scheduled maintenance or wind turbine failure, and other system faults [6], [25], [30], [31]. The availability and reliability issue is particularly important as the repair process is very difficult in the marine environment. The electrical system of a wind farm can be considered as several distinct subsystems. As shown in Figure 2.7, the electrical system of OWF typically consists of five sub-systems [6], [30], [31].

- Wind farm (generation)
- Power collection
- Voltage step up
- Transmission system
- AC grid

The composition of each subsystem depends on whether an AC System, a DC system, or a combination of both are used in the grid integration.

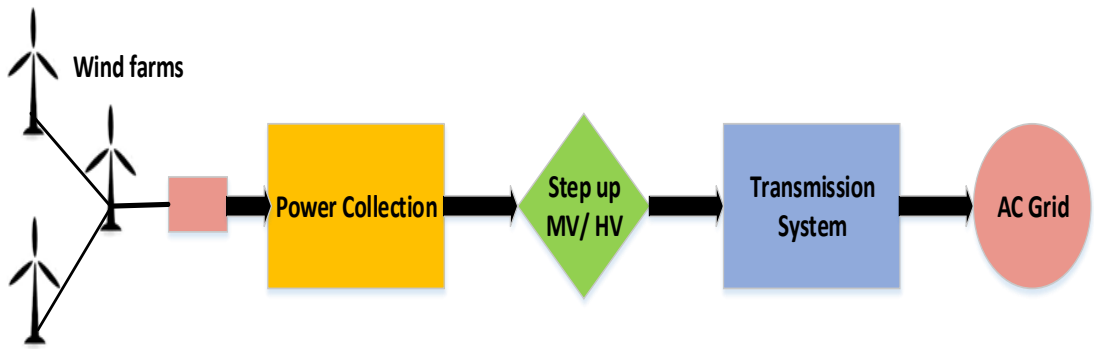


Figure 2.7: The different components on OWF's electrical system

## 2.5 HVAC System

Since the development of transformers, which allow for high power and insulation level, low losses, relatively simple implementation, and low maintenance, HVAC systems have become the dominant technology for electricity transmission and distribution all over the world [32]. Moreover, as the electricity generated within a wind farm is in the form of AC, HVAC presents itself as a logical and rational technique to transfer the power generated offshore into the electric grid.

### 2.5.1 High Voltage Alternating Current Connection (HVAC)

The HVAC connection has been used so far in all offshore wind farms to transport electrical power from the wind farm to the onshore grid [14], [33], [34]. The HVAC solution is the most straightforward technical approach with ease of interconnection, installation and maintenance, operational reliability and cost-effectiveness. However reactive power issues limit the maximum distance of transmission, which is approximately 50km [14], [34], [35]. It is a well-established technology; the following are the main components:

- AC collection system
- Offshore substation with transformers and reactive power compensation equipment
- Three-phase submarine cable
- Onshore substation with transformers and reactive power compensation

The electrical system depends on the distance and the wind farm capacity. For short distances, if the connection voltage is at the distribution level, high voltage transmission may not be necessary and hence the number of voltage transformations is reduced. If the transmission distance is long, the number of cables and the losses are too high and a rise in the transmission voltage is necessary. Horns Rev Wind Farm in Denmark, with a power of 160 MW and a transmission distance of 21 km, is the first offshore wind farm using HVAC, as shown in Figure 2.8. An offshore AC collector platform is used to collect energy from the wind farm and step up the voltages for transmission to the onshore substation [34], [35].

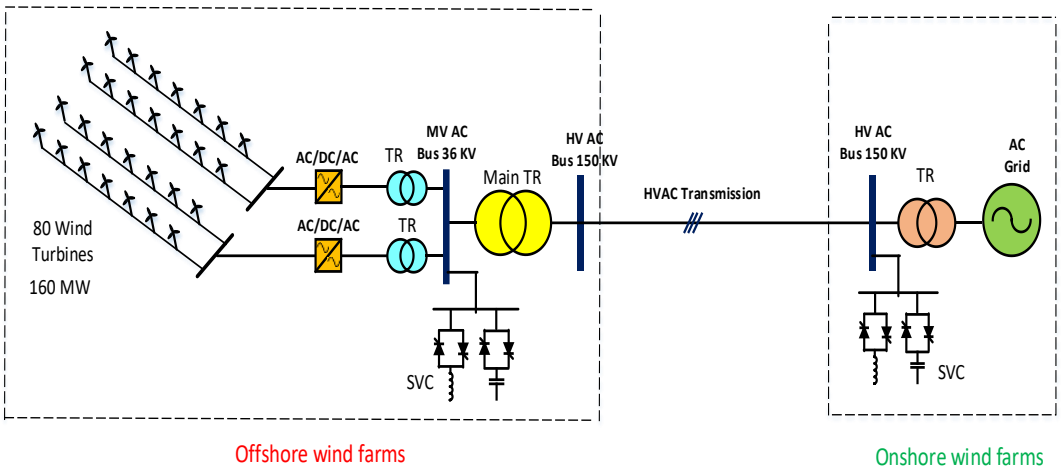


Figure 2.8: The basic configuration of the Horns Rev wind power plant with an HVAC transmission system solution [35]

The distributed capacitance in submarine cables is much higher than the capacitance in overhead lines [25], [35], [36]. Therefore, due to economic and technical reasons, the practical transmission length is short for marine applications. Reactive power increases with voltage and length of the cable and long transmission distances require large reactive compensation equipment at both ends of the line such as shunt reactors, STATCOM, and static var compensator SVC [25], [36]. Therefore, for longer transmission lengths HVDC is the only option.

### 2.5.2 MVAC Collector Systems

There are a number of possible turbine arrangements in wind farm MVAC collector systems, namely, radial layout, star connection, and double-sided ring collector systems [25], [35], [37].

#### 2.5.2.1 Radial Collector Systems

A radial collector system (CS), also known as a string, is that in which a number of offshore wind turbines (OWTs) are connected to a single cable feeder within a string as shown in Figure 2.9. Such a system is used in Barrow, Thorntonbank-1, and Belwind-1 [25].

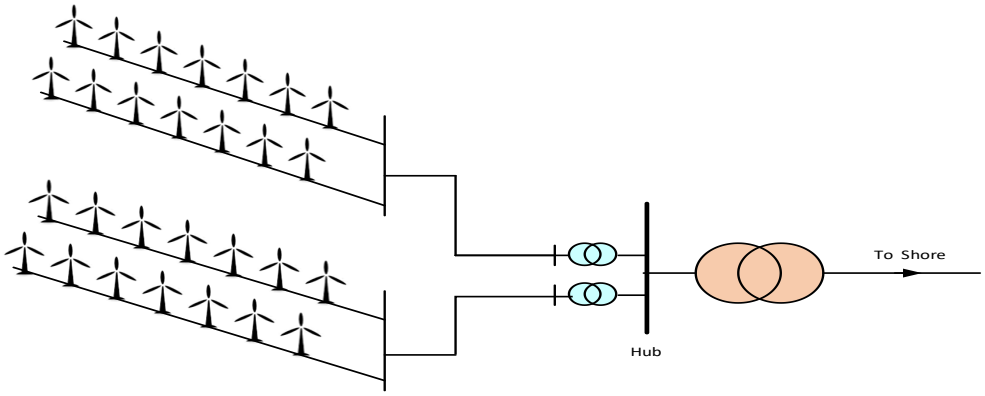


Figure 2.9: AC radial system collection

The number of wind turbines on each string feeder is determined by the capacity of the generators and the maximum rating of the MVAC submarine cable within the string. Its advantages are in the simplicity of control and the shorter total cable length. Its major drawback is poor reliability, as cable or switchgear faults at the hub end of the string can prevent all downstream turbines from exporting power [37].

#### 2.5.2.2 Star Connection

The main purpose of the star connection is to reduce cable ratings and to provide a high level of security for the entire wind farm as illustrated in Figure 2.10. Voltage regulation along the cables between wind turbines is also likely to be better in this design [36], [38], [39]. However, there are additional expenses due to the longer diagonal cable runs and some short sections of higher-rated cabling; but these expenses are not likely to be significant. The main advantages of star topology are better voltage regulation and reliability.

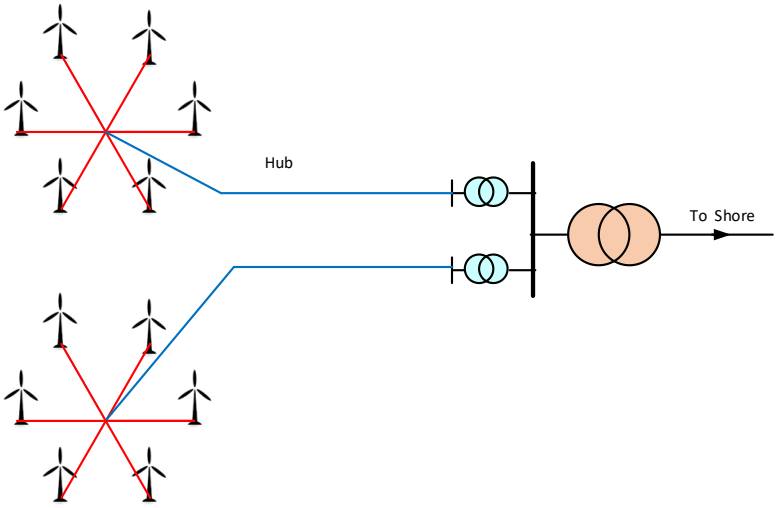


Figure 2.10: AC star system collection

#### 2.5.2.3 Sided Ring

Sided ring design as shown in Figure 2.11, is a way to lower losses through high voltage collection and provide greater security. However, this kind of connection requires much more expensive high voltage cables [14], [36], [38]. This layout has higher reliability compared to the radial layout. In the case of a fault, the radial connection (in normal operation) can be reconfigured and the energy produced is not lost. Because of larger cable sections, longer cable length (connections between collector groups) and, more complex systems (depending on location and number of reconfiguration switches), this solution implies higher investment costs [14], [38].

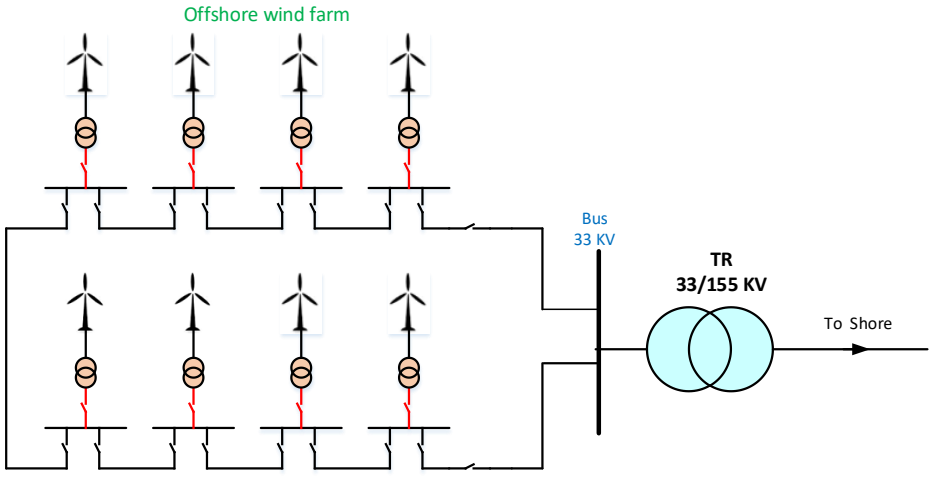


Figure 2.11: Sided ring system collection

## 2.6 HVDC Systems

HVDC is an established technology that has been in commercial use for 60 years. During the first 30 years, it was a niche technology, with a limited number of installations per year. With changes in demand due to evolving environmental needs, HVDC has become a common tool in the design of future global transmission grids [40], [41].

HVDC systems may be used to transmit large amounts of electrical power more economically over longer distances, than an equivalent alternating current (AC) transmission system. This means fewer transmission lines are needed. In addition to significantly lowering electrical losses over long distances, HVDC transmission is also very stable and easily controlled, and can stabilize and interconnect AC power networks that are otherwise incompatible [40].

### 2.6.1 HVDC Connection

As offshore wind farms become larger and more distant from the shore, the argument for using HVDC to transmit the power to the onshore network is strengthened. In Figure 2.12, an example of an offshore wind farm with a DC transmission system is illustrated [42]. The costs of the converter stations, offshore and onshore, are significant in themselves, but when put in the context of the complete project cost, including the cables and the wind turbine generators, the DC system becomes economical.

Two types of converters are available, the Line-Commutated Converter (LCC) and the more recently introduced Voltage-Source Converter (VSC). For offshore wind power, an LCC converter is not suitable, because it requires a strong network voltage to commutate, and wind farms usually have weaker grids that cannot supply such a strong voltage. In addition, the capability to energize the system from shore (black start) is a challenge [41]. These issues can be alleviated by combining the LCC-interface for an offshore wind farm with some auxiliary source of reactive power. The LCC produces considerable AC side current harmonics that require filter banks [41], [43].

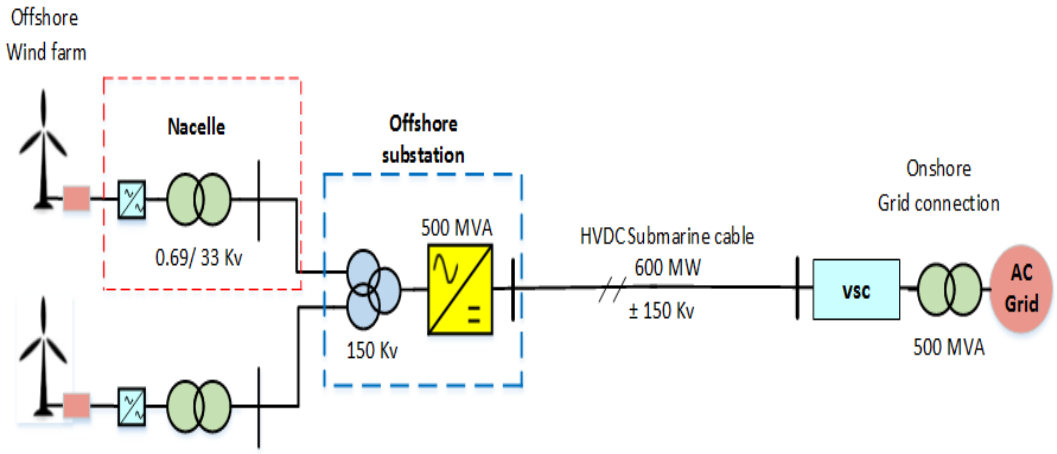


Figure 2.12: A 500 MW wind power plant using one HVDC-VSC system based on a converter station with a 500 MW rating [42]

High power Insulated Gate Bipolar Transistor development has enabled the realization of VSCs which is a very good candidate for HVDC systems with much lower harmonic distortion than HVDC-LCC systems, although with higher power losses [38]. The VSC is able to control active and reactive power independently and generates a voltage on the AC side. It is therefore, able to operate in weak networks [36], [38]. The main drawback of the VSC is its lower current capability. Even for very short durations, over currents cause thermal stresses that degrade or cause permanent damage to the switching elements [38].

During the last decade, there have been several studies focused on the comparison between HVAC and HVDC transmission systems for offshore wind farm [17], [31] [44], [45], [46]. In Table 2.1, a summary of the main features of both technologies when employed to connect offshore wind with the onshore main grid is presented [25], [30].

Table 2.1: Comparison of HVAC and HVDC – VSC point-to-point links for (OWF).

| HVAC transmission system | VSC-HVDC transmission system |
|---|---|
| Reactive current increased losses reduce cable capacity and demand compensation devices | No charging current and no limit on transmission distance beyond practical constraints. |
| Considerable experience in project development and OWF operation | Very little experience in VSC-HVDC links for OWFs |
| Limited control capability on active and reactive power with STATCOMs | Independent full control of active and reactive power at both ends. Black-start capability feasible |
| Lower cost and losses in substations | Higher losses in electronic converters and higher cost of offshore substations. |

### 2.6.2 DC Collection System

The control structure and the different possible configurations of DC collection systems are discussed in [26], [41]. Conceptually, MVDC collector systems are those linking turbines with DC output and an HVDC transmission link to shore. In a general sense, the arrangement of these Collector Systems (CSs) can be one of those previously commented on for MVAC collector systems.

In general, DC collection systems consist of several clusters, which are connected either in parallel or in series [26], [47]. Since the difference between the output power of each turbine and the total power transferred to the shore is significant, several voltage steps are needed. Consequently, a DC-DC converter system is needed for stepping up the voltage in. There are several DC collection schemes for offshore wind farms as discussed below [47].

The pure DC grid in the offshore wind farm is presented in [19], [35], [41] and consists of several clusters, where a number of wind turbines with DC output are connected in parallel in each cluster. These clusters are collected by an offshore DC-DC converter which increases the voltage to a transmission level for the HVDC link connecting to the AC grid onshore [19], [41].

#### 2.6.2.1 Configuration A

The structure of this configuration is depicted in Figure 2.13, and described in [41]. The first MV DC-DC converter is used to step up the voltage after each

turbine, up to the medium voltage level. There is a short cable length between the wind turbine strings and the collection bus of about 5 km and the collection bus voltage is rated at 30 kV, afterward the power is collected and stepped up a second time by HV transmission converter [29], [37], [26]. After that, HV DC voltage is sent by submarine DC cable to an onshore substation. In addition, the platform DC converter is rated at 400 MW.

The main advantage of this configuration is the direct step-up of the voltage after the turbine generator. This leads to reduce DC cable losses at the distribution panel. In addition, this kind of converter system can be controlled individually. One drawback of this converter system is the additional DC-DC converter, which means there are extra losses and a higher investment cost.

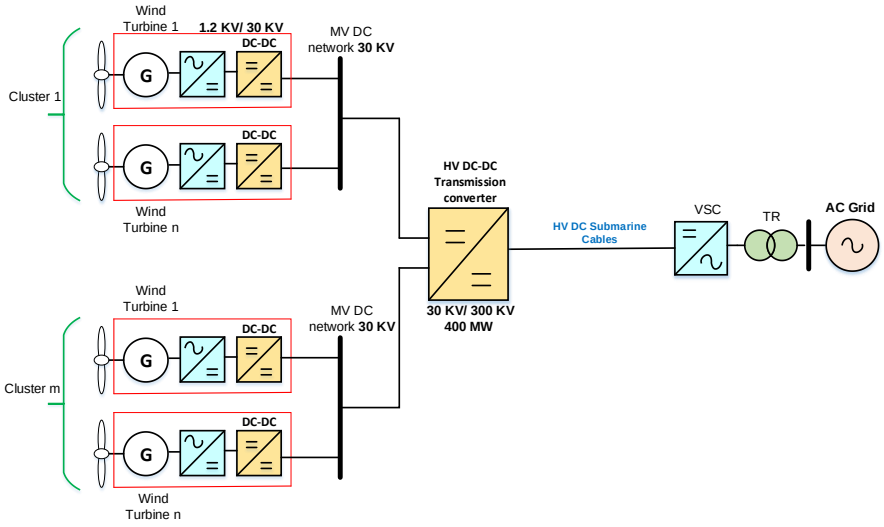


Figure 2.13: Configuration A

### 2.6.2.2 Configuration B

In this arrangement, the power is collected first in the MV network, then a DC-DC converter steps up the voltage to a level suitable for HVDC cable transmission as depicted in Figure 2.14. Since the number of converters is lower, the transformers are eliminated, and this design will lead to lower losses when compared with the arrangement shown in Figure 2.13. However, only two voltage levels with one DC-DC converter are used and consequently, the distribution level strongly depends on the generator voltage [25], [37].

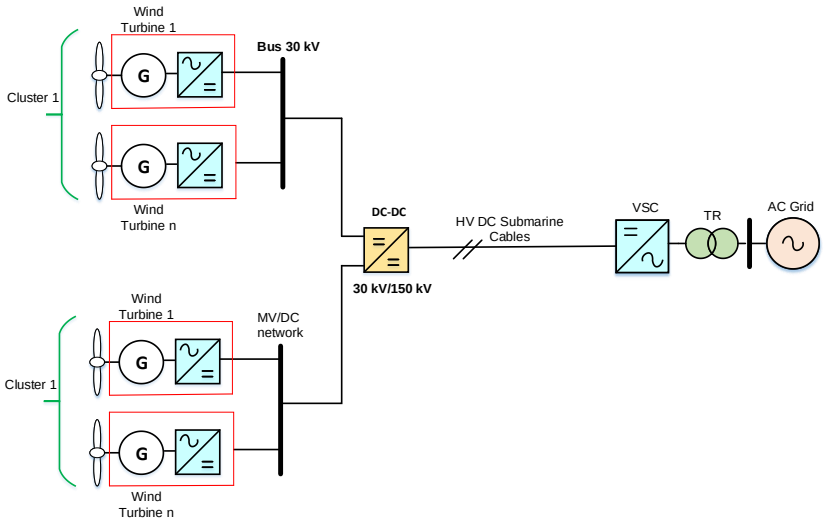


Figure 2.14: Configuration B

### 2.6.2.3 Configuration C

The structure of this configuration is a single DC-DC converter, which is connected directly to each turbine as shown in Figure 2.15. Two voltage levels are used with reduced losses at the distribution level, because of the high voltage. Nevertheless, the output of the DC-DC converter needs to be designed for the transmission voltage with a high power level [37], [26], [47]. In addition, the design of these DC-DC converters is based on the capacity of each turbine generator, which then is reduced the cost of the second DC-DC converter when compared with configuration A.

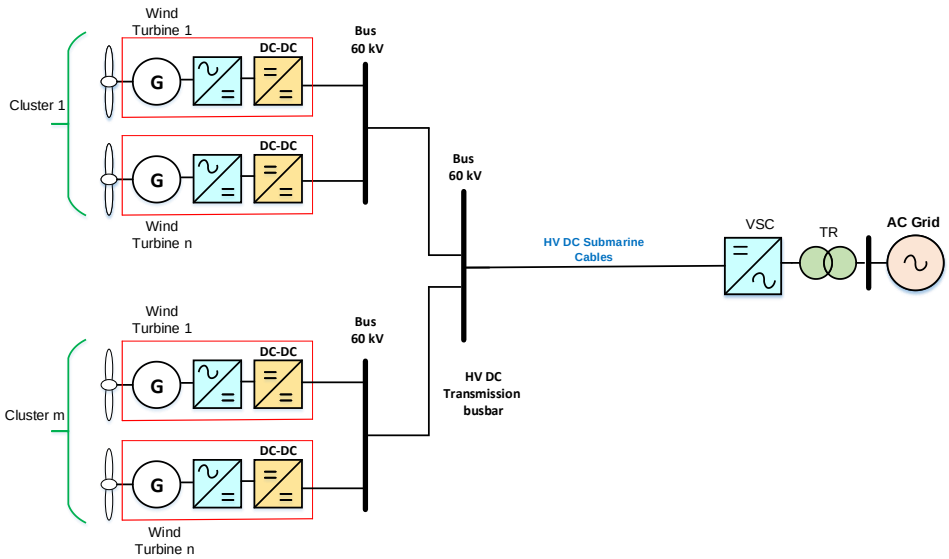


Figure 2.15: Configuration C

### 2.6.2.4 Configuration D

The structure of this configuration is similar to Figure 2.13, but the location of the DC-DC converter is not beside the turbine generator. A group of wind turbines with DC output in strings is connected to HV DC-DC converters [41]. (Referred as MV DC converters). The MV DC-DC converters are placed closer to the turbine's generator. The collection bus voltage in each MV DC-DC converter is rated at 30 kV. The main advantage of this configuration is that the DC-DC converters located at each wind turbines are removed. This helps to reduce the number of power electronic converters in the wind turbines.

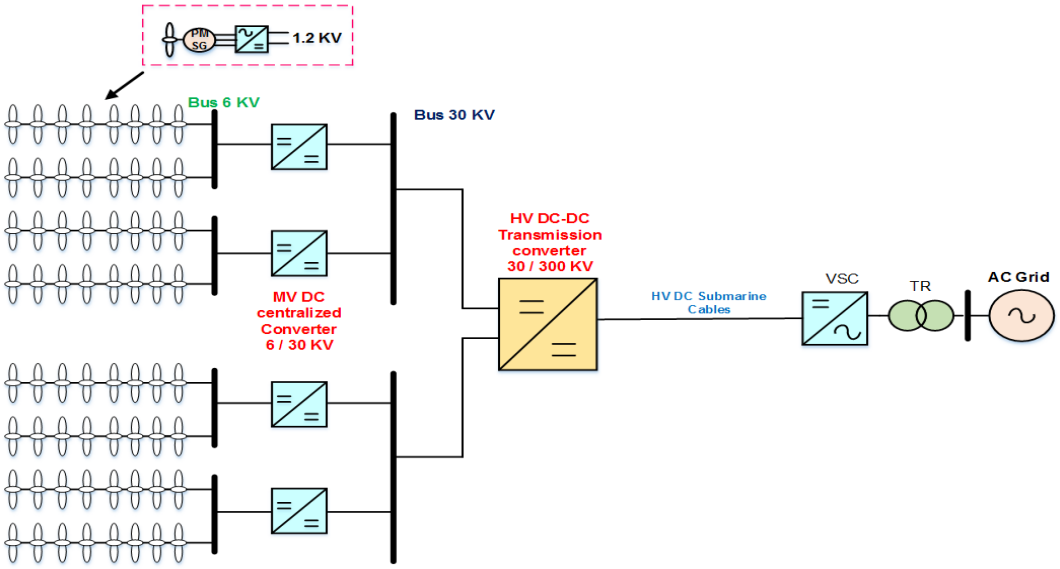


Figure 2.16: Configuration D

### 2.6.2.5 Configuration E

This configuration used to eliminate the DC-DC converter connecting the wind farm to the HVDC link is to connect the wind turbines in series as depicted in Figure 2.17. In this configuration, the HVDC transmission voltage is obtained by adding the output DC voltage of each turbine which are connected in series [41], [43]. The drawback of this configuration is that the output dc voltage for the turbine must be overrated in the case of the loss of a turbine, and the high potential present in the turbines. Nevertheless, the main advantage of using this configuration is reducing the DC-DC converter towards the HVDC link.

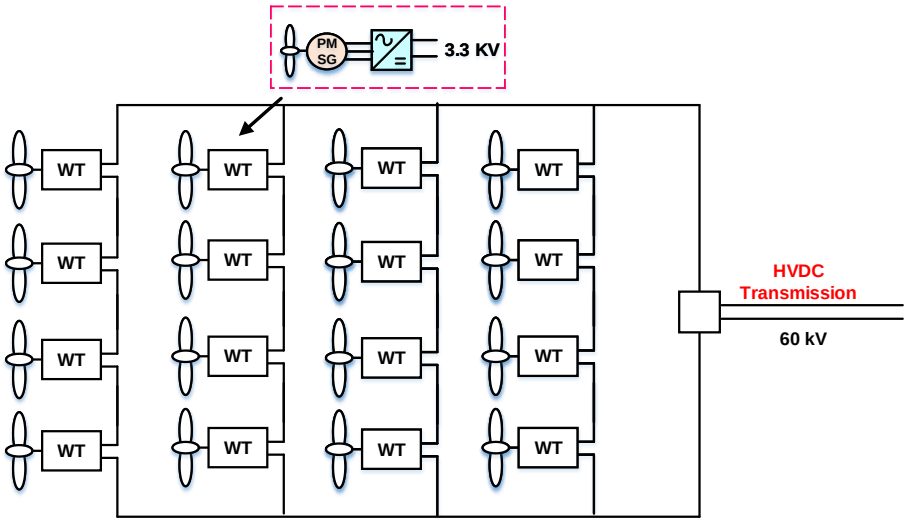


Figure 2.17: Configuration E

### 2.6.3 Characteristic of DC Collection Grids

The purpose of this chapter is to highlight the factors that enable the DC collection grid to be superior to existing AC collection grids. The challenges that need to be addressed are listed as well.

#### Advantages

+ Heavy AC transformer in the turbine is unnecessary.
+ No contribution from reactive power in the grid.
+ Two phases instead of three phases.
+ No skin and proximity effects - only resistive losses in the cables.
+ DC-DC converters can have a modular structure.
+ Pure DC-DC conversion decreases component size

#### Challenges

- Technology is untested in large-scale Megawatt (MW) application
- No DC-standards - regulation essential
- Challenges arise with a DC-DC converter
- Fast DC-breakers to limit short-circuit currents are essential

## 2.7 Summary

In this chapter, a review of the grid integration technologies of offshore wind farms is presented; the layout and components for a wind farm with an internal AC and DC grid are described. A comparison between DC and AC collection systems for offshore wind farms is made. DC collection systems have the advantages of reduced weight and size of the DC cables and DC cables are free from reactive power compensation.

The heavy 50/60 Hz transformers in the offshore transmission platform of AC collection systems can be replaced with smaller size DC-DC converters in DC collection systems. However, the need for a high-power DC-DC converter with high voltage transformation ratios will remain a challenge for DC collection systems. As more large wind farms are planned for offshore locations, HVDC transmission will be a more common transmission solution for new wind farms. In addition, there are suggestions for having multi-terminal HVDC systems connecting several wind farms as in European countries in the North Sea. It was stated that the DC-DC converter, as well as the protection devices for the DC wind farm, are key components that require further development and are not commercially available.

In the next chapter, a general overview of DC-DC converters is presented before particular attention is dedicated to two approaches to DC-DC converters.

# Chapter 3

## Overview of Existing DC-DC Converter Topologies

## 3.1 Introduction

DC-DC converters are key components in a wide variety of fields, such as motor control, switch mode DC power supply, wind farms and photovoltaic (PV) cells [48]. As discussed in Chapter 2 for DC power collection in a wind farm, a MW-level DC-DC converter is required to step up the relatively low DC voltage from the integrated rectifier of the wind generator to a high DC voltage suitable for transmission to shore. Therefore, a DC-DC converter is a core component in a HVDC system for the grid integration of wind farms.

In this chapter, several DC-DC converter topologies including, isolated DC-DC converter, non-isolated DC-DC converter are explained and their possibilities for HVDC application such as wind farms are explored.

## 3.2 DC-DC Converter Topologies

The DC-DC converter topologies can be classified into two types: isolated and non-isolated converter topologies. An isolating transformer is used in the isolated topologies. Table 3.1 shows some basic DC-DC converter topologies.

Table 3.1: DC-DC converter topologies

| **Isolated converters** | **Non-isolated converter** |
|---|---|
| Half Bridge Converter | Boost Converter |
| Full Bridge Converter | Ćuk Converter |
| Dual Active Bridge converter | Buck-Boost Converter |
| Cascaded H-bridge Converter | Multilevel Converter |
| Modular Multilevel Converter | Marx DC Converter |

The block diagram shown in Figure 3.1, represents a conceptual DC-DC converter; where the input current, the input voltage, the output current and the output voltage are denoted by $I_{in}$, $V_{in}$, $I_{out}$, and $V_{out}$ respectively.

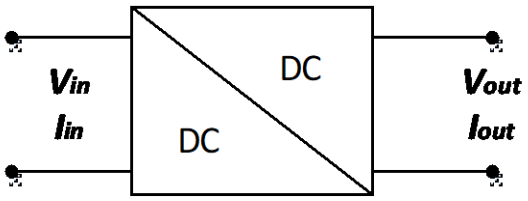


Figure 3.1: DC-DC converter block diagram

The technology of the DC-DC converter is well established for use as the interface between DC systems of different voltage levels. The basic DC-DC converter, in generic terms, contains two switching elements, one series connected, and the other shunt connected as shown in Figure 3.2. In the past force commutated thyristors, Gate Turn off Thyristors (GTO), diodes and bipolar junction transistor (BJT), have been used as the switching elements [49],[50]. However, with the advent of MOSFETs and IGBTs, those two devices are now exclusively used in new designs.

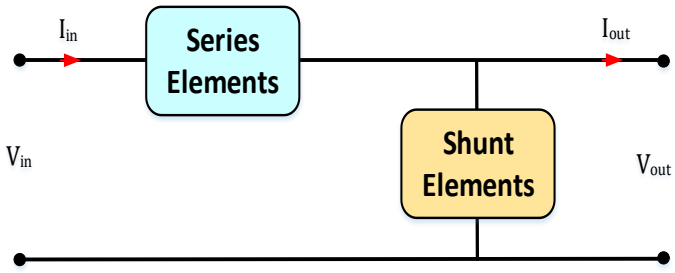


Figure 3.2: Generic DC-DC converter

### 3.2.1 Non-Isolated Converters

The non-isolated DC-DC converter topologies normally use the same reference for their inputs and outputs. A number of non-isolated converter topologies based on the concept described above have been successfully applied at low to medium applications such as switched mode power supplies, traction drives, electric vehicles, railways.

Such converters use one active switch in the circuit and the choice of a single semiconductor switching device that can withstand high DC voltage stresses is limited. Currently, there are two IGBT switches such as 4.5 kV, and the maximum

current is 2400 A, the second IGBT, the voltage rating of a single IGBT is limited to 6.5 kV with a maximum nominal current of 750 A, and the cost is high [51]. Therefore, the operating voltage level in many studies challenges most of the existing technologies since both the input and output of the DC-DC converter must operate above the voltage capability of existing power semiconductors. All such approaches are reviewed and discussed in the following sections.

#### 3.2.1.1 Boost Converter

Boost converter is one of the non-isolated DC-DC converters as shown in Figure 3.3, where its output voltage is always higher than the input voltage ($V_{out} > V_{in}$) [52]. This topology has a simple structure and a few components as depicted in Figure 3.3. The circuit is composed of one IGBT switch, inductor, capacitor, diode, and DC supply. Generally, the Pulse Width Modulation (PWM) is controlling the duty cycle on the boost converter. When the active switch $S_N$ is 'ON', and while the switch $S_N$ is 'OFF', both energies from the input and stored energy are dumped into the output load. The current will charge path from the input through the inductor *L* and to the negative of the circuit.

If the switch $S_N$ is turned 'ON', the input voltage is applied across the inductor *L*, and then the current through the inductor is increased linearly. Meanwhile, the capacitor *C* feeds the load with energy while reducing the voltage across the capacitor. When the switch $S_N$ is turned 'OFF', the current flows through the inductor *L* and supplies the load via the diode '*D*' as shown in Figure 3.3.

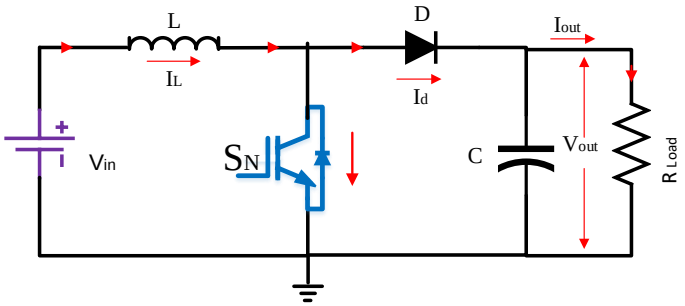


Figure 3.3: Ideal boost converter

In continuous conduction mode, as shown in Figure 3.4, the current through inductor $L$ does not reach zero before the next switching time, but if the inductor current reaches zero before next switching time, then it is called discontinuous condition mode. The relationship between the output voltage $V_{out}$ and input voltage $V_{in}$ can be expressed as

$$\frac{V_{out}}{V_{in}} = \frac{1}{1-d} \tag{3-1}$$

where $d$ is the duty cycle ratio and is defined as

$$d = \frac{t_{on}}{T_S} \tag{3-2}$$

where $T_S$ is the switching time and $t_{on}$ is the conduction time of the switch $S_N$. The output DC voltage in the converter is dependent on the duty cycle $d$ ($\leq 1$) and can be calculated as

$$V_{out} = \frac{V_{in}}{1-d} \tag{3-3}$$

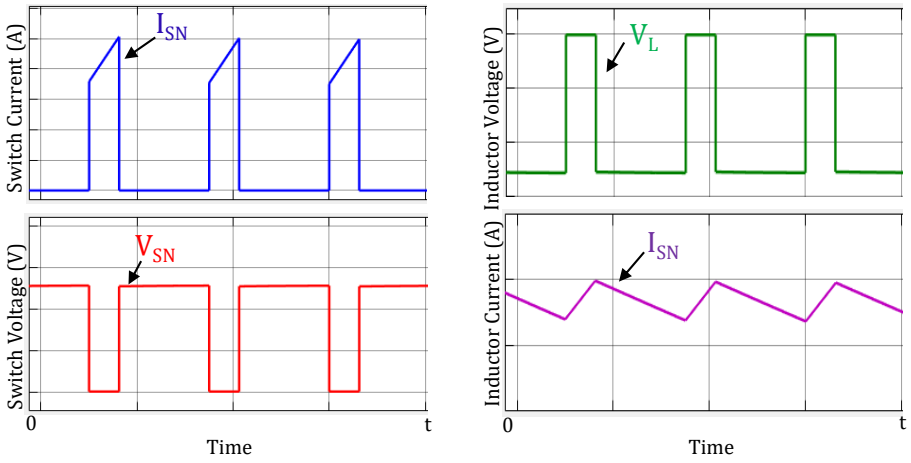


Figure 3.4: Switch current, voltage, inductor current, and voltage waveforms

#### 3.2.1.1.1 Advantages and Disadvantages

There are two main advantages as follows:

+ Very simple converter, it comprises just two active components and two passive components.
+ Its continuous mode operation has low input ripple.

The main disadvantages of this converter are:

- When the duty cycle is high, then the switch current becomes large.
- Unidirectional converter due to the diode *D*.
- High switching frequency. However, it is used in low power applications.

#### 3.2.1.2 Ćuk Converter

This converter, named after Dr. Slobodan Ćuk, who invented it in the 1980's [53], is similar to a boost converter. However, it has a simple structure and a few components as shown in Figure 3.5. This converter is used when a small current ripple is needed with voltage changes [54].

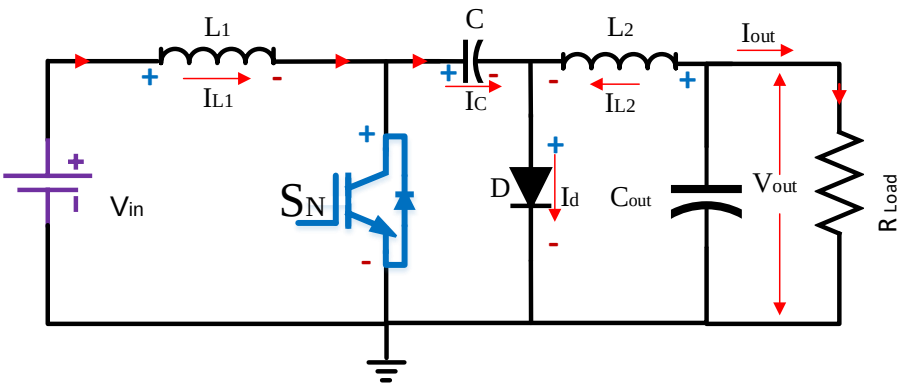


Figure 3.5: Ćuk converter configuration

The Ćuk converter uses the capacitor *C* to transfer the energy instead of using the inductor in the boost converter. Therefore, this converter shifts the energy form the input voltage and the capacitor *C* to the load via inductors $L_1$ and $L_2$. The control switching of the switch is similar in the boost converter.

As shown in Figure 3.6, in the first switching period, the switch $S_N$ is turned 'ON', the current flows through inductor $L_1$. Therefore, the current in inductor $L_1$ increases linearly and the capacitor *C* discharges through inductor $L_2$. In the second switching period, the switch $S_N$ is turned 'OFF', the inductor $L_1$ charges the capacitor *C* via the diode *D* and the inductor $L_2$ feeds the load as shown in Figure 3.6, to achieve low input and output ripple currents the converter usually operates in continuous conduction mode.

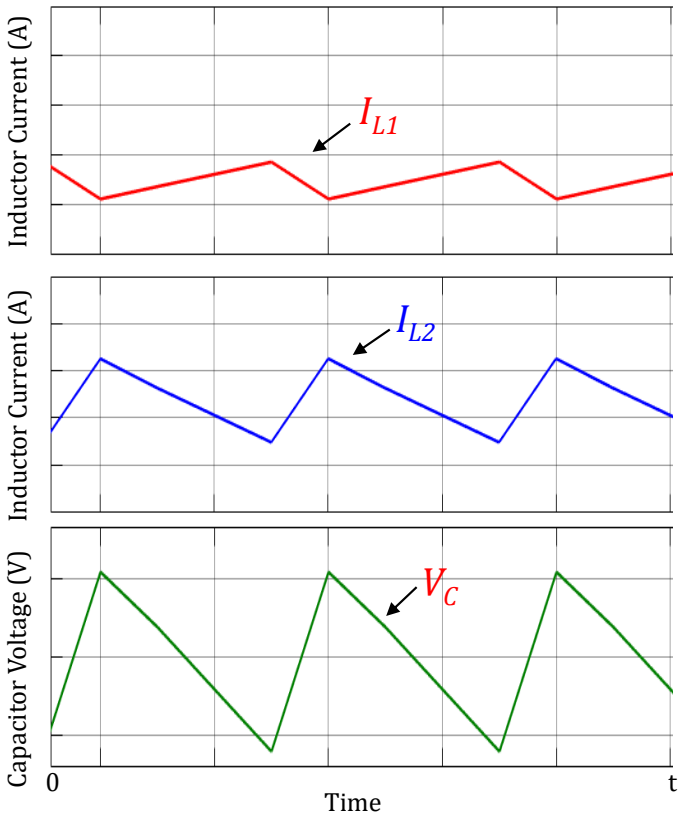


Figure 3.6: Capacitor and inductors waveforms in continuous conduction mode ($d$= 0.75)

Figure 3.7 shows the waveform of switch $S_N$ current and voltage in continuous conduction mode. The output DC voltage in the converter is dependent on the duty cycle '$d$' and can be expressed as;

$$\frac{V_{out}}{V_{in}} = -\frac{d}{1-d} \qquad (3\text{-}4)$$

#### 3.2.1.2.1 Advantages and Disadvantages

The main advantages of the Ćuk converter are

+ In continuous conduction mode, the input and output ripples are small i.e., $I_{out} \geq (V_{out}\, d^2)/(2LF_S)$, where $F_S$ is the switching frequency.
+ Simple construction, it has just two active components (IGBT switch $S_N$ and diode $D$).

+ This converter is suitable for variable voltage and low current application due to its features of wide gain and high switch current stress.

The main drawbacks of this converter are

- The switch $S_N$ must handle the sum of the input and output currents.
- The currents $I_{L1}$ and $I_{L2}$ both flow through the capacitor $C$ to the ground line, therefore the current ripple for the capacitor is significant.
- Unidirectional power flow converter.
- Need to be switched at frequencies higher than the power frequency and the switching frequency can be as high as 50 kHz in some applications.

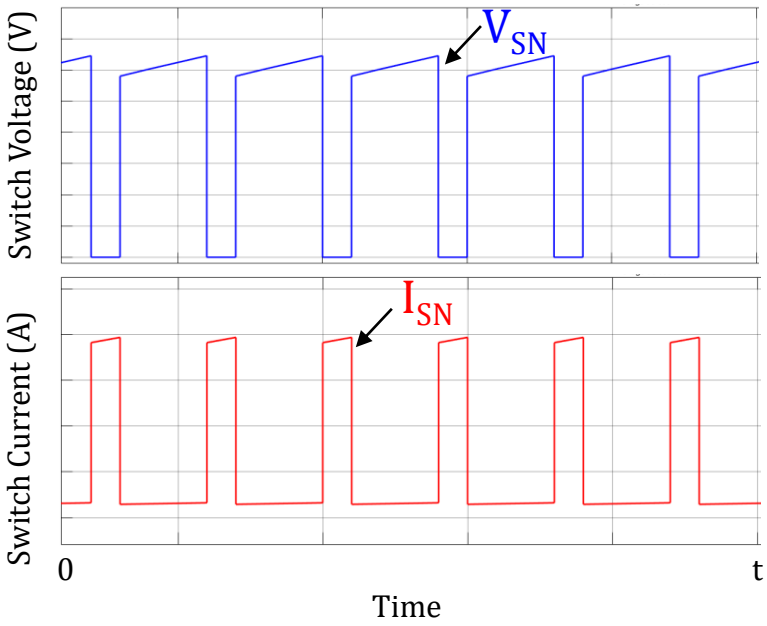


Figure 3.7: Ćuk converter- switch voltage and current waveforms continuous conduction mode ($d$ = 0.75)

### 3.2.1.3 Buck-Boost Converter

This converter is a mix of buck and boost converter, which is used when the output voltage $V_{out}$ is higher or lower than the input voltage $V_{in}$ [55]. Its schematic is illustrated in Figure 3.8. In the first interval, when energizing switch $S_N$ is *'ON'*, the current through the inductor $L$ rises linearly. At this time, the diode $D$ is reverse biased and the capacitor $C_{out}$, supplies the load current, and the capacitor $C_{out}$ is partially discharged.

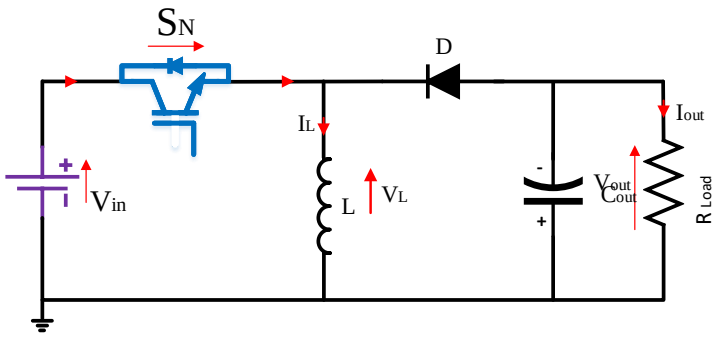


Figure 3.8: Buck-boost converter schematic

During the second interval, when switch $S_N$ is turned 'OFF', the voltage across the inductor reverses. Therefore, the inductor $L$ drains the current through the diode '$D$' (forward bias). This generates a negative output voltage $-V_{out}$ and the energy stored in the inductor and recharges the capacitor will feed the load. The steady state of current, voltage switch $S_N$ and voltage, current inductor waveforms are shown in Figure 3.9.

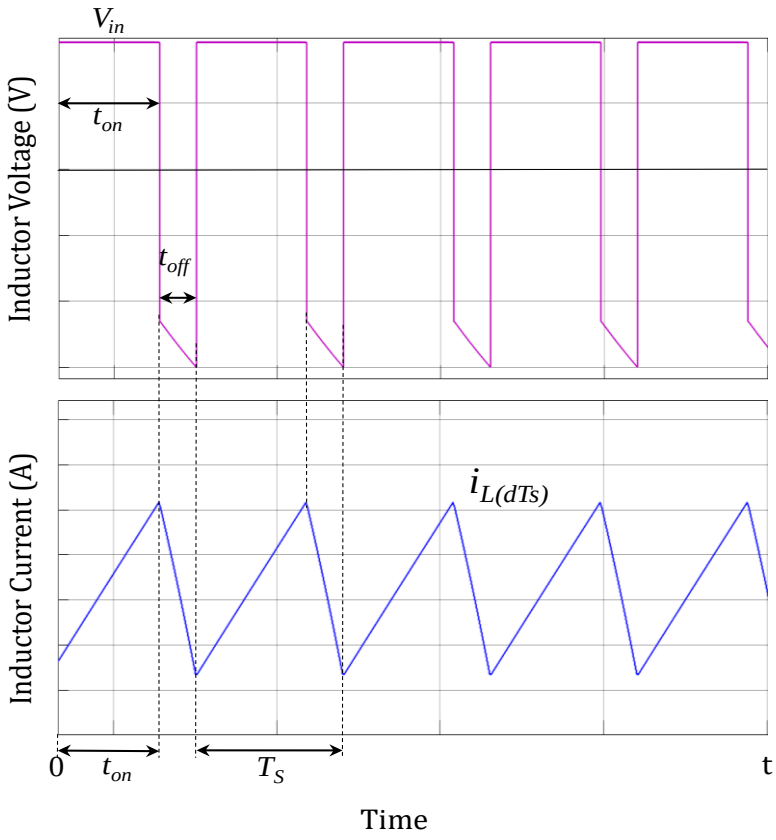


Figure 3.9: Steady-state inductor current and voltage waveform

The relationship between the input voltage, output voltage and the switching time can be given as;

$$V_{in}\, t_{on} = V_{out}\, t_{off} \qquad (3\text{-}5)$$

Therefore, the ratio of the input and output current can be given as

$$\frac{I_{out}}{I_{in}} = \frac{1 - d}{d} \qquad (3\text{-}6)$$

The voltage conversion ratio $N_{(buck\text{-}boost)}$ of the buck-boost converter can be expressed as;

$$N_{(buck\text{-}boost)} = \frac{V_{out}}{V_{in}} = \frac{-\, t_{on}}{T_S - t_{on}} = \frac{-\, d}{1 - d} \qquad (3\text{-}7)$$

where $d$ is the duty cycle, $t_{on}$ is the conduction time and $T_S$ is the total switching time. The duty cycle $d$ is varied, $d = (0\sim1)$. Hence, the magnitude of the output voltage can be higher or lower than the input voltage and opposite in polarity.

#### 3.2.1.3.1 Advantages and Disadvantages

The advantages of the buck-boost converter are

+ Buck-boost converter is able to step up or step-down input voltage.
+ This converter has been successfully applied at low power application [55].

The disadvantages are as follow:

– Buck-boost converters require an input filter to reduce current ripple.
– The polarity of the output voltage is the opposite of the input voltage.
– The output current is discontinuous and hence a large output capacitor is required to reduce ripple voltage.
– Unidirectional power flow.
– Need to be switched at frequencies higher than the power frequency and the switching frequency can be as high as 50 kHz in some applications.

#### 3.2.1.4 Multilevel Converter

The first multilevel converter concept was developed in 1975 [56], then several multilevel DC-DC converter topologies have evolved for high voltage application. These converters comprise a large number of active semiconductor switches to perform the power conversion in small voltage steps. Generally, a multilevel converter uses a series of active switches and several DC capacitors as DC sources to generate and step up the voltage.

Multilevel DC-DC converters can outperform conventional converters and have many advantages [56],[57]:

+ Low switching frequency and decrease switching losses. Hence, its efficiency is improved.
+ Low distortion for the input current.
+ Due to the high number of voltage levels, its output voltage quality is improved.
+ Provide ride-through capability under emergency conditions.

The major drawbacks of the multilevel converter are, a higher number of semiconductor switches and the complex nature of the power circuit and control. As depicted in Figure 3.10, several types of DC-DC multilevel converters exists.

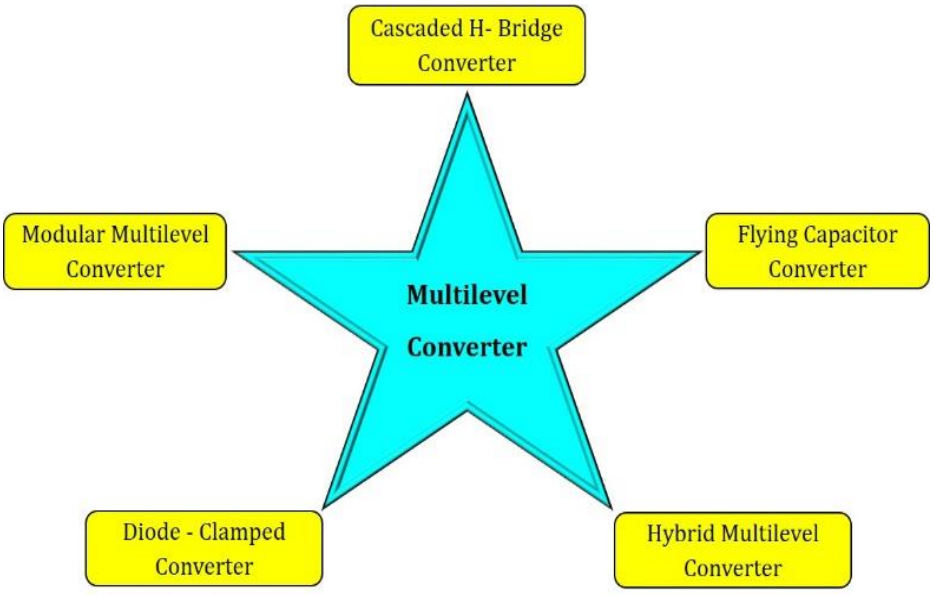


Figure 3.10: Types of multilevel converters

#### 3.2.1.4.1 Flying Capacitor Multilevel Converter

The first flying capacitor multilevel converter was introduced in 1992 [58]. This multi-level converter is similar in structure to the diode- clamped converter, only replaced the clamped diodes with the capacitors. Figure 3.11(a) and Figure 3.11(b) show the structure of four and five-level flying capacitor multilevel converter [59],[60],[61].

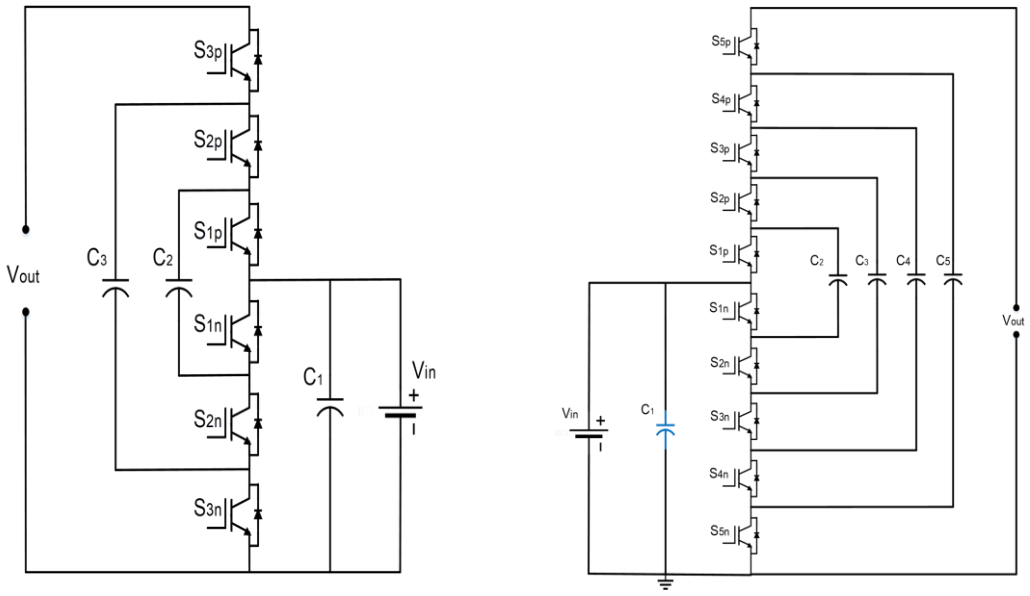


a) Four-level converter b) Five-level converter

Figure 3.11: Structure of flying capacitor multilevel converters

As can be seen, a four-level flying-capacitor multilevel converter consists of three flying capacitors $C_1$, $C_2$, and $C_3$ connected with six active switches $(S_{1p}\text{-}S_{3p})$ and $(S_{1n}\text{-}S_{3n})$. Table 3.2 lists the switching schemes of the converter. The output voltage, equals to $3V_{in}$. The voltages across $C_1$, $C_2$, and $C_3$ are $1V_{in}$, $1V_{in}$, and $2V_{in}$ respectively. The total voltage gain of the configuration can be expressed as

$$\frac{V_{out}}{V_{in}} = (2n+1)\frac{1}{1-d} \qquad (3\text{-}8)$$

where '$d$' is the duty cycle of the flying capacitor converter, and '$n$' is the number of flying capacitors in a top and bottom cell.

Table 3.2: Pattern switching of four-level flying capacitor converter

| Switching state | $S_{1p}$ | $S_{2p}$ | $S_{3p}$ | $S_{1n}$ | $S_{2n}$ | $S_{3n}$ |
|---|---|---|---|---|---|---|
| Sub-period 1 | 1 | 0 | 0 | 0 | 1 | 1 |
| Sub-period 2 | 0 | 1 | 0 | 1 | 0 | 1 |
| Sub-period 3 | 0 | 0 | 1 | 1 | 1 | 0 |

The voltage stress on each switching device is tantamount to the voltage rating of each capacitor. The output voltage gain can be further extended by increasing the level of the converter. However, the advantage of the flying capacitor converter is providing the converter with energy storage [62].

Flying multi-level converters have several drawbacks:

- Suffers from voltage imbalance due to capacitors act as DC voltage sources.
- A high number of active switches and passive components are required.
- At any greater than three level converter, the system reliability is degraded due to a large number of capacitors.

However, in the DC-DC converter application, flying capacitor multilevel converter suffers from control complexity, increase the cost, and tends to reduce the overall reliability and efficiency of the converter.

#### 3.2.1.4.2 Diode-Clamped Multilevel Converter

The first multi-level topology was invented in 1981[63] and called a neutral-point clamped multilevel converter. Most of this topology is used as inverter [64],[65][66]. However, the diode-clamped multilevel converter has some disadvantages:

- A high number of clamping diodes are required when the number of levels gets high, which affects its reliability.
- At high voltage levels, clamping diodes are stressed

Wherefore, diode-clamped multilevel converter topology is impractical in the DC-DC converter, not suitable for DC-DC converter application and therefore, is not discussed further.

#### 3.2.1.4.3 Hybrid- Multilevel Converter

The hybrid multilevel converter has several topologies, but the basic concept of them is employing two-level conversion stage because the 2-level hybrid converter offers a reduced number of passive semiconductors. However, the major drawback is that it can only produce a two-level output voltage, which means that it does require the use of PWM with the consequent large increase of switching losses [67], [68]. In addition, the complexity of balancing the capacitors' voltages in the DC link is also one disadvantage of the hybrid multilevel converter [68].

Further, most Hybrid multilevel converters consists of cells (4 IGBTs and 1 capacitor) as shown in Figure 3.12. These are called "full-bridge" cells, which permit DC faults to be suppressed but require double switches. The other is comprised of 2 IGBTs and 1 capacitor and is called a half-bridge. The idea of the half bridge has solved these shortcomings but requires a high capacitance value.

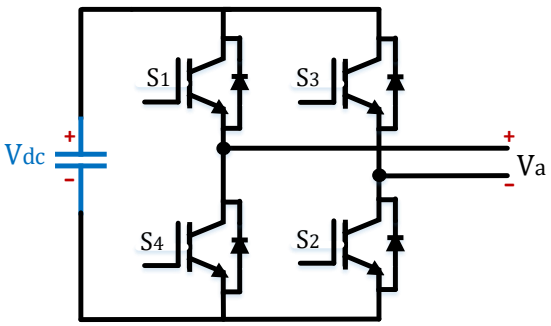


Figure 3.12: One H-bridge cell

#### 3.2.1.4.4 Modular Multilevel Converter

The modular multilevel converter (MMC) was first presented in 2003 in [19-20]. It has been shown to be a suitable topology for high-voltage high-power applications such as high-voltage direct current transmission (HVDC) [21-22]. Therefore, the multilevel concept can be considered for DC-DC conversion [73].

DC-DC conversion is becoming popular in renewable energy applications following the success of this type approach in DC-AC conversion [23-24].

The MMC is obtained by connecting a number of identical cells called "sub-modules" (SM) in series as illustrated in Figure 3.13. It shows a typical half-bridge cell. In the normal operation mode, the two switches are complementary making the $V_{cell}$ equal either to zero, when the cell is turned 'OFF', or equal to $V_{cap}$, when it is turned 'ON'. One arm has two limbs, an upper-limb, and a lower-limb, with the same number of cells.

A "full bridge cell" has four switches as shown in Figure 3.13. This cell can duplicate the operation of the basic commutation cell, and thus operate in all four quadrants where both positive and negative cell DC voltages can be obtained at the output terminal. However, the number of switching devices is doubled compared to the HB commutation cell [25]-[26]. The advantage of a full bridge cell is being able to generate 3 different voltage levels at its terminals, $+V_C$, 0 and $-V_C$, as opposed to the two levels, 0 and $+V_C$, that can be generated by the half-bridge cell $V_{cap}$.

The ability to reverse voltage allows rapid fault current limitation. In addition, Full-bridge cells have the evident drawback of requiring double the number of semiconductors switching, increasing both size and cost. Several solutions have been proposed to mitigate the uneven sharing of the voltage across the devices particularly during the switching operations [25]-[26]. The main solution for this is the rotation of the sequential switching of the devices to ensure that on average the submodule capacitors retain the same energy [75],[77].

As shown in Figure 3.13. The basic building block is the cell or "the submodule in any MMC configuration which can basically be a DC-DC power converter. Cells could be connected in series or in parallel in various topologies in order to meet the requirements for a specific application such as need the converter as step up or step down [78].

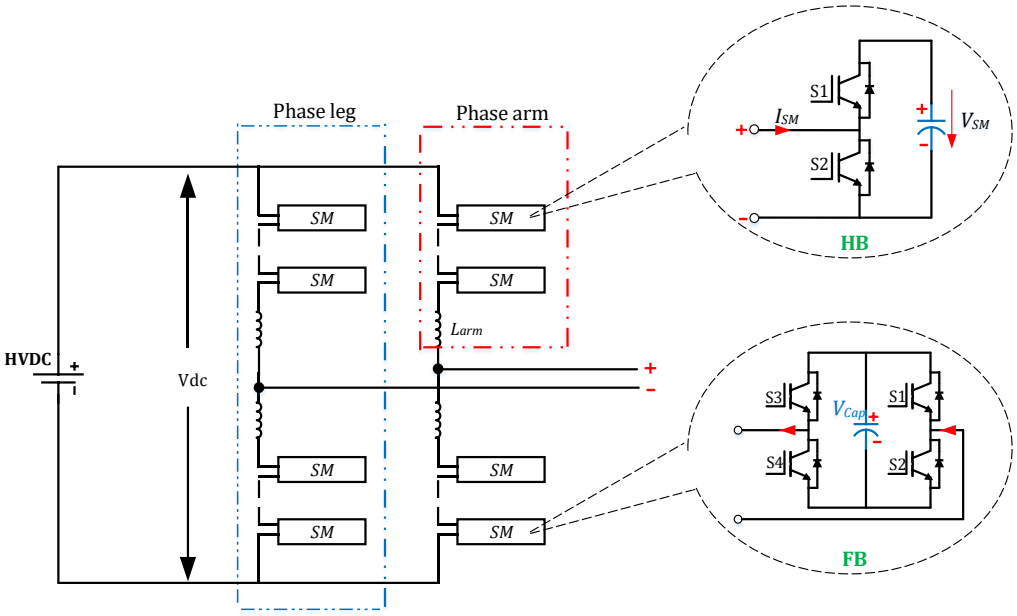


Figure 3.13: Schematic diagram of a modular multilevel converter

Each individual leg and arm of the MMC consists of a number of series connected converter cells, termed submodules. These submodules can, for example, be half- or full-bridges equipped with DC-capacitors. The number of cells turned 'ON' in the upper-limb is complementary to the number of cells turned 'OFF' in the lower-limb on average, making the total voltage stored in the capacitors of each limb equals to the pole-to-pole voltage.

The average capacitor voltage of each cell is then given by

$$V_{cell} = \frac{V_{dc}}{n} \qquad (3\text{-}9)$$

where $V_{cell}$ is the voltage of the cell, $V_{dc}$ is the voltage between the positive and negative poles of the converter and '$n$' is the number of cells in one limb or half the number of cells in one arm. The modular multilevel converter offers some advantages as follow

+ The voltage levels can easily be adjusted by changing the number of series submodules and failed units can be bridged out while keeping the converter operational.
+ The submodules need not be switched simultaneously making timing synchronization less critical compared to other multilevel topologies.

+ The DC-DC MMC can be used either to control the power flow in HVDC grids, where the voltage difference between the input and the output terminals of the converter is small or to interconnect HVDC grids with a significant voltage difference.
+ The internal arms current are continuous.
+ No separate energy sources are required for sub-module capacitors.
+ No common DC link capacitor is required.

However, the MMC converter suffers from three main drawbacks [77][78].

– The required capacitance of the submodules for a given voltage ripple is inversely proportional to the output frequency of the converter.
– Requires a large number of IGBT-diode devices compared to some other multilevel topologies.
– Full bridge MMC converter switching losses more than any other single bridge converter.

### 3.2.2 Isolated DC-DC Converter

There are several available topologies, which isolate input DC voltage from the output DC voltage through a transformer. Since the transformer's size and weight vary inversely with frequency. Each method has some relative advantages, as well as disadvantages, over another method. These are explained in the following subsections.

#### 3.2.2.1 Half Bridge Converter

The Half-Bridge Converter (HBC) has two IGBT switches, working together with two capacitors, as shown in Figure 3.14, it uses a high-frequency transformer in the middle to provide isolation. The switch voltage is the same as the input voltage $V_{in}$, but the drive circuit is more complicated [79],[80][81].

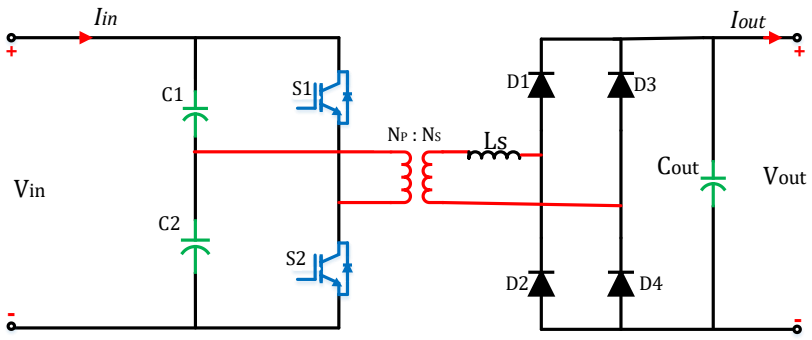


Figure 3.14: Schematic layout of the Half-Bridge converter.

The switches $S_1$ and $S_2$ are switched 'ON' alternatively, thus, creating an alternating voltage and the energy is transferred via the transformer and the diode bridge to the load. When the switch $S_1$ is on, half of the input voltage $V_{in}$ is applied across the winding $N_P$ and a positive flux is induced in the winding $N_S$. When the switch $S_1$ is turned 'OFF', switch $S_2$ is turned '*ON*' and a negative flux is induced in the winding [80]. There are four modes of operation as summarised in Table 3.3.

Table 3.3: Pattern switching of the Half-Bridge converter

| Switching state | $S_1$ | $S_2$ |
|---|---|---|
| Mode1 | 1 | 0 |
| Mode2 | 0 | 0 |
| Mode3 | 0 | 1 |
| Mode4 | 0 | 0 |

Figure 3.15 shows the timing diagram for a half-bridge converter is split over one period because this topology has two switches.

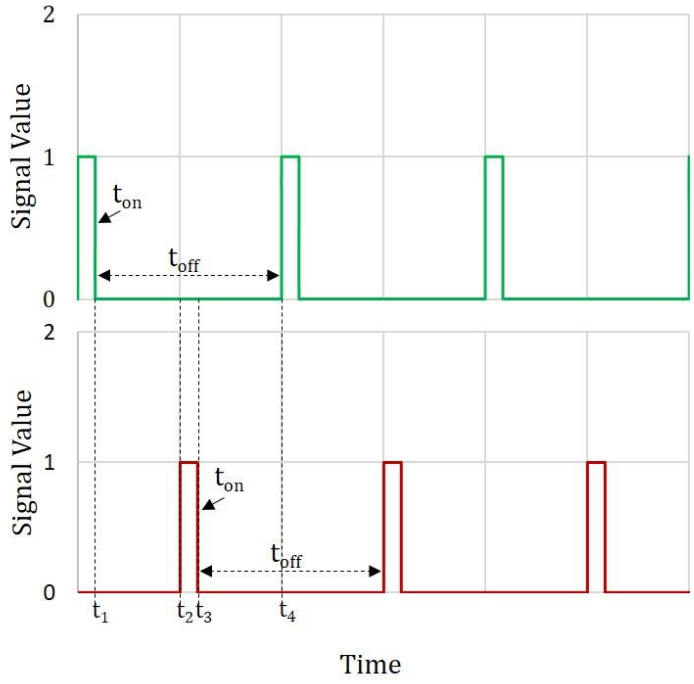


Figure 3.15: Timing diagram of switching ($d$= 0.20)

The primary winding of the transformer must have a voltage-second balance to prevent the transformer core from saturation. This can be achieved by controlling the voltage over the capacitors $C_1$ and $C_2$. The relation between the input voltage $V_{in}$ and the output voltage $V_{out}$ can be expressed as

$$V_{out} = \frac{N_S}{N_p}\frac{V_{in}}{2} \qquad (3\text{-}10)$$

where $N_S$ is the number of turns in the secondary winding of the transformer, $N_P$ is the number of turns in the primary winding of the transformer. The Half-bridge converter requires an isolated High-frequency (HF) transformer isolated, HF switching DC-DC converters 25 kHz due to their small size, light weight and reduced cost [80][82]. Further, in a half bridge converter, the voltage stress imposed on the power semiconductor device (IGBT's) is subject to only the input voltage.

The power switches turn-off under hard switching, turn-off losses of the IGBTs are high at high frequency, and the efficiency of the converter decreases with increasing frequency. In addition, the parasitic oscillations between the parasitic capacitor and the leakage inductance cause electromagnetic interference noise

(EMI). To reduce parasitic oscillations an RC snubber circuit is connected across the primary windings of the transformer.

The half bridge power losses of each switching operation for the current and voltage waveforms of the IGBT are divided into three sections. The leakage loss is only a small part of the total loss, so it has been neglected. The total energy losses during each operating cycle of the IGBT are the sum of the turn-on and turn-off losses, saturated conduction loss as well as the reverse-recovery loss of the integrated freewheeling diode [80][82].

The main advantages of the Half-Bridge Converter

+ The switches can be rated to the input voltage and the anti-parallel diodes clamp destructive switching transients.
+ Low voltage/current stress level, low conduction loss, and constant frequency control.
+ Good utilization of the transformer while working with both positive and negative currents.

The main drawbacks of the Half-Bridge Converter

– The DC gain ratio of the converter is nonlinear, thus higher duty cycle variation is needed for the same input voltage variation, which makes the converter operate further beyond the optimum operating point at high input voltage.
– The primary must have a voltage-second balance to prevent the core from saturation.
– Doubled switch current for the same output power in comparison with the Full Bridge Converter.
– The control circuits must provide isolated drive signals to the switches.

### 3.2.2.2 Full Bridge Converter

As illustrated in Figure 3.16. The Full Bridge Converter (FBC) has four IGBT's working together, and the switch voltage is the same as the input voltage, but the drive circuitry is complicated in comparison with half bridge converters, since there are four switches and the drive circuits have to be separated from the ground [83][84]. The switches $S_1$ to $S_4$ are 'ON' alternatively, thus, creating alternating voltage, and the energy is transferred via the transformer and the diode bridge to the load.

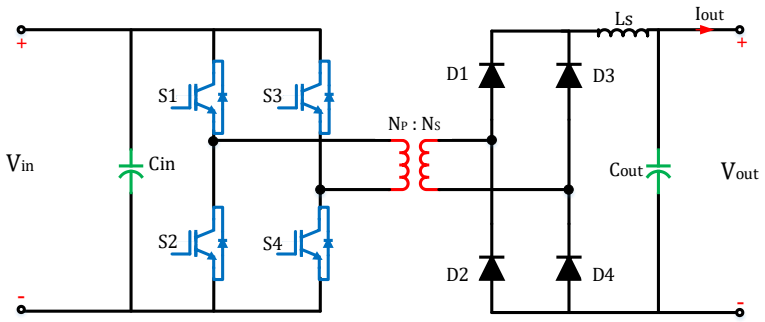


Figure 3.16: Schematic layout of the Full-Bridge converter.

Two modes of operation and switching stated of four IGBTs are summarised in Table 3.4. First, the switches $S_1$ and $S_4$ are 'ON', the supply voltage is applied across the primary winding *Np* and a positive flux is induced in the secondary winding *Ns*; then, the switches $S_1$ and $S_4$ are turned off and the switches $S_2$ and $S_3$ are turned on and a negative flux is induced in the winding *Ns*. The primary must have a voltage-second balance to prevent the transformer core from saturation.

Table 3.4: Pattern switching of four-level flying capacitor converter

| Switching state | $S_1$ | $S_2$ | $S_3$ | $S_4$ |
|---|---|---|---|---|
| Mode1 | 1 | 0 | 0 | 1 |
| Mode2 | 0 | 1 | 1 | 0 |

The voltage conversion ratio of the full bridge converter can be derived by imposing the constant voltages across the output inductor *(Ls).* However, the voltage conversion ratio can be expressed as

$$V_{out} = \frac{N_S}{N_p} V_{in} \qquad (3\text{-}11)$$

In hard-switching duty cycle control, the 'OFF' state is achieved by turning all switches off. Thereby, the output current is freewheeling in the output bridge, and there is no current in the transformer nor in the input bridge [83],[85], [86]. The output power of the full-bridge converter is double that of the half-bridge converter, for the same input voltage and current. In addition, the full bridge converter has good transformer utilization.

The main advantages of the Full Bridge converter are:

3.1.2 Good utilization of the transformer by working with both positive and negative Fluxes.

3.1.3 Double frequency in the output reduces the requirements for an output filter.

3.1.4 The output power is doubled in comparison with the Half-Bridge Converter, since the input voltage, instead of half of the input voltage, is applied to the primary winding.

The main drawbacks of the Full Bridge converter are:

- Narrow zero voltage switching (ZVS) range of lagging-leg switches, high power losses by circulating current, and voltage ringing across rectifier diodes. Especially, with a requirement of the wide input range.
- The control circuits must provide isolated drive signals to the switches.
- The primary must have a voltage-second balance to prevent the transformer core from saturation.
- Its efficiency at different loads is up to 95%, which is lower than other efficiency's converters that reach 99% in HVDC converter applications [84].

### 3.2.2.3 Dual Active Bridge Converter

A Dual Active Bridge Converter (DAB) is a high-power, high power density, and high-efficiency power converter with galvanic isolation as shown in Figure 3.17. Each switching bridge is made up of four high-frequency active controllable switching devices (MOSFETs or IGBTs) in H-bridge connection. Such connection is similar to the one used in full-bridge DC-DC converters [87],[88],[89],[90].

The DAB topology is attractive because it has zero-voltage switching (ZVS), bidirectional power flow, and lower component stresses. A DAB converter consists of two H-bridges and one high- frequency transformer. One H-bridge converts the input voltage to an intermediate High-frequency AC voltage, while another H-bridge converts the high-frequency square wave AC voltage back to the output voltage [41-42].

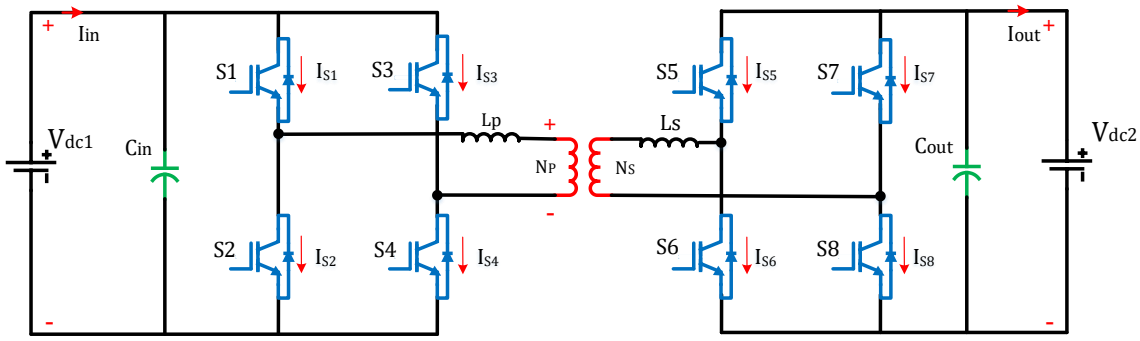


Figure 3.17: Schematic layout of DAB converter.

A high-frequency transformer is used along with high-frequency switching devices because it reduces the weight and volume of passive magnetic devices. Beside galvanic isolation, the high-frequency transformer also has some leakage inductance in its primary and secondary windings, which together act as an energy storage component. The leakage inductance also helps achieve soft switching. During switching transients, the transformer current resonates with the capacitors in parallel with switching devices, limiting the *dv/dt* and *di/dt* across the switches. Soft switching helps to reduce switching loss and achieve higher power efficiency. The relation between the transfer power $P_{DAB}$ and the transformer voltage $V_P$, *AC*, rms are presented in [88], [90].

$$P_{DAB}=\frac{V_P V_S}{\omega L \sigma} d(1-d) \qquad (3\text{-}12)$$

where $P_{DAB}$ is transferred power , $\omega$ the angular frequency, $L_\sigma$ is the total leakage inductance of the transformer, and $d$ is the duty cycle.

A high-frequency transformer is required to reduce the weight and volume of the magnetic core. Compared to those converters using line-frequency transformers, DAB converters use more silicon devices (whose price is continuously going down) while using less copper and a smaller magnetic core (whose price is continuously going up) [41], [43]. DAB converters have become an interesting research topic during recent years. Some researchers focus on improvement of modulation methods. Dual phase-shift modulation has been proposed to reduce reactive power and loss for DAB converters [88]. Hybrid modulation methods have been developed to increase soft-switching range in [88],[89]. Phase shift modulation plus duty-ratio control has been applied to DAB converters to achieve a higher degree of control freedom [88],[89]. Different modulation methods are evaluated and compared in[89].

### 3.2.3 Switched Capacitor DC-DC Converter

The key principle in switching capacitor SC converters is energy conservation. A power source firstly stores some energy in the capacitor in one phase, and then the same amount of energy will be transferred from those energy reservoir components to the output in the other phase, thus allowing for generating a different voltage from the power source. Switching capacitor DC-DC converters can be divided into four topologies as follow:

#### 3.2.3.1 Ladder Switch Capacitor Converter

As demonstrated in Figure 3.18, the ladder converter is comprised of two capacitors and four active switches. The capacitors are charged from the DC supply and discharged into the load. The simplicity of this topology is that it requires a low number of capacitive components and fewer control signals [44].

In the first commutation, the switches $S_1$ and $S_3$ are turned 'ON' to allow the capacitor $C_1$ to be charged form the input DC supply voltage. In the second

commutation, the switches $S_2$ and $S_4$ are turned on after the switches $S_1$ and $S_3$ are turned off, the capacitor $C_1$ recharges the capacitor $C_2$. Hence, the output voltage is double the input voltage $(V_{out} = 2V_{in})$ and the blocking voltages over non-conducting switches are all equal to the input voltage $V_{in}$.

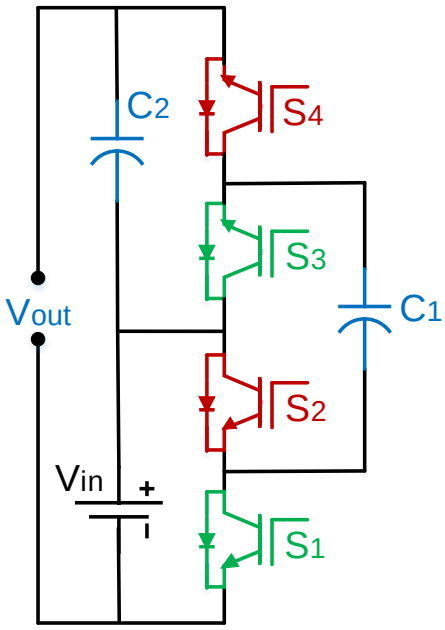


Figure 3.18: Schematic layout of basic DC-DC ladder converter

Ladder topology needs two control signals and a fixed duty-cycle of 0.5, which means ideally, the voltage across each capacitor is the same as the input voltage $V_{in}$. Therefore, the output voltage depends on the number of cells $N_C$.

$$V_{out} = V_{in}(N_C + 1) \tag{3-13}$$

where $N_C$ is the number of capacitor cells. Further, the number of necessary switches $N_S$ and capacitors $N_{cap}$ can be expressed by Equation (3-14) as:

$$N_{Cap} = 2N_C \tag{3-14}$$

$$N_S = N_C + 2 \tag{3-15}$$

However, this topology suffers from two main drawbacks [93],[94].

- Ladder converter requires a relatively large number of switches and this increases the losses.
- The switching frequency has high restrictions. However, this topology is used in low power applications only

### 3.2.3.2 Fibonacci Switch Capacitor Converter

The topology of the Fibonacci switch capacitor SC converter is shown in Figure 3.19. It consists of identical three sub-modules; every sub-module features a string of identical three-switches and one-capacitor cells [95], [96]. The total is ten active switches and four capacitors.

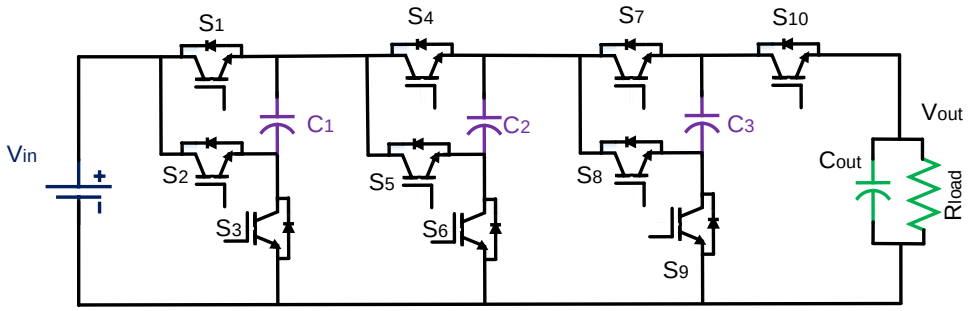


Figure 3.19: Fibonacci SC DC-DC converter

The ideal DC conversion ratio, ($N = V_{out}/V_{in}$), when the converter is unloaded, can be obtained from the converter topology. The example in Figure 3.19 is used to illustrate the discussion. The two switched networks of this converter, corresponding to the two clock phases are listed in Table 3.5.

Table 3.5: Pattern switching of Fibonacci switch capacitor converter

| Switching state | $S_1$ | $S_2$ | $S_3$ | $S_4$ | $S_5$ | $S_6$ | $S_7$ | $S_8$ | $S_9$ | $S_{10}$ |
|---|---|---|---|---|---|---|---|---|---|---|
| Mode1 | 1 | 0 | 1 | 0 | 1 | 0 | 1 | 0 | 1 | 0 |
| Mode2 | 0 | 1 | 0 | 1 | 0 | 1 | 0 | 1 | 0 | 1 |

However, Fibonacci switch capacitor SC converter suffers from many drawbacks, such as the following:

- The number of components in this converter is relatively high, which affects its reliability.

– The switching frequency is high, which that becomes impractical due to unacceptably high losses.

### 3.2.3.3 The Voltage Doubler SC Converter

Figure 3.20 illustrates the ideal switched capacitor voltage doubler. The switched capacitor voltage doubler is composed of four switches, two capacitors $C_1$ and output capacitor $C_{out}$ and load $R$. The basic voltage doubler is required for step-up voltage conversion [94], [97]. It consists of two switching modes. During the first switching mode odd switches $S_1$, $S_3$ are 'ON'. The capacitor $C_1$ is charged to supply voltage through switches $S_1$, $S_3$. Then in the second mode, even switches $S_2$, $S_4$ are 'ON'. In the second mode, the input voltage $V_{in}$ across $C_1$ in the previous phase is transferred to the output load. Thus, $2V_{in}$ voltage appears across the output capacitor $C_{out}$.

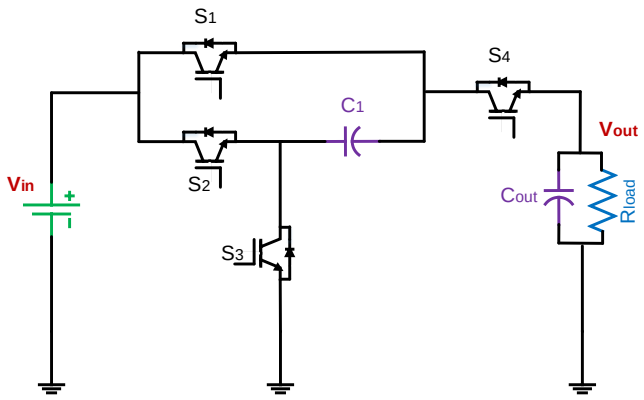


Figure 3.20: Switched capacitor voltage doubler converter

The circuit is therefore called a voltage doubler, as the output voltage of the circuit is twice the input voltage. Thus, the conversion ratio for the voltage doubler is $M = (Vout/Vin) = 2$, whereas for ideal SC converter when unloaded has DC voltage conversion ratio $M = (Vout/Vin)$.

This type of converter has several drawbacks as follow [94]:

– The gate drive signals of this topology must be higher than the input voltage $V_{in}$. While designing the switched capacitor converter area and efficiency of the converter is of prime importance.
– It has high level switching frequency.
– The output voltage conversion is just twice of the input voltage.

– Low efficiency and the high number of components are also major issues.

#### 3.2.3.4 A Series-Parallel DC-DC Converter

As depicted in Figure 3.21, there are many topologies on series-parallel DC-DC converter [73], [97], [98], [99]. However, the series-parallel DC-DC converter is based on the Marx principle where the capacitors are charged in parallel connected to the LV side voltage and discharged in series to produce a high voltage on the HV side. Therefore, the output voltage is derived as:

$$V_{out} = nV_{in} \qquad (3\text{-}16)$$

where *n* is the number of capacitor cells.

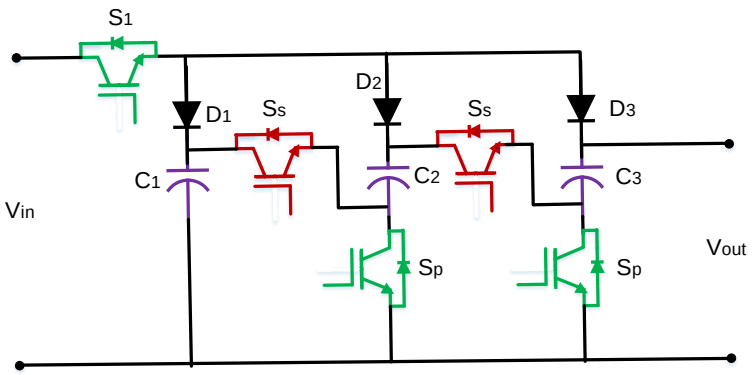


Figure 3.21: Series-parallel DC-DC converter

The drawback of this topology is the large number of switches needed to create a series-parallel converter. Therefore, in Chapter 4, the proposed solution of the Marx DC-DC converter is discussed and described.

## 3.3 Summary

This chapter has presented a review of DC-DC converter topologies used for DC-DC conversion. Half Bridge Converter, Full Bridge Converter, Dual Active Bridge Converter, Modular Multilevel Converter, Boost Converter, Ćuk Converter, Buck-Boost Converter, Multilevel Converter, and Switched Capacitor Converter. Furthermore, their various features have been discussed including; their structure; operation; and control concepts. Some of these non-isolated topologies such as Boost, Ćuk, and Buck-Boost Converters cannot be applied at HVDC and

power levels. However, these topologies are applied in low power DC applications such as DC motor drives, switched mode power supplies, railways etc.

Isolated topologies use a high-frequency transformer, where energy is transmitted via a magnetic field rather than a direct current path. A half-bridge converter is used when the current is low and full-bridge converter is used for higher currents. The dual active bridge is used for bidirectional transfer power, which is not possible with HB and FB configurations. A high-frequency transformer leads to a reduction of the transformer weight and soft switching is used to reduce the switching losses leading to efficiencies of the order of 95%. However, this is still lower than the efficiency of 99.6% achievable with HVDC converters.

Several multilevel converter topologies were discussed in more detail; diode-clamped, flying capacitor, cascaded H-bridge, and multilevel modular converter. Their structure, operation and the advantages and disadvantages of multilevel converter topologies and were presented. Generally, two major disadvantages of multilevel power conversion are the larger number of semiconductor switches required and that complex control is required to maintain the capacitor's voltage balance. The switched capacitor converter is based on charging and discharging of module capacitors in a particular sequence. In some cases, soft switching is used in order to reduce the switching losses enabling a higher frequency operation. If hard switching is used, switching frequencies above the power frequency become impractical due to unacceptably high losses. Switched capacitor topologies are switched at high frequency and the literature does not indicate whether switching at low frequencies is feasible. Further, these topologies have a high number of switches. The purpose of this chapter was to provide both an introduction to existing DC-DC converter topologies as well as some background information regarding other research concerning the DC-DC converter. The next chapter presents a study of Marx DC-DC converter including; single-stage and multi-stage DC-DC converters.

# Chapter 4

## A single-Stage and Cascaded DC-DC Marx Converters

## 4.1 Introduction

In this chapter, the concept behind the Marx converter is explained. It shows how switching device count can be reduced for the same converter power rating. Two types of DC-DC converter topologies are improved and modified based on the Marx converter. The first is called a single stage converter, while the other is called a cascaded stages converter. The performance of the two techniques is compared with Veilleux converter topologies which give better results in terms of power and voltage convergence and accuracy. Then, there is a description of how a reduced number of active switches are incorporated into the proposed technique. The design considerations of these techniques, including controlling both converters, is also discussed. Finally, simulation results for both converter case studies are presented to show the performance of the improved technique in the converters.

## 4.2 System Description

The configuration of an offshore wind farm which includes two DC-DC converters is shown in Figure 4.1, with unidirectional power generators. The arrangement shown in Figure 4.1 forms the basis for the simulation study. In this topology, the cluster is formed by two parallel lines of wind turbines, each containing 5 wind turbines in series. Hence, there is a total of 10 wind turbines, each rated at 5 MW, 1.2 kV [41],[100]. Therefore, the total value of the wind turbine cluster bus voltage is 6 kV and 50 MW. Hence, the DC-DC converter input voltage is 6 kV. The first DC-DC Converter, which is labeled in the yellow square in Figure 4.1 is connected to the collection bus to step-up the voltage to 30 kV for MV transmission using the equations derived in the converter design section. A submarine cable is used to connect the MV converter platform to the main bus of the HV converter. The second DC-DC Marx converter is connected at the end terminal of a DC cable to step up the voltage to 360 kV as illustrated in the blue square in Figure 4.1. Hence the DC-DC converter input voltage is 30 kV and 50 MW.

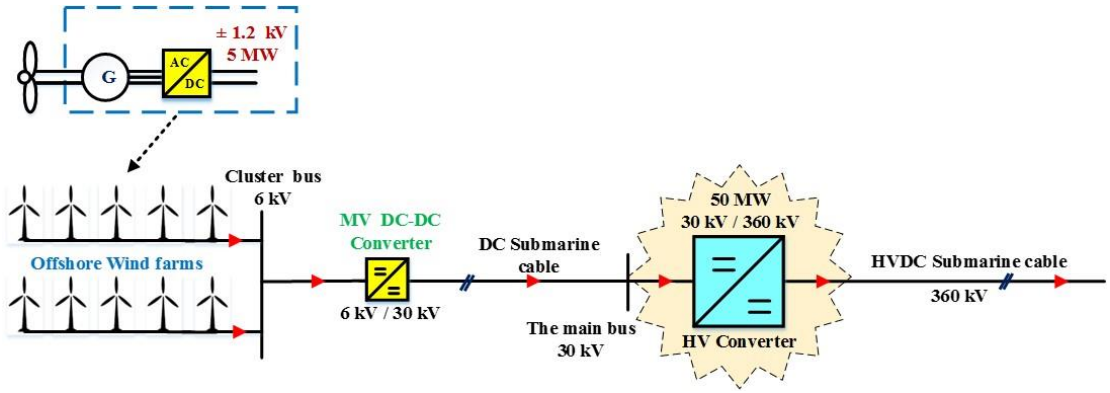


Figure 4.1: Electrical system for the grid connection of a wind farm

## 4.3 Single Stage DC-DC Marx Converter

The proposed converter is modified and improved from Veilleux converter [98]. A Veilleux converter with 5 submodule capacitors achieves a voltage ratio of 1:5. In addition, there are two capacitors at the two terminals to provide smoothing. As shown in Figure 4.2, the switching components are IGBTs and diodes. The capacitors $C_n$= *(1, 5)* are charged in parallel from the LV source by switching the IGBTs $S_{pj}$ *(j=1-4).* The IGBTs $S_S$ *(S =1- 4)* are switched 'OFF' and hence the charging currents flow through $S_{in}$, $D_{in}$, diodes $D_n$ *(n=1-5)* and the IGBTs $S_{pj}$ *(j=1- 4).* In the second sub-period, IGBTs $S_S$ are switched 'ON' and IGBTs $S_{Pj}$ *(j =1- 4)* are switched 'OFF' to connect the capacitors in series to create a high voltage equal to 5 times the LV across the converter HV output.

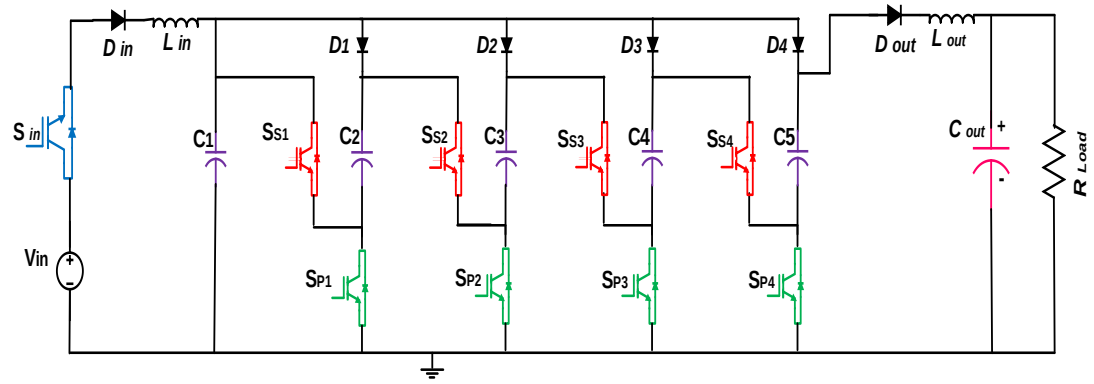


Figure 4.2: Veilleux DC-DC converter

A disadvantage of this topology is that the number of IGBT switches in the charging state $S_P$ is high and the increasing voltage stresses in the IGBTS in successive stages. The number of IGBTs can be reduced from 23 to 13 by

combining the function of 4 IGBTs *($S_{P1}$-$S_{P4}$)* to be performed by 4 diodes and 1 IGBT *($S_{valve}$)* as shown in the next subsection.

### 4.3.1 Circuit Arrangement

The structure of the converter, as depicted in Figure 4.3, can be broken down into three circuits; an input circuit, middle circuit and the output circuit [100]. The converter is aimed at application to a power collection system in an offshore wind farm grid connection system. A possible configuration showing the position of the DC-DC converter is shown in Figure 4.1 which is labeled in the yellow square, and the specifications are used in the design are indicated. Therefore, the input circuit consists of an input inductor $L_{in}$ connected in series with an input diode $D_{in}$. The input DC voltage source of magnitude $V_{in}$ = 6 kV and input HV valve *($S_{valve}$)* is represented as the DC system.

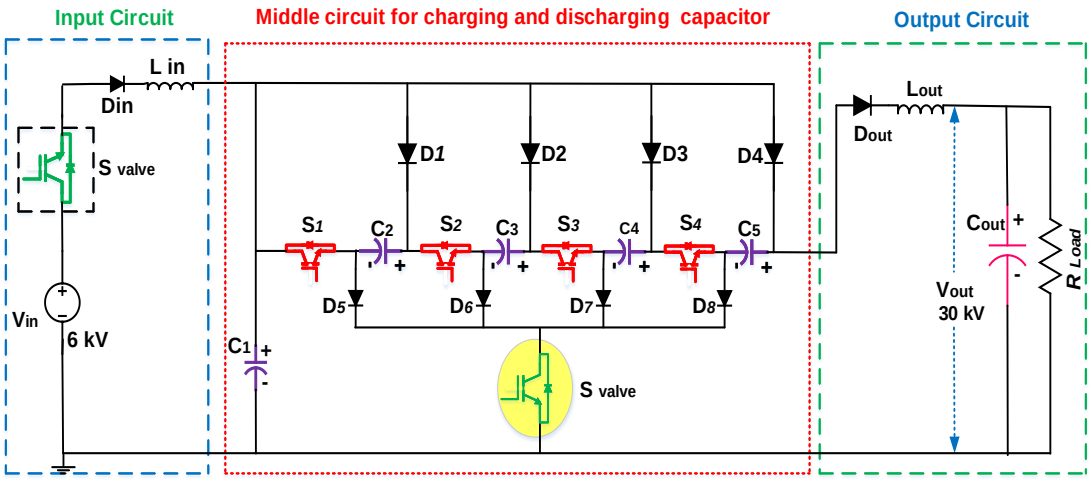


Figure 4.3: Single-stage DC-DC Marx converter block diagram

Depending on the voltages in a particular application, and IGBT ratings, a number of IGBTs in series are needed to form the High voltage valve *($S_{valve}$)*. The middle circuit comprises a number of IGBT switches, capacitors, and diodes $D_{(1\text{-}8)}$. The circuit shown in Figure 4.3 is the generalised single-stage converter with "*n*" number of capacitors. In this converter topology, the number of capacitors denoted by *"n"* is set to 5 to create a voltage amplification of 5. The capacitances in the 5 sub-modules are indicated by $C_n$, where $n$= *(1, 5)*. The switching components are IGBTs $S_{(1\text{-}4)}$, IGBT valve switches $S_{valve}$, and diodes $D_{(1\text{-}8)}$. The output circuit consists of an output diode $D_{out}$ connected in series with the output

inductor $L_{out}$, and one output capacitor $C_{out}$. Based on the designed power rating of the converter, the load modeled by a pure resistor $R_{load}$, is connected in parallel. The switching time operation $T_S$ is divided into two half-cycle of duration $T_S/2$.

### 4.3.2 Basic Principles

The operation can be explained in terms of two equal half cycles $(T_S/2)$. During the first half-cycle, all the cell capacitors $C_n$, $(n = 1, 5)$ in the middle circuit are connected in parallel across the input low voltage (LV). The total charging current flows through the valve $S_{valve}$, diode $D_{in}$, input inductor $L_{in}$, and diodes $D_n$ where $(n=1, 8)$ and through the valve $S_{valve}$. Energy from the input low voltage $V_{in}$ transfers to the cell capacitors as illustrated in Figure 4.4.

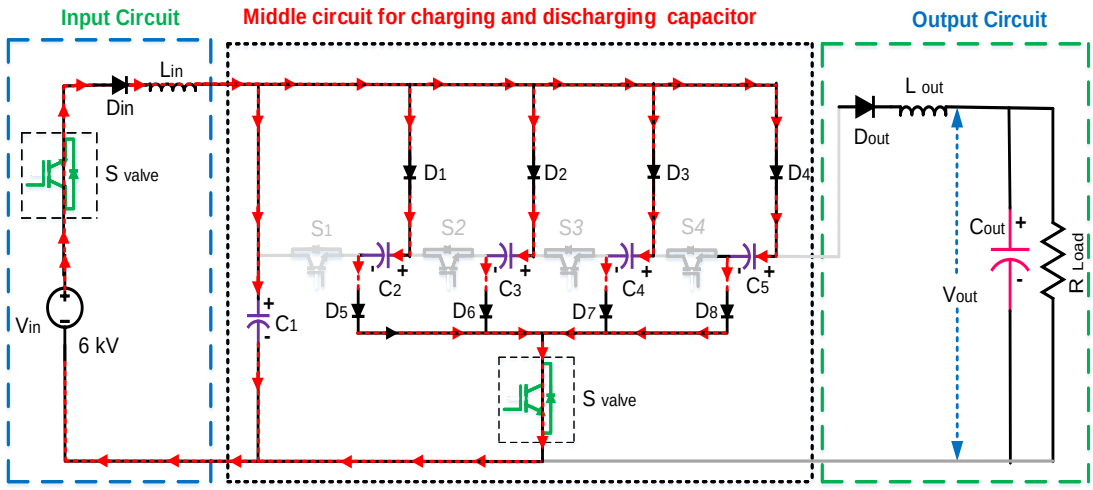


Figure 4.4: Connected the capacitors in parallel during charging

In the second half-cycle, the cell capacitors are connected in series through IGBT switches $(n= 1, 4)$ to produce the higher voltage as shown in Figure 4.5. Energy transfers from the cell capacitors to the output capacitor $C_{out}$. The inductor and capacitor combination must be designed so that the resonance frequency is less than the switching frequency $Fs$. This is used to implement soft switching to reduce the switching losses.

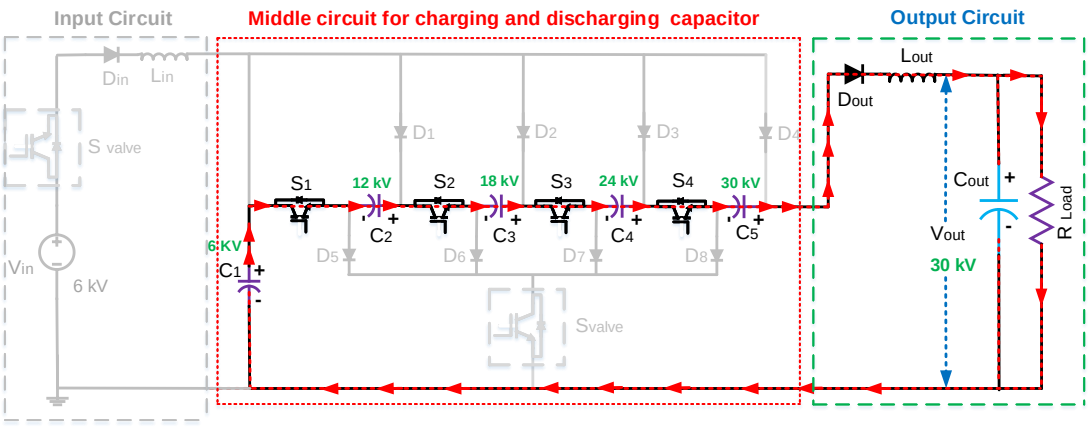


Figure 4.5: Connected the capacitors in series during discharging

The voltage on the capacitors increases by 6 kV from left to right reaching a maximum of 30 kV on the shunt IGBT switch at the HV side as shown in Figure 4.5. With repetition of both of the half-cycles "charging in parallel and discharging in series", the converter delivers the full power with the voltage rating as shown in Figure 4.3.

### 4.3.3 Mathematical Analysis of Single-Stage DC-DC Marx Converter

In this section, the steady-state analysis of the converter shown in Figure 4.1 is presented. The voltage transformation ratio is the same as the number of capacitors in the middle circuit *'n'* and hence;

$$n = \frac{V_{out}}{V_{in}} \qquad (4\text{-}1)$$

Therefore, the output voltage can be driven as;

$$V_{out} = nV_{in} \qquad (4\text{-}2)$$

In the first half -cycle, the IGBT switch $S_{valve}$ is 'ON', the charging will be in parallel as shown in Figure 4.6. Logically, the input voltage $V_{in}$ is higher than the capacitor voltage and the diodes $(D_1\text{-}D_8)$ are forward bias and conduct. The equivalent capacitance in parallel can be expressed as;

$$C_{eq(P)} = C_1 + C_2 + C_3 + C_i + \ldots C_n = \sum_{i=1}^{n} C_i \qquad (4\text{-}3)$$

where $C_{eq\,(P)}$ is the equivalent capacitance of parallel-connected capacitors, and $C_i$ is the capacitance.

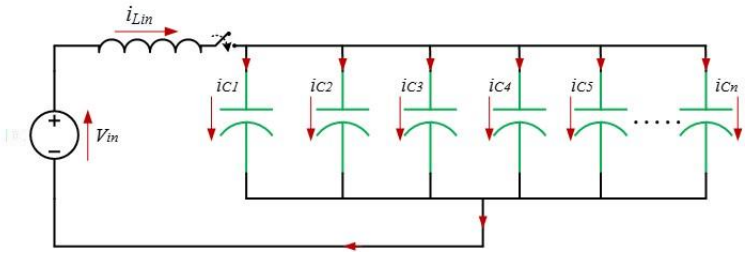


Figure 4.6: Charging capacitors in parallel

The inductor $L_1$ and the equivalent capacitance $C_{eq(P)}$ forms an oscillatory L-C circuit and hence, the current in the inductor $L_1$ is a positive half sine wave during the first half-cycle, as depicted in Figure 4.7(a) as

$$i_{L1} = C_{eq\,(P)} \frac{dv}{dt} = \frac{V_{in}}{\omega L_{in}} \sin \omega (t - t_0) \qquad (4\text{-}4)$$

where $L_{in}$ is the inductor current, and $\omega$ is the resonant frequency. The angular resonant frequency is given by

$$\omega = \frac{1}{\sqrt{L_{in} C_{eq\,(P)}}} \qquad (4\text{-}5)$$

In order to achieve soft switching, the IGBTs must be switched at the resonant frequency of the inductor current waveform. Therefore, the switching frequency can be written as;

$$F_S = \frac{1}{2\pi \sqrt{L_{in} C_{eq\,(P)}}} \qquad (4\text{-}6)$$

The sinusoidal charging current described by Equation (4-4) is sketched in the first-half cycle in Figure 4.7 (a) and Figure 4.7(b). During the first half-cycle, the output inductor current $I_{Lout}$ is zero. From the equivalent circuit shown in Figure 4.6, applying the Kirchhoff's voltage law during switching time $(t_0 \leq t \leq t_2)$ is given as;

$$V_{in} = V_{Lin} + V_C \qquad (4\text{-}7)$$

As depicted in Figure 4.5(e), the voltage equation of capacitor $C_{eq(P)}$ for ($t_0 \le t \le t_1$) is given as:

$$V_C = V_{in} - L\frac{di}{dt}\left[\frac{1}{2}C_{eq\,(P)}\,\omega\,\Delta V_C \sin\ \omega\,(t-t_0)\right] \quad (4\text{-}8)$$

$$V_C = V_{in}\left[\frac{1}{2}\Delta V_C \cos\ \omega\,(t-t_0)\right] \quad (4\text{-}9)$$

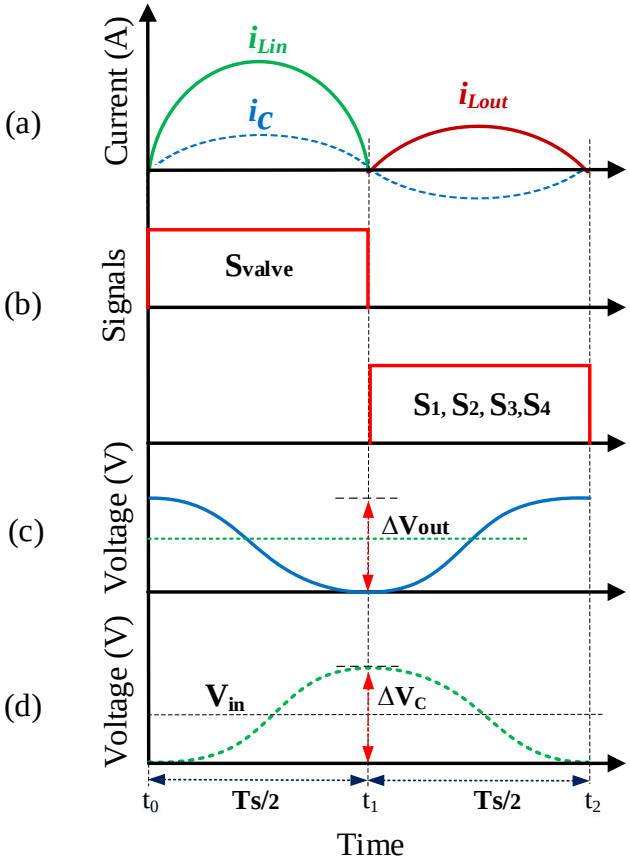


Figure 4.7: Ideal steady-state waveforms

In the second half-cycle, discharging the capacitors in series to the output capacitor $C_{out}$ as shown in Figure 4.8. The inductor current reaches zero and the output inductor current $I_{Lout}$ increases during $T_S/2$. Meanwhile, the output voltage $V_{out}$ is larger than $5V_C$ as shown in Figure 4.7(d) and Figure 4.7(e).

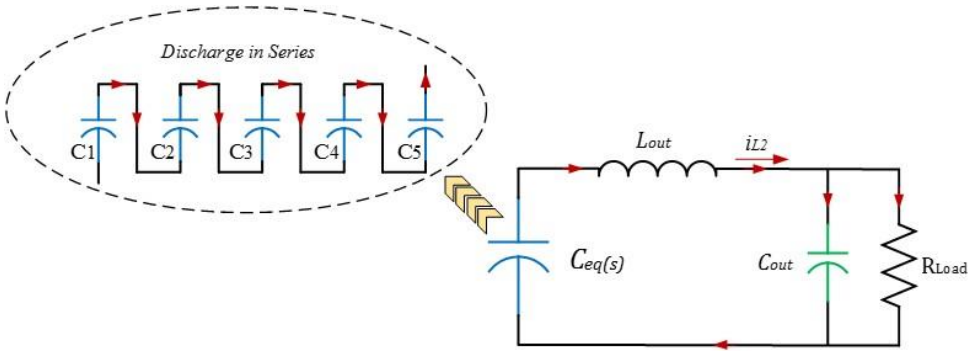


Figure 4.8: Discharging capacitors in series

### 4.3.4 Converter Design

Based on the designed power rating of the converter of 50 MW, the output load under steady-state DC conditions of the DC system can be represented by $R_{Load}$ which can be calculated by

$$R_{load} = \frac{V_{out}^2}{P_{rated}} \tag{4-10}$$

where $P_{rated}$ is the power rating of the converter, and $R_{Load}$ is the load which that is modelled as a pure resistor, and depending on the power rating of the converter, the load can be calculate. The charge transferred to the capacitors in the first-cycle can be expressed as;

$$Q = I_{AV} T_S \tag{4-11}$$

where $I_{AV}$ is the average current in the inductor $L_{in}$, $T_S$ is the switching period and $Q$ is the amount of charge in the switching period and $T_S = (1/F_S)$. Assuming no losses within the converters, it can be shown that

$$Q = \frac{P_{rated}}{nV_{in}} T_S \tag{4-12}$$

The amount of charge can be calculated by the load that is used in the evaluation of the capacitor sizing as

$$Q = \frac{nV_{in}}{R_{load}} T_S \tag{4-13}$$

Hence;

$$Q = \frac{P_{rated}}{nV_{in}F_S} \tag{4-14}$$

From Figure 4.7(e), the charge transferred to the output capacitor results in a voltage change of $\Delta V_{Cn}$ . By using the amount of charge $Q$ and the selected voltage ripple, the capacitance is calculated by using;

$$C_{eq\,(P)} = \frac{Q}{\Delta V_{Cn}} \tag{4-15}$$

where $\Delta V_{Cn}$ is the desired peak-to-peak voltage ripple on the capacitor voltage. Substituting for $Q$ from Equation (4-14) to Equation (4-15) and rearranging;

$$C_{eq\,(P)} = \frac{\left(P_{rated} / nV_{in}\right)T_S}{\Delta V_{Cn}} \tag{4-16}$$

Hence,

$$C_{eq\,(P)} = \frac{P_{rated}}{nV_{in}\,\Delta V_{Cn}\,F_S} \tag{4-17}$$

Substituting for $F_S$ from Equation (4-6) into Equation (4-14) and rearranging $L_{in}$ can be expressed as;

$$L_{in} = \frac{1}{C_{eq\,(P)}}\left[\frac{Q\,nV_{in}}{2\pi\,P_{rated}}\right]^2 \tag{4-18}$$

In order to ensure soft switching the resonant frequency in the second half-cycle must be made equal to $\omega$. Hence,

$$\omega_2 = \frac{1}{\sqrt{L_{out}(C_{eq\,(s)} + C_{out})}} \tag{4-19}$$

where $\omega_2$ is the resonant Frequency of the converter in the second half-cycle, $C_{out}$ and $C_{eq(s)}$ is the output capacitance and equivalent capacitance in series respectively, as depicted in Figure 4.8. To achieve soft switching, the IGBTs during second half-cycle must be switched at the resonant frequency of the output inductor current waveform. Therefore, the switching frequency can be written as;

$$F_S = \frac{1}{2\pi\sqrt{L_{out}(C_{eq\,(s)} + C_{out})}} \tag{4-20}$$

Substituting for $F_S$ from Equation (4-14) into Equation (4-20) and rearranging $L_{out}$ can be expressed as;

$$L_{out} = \frac{1}{\left(C_{eq(S)} + C_{out}\right)}\left[\frac{Q n V_{in}}{2\pi P_{rated}}\right]^2 \qquad (4\text{-}21)$$

As shown in Figure 4.8, the total equivalent capacitance of both output capacitor and equivalent capacitance in series can be calculated as;

$$\left(C_{eq(S)} + C_{out}\right) = \frac{(3C_{eq(s)})(C_{out}/2)}{(3C_{eq(s)} + C_{out}/2)} \qquad (4\text{-}22)$$

The output voltage waveform is not similar to the other voltage capacitor waveforms in the charging state. Nevertheless, the value of the output capacitor depends on the relation between the amount of charge to the load at the half period of time $T_S/2$ and the voltage ripple on the output capacitor. Furthermore, the output capacitor works as charge storage for continuous delivery to the load. Using Equations (4-12), (4-15) and (4-20), the output capacitor value can be calculated using the expression:

$$C_{out} = \frac{\left(P_{rated}/V_{out}\right)\left(T_S/2\right)}{2\pi \Delta V_{Cout}} \qquad (4\text{-}23)$$

By using all the above procedures, the component values of the converter are listed in Table 4.1. All calculations and derivations are detailed in Appendix A.

Table 4.1: System parameters used for DCMC circuit simulation

| Parameter | Symbol | value |
|---|---|---|
| Input Voltage | $V_{in}$ | 6 kV |
| Output Voltage | $V_{out}$ | 30 kV |
| Load current | $I_{load}$ | 1.667 kA |
| Rated power | $P_{rate}$ | 50 MW |
| Switching frequency | $F_S$ | 2 kHz |
| Number of sub-module capacitors | $C_n$ | 5 |
| Sub-module Capacitance | $C_1$-$C_5$ | 694.5 µF |
| Output capacitance | $C_{out}$ | 115 µF |
| Input inductance | $L_{in}$ | 2.53 µH |
| Output inductance | $L_{out}$ | 110 µH |
| Load resistance | $R_{load}$ | 18 Ω |
| IGBT devices | 5SNA 1200G450300 | |

### 4.3.5 Evaluation of Steady-State Operation

As shown in Figure 4.1, the main advantage of this topology is that the DC-DC converters located at each wind turbine are removed. This helps to reduce the number of power electronic converters in the electrical system. This converter has a rated voltage of 6 kV and rated power of 50 MW. The converter was simulated using Matlab/Simulink software package. The configuration studied with 5 module capacitors is shown in Figure 4.3. The parameters of the DC-DC converter were calculated which are given in Table 4.1.

It can be observed that the inductor current waveforms are similar to the ideal shape waveform in Figure 4.7(a). However, the waveforms of input and output inductor currents as depicted in Figure. 4.9, show that the resonating inductor current increases to a peak around 26 kA in 250 µs, which also flows through the IGBT. The current amplitude and the voltage are key parameters in the design of the converter since they define the current and voltage rating for all IGBT switches.

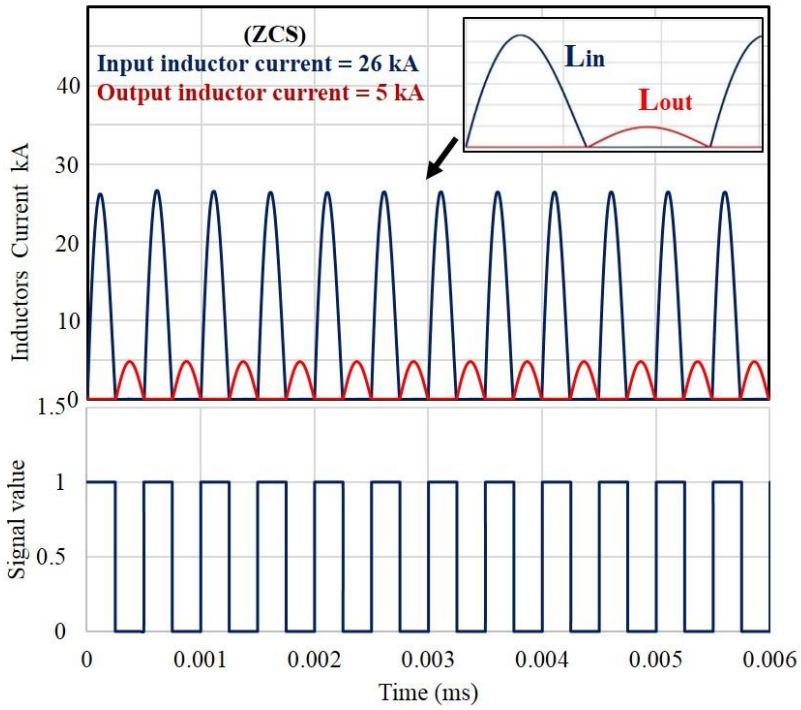


Figure 4.9: Inductor currents simulation waveforms

Therefore, the trade-off analysis for the converter is therefore performed considering peak current and voltage during the converter operation. The inspection of the characteristics of the IGBT ABB HiPak 5SNA 1200G450300, 4.5 kV 1.2 kA High power density [101], shows that this is feasible and the datasheet of the IGBT is attached in Appendix B. As the current begins to reverse in direction, the diode $D_{out}$ blocks the current flow.

As illustrated in Figure 4.10(a), for an input voltage of 6 kV the average output voltage is 29.93 kV, which is very close to the design specification of 30 kV. Hence the DC gain is 4.98 compare well with the theoretical gain of 5. The peak load current of 1.662 kA is very close to the design value of 1.667 kA as shown in Figure 4.10(b).

The input power value is the same as output power with different voltage level and rating current. The output power waveform, shown in Figure 4.10(c), is 49.74 MW. It is close to the designed power as listed in Table 4.1. The reason for that is the drop voltage which is caused by the switching losses.

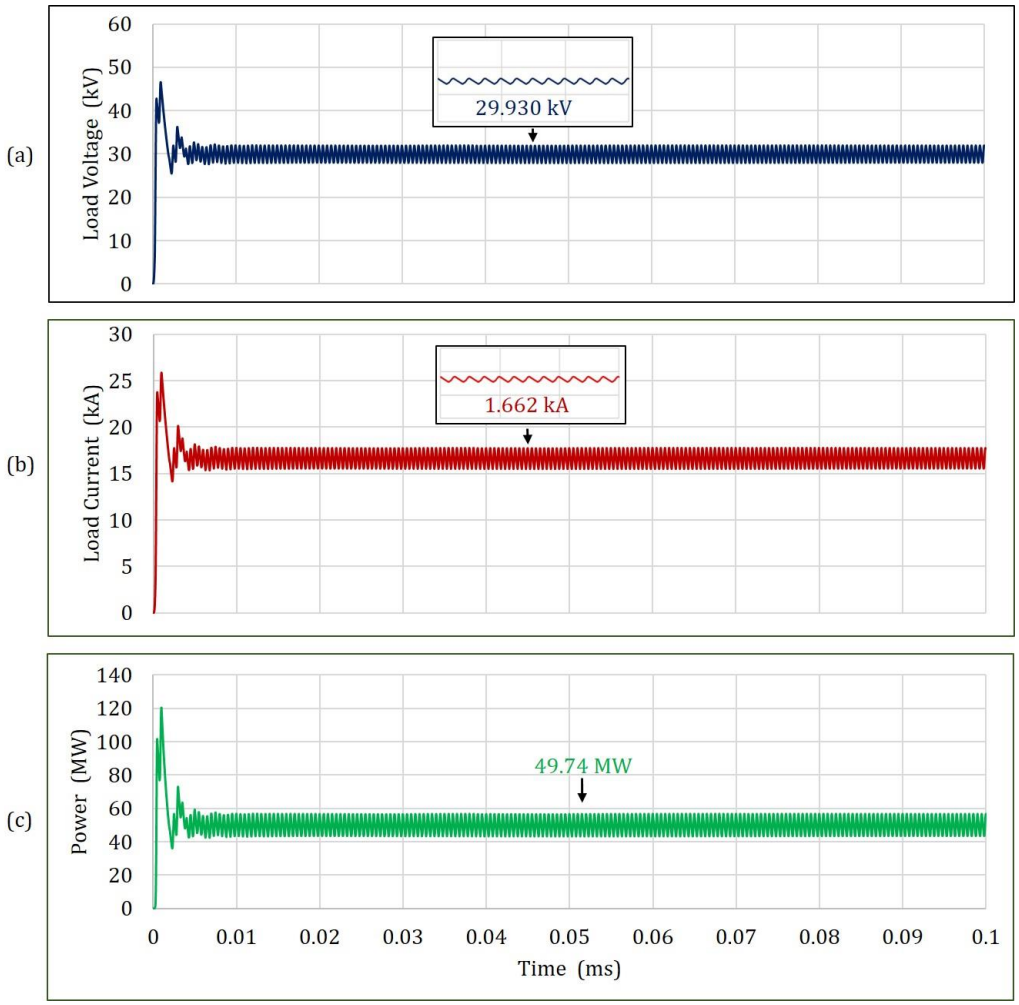


Figure 4.10: Output simulation waveforms, a) Output voltage, b) load current, and c) output DC power

### 4.3.6 Voltage and Current Stresses

Figure 4.11(a), and Figure 4.11(b) show the average DC voltages across diodes *($D_1$-$D_8$)* sequentially increase by 6 kV, and the charging current flows via these diodes *($D_1$-$D_8$)* divided by the number of capacitors in the middle circuit, is 5.3 kA. The voltages across switches $S_{valve}$ labelled as the yellow circuit shown in Figure 4.3, reach a maximum of 24 kV as shown in Figure 11(c). Also, the IGBT switch $S_{valve}$ and diode $D_{in}$ carry the full inductor current $I_{L1}$ during the first half-cycle. The peak current is 26.6 kA at 250 µs as depicted in Figure 4.11(d). The voltage stress on the switches *($S_1$-$S_4$)* is 6 kV during charging of the capacitors in parallel is equal to the $V_{in}$ as shown in Figure 4.11(e). The switching pattern of the converter is illustrated in Figure 4.11(f).

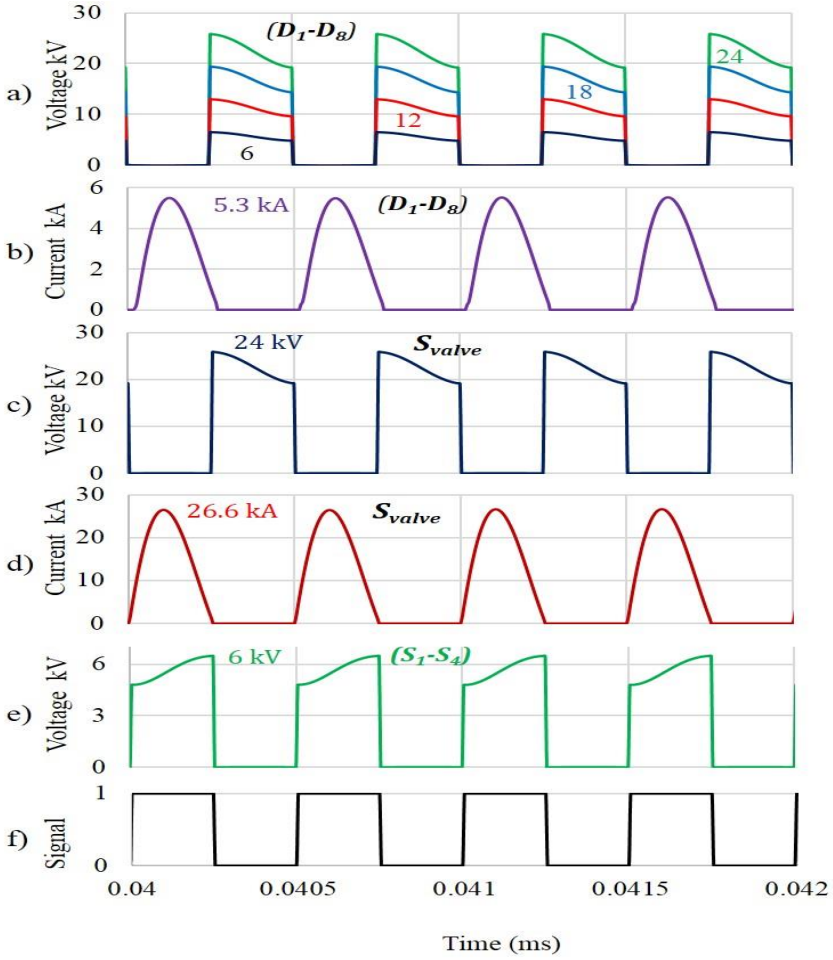


Figure 4.11: IGBT and diode switch simulation waveforms

### 4.3.7 Evaluation of Dynamic Operation

The evaluation of the dynamic characteristics of the converter was carried out by simulation.

#### 4.3.7.1 Change the Load

The change in the load is simulated by changing 50% in the value of the load $R_{load}$, from 18 Ω to 9 Ω at 0.02 ms as shown in Figure 4.12(c). The input inductor current $I_{Lin}$ waveform and the voltage capacitor waveform of the output capacitor are shown in Figure 4.12(a) and Figure 4.12(b) respectively. The designed load voltage is 30 kV and the input voltage $V_{in}$ is unchanged at 6 kV. The high drain in current form the output capacitor decreases the output voltage $V_{out}$ from 29.93 kV to 26.67 kV.

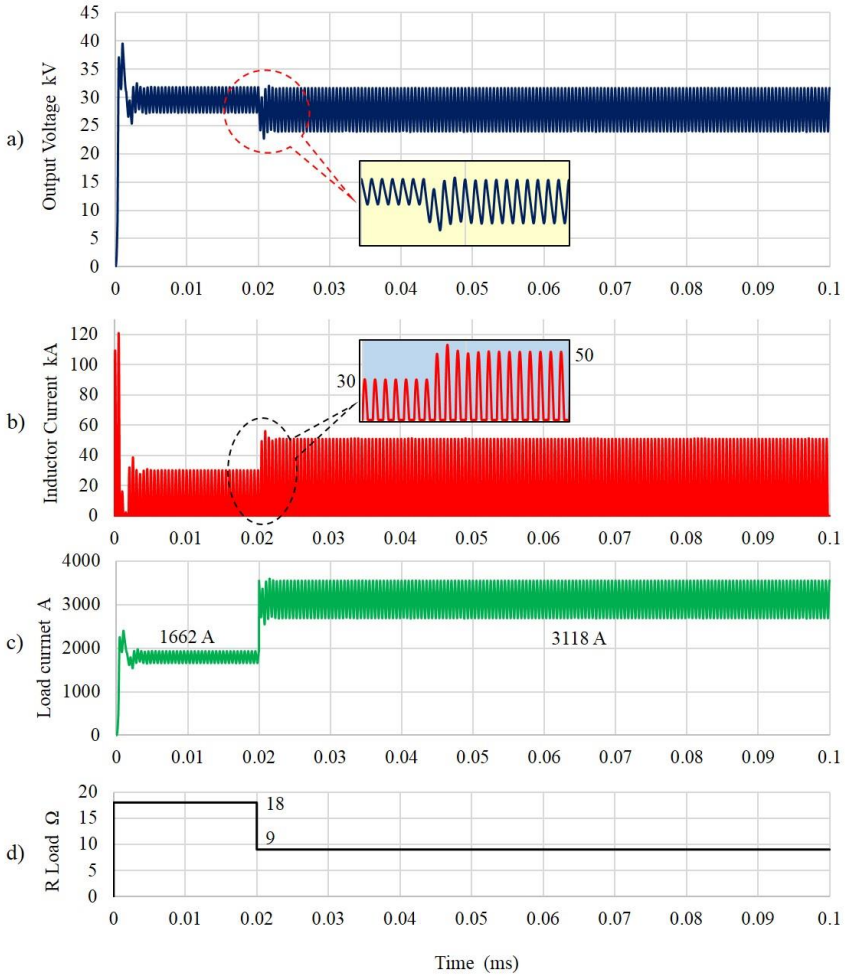


Figure 4.12: Simulation results for output voltage and input inductor current

The transient current was not large in the input inductor as depicted in Figure 4.12(a), and the transient occurred at 0.02 ms during the change of the load, with a settling time of about one cycle. Meanwhile, the ripple output voltage $\Delta V_{Cout}$ has increased from 6.19 kV to 7.02 kV and the percentage is 30%. This value is high because the step-change load is 50%. As the power rating of the converter is 50 MW, at 0.02 ms and during the step change at 0.02 ms, the load current has a step increase from the steady-state value of 1662 A to the transient state value of 3118 A as depicted in Figure 4.12(c).

#### 4.3.7.2 Device and Component Stresses

During step-change of the load, the voltage across the diodes and IGBT switches is close to the design rating, but there is a bit of change in the ripple voltage across the diodes *($D_1$-$D_8$)*, output diode $D_{out}$, and IGBT switches *($S_1$-$S_4$)* as shown in Figure

4.13(a), Figure 4.13(c), Figure 4.13(e), and Figure 4.13(g). This increasing of the ripple voltage affects the output ripple voltage by increasing more than the steady-state output voltage ripple as shown in Figure 4.12(a). The voltages across diodes *($D_1$-$D_8$)* increase by 6 kV, reaching a maximum of 24 kV as shown in Figure 4.13(a). Furthermore, the charging current flows in parallel via diodes *($D_1$-$D_8$)* in the first half-cycle is increased from 5 kA to 10 kA during change in the load as depicted in Figure 4.13(b) and Figure 4.13(d). During the discharge the capacitors in series, the voltage across the switch $S_{valve}$ is the sum of the capacitor voltages in series, reaching 24 kV. Also, during the transient the ripple voltage has increased as shown in Figure 4.13(g). In addition, the current flowing through the switch $S_{valve}$ has doubled as the load is decreased by 50%, and as illustrated in Figure 4.13(h), the current increased from 22.2 kA to 41.46 kA.

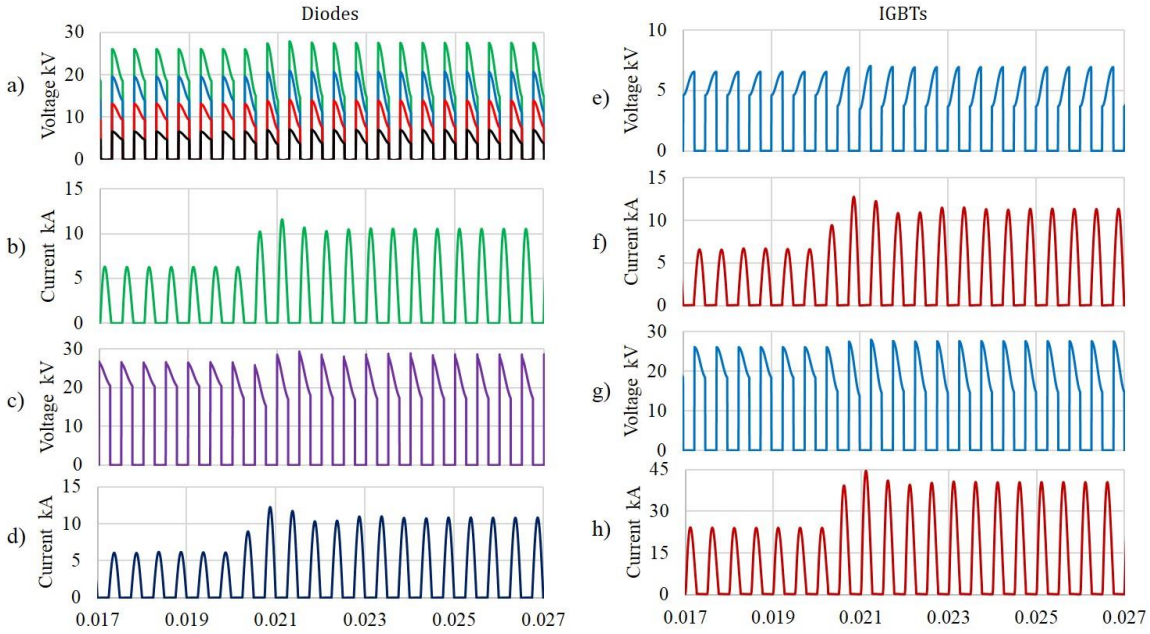


Figure 4.13: IGBT and diode switch simulation waveforms during step change the load. a) Voltage across diodes ($D_1$-$D_8$), b) Current flows diodes ($D_1$-$D_8$), c) Voltage across output diode $D_{out}$, d) Current flows through output diode $D_{out}$, e) Voltage cross IGBT switches ($S_1$-$S_4$), f) Current flows through IGBT switches ($S_1$-$S_4$), g) Voltage cross IGBT switch $S_{valve}$, and h) current flows through IGBT switch $S_{valve}$

### 4.3.8 Comparative Performance Evaluation

A quantitative comparison was carried out using data from the output results by Matlab/ Simulink simulation, and the proposed configuration is evaluated and compared with Veilleux converters in terms of the power device count to highlight its advantages for high-voltage applications as mentioned in section 4.1.

Although a Veilleux converter that avoids using a transformer and uses a Marx converter to transfer power from an offshore wind farm to an onshore substation, would use several of IGBT switches to control the power flow. The improved proposed design has used a smaller number of IGBT switches. Both topologies are operating with the same DC-DC Marx converter principle; hence, the comparison is made for the same three gains, same input voltage, same power rating, same load, same soft switching technique, and same switching frequency [100].

The output voltage and current of both topologies should be 30 kV/ 1667 A as designed. However, the output voltage of the Veilleux topology is 29.59 kV, and the proposed topology is 29.93 kV. In addition, the load current of Veilleux topology is 1644 A, and the proposed topology is 1662 A. Both converter topologies are comprised of several power devices, IGBT switches and diodes connected in series to withstand the rated voltage. The number of IGBTs switches required for gain at 1:5 is only 11 in the proposed topology, but in a Veilleux topology 20 are required, as shown in Figure 4.14.

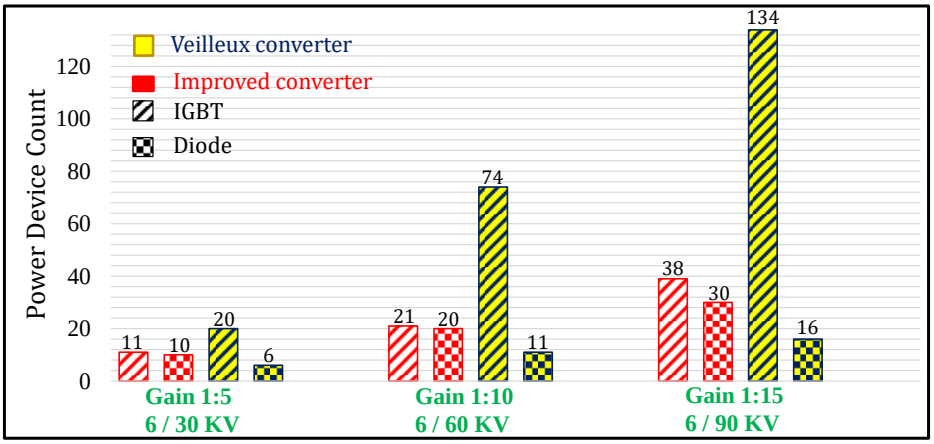


Figure 4.14: Power device count comparison

The voltage level of the switches is an important issue because the devices built to sustain higher voltages are more expensive and achieve higher losses due to doping requirements. In a Veilleux converter, the power device count is directly proportional to the voltage gain ratio and higher than in an improved converter. In 6/60 kV gain ratio, the improved converter device count for diode and IGBTs is 24, but in a Veilleux converter, the IGBT switches count is 81 and diodes number 11. In addition, for the gain ratio 6/90 kV, as shown in Figure 4.14, the count of IGBTs in a Veilleux converter is higher than in the improved converter, in which they number 38 and 171, respectively.

A lower device count means lower losses, fewer failure points, smaller physical size, and lower cost. Based on these comparisons, the improved converter topology has clear advantages over a Veilleux converter in terms of the power device count, and voltage stresses of the switching device. On the other hand, the total number of diodes for the proposed converter is larger than that of the Veilleux converter, but it can be observed that the Veilleux converter requires a larger switch count compared to the improved converter.

## 4.4 Cascaded DC-DC Marx Converter

This topology also modifies and improves the Veilleux Cascaded topology [7], which uses the same method of a single-stage DC-DC converter, except the difference is in a cascaded converter composed of cascaded stages (J, K, L). In order to derive the formula for this converter that will be generally useful in design, the next section will describe and present all the details of the Veilleux cascaded topology and improved cascaded converter. As depicted in Figure 4.15, Veilleux cascaded consists of multi-stages of the Marx modules connected in a cascade comprising three main sections of input, middle, and output section. The middle section consists of three stages, stage 1, stage 2, and stage 3. Stage 1 and stage 3 are identical but the size of the components is different, and every stage consists of two capacitors, three switches, two diodes, and an inductor. Stage 2 has three capacitors, four switches, and three diodes. The overall DC voltage gain is 2x3x2= 12, (1:12). In addition, there is an output capacitor at the output stage to smooth the load voltage. The operation can be divided into two cycles. A

disadvantage of this topology is the high number of IGBT switches in stage 2, and the increased voltage stress in the IGBTs in successive stages.

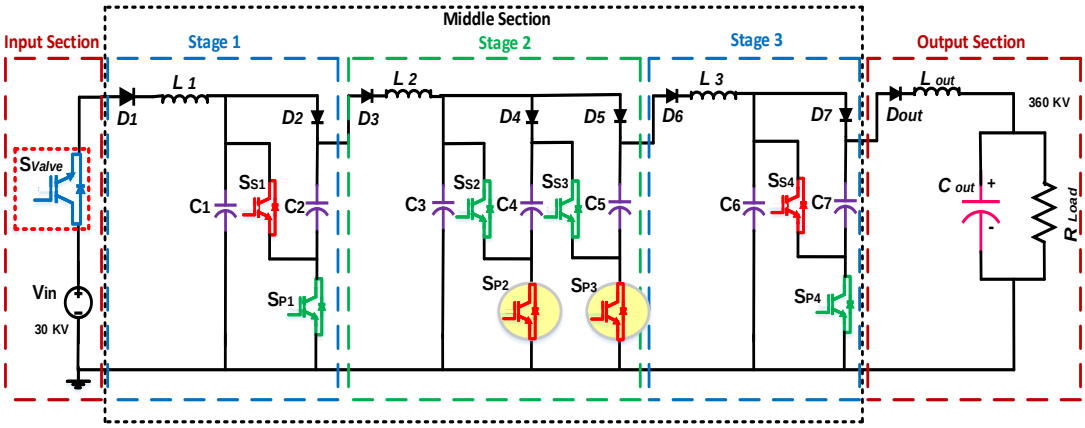


Figure 4.15: Veilleux cascaded Marx DC-DC converter

### 4.4.1 Circuit Arrangement

The structure of the cascaded DC-DC converter is shown in Figure. 4.16. The advantage is that the number of components is reduced as shown later in the document and in the flexibility for increasing the number of stages in the middle section for increasing the gain. The ratings and the component values used for this study are determined for application to the HV converter in a typical wind energy system as illustrated in Figure 4.16. The equivalent circuit is shown in Figure 4.16. The input section consists of an input DC voltage source $V_{in}$ and HV valve $S_{valve}$ comprising series connected IGBTs. The middle section is composed of *'n'* stages; stage 1, stage 2, stage 3 and stage *n*, depending on the voltage gain ratio. Figure 4.16 shows the circuit, a generalised cascaded converter with *'N'* number of stages, and has provided and fixed 3 stages J, K, and L. The converter is comprised of three sections. The number of capacitors in converter stages 1, 2 and 3, are set to 2, 3, and 2 respectively, to create a voltage amplification of 2x3x2= 12. However, the number of capacitors can be J, K, and L respectively and hence; $C_J$, $C_K$ and $C_L$ indicate the capacitors in the stages 1, 2, and 3 respectively.

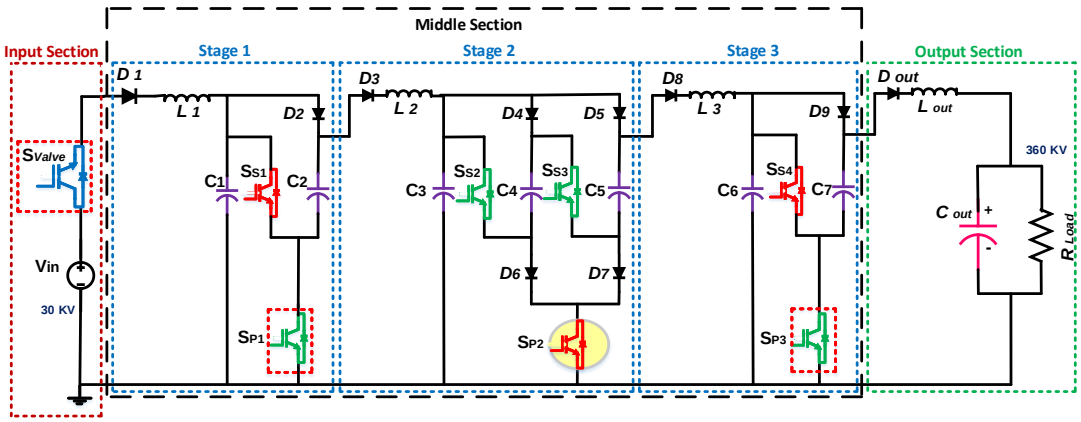


Figure 4.16: Model cascaded DC-DC Marx converter

The switching components in the middle section denoted by $S_{Si}$ ($i$ =1~4) are used to connect the capacitors in series. The IGBT switches denoted by $S_{Pi}$ ($i$ =1~3) are used to connect the capacitors in parallel. The diodes are used to trap the charges in the capacitors and to ensure that they discharge in the correct direction. The output section consists of an output diode $D_{out}$ connected in series with the output inductor $L_{out}$ and output capacitor $C_{out}$. A pure resistive load was selected, $R_{Load}$.

### 4.4.2 Steady-State Operation

The steady-state operation can be explained in terms of two half-cycles. In simple terms, the IGBTs are switched so that the charges for capacitors are pumped from left to right sequentially resulting in a high voltage at the converter output. The switching of the IGBTs and diodes is summarised in Table 4.2 and Table 4.3 respectively.

Table 4.2: IGBT switching logic for the improved converter

| Switches | $S_{Valve}$ | $S_{P1}$ | $S_{P2}$ | $S_{P3}$ | $S_{S1}$ | $S_{S2}$ | $S_{S3}$ | $S_{S4}$ |
|---|---|---|---|---|---|---|---|---|
| First half cycle | 1 | 1 | 0 | 1 | 0 | 1 | 1 | 0 |
| Second half cycle | 0 | 0 | 1 | 0 | 1 | 0 | 0 | 1 |

Table 4.3: Diodes switching logic for the improved converter

| Switches | $D_1$ | $D_2$ | $D_3$ | $D_4$ | $D_5$ | $D_6$ | $D_7$ | $D_8$ |
|---|---|---|---|---|---|---|---|---|
| First half cycle | 1 | 1 | 0 | 0 | 0 | 0 | 0 | 1 |
| Second half cycle | 0 | 0 | 1 | 1 | 1 | 1 | 1 | 0 |

The corresponding sub-circuits are shown in Figure 4.17(a) and Figure 4.17(b), respectively where the 'ON' and 'OFF' devices are shown in green and light grey, respectively. During the first half-cycle, capacitors in stages 1 and 3 are connected in parallel and are being charged through the inductors $L_1$ and $L_3$. The capacitors in Stage 2, which have been charged in the previous cycle are in series and discharge into stage 3 capacitors. Diodes $D_1$, $D_2$, $D_8$, and $D_9$ are conducted.

In the second half-cycle, the devices are switched so that the capacitors in stage 1, 3 and stage 2 are in parallel and series respectively. Hence, capacitors in stages 1, 3 and 2 are charged and discharged respectively.

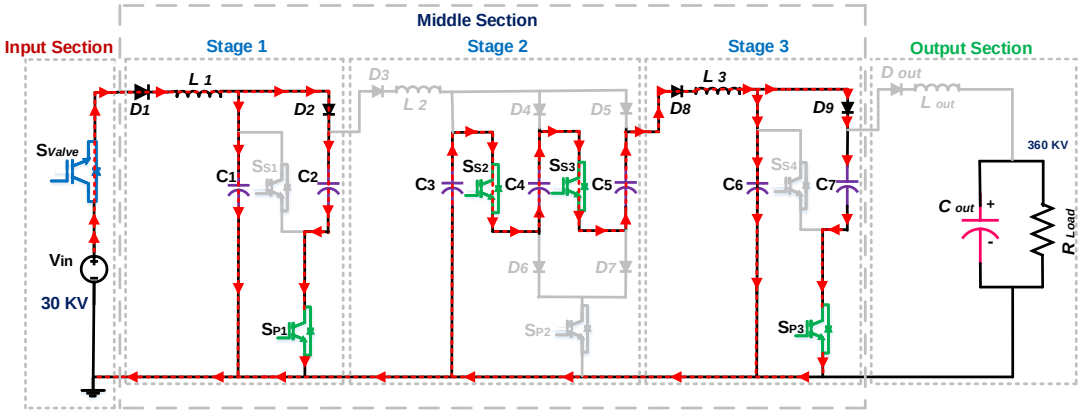


a) First half-cycle configuration

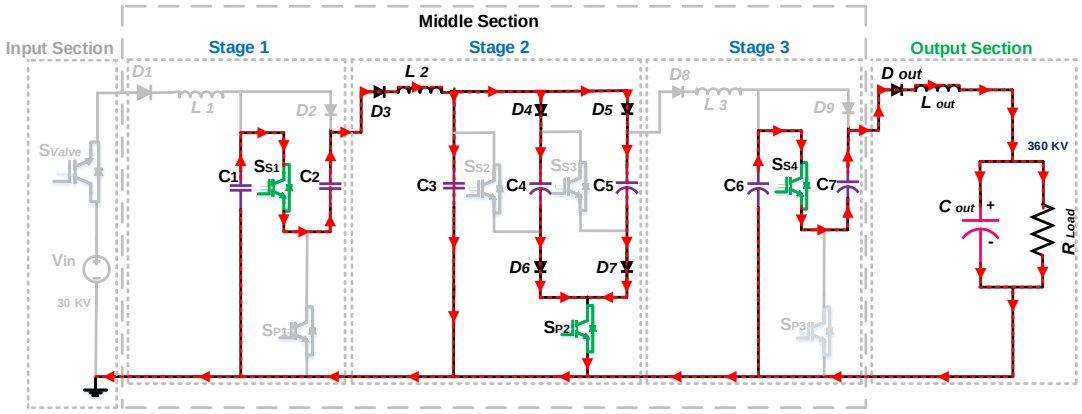


b) Second half-cycle configuration

Figure 4.17: The arrangement for switching time of cascaded DC-DC converter

### 4.4.3 Analysis and Design of the Converter

The analysis and design of this converter represents a different method if compared with a single-stage converter, because this converter has been connected in cascaded and contents of four determinations. Firstly, it is assumed that the cascaded DC-DC converter has already reached steady-state operation. The gain of the converter increases as by a geometric series which depends on the number of capacitance cells in stage 1 *(J)*, stage 2 *(K)*, and stage 3 *(L)*. The voltage transformation ratio $V_{TR}$ is given as;

$$V_{TR} = \frac{V_{out}}{V_{in}} = N_{CJ}\, N_{CK}\, N_{CL} \qquad (4\text{-}24)$$

where $V_{out}$ and $V_{in}$ are the output and input voltages, respectively. The equivalent capacitance in stage 1 is similar to the Equation (4-3). During the first half-cycle, the inductor $L_1$ and the equivalent capacitance $C_{eq\ (J)}$ forms an oscillatory L-C circuit and hence the current in stage 1 is the same as in Equation (4-4). The angular resonant frequency in stage 1 is given by;

$$\omega_1 = \frac{1}{\sqrt{L_1 C_{eq(J)}}} \qquad (4\text{-}25)$$

In order to achieve soft switching, the IGBTs must be switched at the resonant frequency of the inductor current waveform. Therefore, the switching frequency can be written as;

$$F_S = \frac{1}{2\pi\sqrt{L_1 C_{eq(J)}}} \qquad (4\text{-}26)$$

As mentioned, the converter's structure includes stage 1, stage 2, stage 3, and output stage parameters, and the next sub-section presents the determination of parameters.

#### 4.4.3.1 Determination of Stage 1 Parameters

In this stage there are two capacitors which are charged in parallel in the first half-cycle as shown in Figure 4.18

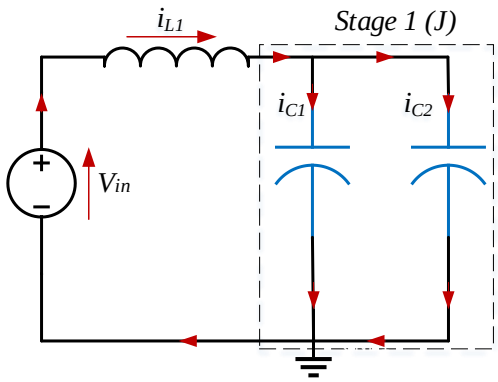


Figure 4.18: Charging capacitors in parallel (stage 1)

From Figure 4.18, in the first half-cycle, the inductor current $i_{L1}$ is divided into two charge current capacitors $i_{C1}$ and $i_{C2}$. However, the charge transferred to the capacitors in stage 1 can be expressed as in the Equation (4-14). When the inductor current $i_{L1}$ reach zero and becomes reversed, the diode $D_{in}$ blocks flowing back current to the input voltage $V_{in}$.

Figure 4.19(a) shows the inductor current $i_{L1}$ waveform and the switching time of the active switches, which is divided into two half-cycles as shown in Figure 4.19(b). The two half-cycles are chosen to operate with equal duration, $T_S/2$, where $T_S$ is the periodicity of the switching frequency $F_S$. Furthermore, Figure 4.19 shows the circuit topology for the time period $t_0 \leq t_1 \leq t_2$, where $(t_0\text{-}t_1) = (t_1\text{-}t_2) = T_S/2$. The inductor current $i_{L1}$ is a positive half-sine wave during the first period, charging the first stage capacitors in parallel at time $T_S/2$. However, this current is divided into (J) to charge the capacitors through the capacitor current $I_{CJ}$ as depicted in Figure 4.19(c).

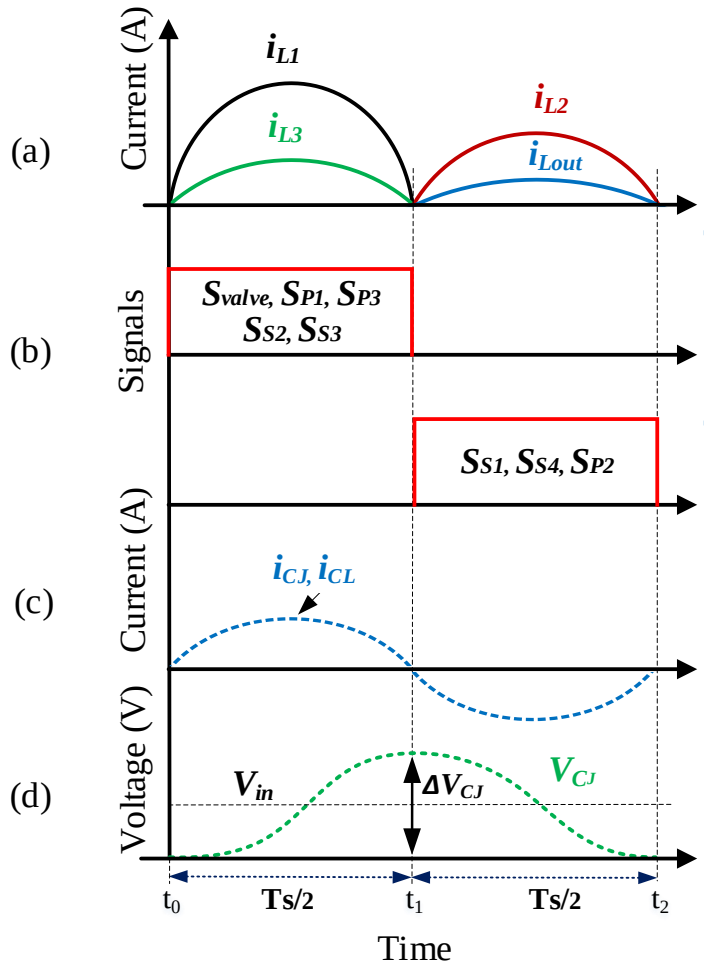


Figure 4.19**:** Steady-state waveforms model cascaded DC-DC converter

From Figure 4.19(d), the charge transferred to stage 1 capacitors results in a voltage change of $\Delta V_{CJ}$, which is given as in the Equation (4-17). Substituting for $Q$ from Equation (4-17) to Equation (4-27) and rearranging, then the equation for the equivalent capacitance in the first stage is:

$$C_{eq(J)} = \frac{P_{rated}}{N V_{in} \Delta V_{C(J)} F_S} \qquad (4\text{-}27)$$

Hence,

$$C_J\big|_{j=1,J} = \frac{P_{rated}}{N V_{in} \Delta V_{C(J)} F_S} \frac{1}{J} \qquad (4\text{-}28)$$

Substituting for $F_S$ from Equation (4-30) into Equation (4-17) and rearranging $L_1$ can be expressed as;

$$L_1 = \frac{1}{C_{eq(J)}}\left[\frac{Q\,NV_{in}}{2\pi\,P_{rated}}\right]^2 \qquad (4\text{-}29)$$

### 4.4.3.2 Determination of Stage 2 Parameters

In this stage, in the first half-cycle, capacitors will discharge in series via inductor current $L_3$ to charge the capacitors in stage 3 in parallel. In the second half-cycle will charge capacitors in parallel by inductor current $L_2$ via discharge the capacitors in series in stage 1 as illustrated in Figure 4.20.

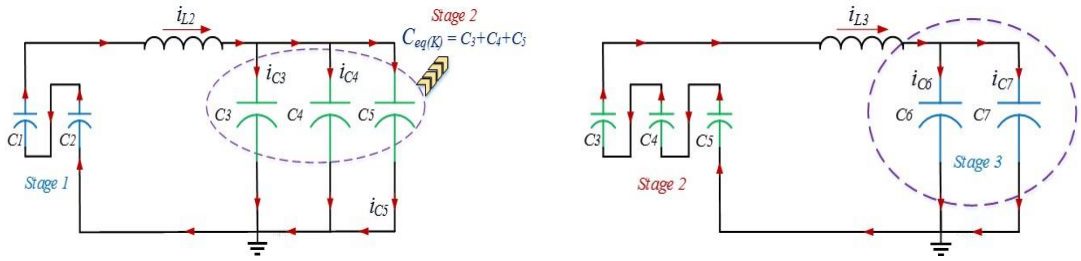


a) Charging stage 2 in parallel b) Discharging stage 2 in series

Figure 4.20: Stage two for the two half-cycle operations

In order to ensure soft switching, the resonant frequency in the second half-cycle must be made equal to $\omega_2$. Hence,

$$\omega_2 = \frac{1}{\sqrt{L_2(C_{eq(J)} + C_{eq(K)})}} \qquad (4\text{-}30)$$

The capacitance of both stages $C_J$ in series and $C_K$ in parallel. As shown in Figure 4.20(a), the number of capacitors (K) in stage 2 are connected and charged by the number of series capacitors (J) in stage 1. Therefore, the equivalent capacitance of this state is given as;

$$C_{eq(J+K)} = \frac{(C_J/2)(3C_K)}{(C_J/2)(3C_K)} \qquad (4\text{-}31)$$

Figures 4.19(a) and 4.19(c) show the waveform of the inductor current $i_{L2}$ and the capacitor current $i_{CJ}$. In stage 2, from ($t_1$-$t_2$) the inductor current $i_{L2}$ has the same value with opposite polarity current of capacitor current $i_{CJ}$. However, this

current has been divided into a number of capacitors (K) in stage 2. By combining Equation (4.30) and (4.31), inductor $L_2$in stage two can be calculated as:

$$L_2 = \left(\frac{2K^n}{C_{eq(K)}}\right)\left(\frac{C_J}{J^n}\right)^2 \qquad (4\text{-}32)$$

However, the capacitance values in stage 1, 2 and 3 are chosen so that percentage of ripple on all the capacitors is the same. Therefore, the capacitance $C_K$ in the stage 2 can be expressed as;

$$C_K = \frac{C_J}{N_{CJ}+N_{CK}+N_{CL}} \qquad (4\text{-}33)$$

#### 4.4.3.3 Determination of Stage 3 Parameters

Figure 4.19(a) shows the inductor current $i_{L3}$ as a positive half-sine wave during charging the capacitors $C_L$ in the first half-cycle from $(t_0\text{-}t_1)$. Therefore, the inductor current has been divided into a number of the capacitors in stage 3*(L)* as illustrated in Figure 4.21 and can be expressed as;

$$i_{L3} = (C_6 + C_7)\frac{dv}{dt} = i_{C6} + i_{C7} \qquad (4\text{-}34)$$

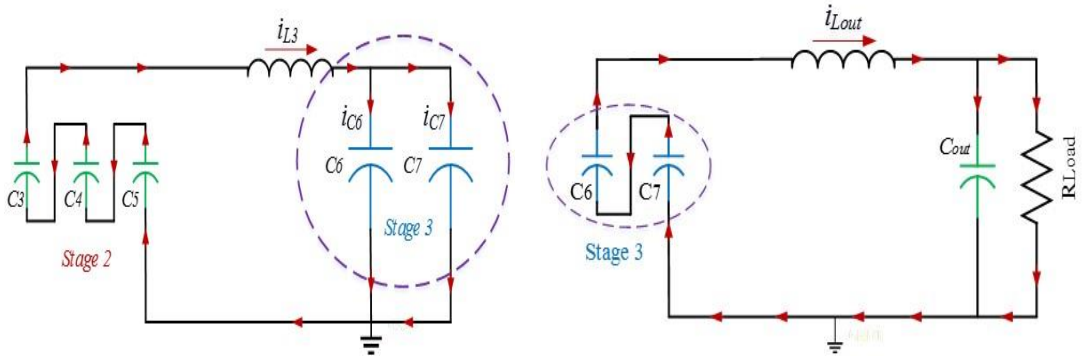


a) Charging stage 3 in parallel b) Discharge stage 3 in series

Figure 4.21: Stage three during two half-cycle operations

In the second half-cycle $(t_1\text{-}t_2)$, the sum of capacitor currents $i_{CL}$ is equal to the output inductor current $i_{Lout}$ as shown in Figure 4.21(b) and can be expressed as;

$$i_{Lout} = (i_{C6} + i_{C7}) \tag{4-35}$$

Using the same way, inductor $L_2$ was derived, inductor $L_3$ can be obtained as;

$$L_3 = \left(\frac{2L^n}{C_{eq(L)}}\right)\left(\frac{C_K}{K^n}\right)^2 \tag{4-36}$$

In order to maintain the relative voltage ripple $(\Delta V_{CL}/VC_L)$ the same as with $(\Delta VC_K/VC_K)$ for capacitor K, it is necessary to make $C_L$ as;

$$C_L = \frac{C_K}{N_{CJ}+N_{CK}+N_{CL}} \tag{4-37}$$

The relationship between ripple voltage and capacitor voltage in the first stage is the same in stages 2 and 3, and can be shown as:

$$\frac{\Delta V_{CJ}}{V_{CJ}} = \frac{\Delta V_{CK}}{V_{CK}} = \frac{\Delta V_{CL}}{V_{CL}} \tag{4-38}$$

#### 4.4.3.4 Determination of Output Stage Parameters

As illustrated in Figure 4.21(b), the output stage is charged from $(t_1\text{-}t_2)$, and the electric charge in stage 3 is transferred in series to the output capacitor $C_{out}$ through an output inductor $L_{out}$ and an output diode $D_{out}$. The size of the output inductor depends on the output voltage and the amount of charges which needs to be transferred. The value of the output inductor depends on the peak-to-peak output current $\Delta I_{Lout}$ and can therefore be expressed as;

$$L_{out} = \left(\frac{NV_{in}\,T_s}{\Delta I_{Lout}}\right) \tag{4-39}$$

The output voltage waveform is not similar to the other voltage capacitor waveforms in the middle stage. Nevertheless, the value of the output capacitor depends on the relation between the amount of charge to the load at the half period of time $T_S/2$, and the voltage ripple on the output capacitor. Furthermore, the output capacitor works as charge storage for continuous delivery to the load. The Equation can be written as:

$$C_{out} = \frac{(P_{rated} / V_{out})(T_S / 2)}{2\pi \, \Delta V_{Cout}} \qquad (4\text{-}40)$$

where $\Delta VC_{out}$ is the desired peak-to-peak voltage ripple on the output capacitor. By using all the above stages procedures, the component values of the converter are listed in Table 4.4. Furthermore, overall the calculation is explained in Appendix A.

Table 4.4: Parameters used for cascaded DC-DC converter simulation

| Parameter | | | Value/ model |
|---|---|---|---|
| Number of stages | | n | 3 |
| Number of capacitors in each stage | | $N_{CJ}$ $N_{CK}$ $N_{CL}$ | 2, 3, 2 |
| Input Voltage | | $V_{in}$ | 30 kV |
| Output Voltage | | $V_{out}$ | 360 kV |
| Load Current | | $L_{out}$ | 138.89 A |
| Rated power | | $P_{rated}$ | 50 MW |
| Switching Frequency | | $F_S$ | 2 kHz |
| Output Load Resistance | | $R_{Load}$ | 2592 Ω |
| IGBT | | | 5SNA 1200G450300 |
| Fast recovery diode | | | 5SDF13H4501 |
| Capacitors | | Inductors | |
| $C_J$ | 694.5 µF | $L_1$ | 5.3 µH |
| $C_K$ | 99.21 µF | $L_2$ | 40 µH |
| $C_L$ | 14.17 µF | $L_3$ | 400 µH |
| $C_{out}$ | 300 µF | $L_{out}$ | 2.2 mH |

### 4.4.4 Evaluation of Steady-State Operation

This topology is represented with DC voltage source 30 kV, rated power 50 MW as shown in Figure 4.15. The HV converter, whose equivalent circuit is shown in Figure 4.15, was simulated by Matlab/Simulink software package. The converter parameters are listed in Table 4.4 were calculated using the design equations derived in the design section.

Current waveforms and switching pattern are shown in Figure 4.22(a) and Figure 4.22(b). Figure 4.22(a) shows the resonant nature of the currents through inductors and IGBTs allowing soft switching at current zeros leading to a reduction in switching losses. Also, Figure 4.22(a) shows the switching signals clearly indicating soft switching at a frequency of 2 kHz.

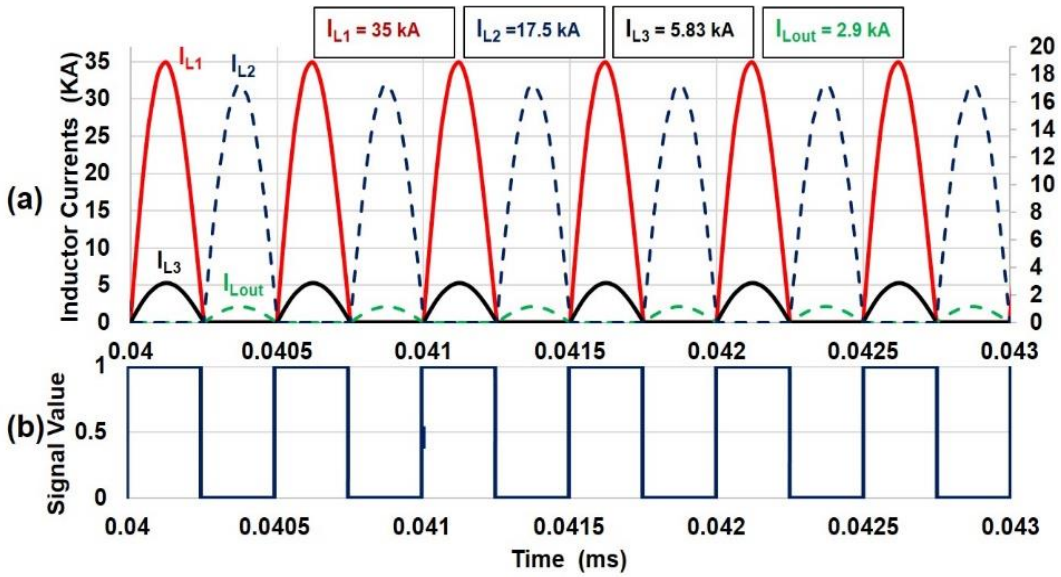


a) Inductor current waveforms (ZCS) b) Switching pattern

Figure 4.22: Matlab / Simulink simulation results of the proposed converter

Figure 4.23 shows the load voltage and current waveforms confirming that the design specifications are met. The DC amplification gain of the simulation is 11.96, which is very close to the design value of 12. The resonating inductor current, which flows through the IGBT increases to a peak $I_{L1}$= 35 kA in 250 µs, which is within the capability of modern IGBTs and all the IGBTs that used in the cascaded converter is 4.5 kV 1200 A and has manufactured by ABB [101].

As shown in Figure 4.22, at each successive stage, the peak currents of $I_{L1}$, $I_{L2}$, $I_{L3}$, $I_{Lout}$ are decreased by a factor of 1/N, and as the voltage stages are increased by 'N'. However, the peak inductor currents are decreased in multiples of ½, ⅓, and ½. Which depends on the number of capacitors in each stage. Furthermore, the output power has an average of 48.005 MW as shown in Figure 4.24, it is closer to the design value of a power rating of 50 MW as listed in Table 4.4.

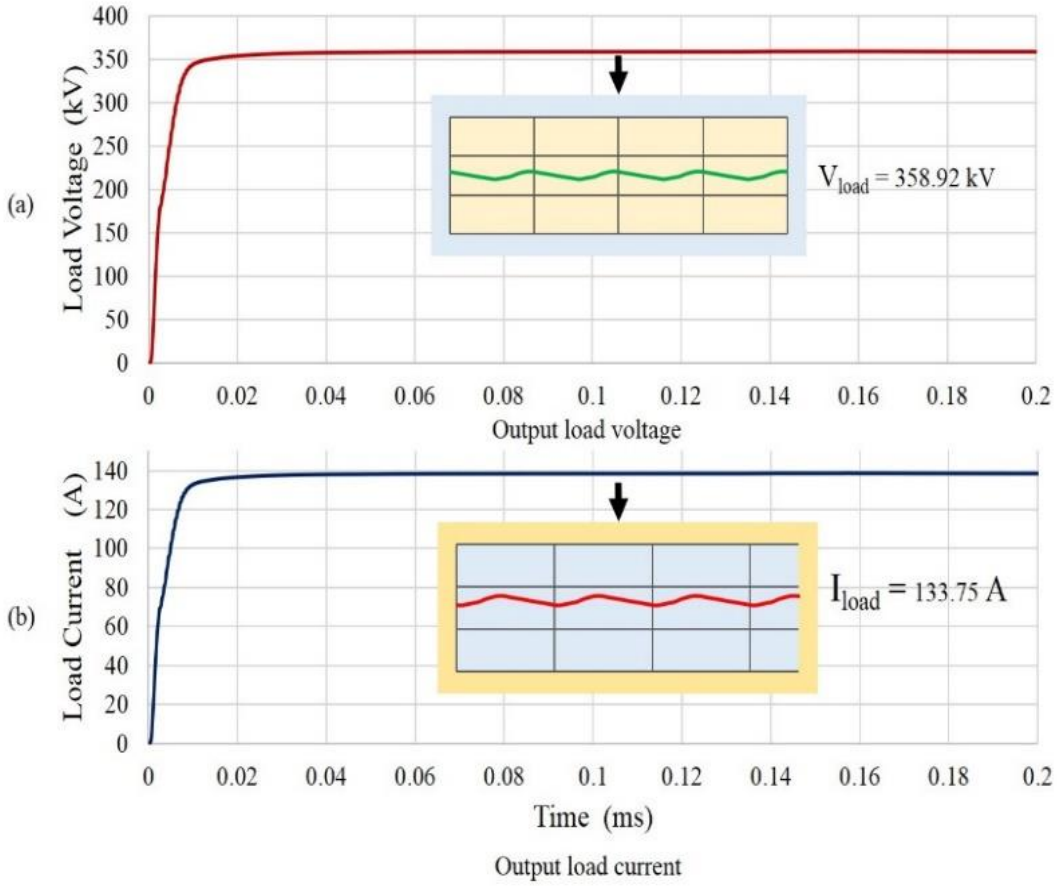


Figure 4.23: Simulation waveforms of the cascaded DC-DC converter

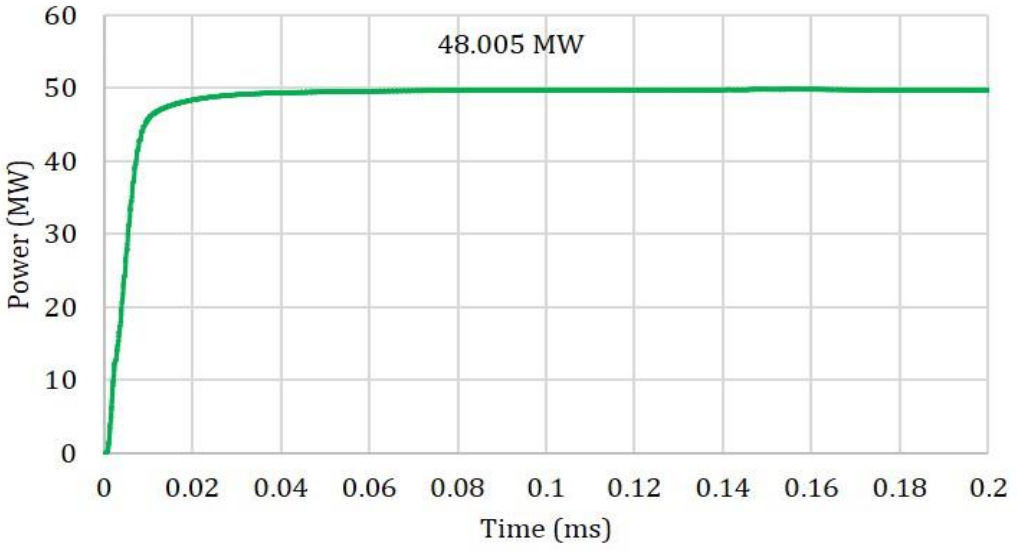


Figure 4.24: Output power waveforms of the cascaded DC-DC converter model

As seen in Figure 4.22, the respective peak inductor currents in consequent stages decrease according to the number of capacitors in the previous stage. The effect can be generalised as shown in Table 4.5. The proposed cascaded configuration is evaluated and compared with a Veilleux converter in terms of the power device count to highlight its advantages in high-voltage applications.

Table 4.5: Shows the peak inductor currents and voltage across capacitors

| Parameters | Stage 1 | Stage 2 | Stage 3 | Output section |
|---|---|---|---|---|
| Number of capacitors | *2* | *3* | *2* | *1* |
| Peak inductor currents relation | $I_{L1}$ | $I_{L2} = I_{L1}/2$ | $I_{L3} = I_{L2}/3$ | $I_{Lout} = I_{L3}/2$ |
| Number of stages | $J$ | $K$ | $L$ | $L_{out}$ |
| Peak inductor currents | $I_{L1}^{P}$ | $I_{L2}^{P} = I_{L1}^{P}/J$ | $I_{L3}^{P} = I_{L2}^{P}/K$ | $I_{out}^{P} = I_{L3}^{P}/L$ |
| Voltage cross capacitors | $V_{C1}=V_{C2}=V_{in}$ | $V_{C3}=V_{C4}=V_{C5} = JV_{in}$ | $V_{C6}=V_{C7}= JKV_{in}$ | $V_{out}= JKLV_{in}$ |

The IGBT considered for this study are 4.5 kV and 1200 A, and the datasheet of this IGBT switch is attached in Appendix B. The total number of IGBTs can be reduced from 52 to 38 by combining the function of 2 IGBT switches $(S_{P2}\text{-}S_{P3})$ to be performed by 2 diodes and 1 IGBT $(S_{valve})$ as illustrated in the yellow circle in Figure 4.16.

As shown in Figure 4.25, the average DC voltages across capacitors increase and their values depend on the number of capacitors in each stage as depicted in Table 4.5. Capacitor voltages in stage 1, stage 2, and stage 3 are charging by 29.97 kV, 59.69 kV, and 179.47 kV, respectively. The discrepancy between design charging voltage and simulation results is mainly due to small resistance of the IGBT switches and diodes, which have been omitted in the mathematical analysis equations, but it is included in the simulation.

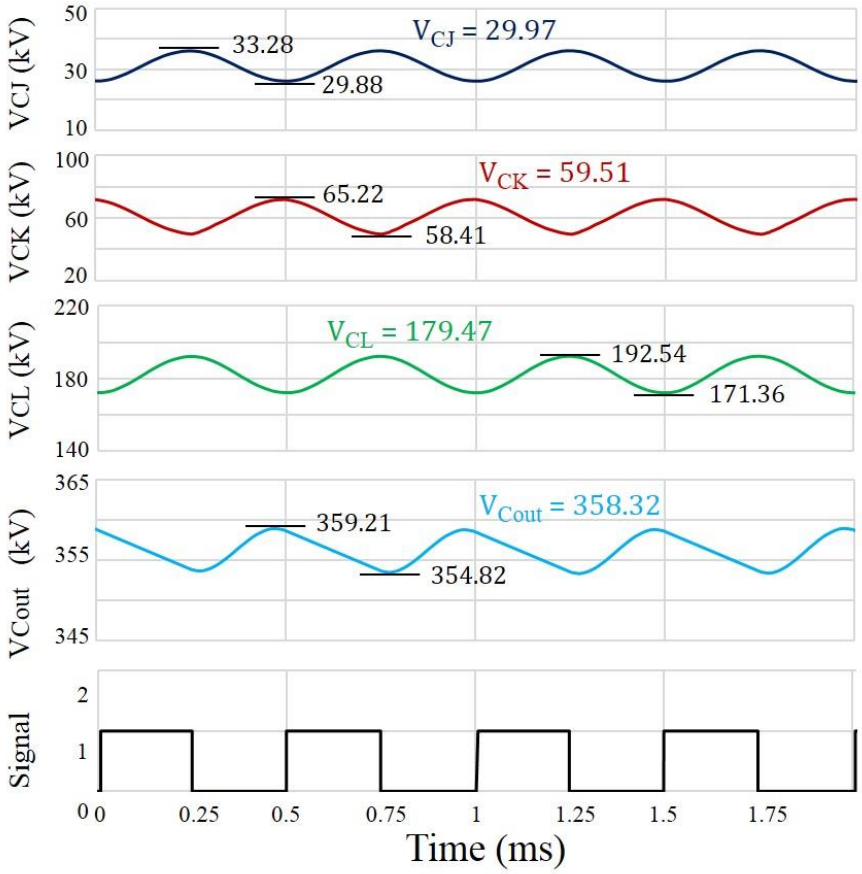


Figure 4.25: Simulation results capacitor voltage waveforms in the two half-cycle operations

Table 4.6 lists the value computed from the simulation and theoretical value. As depicted, these values can show agreement to within 0.9% in accuracy and by having the same relative capacitor voltage ripple between three stages (J, K, L).

Table 4.6: Design value and simulation results of capacitor ripple voltage in 3 stages

| Parameters | Design Value (kV) | Simulation Value (kV) | ΔVC (kV) | $\frac{\Delta VC}{VC}$ |
|---|---|---|---|---|
| $VC_J$ | 30 kV | 29.97 | 3.4 | 0.1134 |
| $VC_K$ | 60 kV | 59.51 | 6.81 | 0.1144 |
| $VC_L$ | 180 kV | 179.474 | 20.9 | 0.1165 |

The percentage ripple voltage is in agreement with the designed Equation (4-38). The discrepancy is mainly due to small snubber resistance of active switches, which have been omitted in the analytical formulas, but it was included in the simulation.

### 4.4.5 Evaluation of Dynamic Operation

#### 4.4.5.1 Load Step Change

The transient response characteristics operation of a model cascaded converter has been evaluated and performed by step change on the load side. As in the single stage converter in section 4.3.7, the step change on the load side is decreased by 50% from 2.592 kΩ to 1.296 kΩ which represents an increase in power from 50 MW to 96.7MW, because the load step decreased by half. The disturbance of the converter is applied and its stability is evaluated.

Firstly, in normal load 2592 Ω, the converter is working in steady-state operation and the output results as illustrated in Figure 4.26 are normal as designed. Nevertheless, at time 0.05 ms, the load is a step decreased which represents a step increase in load current 137.7 A, corresponding to a step decrease in the load 50%. In addition, the output voltage $V_{out}$ is decreased 2.8 kV, which is caused by the drain current from the output capacitor $I_{Cout}$. Meanwhile, the inductor current $i_{L1}$ is also increased and delay corresponds to one cycle, as the converter has multi-stages in response.

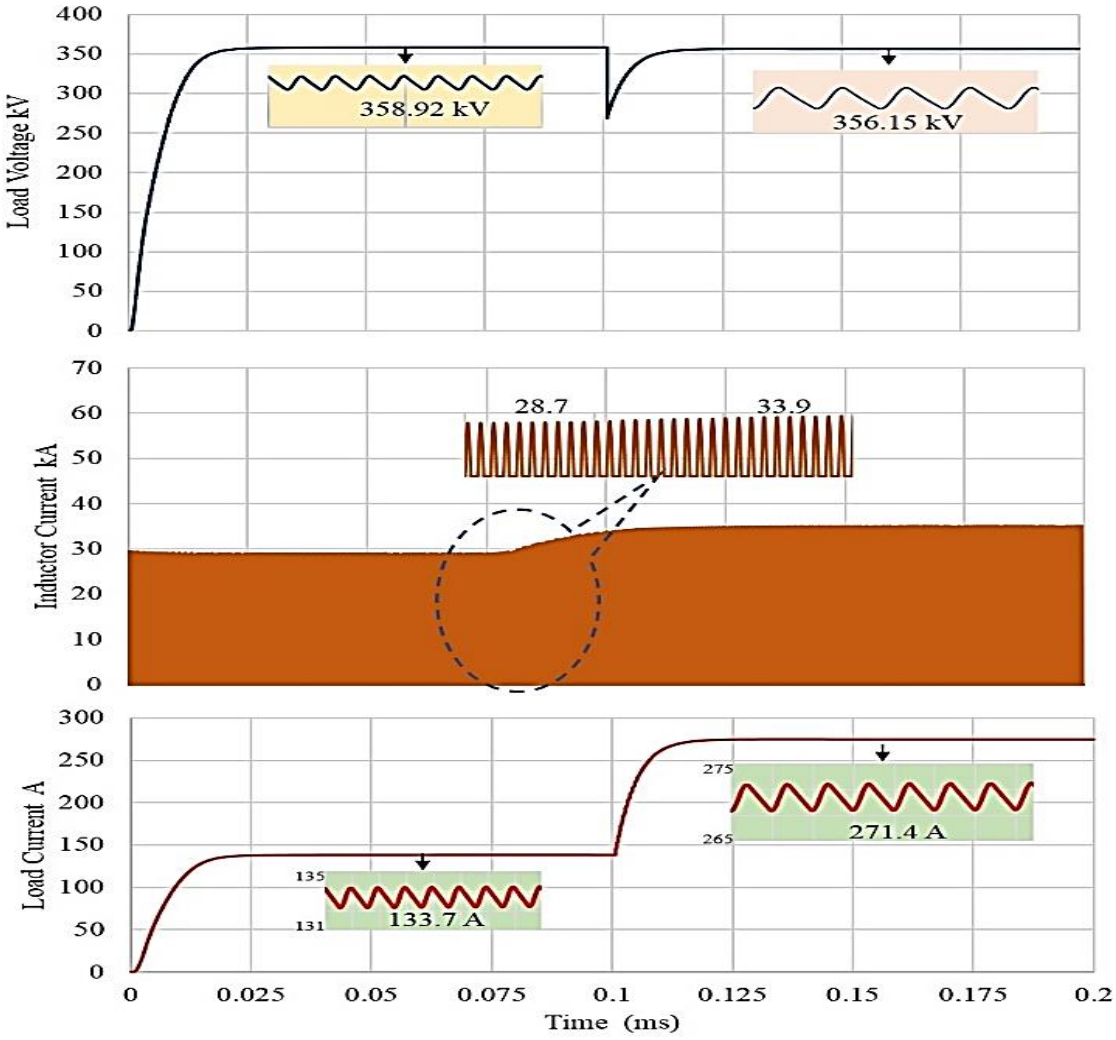


Figure 4.26: Transient operation waveforms

#### 4.4.5.2 Device and Component Stresses

Through out steady-state operation, the voltage and current stress on the devices and components are at normal levels. But in the dynamic-state during step change in the load of 50%, the load current and power transfer are increased. Meanwhile, the voltage has slightly decreased, and the load current has increased to double the steady-state load current. The IGBT switches $S_{valve}$ carry the full inductor current $i_{L1}$ as illustrated in Figure 4.27, where the peak current before step in load at 0.1 s was 35 kA and it has reached 36 kA at 0.15 s.

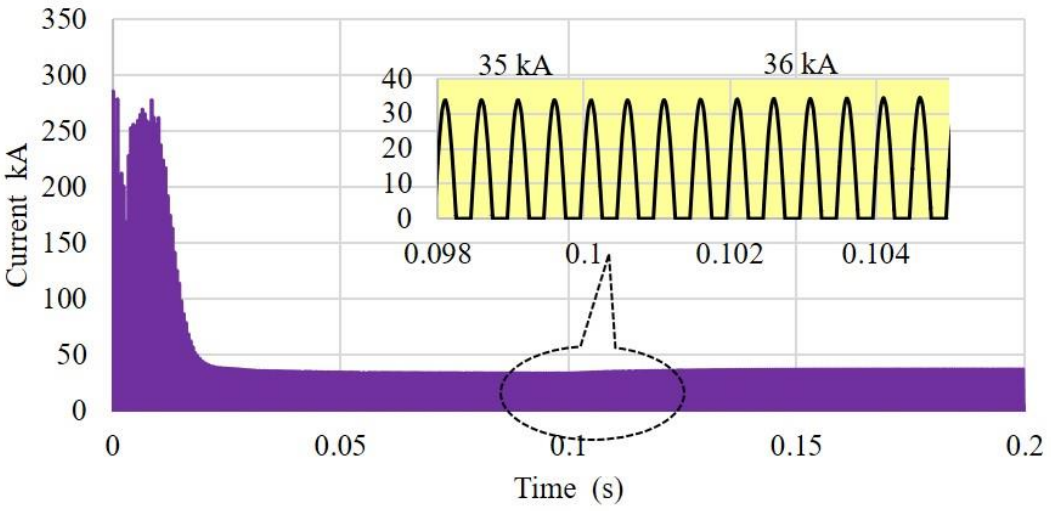


Figure 4.27: Current flows through IGBT switch $S_{valve}$

The voltages across IGBT switches *($S_{P1}$-$S_{P2}$)* have increased by the number of capacitors in each stage from left to right in sequential 30, 120, 180 kV as shown in Figure 4.28. IGBT switch $S_{P2}$ in stage 2 has two capacitors charged by 60 kV from stage 1. Therefore, the voltage across this device is the sum of discharge voltage in series, which is 120 kV as depicted in Figure 4.28 (e). This means that the devices in each stage see different voltages causing manufacturing issues and requiring a series connection of devices.

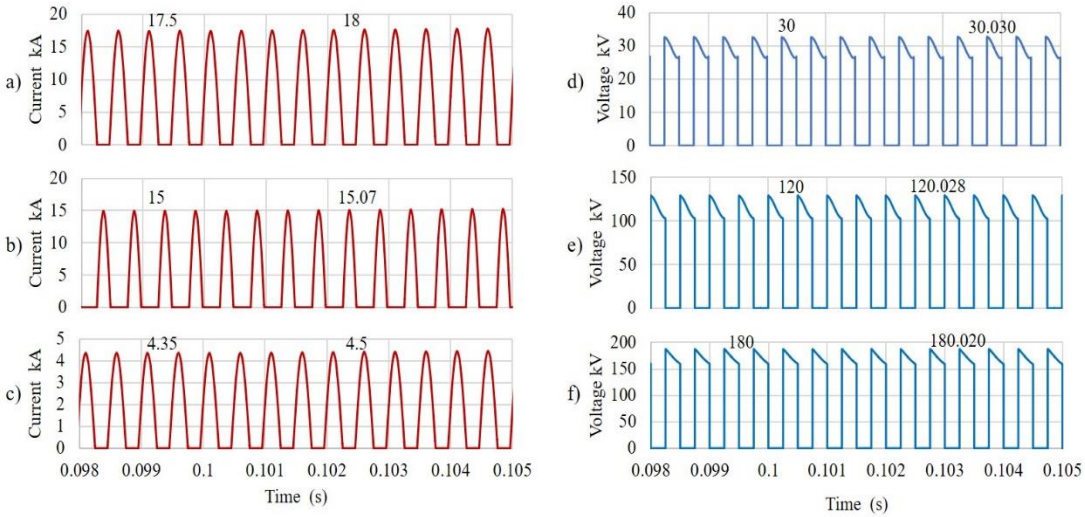


Figure 4.28: Voltage across and current flows through IGBT ($S_{P1}$- $S_{P4}$)
a) Current flows through switch $S_{P1}$, b) Current flows through a switch ($S_{P2}$) c) Current flows through a switch $S_{P3}$, d) Voltage across switch $S_{P1}$, e) Voltage across a switch $S_{P2}$, f) Voltage across a switch $S_{P3}$

In Figure 4.28(b) and Figure 4.28 (c), the current flows through the IGBT switches *($S_{P1}$-$S_{P3}$)* at 0.1s are also very little changed almost negligible and have decreased sequentially and independent of the number of capacitors in each stage. In steady-state, the current at switch $S_{P1}$ is half of the inductor current $L_1$ and the current is 17.5 kA. In addition, the current has increased to 18 kA during the step-in load.

The voltages across IGBT switches *($S_{S1}$-$S_{S4}$)* have increased sequentially and depending on the number of capacitors in each stage. But when the load has step changed, the voltage across these switches does not change as shown in Figure 4.29. On the contrary, currents flowing through these switches are decreased and depend on the discharge voltage levels. Otherwise, currents have increased a little during step change in the load, but this increase does not affect the current device rating. The value of the voltage across and the current flows through diode $D_1$ is the same voltage and current as switch $S_{valve}$. From Kirchhoff's current law, the current flows through diode $D_2$ in stage 1, equals half the value of the inductor current $L_1$ and current flows to switch $S_{P1}$ as shown in Figure 4.28(a). The voltage across diode $D_2$ is the same voltage across switch $S_{S1}$ as depicted in Figure 4.29(a).

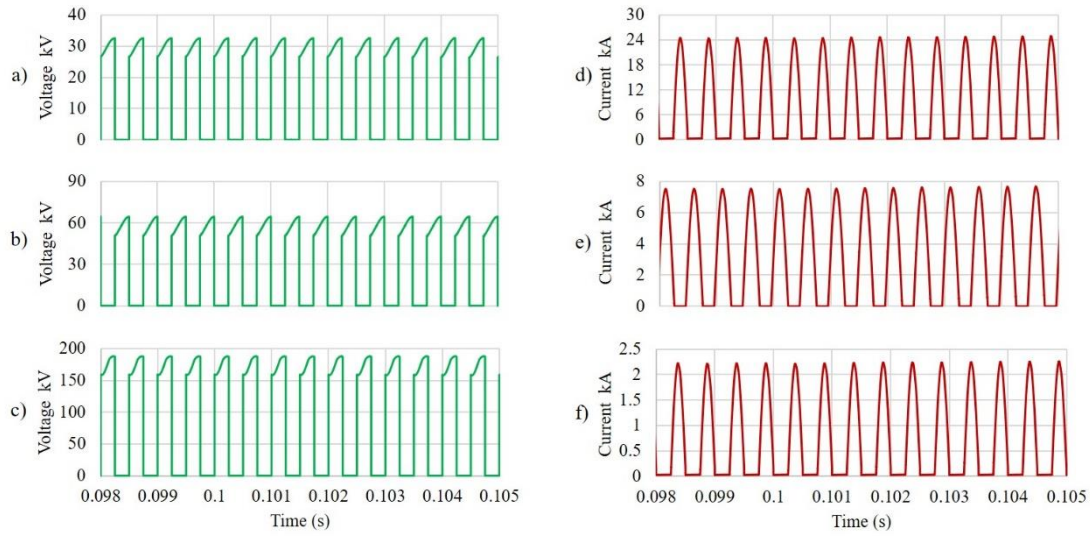


Figure 4.29: Voltage across and current flows through IGBT $S_{Si}$
a) Voltage across switch $S_{S1}$, b) Voltage across switch ($S_{S2}$, $S_{S3}$), c) Voltage across switch $S_{S4}$, d) Current flows through switch $S_{S1}$, e) Currents flow through switches ($S_{S2}$, $S_{S3}$), f) Current flows through switch $S_{S4}$

### 4.4.6 Semiconductor and Component Ratings

This section presents the component and power semiconductor device ratings in the multistage converter. The analysis covers the configuration of capacitors and inductors for all multi-stages with different numbers of capacitors and evaluates the power at the peak current on the components and the maximum voltage withstood across the device and components as illustrated in Equation (4-24).

The multi-stage Marx converter has different semiconductor devices and components depending on the number of stages and the number of components in each stage. The passive components in the converter are considered such as capacitors and inductors. Also power semiconductor devices as IGBTs and diodes.

$$P_{rating} = I^{peak} V_{\max} \qquad (4\text{-}41)$$

The following assumptions are made:

- Inductor losses are neglected.
- The converter is assumed to operate in the steady-state.
- When two components are connected in series, voltage sharing is not considered. It is assumed that each component should withstand the full voltage.
- In a single stage, the relation between the voltage ripple of charging capacitors $\Delta VC_n$ and the output voltage capacitor ripple can be expressed as:

$$\Delta VC_{out} = n\Delta VC_n \qquad (4\text{-}42)$$

- The load current $I_{Load}$ evaluation is the current flow through the load. It is labeled as $I_{Load}$ and it is calculated as;

$$I_{peak} = \left( n\frac{V_{in}}{R_{load}} \right) \qquad (4\text{-}43)$$

In multi-stage cascaded converters the peak current depends on the number of stages J, K, L and can be expressed as

$$I_{peak} = \left( N_{CJ}\, N_{CK}\, N_{CL} \frac{V_{in}}{R_{load}} \right) \qquad (4\text{-}44)$$

The power electronic components in the circuit evaluated are IGBTs and diodes. For the passive components, capacitors and inductors are considered.

#### 4.4.6.1 IGBT

In a single-stage converter circuit, there are several IGBTs, which are divided in two sections. One of them has two IGBTs $S_{valve}$, connected on series directly with the input voltage as shown in Figure 4.3, and these IGBTs carry the complete inductor current of the circuit since it is connected to a fixed input voltage $V_{in}$, it has to withstand only half the voltage ripple of $C_n$. The current inductor $L_{in}$ is divided among the parallel-connected capacitors. However, the voltage withstands fixed for the same value of input voltage $V_{in}$. Meanwhile, the inductor current $L_{in}$ is distributed to diodes $D_1$, $D_2$, $D_3$, and $D_4$, but the voltage is independent of the capacity of the capacitor.

The cascaded converter has two kinds of IGBTs. The first switch is composed of two switches $S_{vave}$, $(S_{P1}$-$S_{Pn})$, and $(S_{S1}$-$S_{Sn})$ shown in Figure 4.16. The switch $S_{valve}$ is carrying the total inductor current $I_{L1}$ of stage 1, which is able to withstand half of the voltage ripple of the capacitor in the first stage $C_J$. The current of switch $S_{vave}$ is the same current of inductor $L_1$. Meanwhile, the inductor current $I_{L1}$ is divided into the two parallel connected capacitors as illustrated in Figure 4.17. Equations for the parameter ratings of IGBTs are validated with simulation results and given in Table 4.7.

Table 4.7: IGBTs rating

| IGBT | Voltage | Current |
|---|---|---|
| $S_{Valve}$ | $V_{in}$ | $(I^P=IL_1=IL_{in})$ |
| $S_1$<br>$S_2$, $S_3$<br>$S_4$ | $V_{in}+ (\Delta VC_J/2)$,<br>$JV_{in}+(\Delta VC_K/2)$,<br>$KV_{in}+(\Delta VC_L/2)$, | $(IL_{in}/n)$, $[(I_{L1}/J, (I_{L2}/K), (I_{L3}/L)]$ |
| $(S_{P1}$-$S_{Pn})$ | $(N_{CJ}\ N_{CK}\ N_{CL})\ V_{in}+$ $(\Delta VC_n/2)$ | $(I_{L1}/J)$, $(I_{L2}/(K-1)$, $(I_{L3}/L)$ |

#### 4.4.6.2 Diode

As illustrated in Figure 4.3, and Figure 4.16, two sets of diodes need to be analyzed. The first is the series diode, which is connected in series with the inductor as shown in the single stage converter such as $D_{in}$, and in a cascaded stage converter as $D_1$. These diodes have to carry the inductor current and to

withstand the input voltage with a lower power rating which is smaller if compared with the other diode in the output voltage $D_{out}$. The largest voltage difference occurs at the end of the charging phase: the final capacitors $C_5$ and $C_L$ in both converters are reaching their peak voltage ripple while the previous capacitor is at its lowest. The general expression for the power rating of the series diode and output diode are expressed in Table 4.8.

Table 4.8: Diodes rating

| Diode | Voltage | Current |
|---|---|---|
| $D_{in}$ | $V_{in}$ | $I^P=IS_{valve}= IL_{in}= IL_1$ |
| $(D_1\text{-}D_9)$ | $nV_{in}$, $[(N_{CJ}\ N_{CK}\ N_{CL})\ V_{in}]$ | $(IL_{in}/n)$, $[(I_{L1}/J, (I_{L2}/K), (I_{L3}/L)]$ |
| $D_{out}$ | $nV_{in}+\Delta VC_{out}$, $[(N_{CJ}\ N_{CK}\ N_{CL})\ V_{in}]+\Delta VC_{out}$ | $(I^P/n=IL_{out})$, $(I^P/[(N_{CJ}\ N_{CK}\ N_{CL})\ V_{in}]=I_{Lout})$ |

#### 4.4.6.3 Capacitor

In both converters, there are only two kinds of capacitors $(C_n, C_{J,K,L})$, and $C_{out}$. The charging current requirement of these capacitors is the same current value as the diodes in each stage. Also, the current of the output capacitors $C_{out}$ is evaluated as the peak inductor current from $L_{out}$ minus the average current in the load $I_{Load}$. The voltage rating of these capacitors is based on the capacitor voltage ripple. Table 4.9 gives the equations for capacitor's rating.

$$\Delta VC_{J,K,L}=(N_{CJ}\ N_{CK}\ N_{CL})\ \Delta VC \qquad (4\text{-}45)$$

Table 4.9: Capacitor rating

| Capacitor | Voltage | Current |
|---|---|---|
| $C_n$ | $nV_{in}$ | $(P_{rate}/V_{out})/n$ |
| $C_{J,K,L}$ | $(N_{CJ}\ N_{CK}\ N_{CL})\ V_{in}$ | $(P_{rate}/V_{out})/\ (N_{CJ}\ N_{CK}\ N_{CL})$ |
| $C_{out\ (single\ stage)}$ | $V_{out}+ 0.5\Delta VC_{out}$ | $I^P/n\text{-}(V_{out}/R_{Load})$ |
| $C_{out\ (cascaded\ stage)}$ | | $I^P/(N_{CJ}\ N_{CK}\ N_{CL})$ - $(V_{out}/R_{Load})$ |

The voltage ripple of the capacitor depends on the number of capacitors in the stage. However, the voltage ripple can be expressed as

#### 4.4.6.4 Inductor

There are three inductors in the cascaded converter and two inductors in the single stage converter. The current requirement for both inductors $L_{in}$ and $L_{out}$ is the peak current caused from the charging and discharging of the capacitors in two half cycle operations. The current of inductors in stage 2 depends on the number of capacitors in this stage. The inductors have to withstand the maximum voltage. Table 4.10 lists the equations for parameter rating of the inductor in both converters.

Table 4.10: Inductor rating

| Capacitor | Voltage | Current |
|---|---|---|
| $L_{in}$ | $0.5\Delta VC_n$ | $I^P=Vin/\omega\ L_{in} \sin\omega(t-t_0)$ |
| $L_1$ | $0.5\Delta VC_{J,K,L}$ | |
| $L_{J,K,L}$ | $[(N_{CJ}\ N_{CK}\ N_{CL})\ -1]Vin+0.5\Delta VC_{J,K,L}$ | $I^P/[(N_{CJ}\ N_{CK}\ N_{CL})\ -1]$ |
| $L_{out\ (single\ stage)}$ | $nV_{in}+0.5\Delta VC_n$ | $I^P/n$ |
| $L_{out\ (cascaded\ stage)}$ | $(N_{CJ}\ N_{CK}\ N_{CL})\ V_{in}+0.5\Delta VC_{J,K,L}$ | $I^P/(N_{CJ}\ N_{CK}\ N_{CL})$ |

### 4.4.7 Comparative Performance Evaluation

As in section 4.3.8 a comparative performance evaluation of a single-stage converter, also in this sub-section a quantitative comparison was carried out using data from the output results by Matlab/Simulink simulation, and the proposed configuration is evaluated and compared with Veilleux cascaded converter terms of the power device count, to highlight its advantages for high-voltage applications as mentioned in section 4.1.

Both cascaded converter topologies are operating with the same DC-DC converter principle; hence, the comparison is made for the same three gains, same input voltage, same power rating, same load, same soft switching technique, and same switching frequency [2].

Figure 4.28 and Figure 4.29 shows that the maximum voltage stress of the IGBT switches reaches 180 kV. However, for all the converters, each switch or diode is made up of several parallel-connected devices to withstand the rated voltage. The total number of devices for varying voltage gains are shown in Figure 4.30 that shows the device count comparison with different gains between the Veilleux Cascaded converter and the improved cascaded converter.

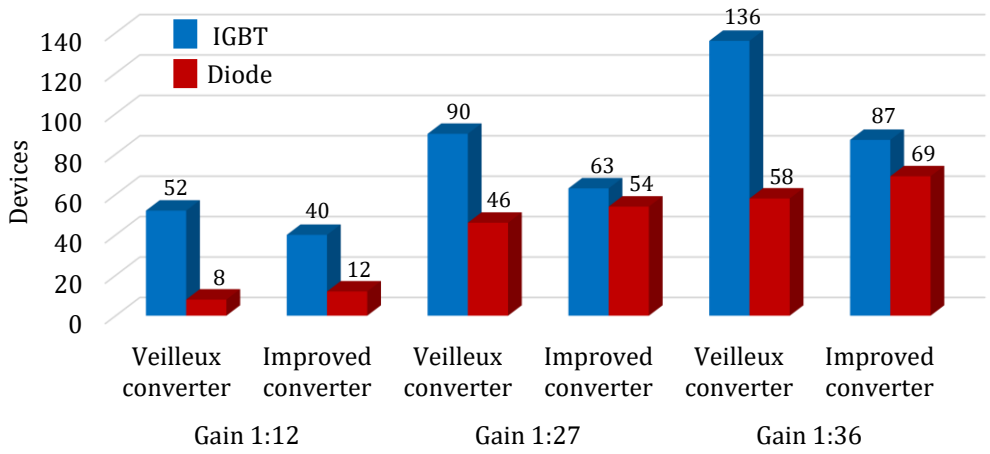


Figure 4.30: Components count for DC-DC converter topologies comparisons between Veilleux converter and improved converter

Figure 4.30 illustrates a comparison of designs to give voltage gains of 1:12, 1:27, and 1:36. The number reduces by 27%, 30% and 37% as the gain increases by 12, 27, and 36, respectively. However, the diode count increases by a small margin. However, diodes are cheaper and easy to connect in series.

Furthermore, Figure 4.31 shows that the output voltage in the improved converter is a bit higher than that of Veilleux converter [103], but both topologies perform equally well. Several HV DC-DC topologies have a high gain ratio, but not always with a reduced number of semiconductor component as one of the major goals. Therefore, the process for improving topology concentrated on reducing the number of devices.

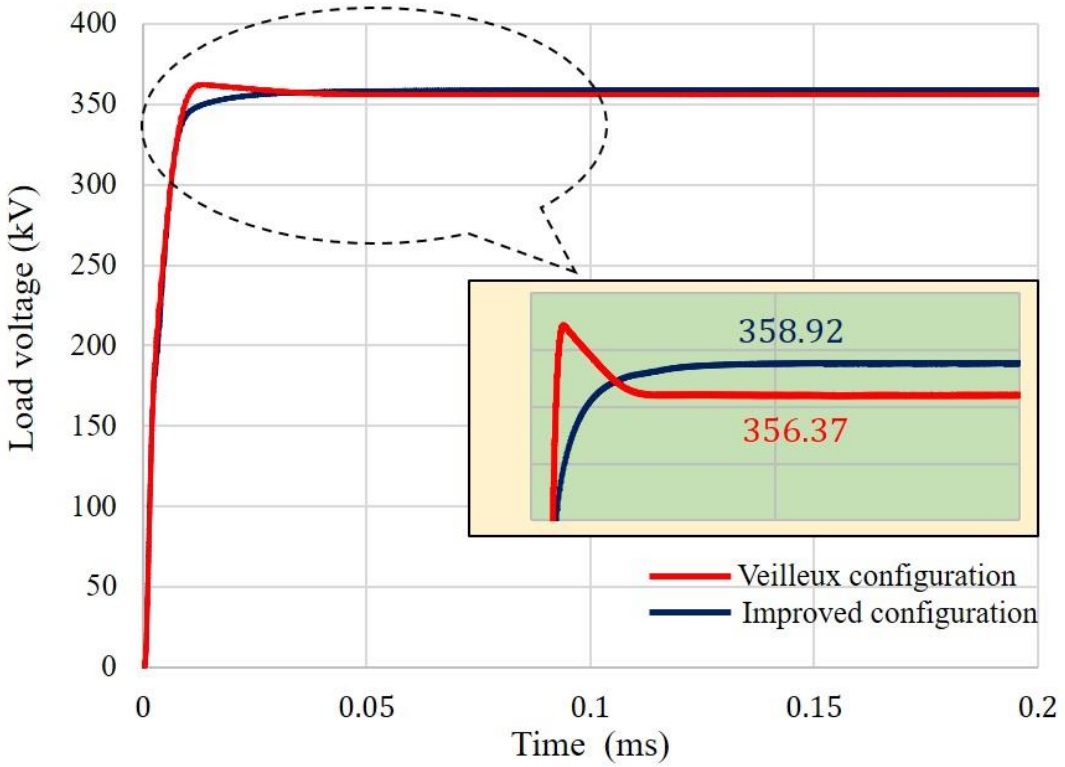


Figure 4.31: Load voltage comparisons between Veilleux converter and improved converter

### 4.4.8 Comparative between a Single-Stage and Multi-Stage Converter

A quantitative comparison was carried out for both model converter topologies at 50 MW, 6 kV/72 kV and were designed and simulated using Matlab/Simulink package software. Single-stage and multi-stage converters are evaluated and compared in terms of the power device count, to highlight the advantages for high-voltage applications. Both converter topologies operate under the same DC-DC Marx converter principle; hence, the comparison is made for the same voltage gain (n=12), the same input voltage of 6 kV, the same power rating of 50 MW, the same load, the same soft switching technique, and the same switching frequency. Figure 4.32 shows the simulation results for a single stage and a multi-stage converter. The DC gains obtained from a single-stage and a multi-stage converter are 11.81 and 11.92 respectively, and have been compared with the theoretical gain of 12.

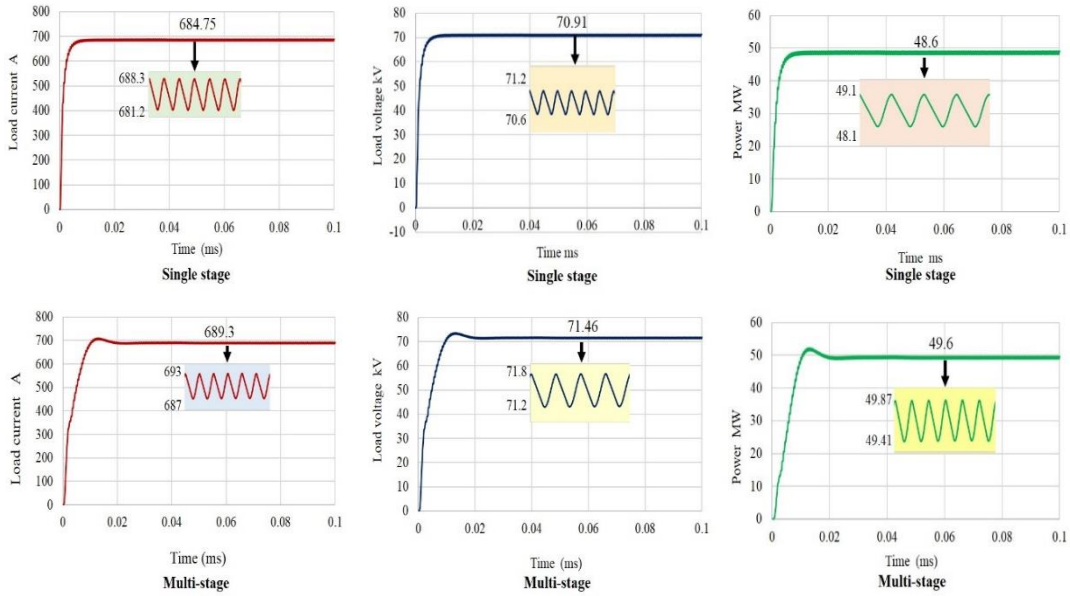


Figure 4.32: Load voltage, load current and load power waveforms both of converters

The output voltage, current, and power of the converter should be 72 kV/ 694.5 A and 50 MW as designed. It can be seen that both circuit output voltages are 70.91 kV and 71.46 kV respectively, which is very close to the design specification of 72 kV. Figure 4.32 shows that the output voltage in the multi-stage converter is higher than that of the single-stage converter, but both topologies perform equally well. Compared with Veilleux cascaded topology that have a high gain ratio, he does not demonstrate a similar reduction in semiconductor components in the same application, perhaps because this has not been a focus area for the designers [6],[7]. Also, the peak load current of both converters is 684.75 A and 689.3 A, which is very close to the design value of 694.5 A.

In addition, the load power of both converters as shown in Figure 4.32 is 48.6 MW and 49.6 MW. For both configurations, IGBT switches are comprised of several series-connected power devices to withstand the rated voltage. Figure 4.33 shows an active and passive component count comparison with a different gain voltages, between both of the converter topologies. For both configurations, IGBT switches and diodes are comprised of several series-connected power switches to withstand the rated voltage. Currently, the high voltage has a maximum blocking voltage rated up to 6.5 kV 600 A, but the ratings of the IGBT considered

for this study are 4.5 kV and 1200 A. The required number of IGBT switches and diodes is mainly determined by peak current and peak voltage. The number of capacitors is calculated based on the required voltage rating and capacitance. The input and output sections of both converter topologies require the same number of active switches.

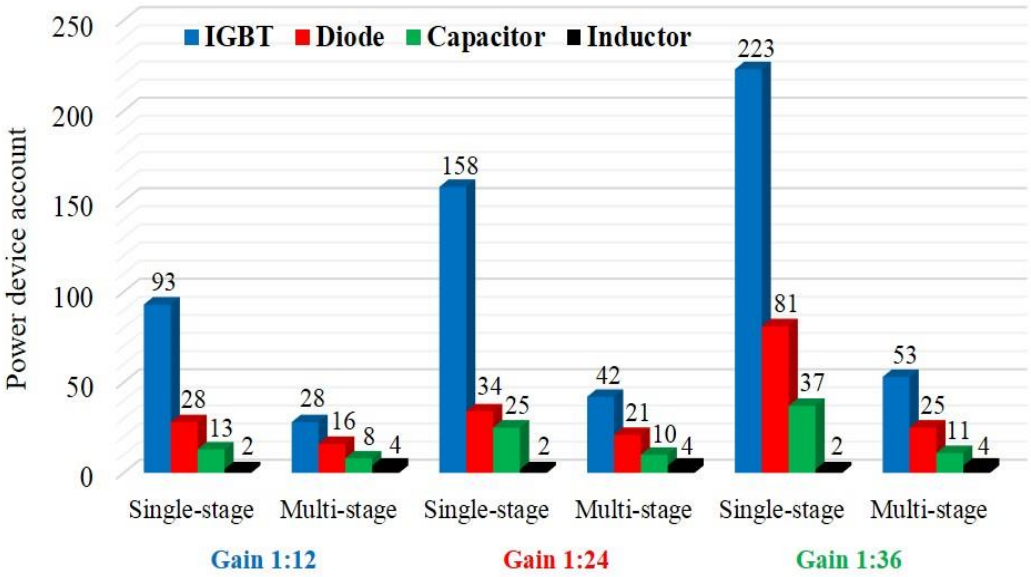


Figure 4.33: Components count for DC-DC converter topologies comparisons between single-stage and multi-stage converters

As shown in Figure 4.33, the comparison of designs includes three different voltage gains of 1:12, 1:24, and 1:36. The number of IGBT switches and capacitors in multi-stages is reduced when compared with a single-stage component, except for the inductor count which increases by a fixed small margin of only 2 which can be increased by the number of stages in the middle section of the multi-stage converter. In the multi-stage topology, the increase in the active switches 24% depends on the voltage gain, while in the single-stage topology there is a large increase in the active and passive components of 69%. The reduction in the component count in the multi-stage converter leads to a reduction in weight, cost, and complexity. From these results, the multi-stage converter is small in size, and costs is 50% less than a single-stage converter if the voltage gain of the converter is large.

## 4.5 Summary

In this chapter, two converter topologies based on the DC-DC Marx converter are presented. It is shown that they are capable of voltage conversion at high power and high voltage. These converters are modified and improved by reducing the number of switches for the same power rating. Both of them are stepping-up to HVDC following the general Marx concept, which is charging the capacitors in parallel and reconnection of the charged capacitors in series.

In a single-stage converter, the transfer of electrical charge from the input voltage to the load is by diodes in series with inductors, capacitors, and L-C resonance. All diodes ensure that the charge transfer in each cycle is unidirectional and when the current reaches zero, diodes stop conducting and block. The design of the L-C components in the converters are also presented. However, a good agreement is observed between the design and the simulation results.

Both improved DC-DC converters can achieve gain with reduced components. The reduction increases with the increase in voltage gain. Soft switching can be implemented and a method for calculating the resonant component values and the switching frequency is presented. The operation for both converters has been validated by simulation using Matlab/Simulink software package.

Both converters operate as unidirectional converters and transferred energy in one direction. During doldrums (a belt of calms and light winds) and for maintenance work, it is necessary to supply an offshore wind farm with an auxiliary power. Therefore, reverse power for offshore wind farm needs additional components. Hence, the bidirectional DC-DC converter is required for an offshore wind farm. In the next chapter, a novel bidirectional Modular power DC-DC convert is introduced.

# Chapter 5

# Analysis, Design, and Evaluation of the Steady-State Operation of the Bidirectional Modular Converter

## 5.1 Introduction

This chapter presents a novel bidirectional modular DC-DC converter based on the Marx generator principle of operating in both modes and the investigation is undertaken to show its operation in both directions. The concept and the operational principle of bidirectional converter are explained as well as design steps. The topology is capable of achieving step-up and step-down voltage transformations at kV level and is able to handle MW level power transfers in both directions. The main features of this topology are the absence of a high-frequency transformer, reduced weight, volume, and soft switching to reduce the switching losses. The performance of the converter is verified by extensive Matlab/Simulink software package.

## 5.2 System Description

The location of the novel converter discussed in this chapter is shown within the blue star in Figure 5.1. The wind farms cluster is formed of two parallel lines of wind turbines, each containing 5 wind turbines in series. Hence, there is a total of 10 wind turbines; each rated at 5 MW, 1.2 kV [41], [100],[104]. The total power is 50 MW and the voltages are 6 kV and 30 kV. In this case, the power flow through the DC-DC converter needs to be in both directions.

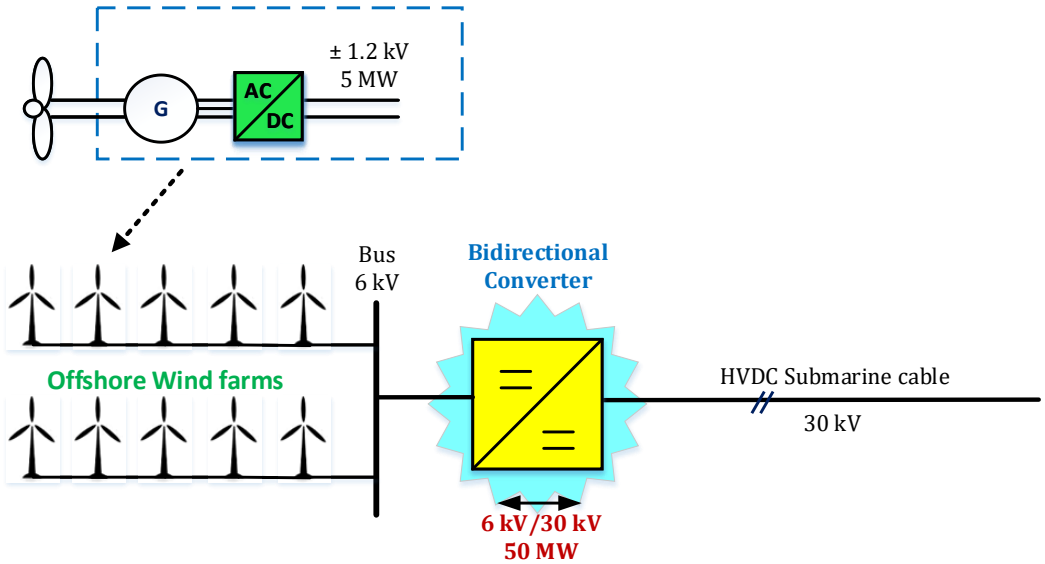


Figure 5.1: DC collection topology system of a wind farm

During normal generation, the power flow is from the wind farm to the grid. However, when the wind farm is not generating, the auxiliaries in the wind farm require a small amount of power, which must be drawn from the grid. Therefore, the DC-DC converter needs to be bidirectional [105],[106]. The DC-DC Converter is required to transfer the power in both directions and is connected to the collection bus tie interconnect at the 6 kV side to the 30 kV side. The forward and reverse powers are 50 MW and 5 MW. As the emphasis is on converter operation, the system shown in Figure 5.1, was reduced to the circuit shown in Figure 5.2. The two systems on either side of the converter are represented by two DC voltage sources $V_L$ and $V_H$ behind equivalent resistances and inductances. In practice, the power flow is controlled by the VSC at the onshore substation. However, the power flow was controlled by varying the resistance values $R_1$ and $R_2$ on both sides.

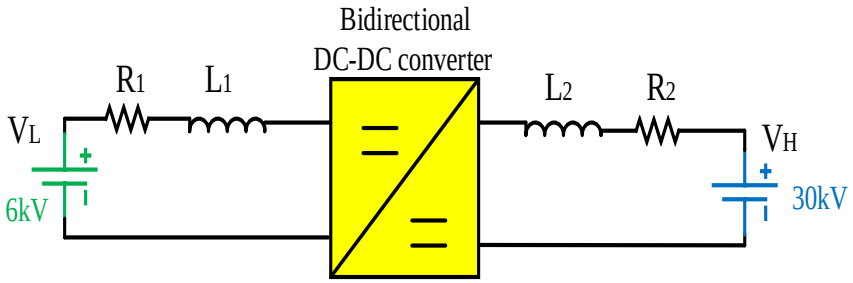


Figure 5.2: Proposed converter between two DC supply

## 5.3 Bidirectional Modular DC-DC Converter

### 5.3.1 Circuit Configuration

The power circuit of the proposed converter is shown in Figure 5.2. This converter is comprised of three circuits. The first circuit consists of inductor $L_1$ connected in series with a capacitor $C_A$ and the DC system of the offshore wind farm is presented as a DC supply $V_L$. The second circuit composed of *'n'* modules, inside the modules are sets of anti-parallel IGBT switches connected in series with diodes *($S_F$, $D_F$)*, *($S_R$, $D_R$)* and capacitors *($C_1$-$C_5$)*. Each capacitor has two anti-parallel IGBT switches connected in series with diodes and one antiparallel switch without the diode. These switches are used to control the charge and

discharge of capacitors. The converter can be boost or buck the voltage by replacing the number of modules. This converter application has fixed with five modules *(n=5)*. As depicted in Figure 5.3, each group of two anti-parallel switches with diodes, one capacitor, and one anti-parallel switch are called one module. The proposed converter has five of these identical modules as illustrated in Figure 5.3. The third circuit is a similar first circuit that consists of one inductor $L_2$ and one capacitor $C_B$.

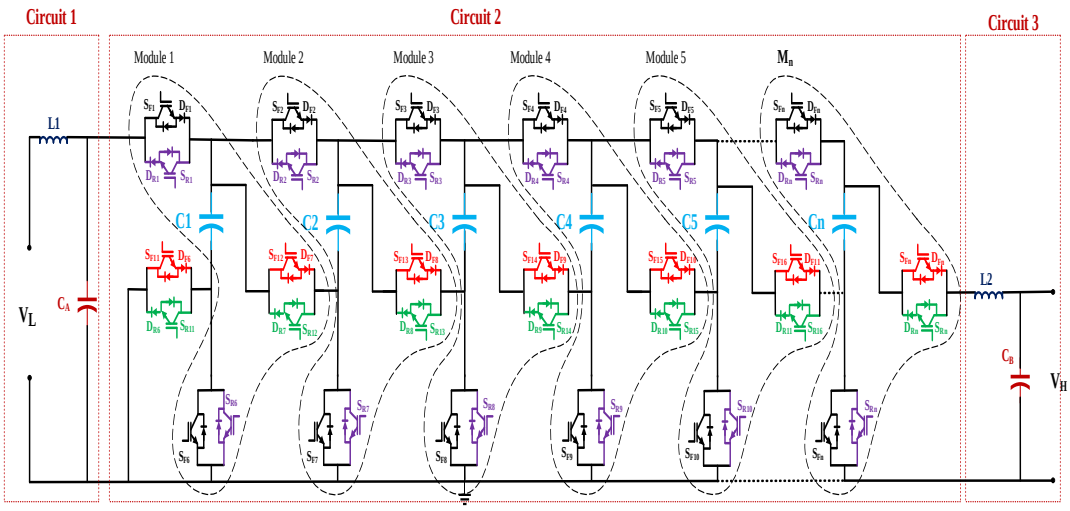


Figure 5.3: Bidirectional Marx DC-DC converter topology

### 5.3.2 The Steady-State Operation

The operation of the converter is based on the Marx generator concept. Five modules are identical and used to achieve a voltage ratio of 1:5. Further, this converter boosts the voltage from 6 kV/30 kV and vice versa. In this study, bidirectional DC-DC converters are considered which transfer energy between two DC sources, with a range of power levels up to 50 MW in the forward direction and up to 5 MW in the reverse direction. All the IGBTs are switched at zero current (ZCS) to reduce the switching losses.

In addition, all the switches must be capable of bidirectional blocking and forward conducting. The converter operation can be divided into two modes of operation; Forward Mode (FM) and reverse mode (RM).

#### 5.3.2.1 Forward Mode

In this mode, the energy flows from the low voltage side to the high voltage side. Forward-mode can also be divided into two half-cycles. In the first half-cycle *($t_0$-$t_1$)* as shown in Figure 5.4(a), the ideal waveforms of the inductor currents of $iL_1$ and $iL_2$. The switching cycle ends at $t_2$, and the inductor current $iL_2$ reaches zero.

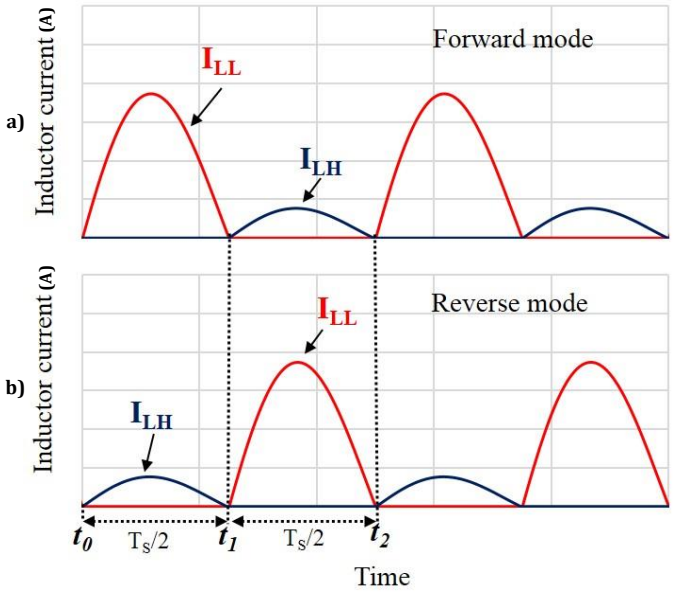


Figure 5.4: Inductor current waveforms during both modes

The charging current flows through five capacitors *($C_1$-$C_5$)* in parallel by switching 'ON' switches *($S_{F1}$-$S_{F10}$)* and *($D_{F1}$-$D_{F5}$)*, while all the other switches are turned 'OFF', as shown in Figure 5.5. The diodes *($D_{F1}$-$D_{F5}$)* block the reverse current flow.

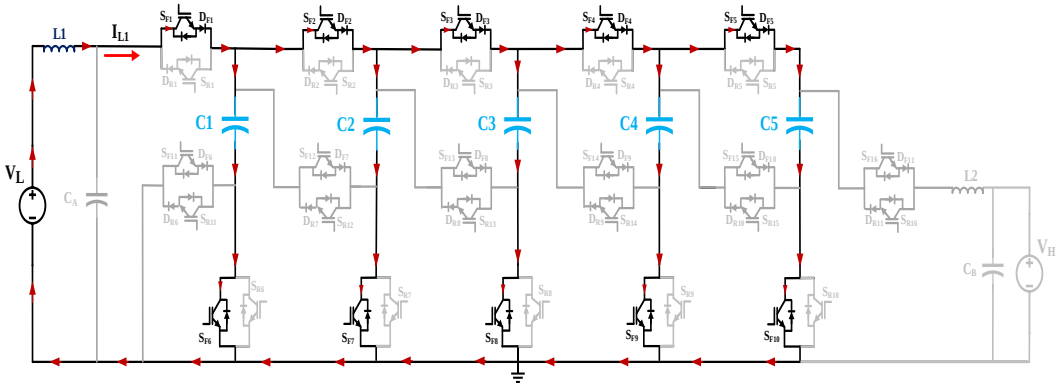


Figure 5.5: Switching and corresponding current flow directions of charging capacitors in parallel in forward mode

In the second half-cycle *($t_1$-$t_2$)* the capacitors that were charged during the first half-cycle are discharged in series to create the high voltage on the HV side by switching 'ON' switches *($S_{F11}$-$S_{F16}$)* and *($D_{F6}$-$D_{F11}$)*, while diodes *($D_{F6}$-$D_{F11}$)* block the reverse current flow during capacitor discharge in series. The inductor waveforms are shown in Figure 5.4(b). In this case, as there are 5 modules the voltage gain is 5 and the electric charges is transferred from the five series-connected capacitors *$C_1$, $C_2$, $C_3$, $C_4$* and *$C_5$* to the capacitor $C_H$ as depicted in Figure 5.6.

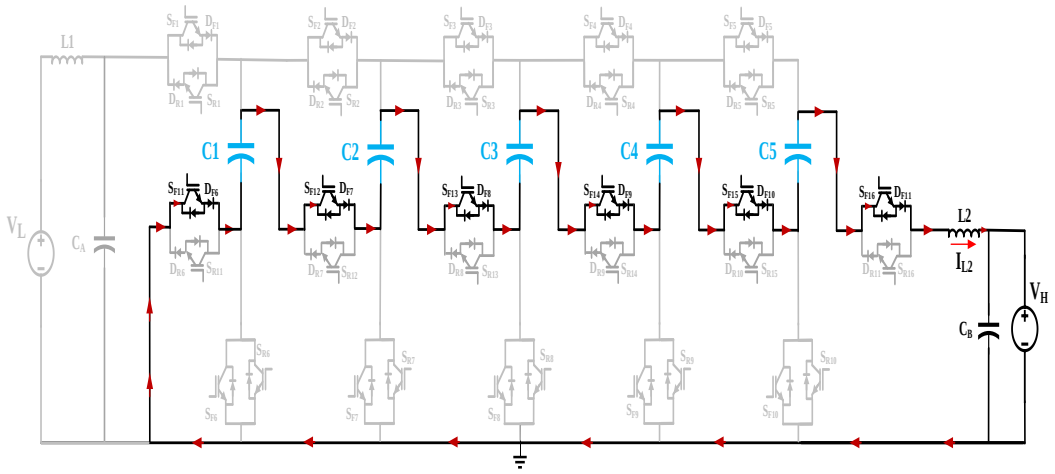


Figure 5.6: Switching and corresponding current flow directions of discharging capacitors in series in forward mode

### 5.3.2.2 Reverse Mode

Figure 5.7(a) shows the current flows from high voltage $V_H$ to the low voltage $V_L$. In the first half-cycle, inductor current $iL_2$ charges the five capacitors *($C_1$-$C_5$)* in series in time interval *($t_0$-$t_1$)*, by switching 'ON' switches *($S_{R11}$-$S_{R16}$)* and diodes *($D_{R6}$-$D_{R11}$)*, are connected in series with switches *($S_{R11}$-$S_{R16}$)* to ensure unidirectional transfer of charge from the voltage source $V_H$, to series-connected capacitors and which are forward biased, while all the other switches are turned 'OFF'. In the second half-cycle, the switches *($S_{R11}$-$S_{R16}$)* and diodes *($D_{R6}$-$D_{R11}$)*, are turned 'ON', and the capacitors are discharged in parallel in the time interval *($t_1$-$t_2$)* to the low voltage $V_L$ through inductor $L_1$ as depicted in Figure 5.7(b).

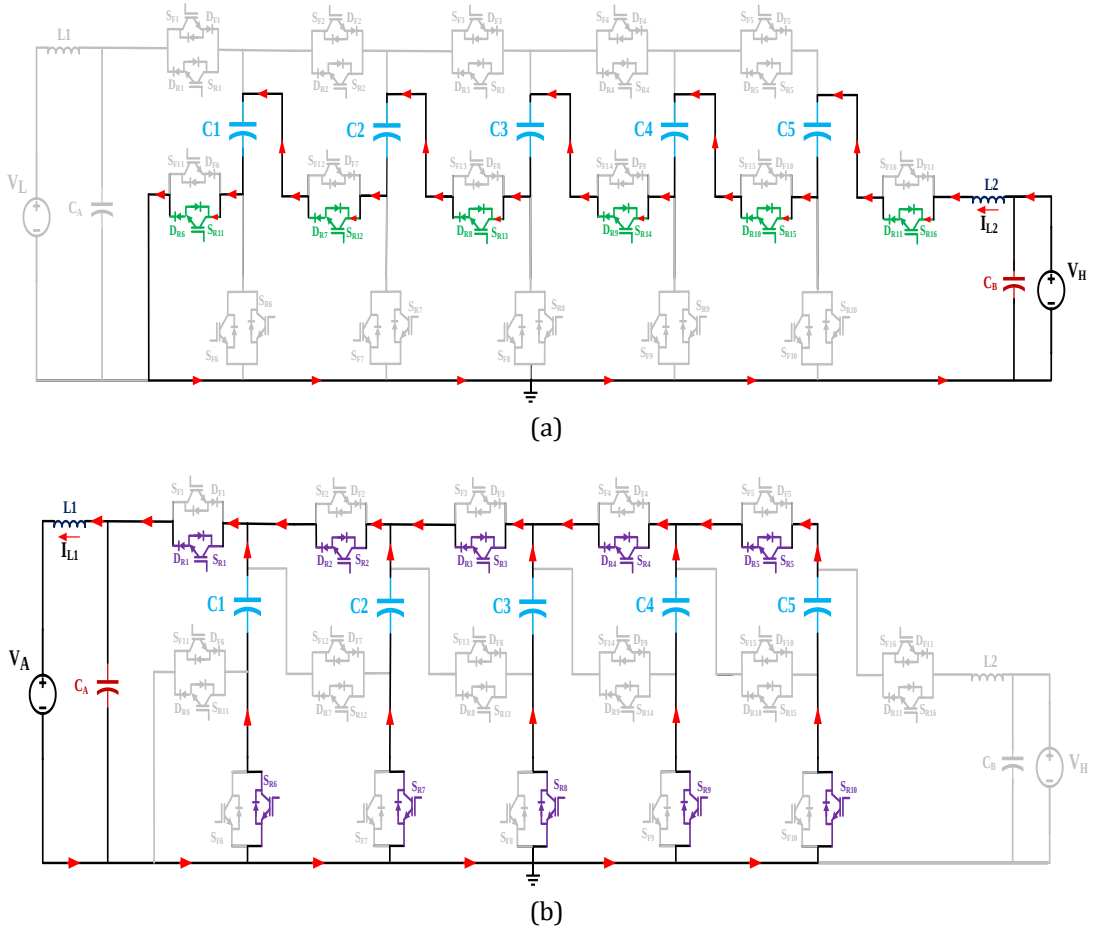


Figure 5.7: Switching and corresponding current flow in reverse mode
a) Switching and corresponding current flow direction of charging capacitors in series, b) Switching and corresponding current flow direction of discharging capacitors in parallel

### 5.3.3 Analysis and Design of the Proposed Converter

For clarity in presentation, Figures are shown for charging and discharging in both mode operations have been drawn with n=5 capacitors in circuit 2. This section of this chapter goes through the analysis and design of the bidirectional converter assuming that periodic steady-state has already been reached. Also, the switching time is $T_S=(1/F_S)$, and it is divided into two half-cycles. By neglecting the losses and impact of the soft switching.

#### 5.3.3.1 Forward Mode (Boost Voltage)

In this mode, the converter steps-up the voltage and the power flow is transferred from the low voltage source to the high voltage source. The output voltage gain, in forward mode operation, depends on the number of capacitors in the second

circuit of the converter and is similar to Equation (4-1) in Chapter 4. Therefore, the gain voltage can be given as

$$n = \frac{V_H}{V_L} \tag{5-1}$$

where $V_H$ is the high voltage, $V_L$ is the low voltage, and '$n$' is the number of capacitors in circuit 2 as depicted in Figure 5.3. In the first half-cycle, by switching 'ON' switches $(S_{F1}\text{-}S_{F10})$, and the diodes $(D_{F1}\text{-}D_{F5})$ are in forward bias and conduct. However, five capacitors are charged in parallel as illustrated in Figure 5.8.

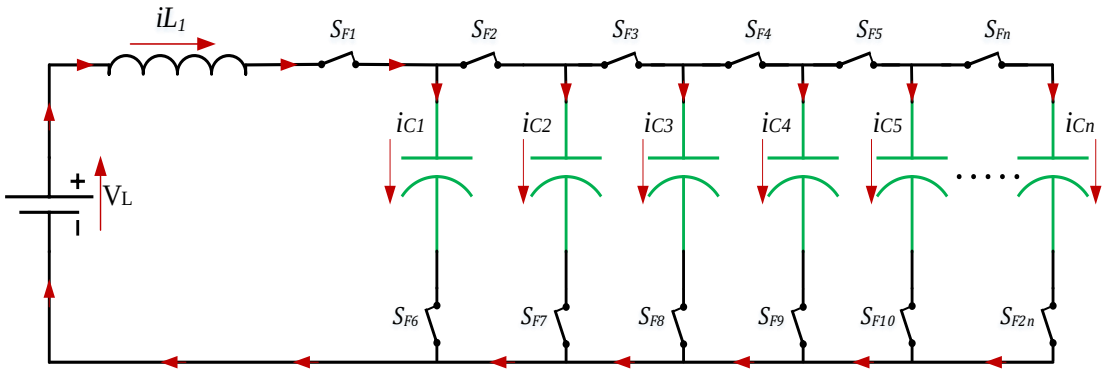


Figure 5.8: Equivalent circuit of charging capacitors in parallel

The inductor current $iL_1$ is divided into the five capacitors to charge in parallel through capacitor current $(iC_1\text{-}iC_n)$ as shown in Figure 5.8. It is clear that the low input voltage $V_L$ is higher than the capacitor voltage $V_C$ as depicted in Figure 5.9 (d). However, the equivalent capacitance in parallel is the same as in chapter 4 in Equation (4-3). The duty cycle is fixed and $d$=50% as shown in Figure 5.9(b). It is divided into two half-cycles and to prevent the short circuit during charging and discharging the capacitors. When $t_0 \leq t \leq t_2$, the peak current of inductor $L_1$ is given as;

$$I_{L1}^{P} = V_L \sqrt{\frac{C_{eq\,(FP)}}{L_1}} \tag{5-2}$$

where $L_1$ is the inductor current, $C_{eq(FP)}$ is the forward equivalent capacitance in parallel connection, and $\omega_F$ is the resonant frequency in forward mode operation. The resonant frequency Equation is similar to Equation (4-5) and can be calculated as;

$$\omega_F = \frac{1}{\sqrt{L_1 C_{eq(FP)}}} \qquad (5\text{-}3)$$

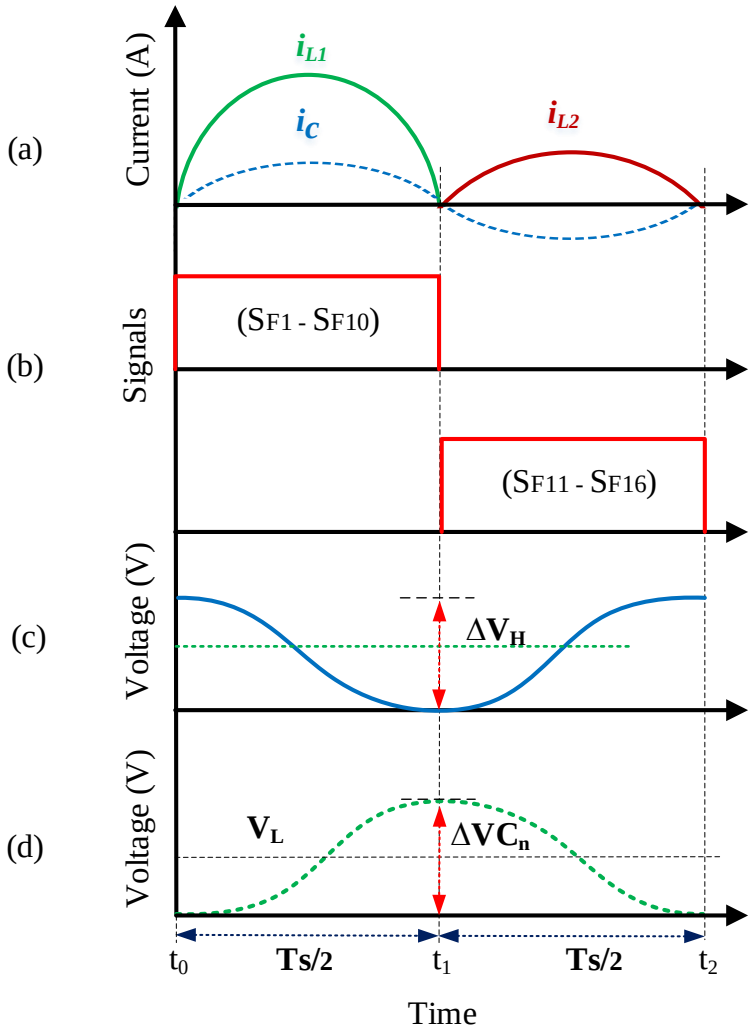


Figure 5.9: Ideal resonant waveforms for voltages and currents in forward mode
a) Inductor currents, b) Switching pattern, c) Output capacitor voltage ripple, d) charging capacitor voltage ripple in the circuit 2

From Figure 5.8, the switching frequency $F_{SF}$ also is similar to Equation (4-6) and can be written as;

$$F_{SF} = \frac{1}{2\pi\sqrt{L_1 C_{eq(FP)}}} \qquad (5\text{-}4)$$

In the second half-cycle, the capacitors are discharged in series. However, the equivalent capacitance in series is given as

$$C_{eq\,(FS)} = 1\Big/\left(\frac{1}{C_1}+\frac{1}{C_2}+\frac{1}{C_3}+....+\frac{1}{C_n}\right) \qquad (5\text{-}5)$$

where $C_{eq(FS)}$ is the forward equivalent capacitance in series, and $C_1$ to $C_n$ are the capacitance values of every individual capacitor in the series connection. In the second half-cycle, the capacitors discharge in series to the capacitor $C_B$ as shown in Figure 5.10. However, the Equation (5-5) can be generalised to;

$$\frac{1}{C_{eq(FS)}} = \sum_{i=1}^{n} \frac{1}{C_{eq(FS)}} \qquad (5\text{-}6)$$

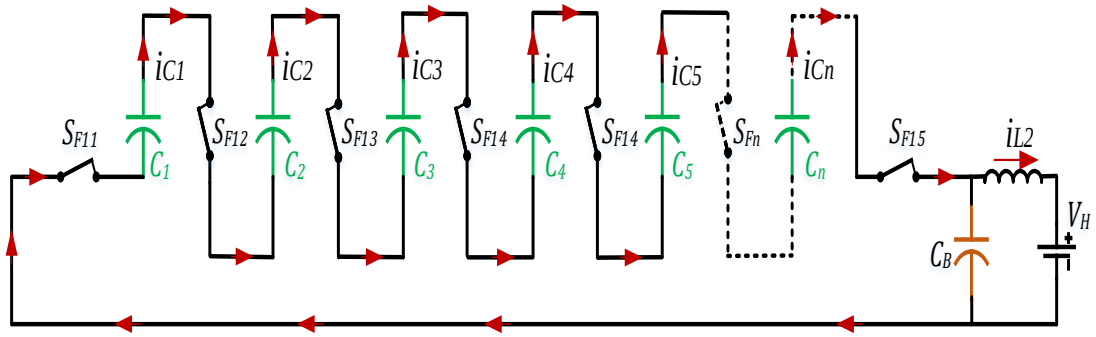


Figure 5.10: Equivalent circuit of discharging capacitors in series

As shown in Figure 5.10, when the switches $(S_{F11}\text{-}S_{Fn})$ are 'ON', the voltage across the *'n'* series connected $(C_1\text{-}C_n)$ is given as:

$$nVC_{Fn}(T_S/2) = M\left(V_L + 0.5\Delta V_{Cn}\right) \qquad (5\text{-}7)$$

where $\Delta VC_{Fn}$ is the ripple capacitor voltage in the forward mode. As illustrated in Figure 5.9(d), the inductor current $iL_1$ has reached zero and the inductor current $iL_2$ has increased during $0.5T_{FS}$. Whilst the voltage $V_H$ is larger than $5VC_{Fn}$ as shown in Figure 5. 9(c) and Figure 5. 9(d). The Equation of the capacitor voltage in the second circuit $VC_{Fn}$ is similar to the Equation (4-9) in Chapter 4 and is given as;

$$VC_{FN} = V_L - L_1\frac{di}{dt}\left[\frac{1}{2}C_{eq\,(FP)}\,\omega_F\,VC_{FN}\sin\omega_F\,(t-t_0)\right] \qquad (5\text{-}8)$$

#### 5.3.3.2 Reverse Mode (Buck Voltage)

In this mode of operation, the voltage is stepped-down, and the power is transferred from the high voltage side $V_H$ to the low voltage side $V_L$. The voltage gain in the reverse mode is given as:

$$n = \frac{V_H}{V_L} \tag{5-9}$$

This mode of operation is divided into two half cycles, the operation is the opposite of the forward mode operation. However, in the first half-cycle, five capacitors are charged in series as illustrated in Figure 5.9 by switching 'ON' switches *($S_{R11}$-$S_{R16}$).*

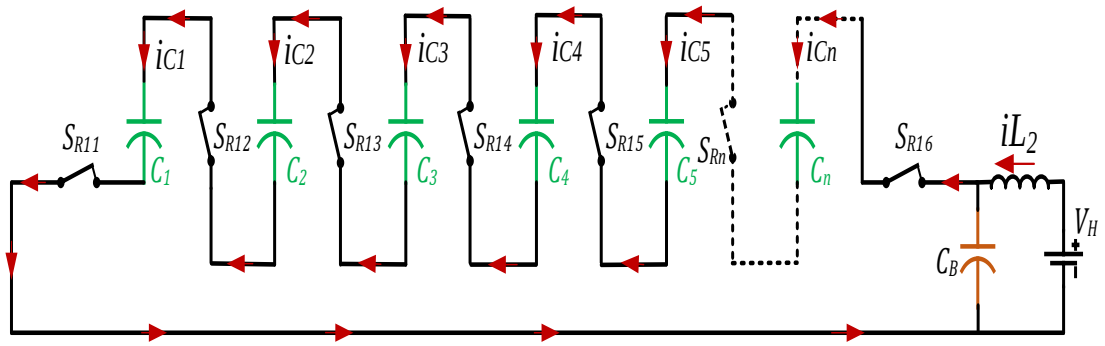


Figure 5.11: Equivalent circuit of charging capacitors in series mode

The equivalent capacitance in series is illustrated in Equation (5-6). However, the high voltage side can be given as;

$$V_H = L_2 \frac{di}{dt} + \frac{Q}{C_{eq\,(RS)}} \tag{5-10}$$

and could be as;

$$V_H = L_2 \frac{di}{dt} + \frac{1}{C_{eq\,(RS)}} \int_0^t i(t)dt \tag{5-11}$$

In the first half-cycle, the inductor $L_2$ is limited by the charged current for the capacitors in series as shown in Figure 5.12(a), the duty-cycle in this mode is fixed *d=0.5* as depicted in Figure 5.12(b). High voltage side $V_H$ is higher than the capacitor voltage $V_C$ as depicted in Figure 5.10(d). However, the equivalent

capacitance in series is the same as in Equation (5-6). Therefore, the capacitor voltage $VC_{eq(RS)}$ is similar to Equation (4-8) and can be expressed as;

$$VC_{eq(RS)} = V_H - L_2 \frac{di}{dt}\left[\frac{1}{2} C_{eq(RS)}\ \omega_R \Delta VC_n \sin \omega_R (t - t_0)\right] \quad (5\text{-}12)$$

where $\omega_R$ is the resonant frequency in the reverse mode operating, wherein the voltage capacitor in circuit 2 can be given as;

$$VC_n = V_H - \left[\frac{1}{2} \Delta VC_n \cos \omega_R (t - t_0)\right] \quad (5\text{-}13)$$

It is clear that the inductor current is the same value as the charging current of all the capacitors as illustrated in Equation (5-12);

$$I_{L2} = I_{C1} = I_{C2} \ldots\ldots I_{Cn} \quad (5\text{-}14)$$

From Kirchhoff's Law and as depicted in Figure 5.11, the inductor current $i_{L2}$ can be given as;

$$i_{L2} = iC_{n(RS)} = \frac{V_H}{\omega L_2} \sin \omega (t - t_0) \quad (5\text{-}15)$$

and generalised as;

$$I_{L2}^{P} = V_H \sqrt{\frac{C_{eq(RS)}}{L_2}} \quad (5\text{-}16)$$

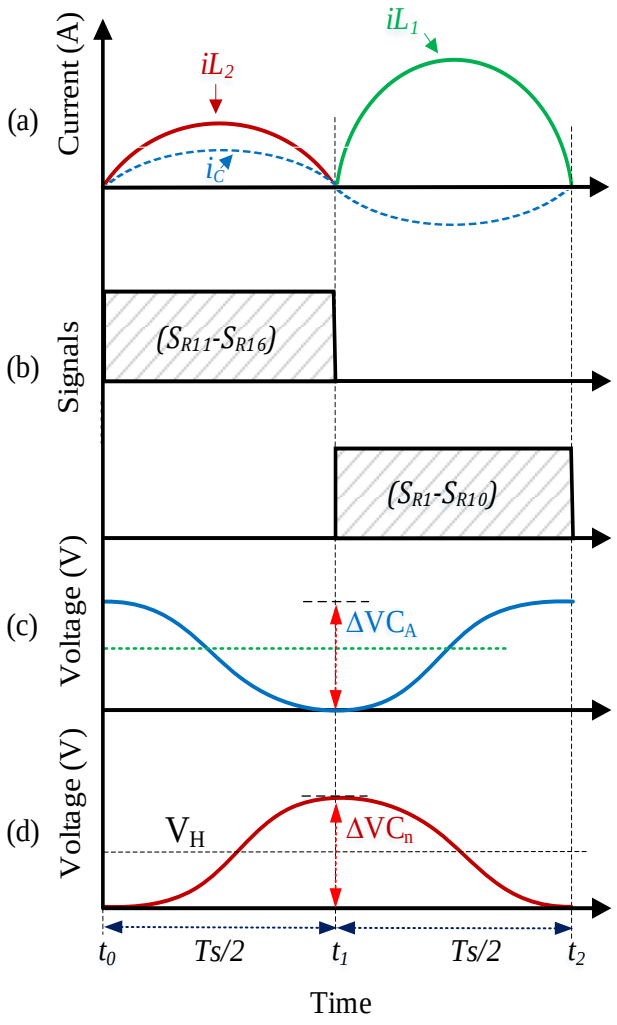


Figure 5.12: Ideal resonant waveforms for voltages and currents in reverse mode

a) Inductor currents
b) Switching pattern
c) Output capacitor voltage ripple
d) Charging capacitor voltage ripple in the circuit 2

In the second half-cycle, the capacitors are discharging in parallel, and the current flows from five capacitors to the inductor $L_1$. The equivalent circuit is shown in Figure. 5.13, the equivalent capacitance in parallel $C_{eq(RP)}$ can be expressed as

$$C_{eq(RP)} = C_1 + C_2 + ....C_n = nC_n \qquad (5\text{-}17)$$

and generalised to;

$$C_{eq(RP)} = \sum_{i=1}^{i} C_i \qquad (5\text{-}18)$$

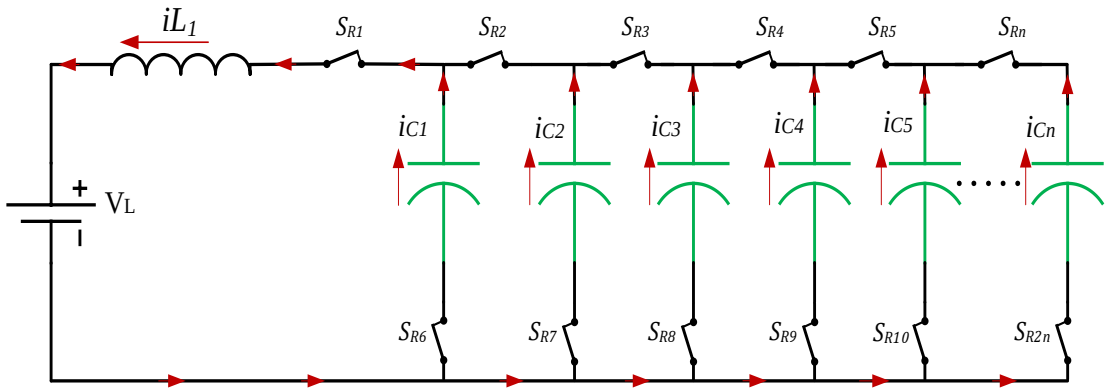


Figure 5.13: Equivalent circuit of discharging capacitors in parallel

However, the inductor current $L_1$ is the sum of the current of the capacitors in parallel, therefore, the equation of inductor current $I_{L1}$ can be expressed as;

$$iC_{eq(RP)} = I_{L1} = \frac{V_H}{\omega_R L_1} \sin \omega (t - t_0) \qquad (5\text{-}19)$$

where $iC_{eq(RP)}$ is the total current of five capacitors connected in parallel. As shown in Figure 5.12(a), the resonating inductor current increases to a peak and then it decreases to a negative value, but the diode which is connected in series with the IGBT switch blocks the current flow in reverse. The capacitor voltage $V_{Cn}$ in circuit 2 is the same value (Ohm's law).

The full design Equation derivation is explained in Appendix A. By neglecting the losses of the converter and based on the designed rating of the converter. The Equations are similar to the Equations in chapter 4. Especially, in the forward mode (boost voltage), the only difference is integrating the reverse mode operation (buck voltage). However, this converter has three kinds of capacitors $C_n$, $C_A$, and $C_B$ and two inductors $L_1$, and $L_2$.

#### 5.3.3.3 Determination of Capacitance Values

There are three different capacitances. Capacitor $C_A$ in circuit 1, five identical capacitors $C_n$ in circuit 2, and one capacitor $C_B$ in circuit 3. The capacitor in the circuit 2 depends on the charge transferred to the capacitor $C_B$ in voltage and the selected ripple voltage. However, the capacitor can be calculated as

$$C_n = \frac{Q}{\Delta V_{Cn}} \tag{5-20}$$

where $\Delta V_{Cn}$ is the voltage ripple of capacitors in circuit 2. The capacitor $C_A$ in low voltage side serves as charge storage for continuous delivery during the step-down mode. The value of the capacitor $C_A$ depends on the amount of charge as shown in Equation (4-14), and the voltage ripple on it. Hence, it can be shown that,

$$C_A = \frac{\left(P_{rated} \big/ V_A\right)\left(T_S \big/ 2\right)}{2\pi\, \Delta V C_A} \tag{5-21}$$

where $\Delta VC_A$ is the ripple voltage on the low side voltage capacitor of $C_A$. The Equation of the capacitor in the high voltage side $C_B$ is similar to the capacitor in low side $C_A$ and can be expressed as;

$$C_B = \frac{\left(P_{rated} \big/ V_B\right)\left(T_S \big/ 2\right)}{2\pi\, \Delta V C_B} \tag{5-22}$$

#### 5.3.3.4 Determination of Inductance Values

This converter has only two inductors $(L_1\text{-}L_2)$. They serve to limit the charging currents in both directions and accrue a zero-current switching with capacitors (L-C circuit). In Chapter 4, Equation (4-15), the inductor current $IL_1$ depends on the number of capacitors $C_n$ in circuit 2. However, the inductor $L_1$ has to be designed to carry the peak current and maximum power rating of the converter. Amalgamating Equation (4-6) into Equation (4-14) and rearranging;

$$L_1 = \frac{1}{C_{eq\,(FP)}}\left[\frac{Q\,n V_L}{2\pi\, P_{rated}}\right]^2 \tag{5-23}$$

The size of the output inductor depends on the output voltage and the amount of charge that needs to be transferred. Also, the value of the output inductor depends on the peak-to-peak of output current $\Delta I_{L2}$ and can be expressed as;

$$L_2 = \left[\frac{(n V_L - V_l)\, T_S / 2}{2\Delta I L_2}\right] \tag{5-24}$$

where $V_l$ is the voltage across the inductor $L_2$. The converter parameters in Table 5.1 were calculated by using all the above design Equation procedures.

Table 5.1: Converter parameters used for circuit simulation

| Parameters | | value | |
|---|---|---|---|
| Number of modules | | 5 | |
| Low Voltage | ($V_L$) | 6 | kV |
| High Voltage | ($V_H$) | 30 | kV |
| Inductor | ($L_1$) | 2.53 | µH |
| Inductor | ($L_2$) | 110 | µH |
| Capacitor | ($C_n$) | 694.5 | µF |
| Capacitor | ($C_L$) | 83 | µF |
| Capacitor | ($C_H$) | 116 | µF |
| Rated power | ($P_{rate}$) | +50, -5 | MW |
| Frequency | ($F_S$) | 2 | kHz |

### 5.3.4 Evaluation of Steady-State Operation

As shown in Figure 5.2, the bidirectional DC-DC Converter allows transferring of the power in both directions between two DC sources 6 kV/30 kV. The forward and reverse powers levels are 50 MW and 5 MW. Using the Equations derived in section 5.3.3, the parameters of this converter used for the simulation were calculated and are listed in Table 5.1.

The switching frequency $F_S$ of the converter is determined by the L-C resonances in the circuit and has fixed in 2 kHz, and also the fixed duty cycle of $d$=50% was used. The converter is simulated in Matlab/Simulink, using the Sim Power System toolbox. The waveforms of the voltage, current, and power during forward mode are depicted in Figure 5.14.

The DC gain obtained by the simulation is 4.9, which is very close to the design value of 5. The output voltage, current, and power of the converter in forward mode operation should be 30 kV/ 1667 A, 50 MW as designed. However, the output voltage of the proposed converter is 29.97 kV and the current is 1659 A. In addition, the load power is 49.7 MW as shown in Figure 5. 14(c).

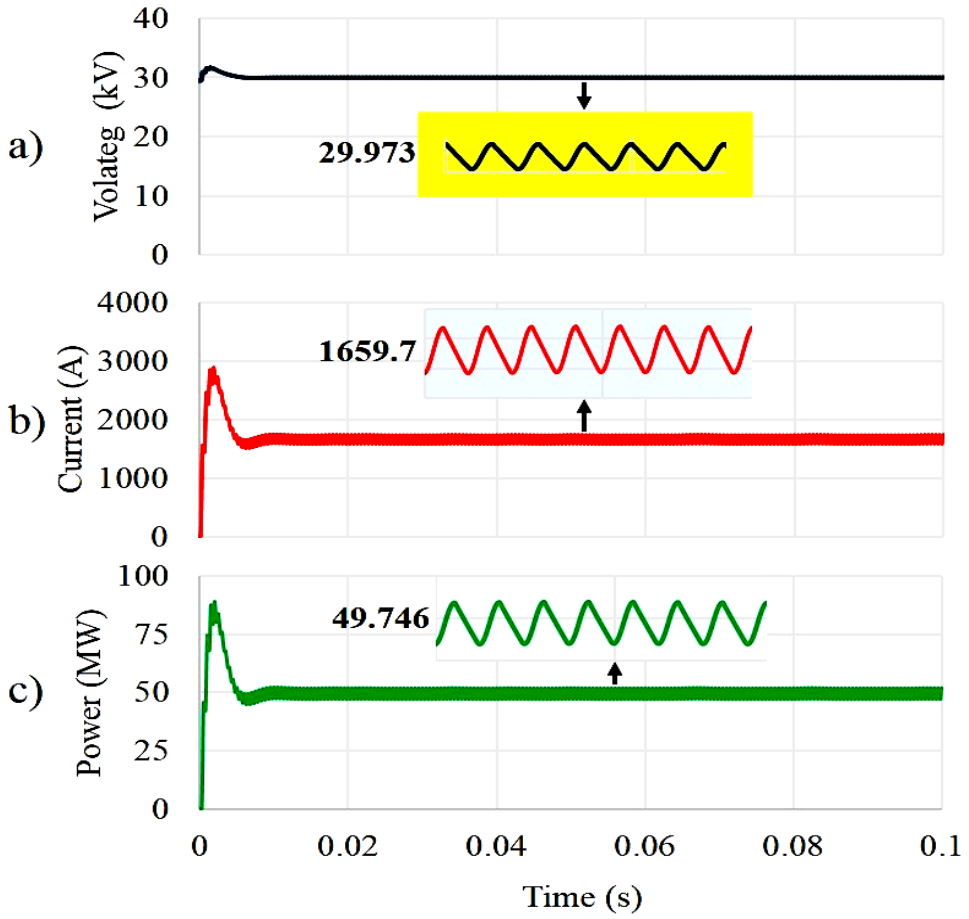


Figure 5.14: Simulation waveforms of the forward mode operating

Reverse mode waveforms of voltage, current, and power are shown in Figure 5.15. The voltage gain obtained by the simulation (0.201), is very close to the theoretical value of 0.2. Regarding the design of voltage gain converter, the output voltage as illustrated in Figure 5.15(a) is 5.9 kV, and it is close to the designed value to within 31 volts. The ripple voltage can be reduced by increasing the value of the capacitor in the high voltage side $C_B$. As well, the current is close to the design value within 11 A. During reverse power at 5 MW, the output power as depicted in Figure 15.5(c) is also close to the design value with different within 0.1 MW.

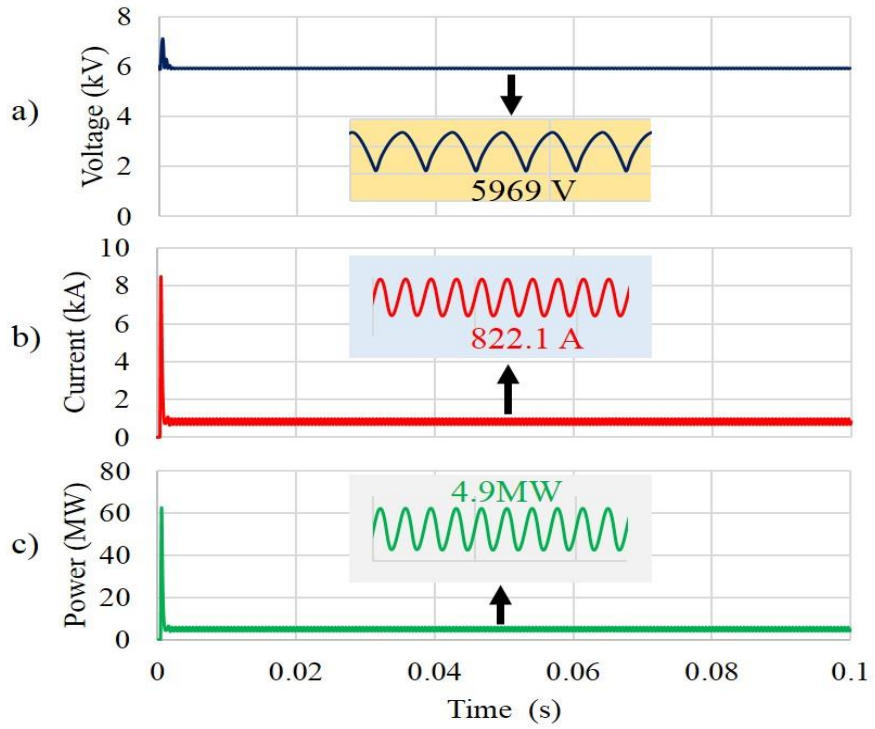


Figure 5.15: Simulation waveforms of the reverse mode operating.

### 5.3.5 Voltage and Current Stresses

#### 5.3.5.1 Forward-Mode:

As illustrated in Figure 5.16(a) and Figure 5.16(b), IGBT and Diode currents in modules 1,2,3,4 and 5 increase, peaking at 18.6 kA in 250 µs in the last module. IGBTs capable of this duty are commercially available [101].

During discharging of the capacitors in series, the voltage across the IGBT switches $S_C$ is 6 kV as shown in Figure 5.16(c). However, the voltages across switches $S_B$ increases by 6 kV from left to right reaching a maximum of 24 kV on the shunt IGBT switch at the HV side as shown in Figure 5.16 (d). This means that the devices in each module receive different voltages causing manufacturing issues and requiring a series connection of devices. In addition, a reverse voltage of 6 kV appears across switches $S_A$ as illustrated in Figure 5.16 (e).

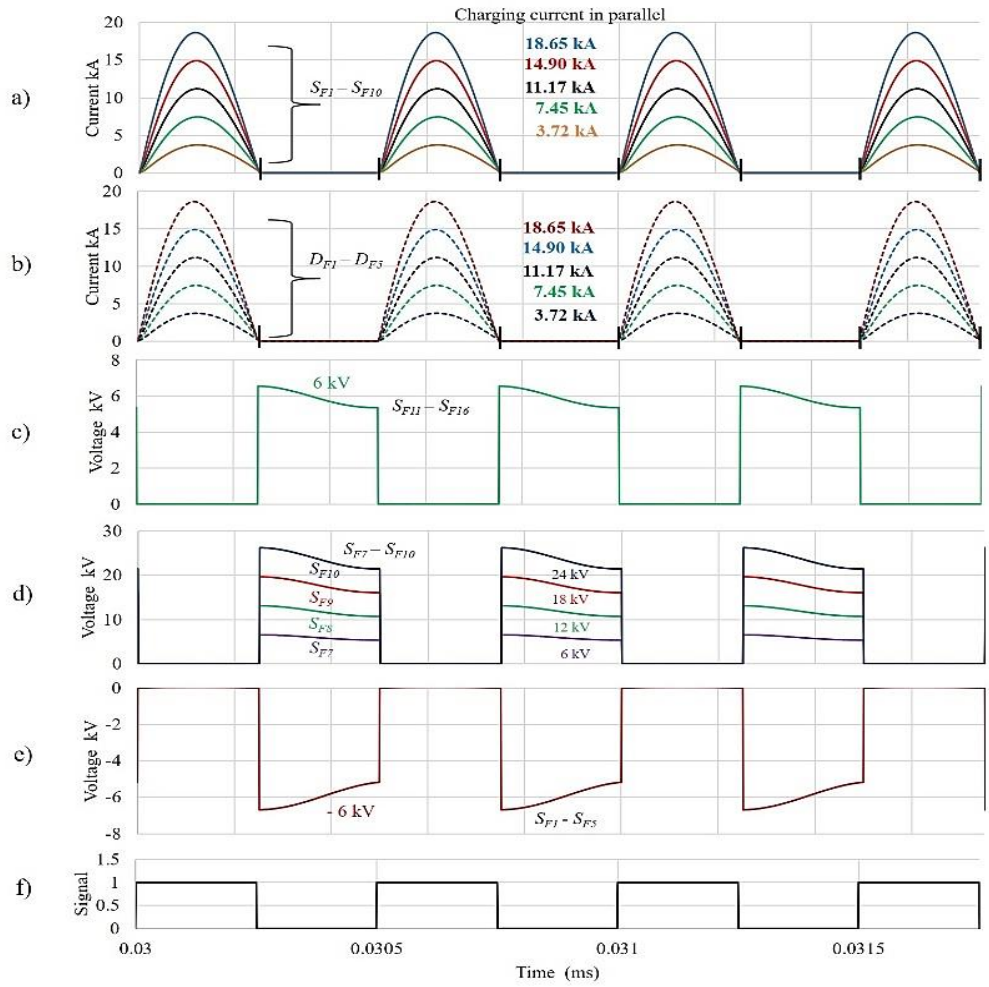


Figure 5.16: IGBT and diode switch simulation waveforms of forward mode operation

(a) Charging current through IGBTs,
(b) Charging current through diodes,
(c) The voltage across cells ($S_{F11}$-$S_{F16}$)
(d) The voltage across cells ($S_{F6}$-$S_{F10}$)
(e) The voltage across cells ($S_{F1}$-$S_{F5}$)
(f) Switching pattern.

Table 5.2 listed under the column labeled “Analytical” are the values computed from a mathematical solution of peak capacitor charging current, and the other column labeled “simulation” showing values computed from simulation result.

The different values of the capacitor current in each capacitor is fixed and decreased from capacitor current $I_{C1}$ to $I_{C5}$ by the gain 5. Otherwise, the simulation value is close to the design value as shown in Table 5.2. As shown in Figure 5.17, The IGBT switch $S_{F1}$ carries the full inductor current during the forward mode.

Table 5.2: Analytical and simulation results of current capacitors

| Capacitor currents | | | | |
|---|---|---|---|---|
| | | Analytical value | Simulation Value | Difference |
| $I_{C1}$ | (kA) | 19.5 | 18.65 | 0.85 |
| $I_{C2}$ | (kA) | 15.6 | 14.9 | 0.7 |
| $I_{C3}$ | (kA) | 11.7 | 11.17 | 0.53 |
| $I_{C4}$ | (kA) | 7.8 | 7.45 | 0.35 |
| $I_{C5}$ | (kA) | 3.9 | 3.72 | 0.18 |

Since it is connected to the fixed low DC voltage side VA, this switch has to withstand half of the voltage ripple of the capacitor $\Delta VC_n$ in circuit 2. The current flows in sequence through switches $(S_{F1} - S_{F5})$ during charging in parallel as shown in Figure 5.8. The switches in the bottom of the converter $(S_{F6} - S_{F10})$ are connected in series with switches $(S_{F1} - S_{F5})$ carrying the same current as switches $(S_{F6} - S_{F10})$. The current switches in the circuit 2 of the converter $(S_{F11} - S_{F16})$ are fixed to discharge the capacitors in series. But the voltage increases sequentially and independent of a number of modules '*n*'. Equations for the IGBT switches rating are given in Table 5.3.

There are two sets of diodes that need to be analysed, the first set is the series diode which is connected in series with the IGBT switches in the top of the converter $(D_{F1} - D_{F5})$. These diodes have to carry the same current rating as IGBT switches $(S_{F1} - S_{F5})$ and withstand the same voltages as the switches. Diode $D_{F1}$ carried a complete inductor current as in the switch $S_{F1}$ because it is connected in series and withstands a voltage which is half of the ripple capacitor voltage $\Delta VC_n$. The second set is series connected diodes $(D_{F6} - D_{F11})$ with IGBT switches $(S_{F11} - S_{F16})$.

The current rating of the diodes is the same as for the IGBT switches because they are connected in series, but the large voltage they are each required to withstand is close to the high DC voltage side $V_B$. There are two sets of capacitors in step-up mode, the first set is the capacitors in circuit 2 for which is identical value is designed. The current and voltage requirements for the capacitors $(C_1 - C_5)$ are the same as for the IGBT switches $(S_{F1} - S_{F5})$. For the second set of capacitor $C_B$ in

circuit 3, voltage rating is based on the number of modules in circuit 2, the power rating of the converter, and on the capacitor voltage ripple. The current is evaluated as in the peak current of inductor $L_2$ in a half-cycle. There is one inductor $L_1$, and its current requirement is the peak current during charging of capacitors in parallel, while, it has the same voltage rating as the low DC voltage side. Table 5.3 lists the equations of parameters for rating of voltage and current. The general equations of peak current and ripple voltage capacitor are shown in Equation (5-16) and Equation (5-20), respectively.

Table 5.3: Device and component rating of step-up mode

| Parameter | Current | Voltage |
|---|---|---|
| IGBT $(S_{F1})$, Diode $(D_{F1})$ | $I^P$ | $0.5\,\Delta VC_n$ |
| IGBT $(S_{F2} - S_{F16})$, Diode $(D_{F2} - D_{F10})$ | $I^P/n$ | $(nV_A + 0.5\Delta VC_n)$ |
| Inductor ( $L_1$ ) | $I^P$ | $0.5\,\Delta VC_n$ |
| Capacitor ( $C_n$ ) | $I^P/n$ | $(nV_A + 0.5\Delta VC_n)$ |
| Capacitor ( $C_B$ ) | $P_{rate}/nV_A$ | $(nV_A + 0.5\Delta VC_n)$ |

#### 5.3.5.2 Reverse Mode

The peak current in reverse mode operating is 2.6 kA as depicted in Figure 5.17(a) during discharge of the capacitors in parallel. Figure 5.17(b) shows the voltage stress on the switch $S_b$ is 6 kV during discharge in series is equal to the $V_H/5$. The charging current in series is the same as through the IGBT switches *($IS_{R11}$- $IS_{R15}$* = 536 A*)* as shown in Figure 5.17(c). One can see that the voltage across switches $S_b$ sequentially decreases in 6 kV steps as illustrated in Figure 5.15(d). Similarly, in the forward mode, the switching pattern is illustrated in Figure 5.15(e).

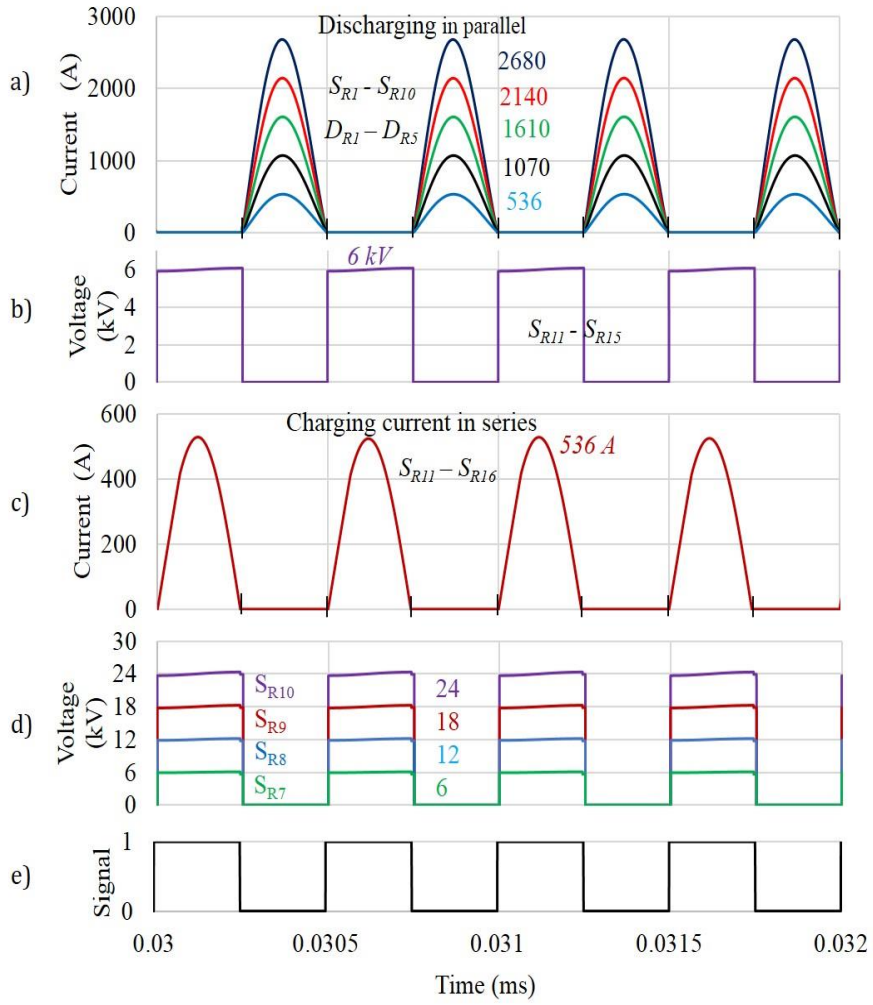


Figure 5.17: Simulation waveforms of the forward mode operation.

There are two sets of IGBT switches and diodes, and for the first set switches and diodes *($S_{R11}$- $S_{R16}$)* and *($D_{R6}$- $D_{R11}$)* the current rating is the same and fixed during charging of the capacitors in series and the same peak inductor current $L_2$ as shown in Figure 5.12(a). However, the voltage decreases sequentially from *($S_{R11}$–$S_{R16}$)* and is dependent on the number of modules '*n*' in circuit 2. For the second set of switches and diodes *($S_{R1}$-$S_{R10}$)* and *($D_{R1}$-$D_{R5}$),* its rating current is increased sequentially from high voltage to the low voltage side by the same value as the first module and dependent on the number of modules. However, the voltage it withstands is fixed and is only half voltage ripple of capacitors *($C_1$–$C_5$).*

The current rating of the capacitor $C_A$ in circuit 1 is the same as the switch $S_{R1}$ and diode $D_{R1}$, but the voltage rating is based on the capacitor voltage ripple.

Furthermore, the inductor $L_2$ is connected in series with high DC voltage side $V_B$. As mentioned before, this inductor has to withstand the full voltage regardless of the IGBT switch $S_{R16}$ and diode $D_{R11}$ connected in series. Therefore, this inductor has the same voltage rating as these switches. Its rating current is the peak current from the charge transfer in both modes of operation. Overall Equations for the parameters rating are summarised and listed in Table 5.4.

Table 5.4: Device and component rating of step-down mode

| Parameter | Current | Voltage |
|---|---|---|
| IGBT $(S_{R11} - S_{R16})$, Diode $(D_{R6} - D_{R11})$ | $I^P/n$ | $0.5\,\Delta VC_n/n$ |
| IGBT $(S_{R1} - S_{R10})$, Diode $(D_{R1} - D_{R5})$ | $I^P$ | $(nV_A - 0.5\Delta VC_n)$ |
| Inductor ( $L_2$ ) | $I^P/n$ | $0.5\,\Delta VC_n/n$ |
| Capacitor ( $C_A$ ) | $I^P$ | $(nV_A - 0.5\Delta VC_n)$ |

## 5.4 Summary

A bidirectional DC-DC Marx converter is presented in this chapter and is shown to be capable of providing the flow of high power from low voltage side to the high voltage side consisting of 'n' modules and stepping up and down the voltage following the classic Marx concept of charging the capacitors in parallel and discharging in series and vice versa. The transfer of electric charge from input and output capacitors is by the resonant L-C circuit. The diode is connected in series with IGBT switches to block the reverse current. Mathematical analysis of the converter is presented, providing knowledge for the design methodology of the converter.

The simulation demonstrates the ability of the converter to interface a 6 kV system with a 30 kV system leading to a gain of 5. The gain can be increased for application to higher voltages by increasing the number of modules. Therefore, the converter is easily scaled up or down. Resonance between the inductors and capacitors is used to determine the switching frequency enabling soft switching to reduce the losses.

# Chapter 6

# Application of the Bidirectional Modular Converter to Wind farm Power Collection

## 6.1 Introduction

In Chapter 5, the bidirectional modular converter (BMC) was presented, analysed and tested. Studies carried out on its application to an offshore wind farm are reported in this chapter. As explained in the literature review of the thesis (Chapter 2), by using a DC collector network in the offshore wind farm the use of heavy AC power transformers can be avoided and the number of power electronic conversion stages can be reduced. This leads to a reduction in the cost of structures in the offshore wind farms.

A 50 MW 6 kV DC bidirectional modular converter is used for power collection in this study. The operation of the bidirectional power flow from the offshore wind farm to the AC system via a DC-DC converter and VSC is explained. Finally, steady-state and dynamic-state performances are evaluated by simulation.

## 6.2 Electrical System for the Grid Connection of the Offshore Wind Farm

Recently there has been much interest in using HVDC for the grid integration of wind farms [37],[107],[108]. Therefore, it makes sense to use DC for the collection of power from individual wind generators leading to a reduction in the number of conversion stages thereby reducing cost. One possible DC collection and transmission system for the grid integration of wind farms is shown in Figure 6.1.

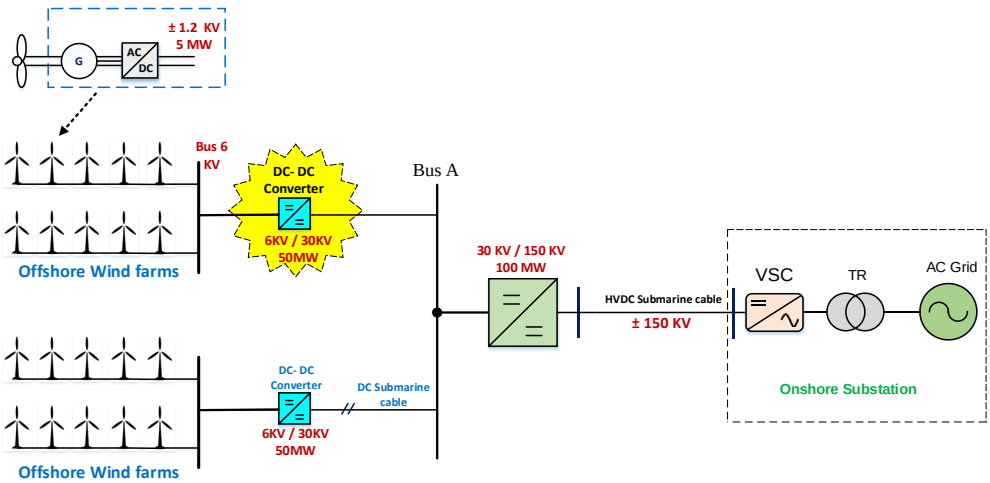


Figure 6.1: DC collection system for the grid connection of a windfarm

There are ten turbines in two parallel lines, each line comprising five series-connected wind turbines, each rated at 5 MW and connected through a bidirectional DC-DC converter which interfaces 6 kV and 30 kV systems.

Another DC-DC converter steps up the voltage to 150 kV for transmission via submarine cables to the onshore substation via a Voltage Source Converter (VSC). The studies reported in this chapter are focused on the power collection bi-directional converter highlighted by a yellow star.

## 6.3 Modelling the System

The reduced configuration of the wind farm with a bidirectional modular converter for modelling purposes is shown in Figure 6.2. In Figure 6.1 the connection of two wind farms is shown. For the study, only one wind farm is considered. The system to the right of the bus A is modelled by an equivalent cable, VSC and AC system. The 30 kV/150 kV DC to DC converter is simply considered as a voltage transformation device.

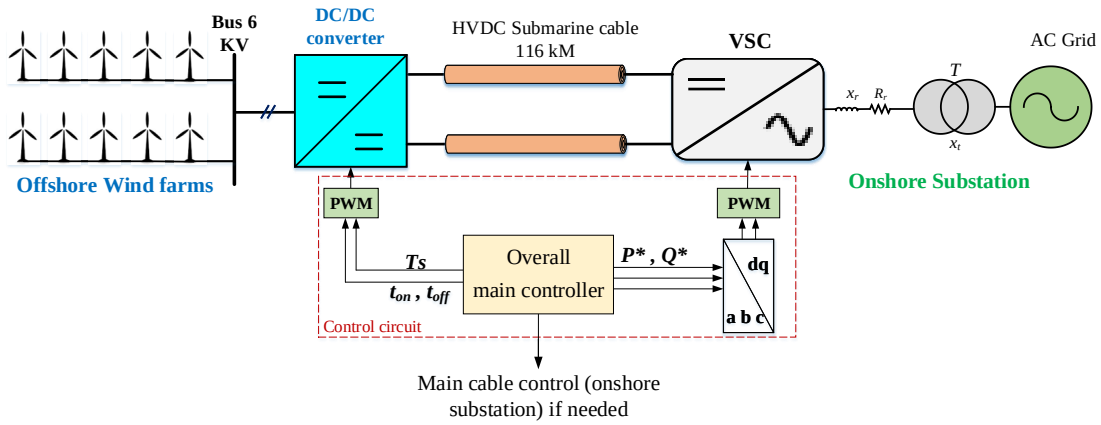


Figure 6.2: The model of the DC-DC converter connected to the AC system for simulation

### 6.3.1 Wind Farm

The wind farm considered in this study is explained in [41]. Each wind turbine consists of a Permanent Magnet Synchronous Generator (PMSG) rated at 690 V, and an AC-DC converter. The output DC voltage of the wind turbine is 1.2 kV. As shown in Figure 6. 3, each wind turbine converter is composed of a diode rectifier to rectify the variable frequency AC generated power from the PMSG to DC. The

diode rectifier is robust and not expensive. Then the DC voltage steps-up and is regulated by the DC-DC boost converter. This small converter is installed inside the PMSG pole.

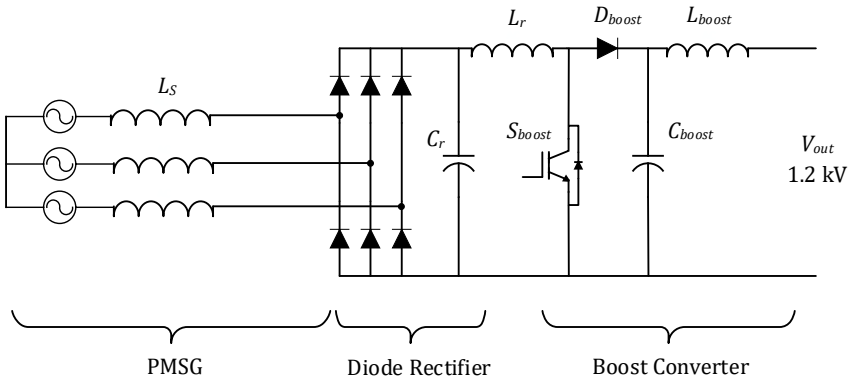


Figure 6.3: Wind turbine converter

The duty cycle of the converter is available to regulate the voltage during variable wind. The gain of the DC-DC boost converter can be calculated as

$$N_{boost} = 1/(1- d) \quad (6\text{-}1)$$

where $N_{boost}$ is the gain boost converter, and $d$ is the duty cycle. By neglecting the voltage drop associated with the DC transmission line to the DC-DC converter, the output voltage $V_{out}$ at the DC-DC converter is assumed to be 1.2 kV. During maintenance work and doldrums (light and calm winds), the auxiliaries in the wind farm require a small amount of power which must be drawn from the grid. Therefore, a model of the wind farm must be able to source and sink current. The focus of the study is on the power collection DC to DC converter and therefore the behaviour of the wind farm itself is of secondary importance. Therefore, the wind farm is modelled by a DC source of 6 kV, 50 MW.

### 6.3.2 Bidirectional Modular Converter

The bidirectional DC-DC converter is not required to regulate the voltage. It acts as an interface between the two voltage levels. The full analysis is given in Chapter 5. The structure of a bidirectional converter is depicted in Figure 5.3. As one can see in Figure 6.1, the bus '*A*' voltage is 30 kV and hence, the gain of the DC-DC converter is set to 5. Using the design Equations derived in chapter 5 the

converter parameters were calculated in Appendix A, and the parameters are listed in Table 6.1.

Table 6.1: Parameters of the model used in simulations

| Converter | | value | |
|---|---|---|---|
| Number of modules | (n) | 5 | |
| Input Voltage | ($V_A$) | 6 | kV |
| Output Voltage | ($V_B$) | 30 | kV |
| Inductor | ($L_1$) | 2.53 | µH |
| Inductor | ($L_2$) | 110 | µH |
| Capacitor | ($C_n$) | 694.5 | µF |
| Capacitor | ($C_A$) | 83 | µF |
| Capacitor | ($C_B$) | 116 | µF |
| Rated power | ($P_{rate}$) | +50, -5 | MW |
| Frequency | ($F_S$) | 2 | kHz |
| AC voltage | ($V_{ac}$) | 18.6 | kV |

### 6.3.3 Submarine DC Cable

The long distance between an offshore platform and onshore substation require HVDC transmission, one of long transmission via submarine cables. However, DC cables have three main components uniformly distributed along the cable such as resistive, inductive and capacitive components, which are significant and need to be considered in the simulation of the HVDC transmission system.

There are three cable technologies available for HVDC applications namely. Mass Impregnated (MI), Self-Contained Fluid-Filled (SCFF), and Crossed Linked Polyethylene (XLPE) [109]. XLPE cable technology has been in use for several years in HVDC applications and offshore HVDC interconnectors based on VSC converter technology used for DC cables with cross-linked polyethylene (XLPE) insulation. They are mainly used with VSC converters enabling power flow to reverse without polarity reversal [110], [111]. XLPE for a HVDC cable system is available with a rating of up to 1200 MW at DC voltage of up 320 kV. The data for XLPE is found in [111], [112]. However, ABB has recently developed a new XLPE HVDC cable system, which has a voltage capacity of 525 kV [111]. Overall the modeling of HVDC cables is based in on the data in [111], [113], and the data for DC cables used are listed in Table 6.2.

Table 6.2: DC cable parameters

| DC cable | value | |
|---|---|---|
| R | 0.011 | Ω/km |
| L | 2.615 | mH/km |
| C | 0.1908 | μF/km |
| Length | 116 | km |
| $\pi$ | 8 | |

### 6.3.4 Modelling of the VSC

For the VSC-HVDC system, this converter can act as either an inverter or a rectifier, as power flow through the converter can be controlled and can be directional. For steady-state studies, the DC-DC converter does not need to be represented by a full switching model and AC side harmonics are not considered. Instead, the simple 2-level averaged VSC model as depicted in Figure 6.4, based on direct quadrature *(d-q)* synchronous reference frame is used [107],[114]. Because an averaged model is sufficient and gives good results.

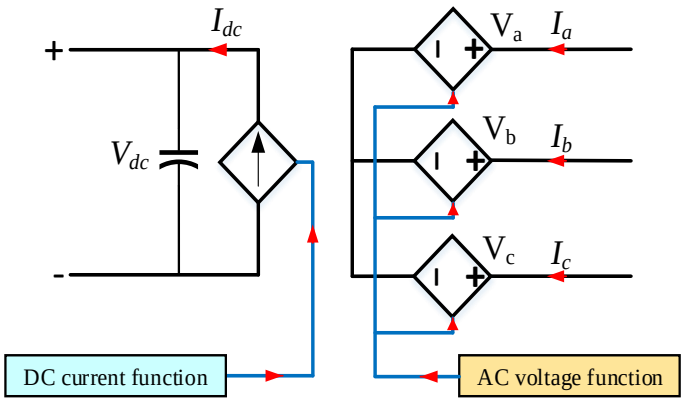


Figure 6.4: Averaged model of the VSC

The AC side of the VSC has a three phase *(abc)* reference frame and comprises three voltage-controlled [115],[116] current sources. By using the principle of power conservation and the principle of power balance between the DC side and the AC side, the calculation of the DC side of VSC neglecting its losses, the controlled current $I_{dc}$ on the DC side is given as the following Equation:

$$V_{dc}\, I_{dc} = v_a i_a + v_b i_b + v_c i_c \tag{6-2}$$

$$I_{dc} = \frac{v_a i_a + v_b i_b + v_c i_c}{V_{dc}} \tag{6-3}$$

The instantaneous active and reactive power at the grid connection point in *dq* coordinates are given by;

$$P = \frac{3}{2}(v_d i_d + v_q i_q) \tag{6-4}$$

$$Q = \frac{3}{2}(v_q i_d - v_d i_q) \tag{6-5}$$

### 6.3.5 AC Grid

The AC grid is a part of the VSC-HVDC link and consists of an ideal step-up transformer represented with the inductance $X_t$ which connects the VSC with the transformer to the AC grid. The phase reactor is important for calculation during steady-state operation and fault mode. The phase reactor is represented by $R_r$ and $X_r$ as shown in Figure 6.2. The AC system equivalent impedance circuit is shown in Figure 6.5.

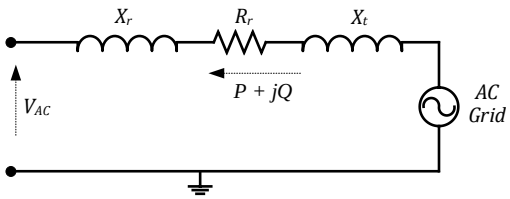


Figure 6.5: Equivalent circuit of the AC system

As can be seen, a general equation, the impedance of the reactor can be calculated as

$$Z = \sqrt{R_r^2 + (X_r^2 + X_t^2)} \tag{6-6}$$

where Z is the impedance, and the inductive reactance $X_r$ is given as

$$X_r = 2\pi f L = \omega L \tag{6-7}$$

The power of the system is 50 MVA. The short circuit of the system involves all three phases. The short circuit current $I_{SC}$ develops under transient conditions depending on the reactance $X$ and the resistance $R$ that make up short circuit impedance $Z_{SC}$. So, the impedance of the AC power system and the lines during three-phase short circuit can be calculated as;

$$Z_{SC} = \sqrt{\sum (R_r)^2 + \sum (X_r + X_t)^2} \qquad (6\text{-}8)$$

where $\sum R_r$ is the sum of series resistances, and $\sum(X_r + X_t)$ is the sum of the series reactance of the transformer and the line.

### 6.3.6 System Control Circuit

The system control circuit is composed of two main circuits, VSC control circuit, and a bidirectional DC-DC converter control circuit.

#### 6.3.6.1 VSC Control Circuit

In the VSC two electrical variables, $i_d$ and $i_q$ are controlled to vary the active and reactive power separately. One of the main control blocks of the VSC is inner current control, outer $P$, $Q$ and $V_{dc}$ control which include a Phase-Locked Loop (PLL) to adjust the grid angle. A classic scheme of a PLL is based on the d-axis voltage feedback by a PI controller to obtain the grid angular velocity and an extra integrator to obtain the angle. PI-controllers have the form;

$$K_S = K_p + \frac{K_i}{s} \qquad (6\text{-}9)$$

where $K_p$ is the proportional gain, $K_S$ is the transfer function, and $K_i$ is the integral gain. The PPL integrated into the VSC control can be described as follows:

$$K_{PLL} = \frac{K_{p\text{-}pll} + K_{i\text{-}pll}}{s} \qquad (6\text{-}10)$$

where $K_{i\text{-}pll}$ is the PLL integral gain, and $K_{p\text{-}pll}$ *is* the PLL proportional gain. The inner control loop controls the *d-q* axis parameters of the VSC's reference voltage. The current reference in the inner current control $i^*_d$, $i^*_q$ to get the desired reactive, and active power $(Q^*, P^*)$ is as shown in Figure 6.6. The current references $i^*_d$ and $i^*_q$ can be derived as:

$$i_q^* = \frac{2}{3}\frac{P^*}{v_q} \qquad (6\text{-}11)$$

$$i_d^* = \frac{2}{3}\frac{Q^*}{v_d} \qquad (6\text{-}12)$$

The response from $i_d$ to $i_d^*$ is based on a first-order transfer function whose rise time is given by $\tau_{id}$, which can be freely chosen. It should be sufficiently small for a fast-current controller. Therefore, the parameters for the PI-controller are;

$$K_p = \frac{X_r}{\omega} \quad , \quad K_i = \frac{R_r}{\tau_{id}} \qquad (6\text{-}13)$$

where $\tau_{id}$ is the closed loop time constant of the electrical system. This constant must be chosen considering the converter physical restriction. The calculated PI-parameters for the current controller can be found in Appendix C. The DC side of the VSC is derived using the principle of power conservation, meaning the power on the AC side must be equal to the power on the DC side plus the converter losses.

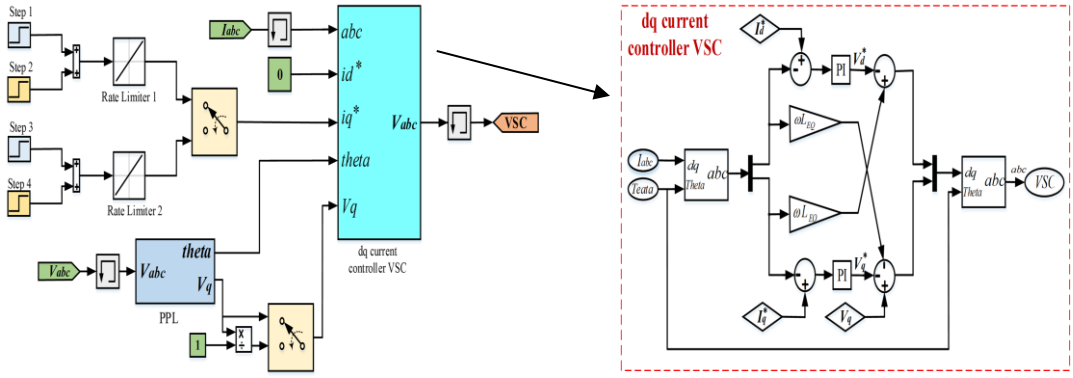


a) VSC control circuit b) dq inner control circuit

Figure 6.6: The main control circuit of VSC

Neglecting converter losses, The DC side can be also computed on the *dq0* reference frame and can be expressed as;

$$I_{dc} = \frac{3}{2V_{dc}}(v_d\, i_d + v_q\, i_q) \qquad (6\text{-}14)$$

#### 6.3.6.2 DC-DC Converter Control Circuit

A fixed frequency switching pattern is applied to the circuit cells. Meanwhile, the control circuit is controlled by the signal received from the VSC. There are two signals, one for boost (forward) converter switching, and the other for buck (reverse) converter switching as shown in Figure 6.7. In order to avoid high switching losses in the semiconductors, ZCS is implemented, making use of the two L-C resonant circuits established in the DC-DC Marx converter during the two main half-cycles subintervals ($t_{on}$ and $t_{off}$) for both modes. Details of the control circuit of the bidirectional DC-DC converter is given in Appendix C.

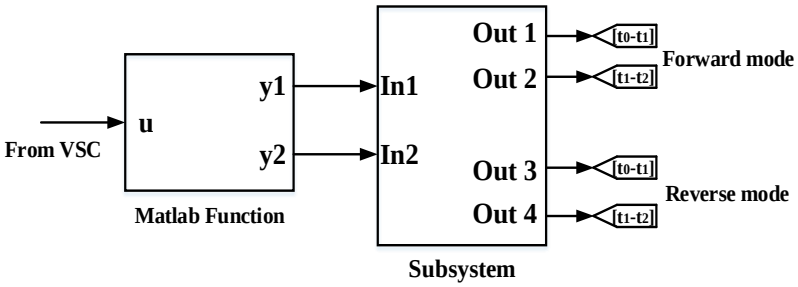


Figure 6.7: Control circuit of the DC-DC converter

## 6.4 Evaluation of the Steady-State Operation

In this section, the operation of the 50 MW bidirectional converter is investigated by using the Matlab/Simulink software package. The design of the converter including the parameters calculation and selection was based on the system explained in sub-section 6.3.1. The values used to the model the overall system are summarised in Table 6.1. As previously described, the study has two modes of operation forward and reverse. The inductor current waveforms during both modes of operation are shown in Figure 6.8 and illustrate resonance and that the current reaches zero before the end of each of the switching period in both modes. The maximum current occurred in the forward mode and is equal to 28 kA. The minimum current occurred in the reverse mode and is equal to 0.5 kA. The reason for the high current in the inductor $L_1$, is the delivery of MW at a relatively low voltage of 6 kV.

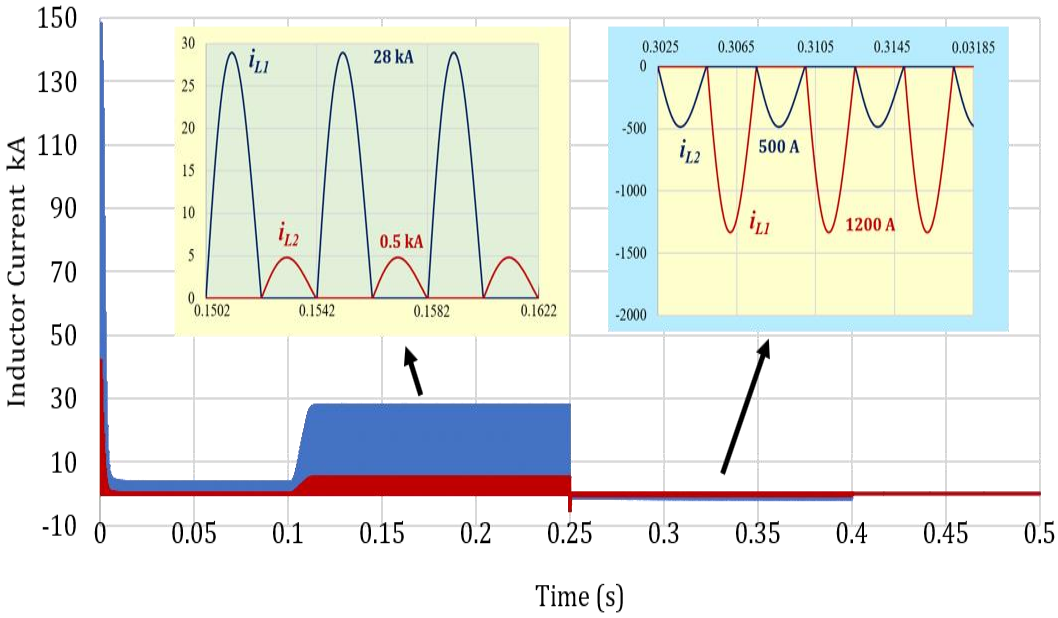


Figure 6.8: Inductor current waveforms during both mode operations

After the unloaded system has reached steady-state as depicted in Figure 6.9, at time 0.1 s, the power demand for AC system through VSC and is ramped for 50 MW, then the power demand is inverted to -5 MW at time 0.25 s, which the power flow is from the AC system to the converter through the DC link.

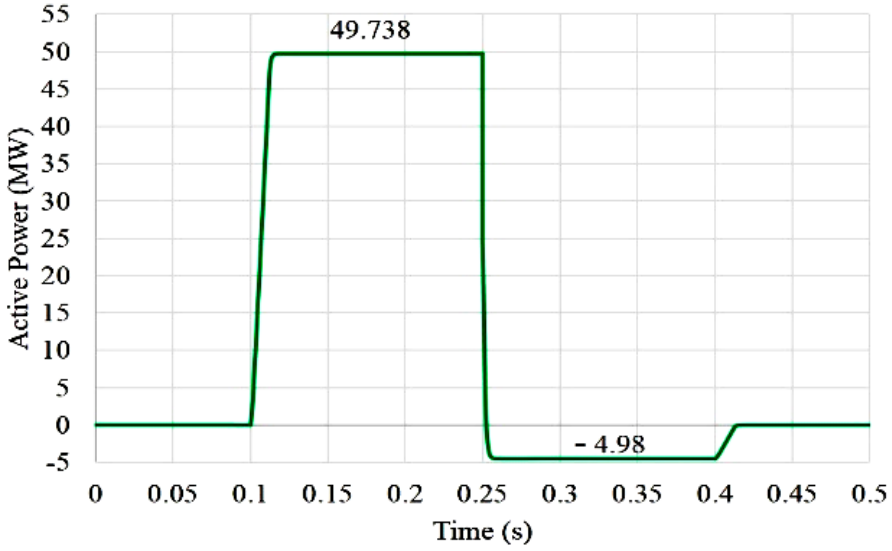


Figure 6.9: DC power flows in both modes

The forward and reverse powers of 49.7 MW and 4.9 MW, respectively are shown in Figure 6.9 and very close to the designed power rating of 50 MW and 5 MW. During both modes of operation, the reactive power demand of the VSC is kept at zero and the reference active power in the VSC is 50 MW and 5 MW as shown in Figure 6.10.

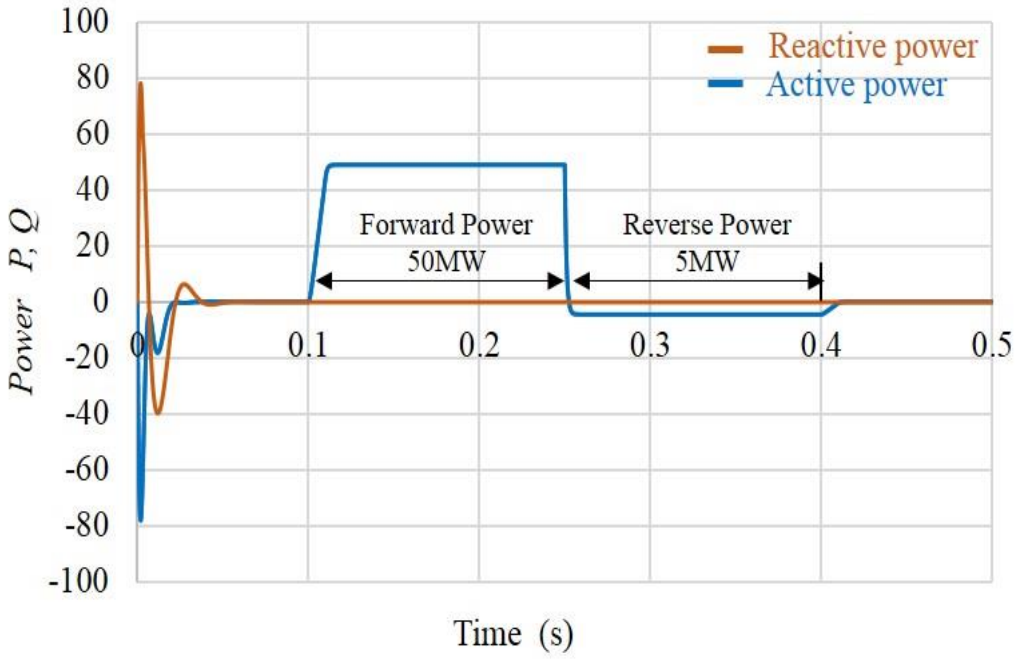


Figure 6.10: Power flows in forward and reverse modes

The AC side of the VSC in the phase *(a, b, c)* reference frame is composed of three voltage-controlled sources as;

$$V_j = 0.5\, V_{dc}\, m_j, \qquad j = a,\ b,\ c \tag{6-15}$$

where $m_j$ corresponds to the modulation function and is obtained from the *dq*0-*abc* transformation of the reference voltage $V^*_{abc}$. Figure 6.11(a) shows that the three-phase AC voltage of the system is constant in both modes of operation. The control system for VSC station has been implemented in the *(d-q)* synchronous reference frame, with control of the active power and DC voltage. The angle of the transformation is detected from the AC voltage side ($V_a$, $V_b$, $V_c$). This angle is necessary to synchronize the system with the AC grid and calculate the park transformation, which is obtained by means of a PLL.

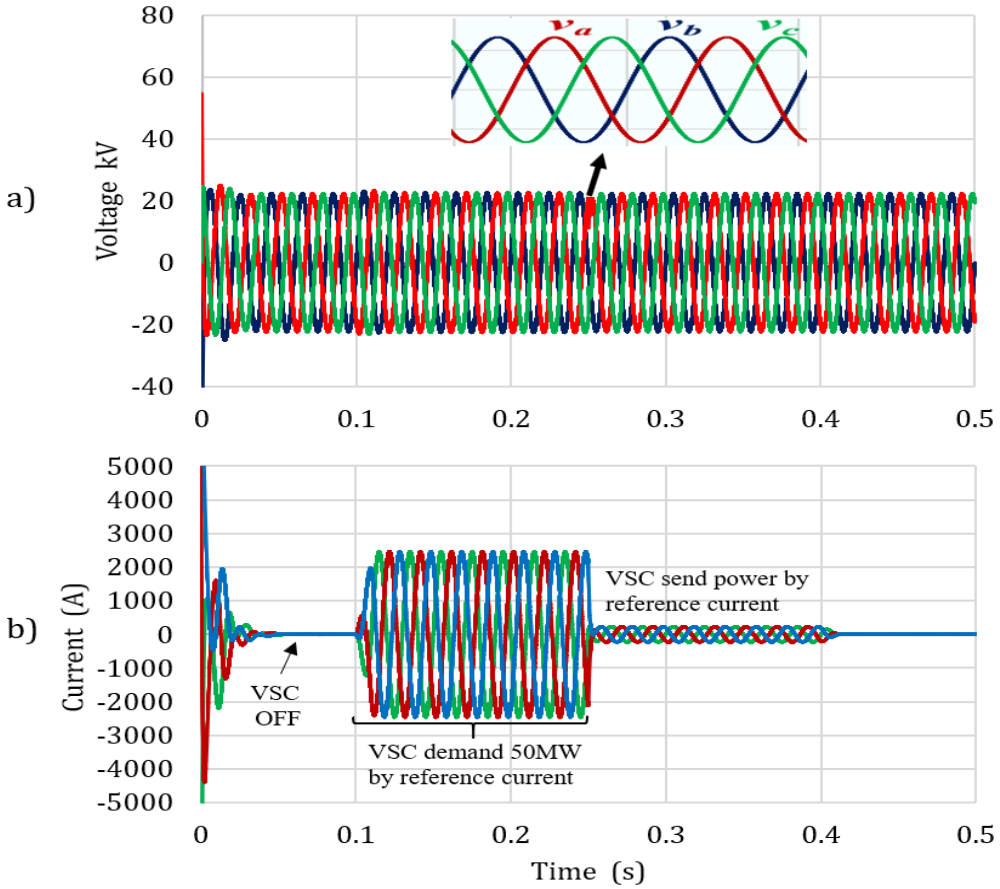


Figure 6.11: AC voltage and current waveforms
a) Three phase AC voltage waveforms
b) AC current waveforms

The current source of the VSC Model determines the active power exchange between the AC side and DC side. Figure 6.11(b) shows the reference variable AC current side in the VSC. At time 0.1s the VSC demands active power by injecting AC reference current until time 0.25 s. Then the VSC inverts the power to the DC link through bidirectional converter until time 0.4 s. From the DC voltage waveform shown in Figure 6.12, it can be seen that the initial no-load voltage of 33 kV drops to the rated voltage of 30 kV at 0.1 s when the VSC demands the rated power of 50 MW. At time 0.25 s, the VSC sends a signal to the converter demanding a reverse power of 5 MW as shown in Figure 6.9.

The power flows from the AC system to the wind farm through the VSC, the DC link and the DC-DC converter. At 0.4s the bidirectional converter is turned off by a signal from the VSC whilst, the VSC still sends power through DC link towards the offshore wind farm which leads to the rise in the DC-DC converter terminal voltage.

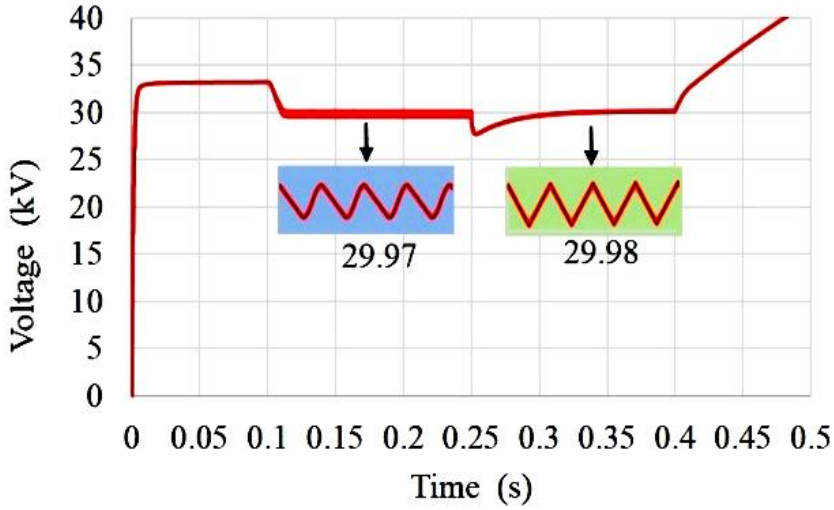


Figure 6.12: DC voltage waveform in both modes

During the simulation, the reactive power demand is kept at zero by keeping the quadrature axis current $I_q$ at zero. The notch in the voltage waveform at 0.25s is due to the charge mismatch of the capacitor $C_H$ when the current flow reverses. The settling time is less than 5 ms. The voltage ripple is 2.4 kV. As shown in Figure 6.13, the forward and reverse currents are 1661.7 A and 165.3 A respectively.

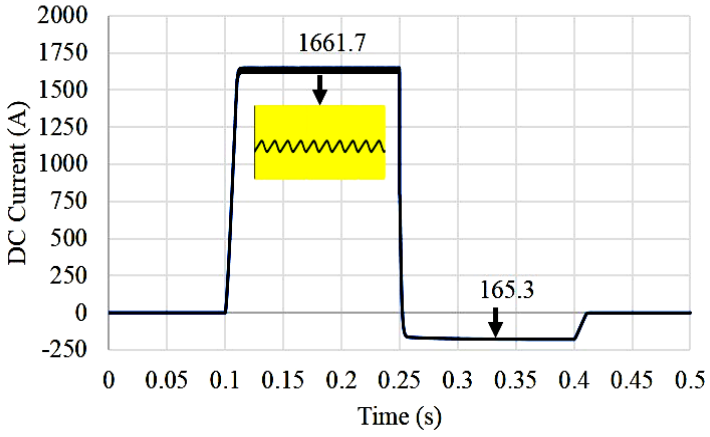


Figure 6.13: DC voltage waveform in both modes

## 6.5 Device and Component Stresses

### 6.5.1 Forward IGBT Devices

As shown in Figure 6.14, the IGBT switch $S_{F1}$ carries the full inductor current $I_{L1}$ during the step-up mode. The peak current is 27.8 kA at 250 µs in the module $(S_{F1}, S_{F10})$ and the charging current sequentially decreases by the number of the modules as illustrated in Figure 6.14. IGBTs capable of this duty are commercially available, an example is the IGBT 5SNA 1200G450300 [101]. Since it is connected to the fixed low DC voltage side $V_A$, this switch has to withstand half of the voltage ripple of the capacitor $\Delta V_{Cn}$ in stage 2.

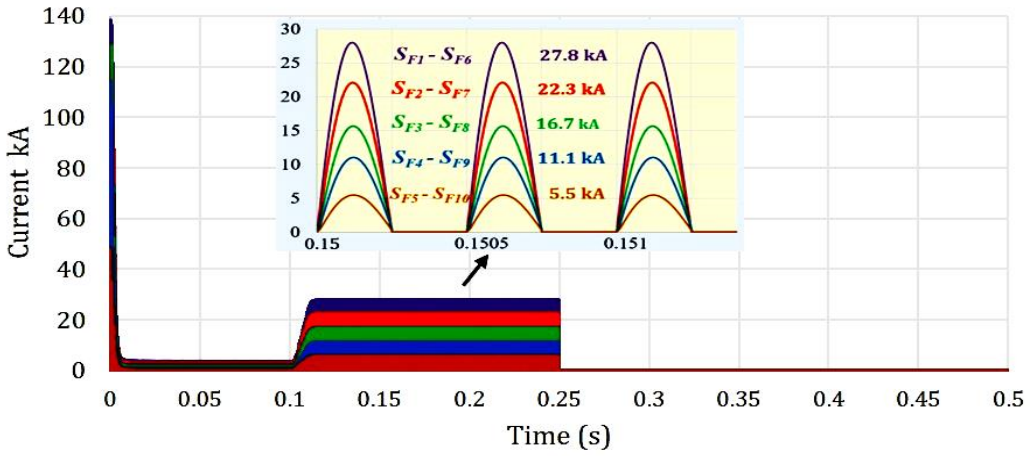


Figure 6.14: Parallel charging current in forward mode operating

The voltages across switches $(S_{F6}, S_{F10})$ increase by 6 kV from left to right, reaching a maximum of 24 kV on the shunt IGBT switch at the HV side as shown in Figure 6.15(a). This means that the devices in each module see different voltages causing manufacturing issues and requiring a series connection of devices. In addition, the current switches ($S_{F11}$ - $S_{F16}$) in circuit 2 of the converter are fixed during the discharge of the capacitors in series is 5.35 kA as shown in Figure 6.15(b), but the voltage increases sequentially and independent of the number of modules '*n*'. Furthermore, the voltages across switches $(S_{F11}, S_{F16})$ is fixed by 6 kV during both modes of operation as shown in Figure 6.15(c).

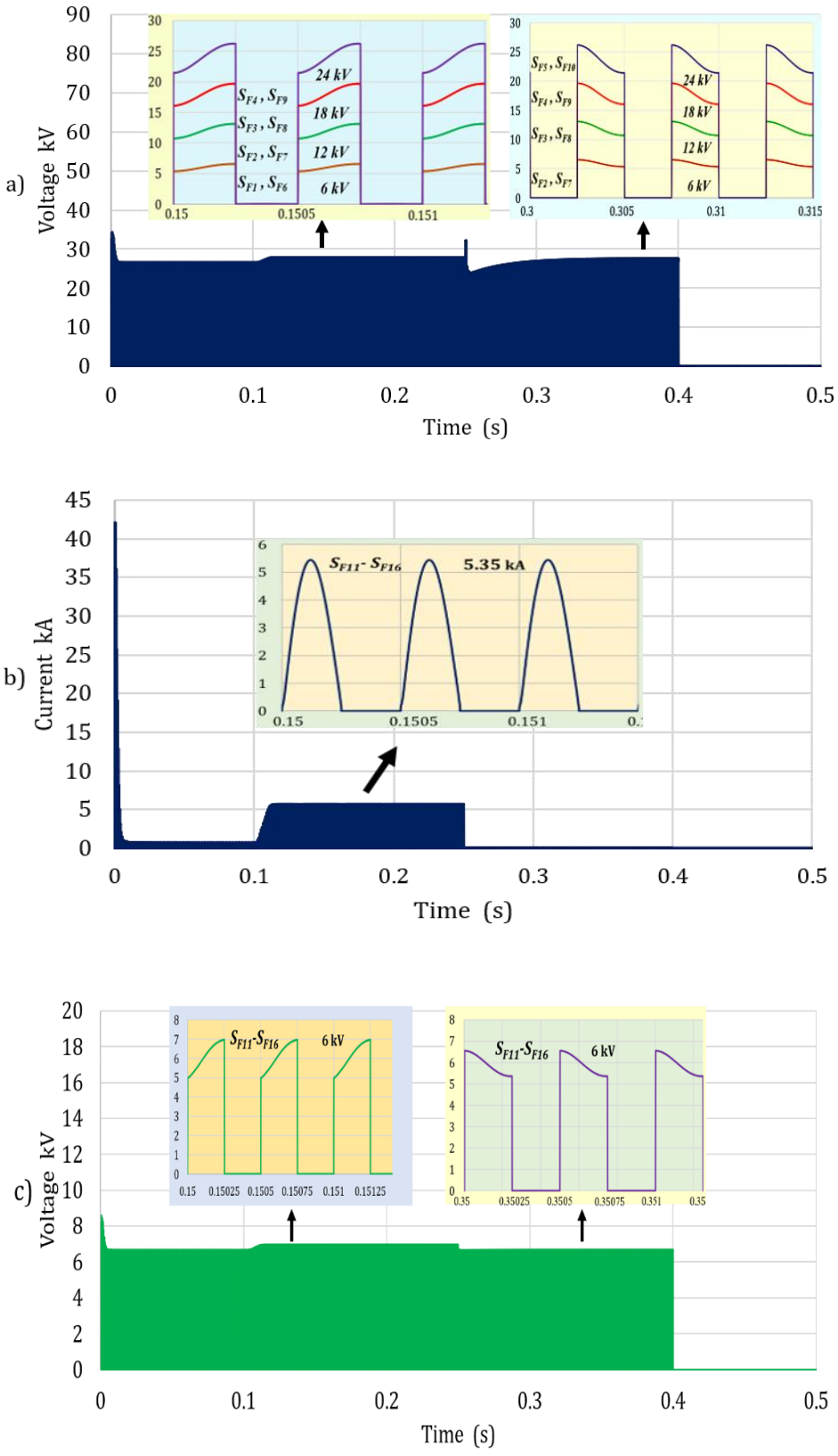


Figure 6.15: Current and voltage stresses on IGBT during forward mode operation

a) Voltages across IGBT switches during both modes operating, b) Discharging current in series through IGBT switches in FM, c) Voltages across IGBT switches during both modes operating

### 6.5.2 Reverse IGBT Devices

During reverse mode, from time zero to 0.25 s, the reverse IGBT is in reverse bias with the current direction and the current would not be able to flow through these IGBT switches, the charging current in series is the same as through the IGBT switches *($S_{R11}$ –$S_{R15}$)* = 537 A as depicted in Figure 6.16.

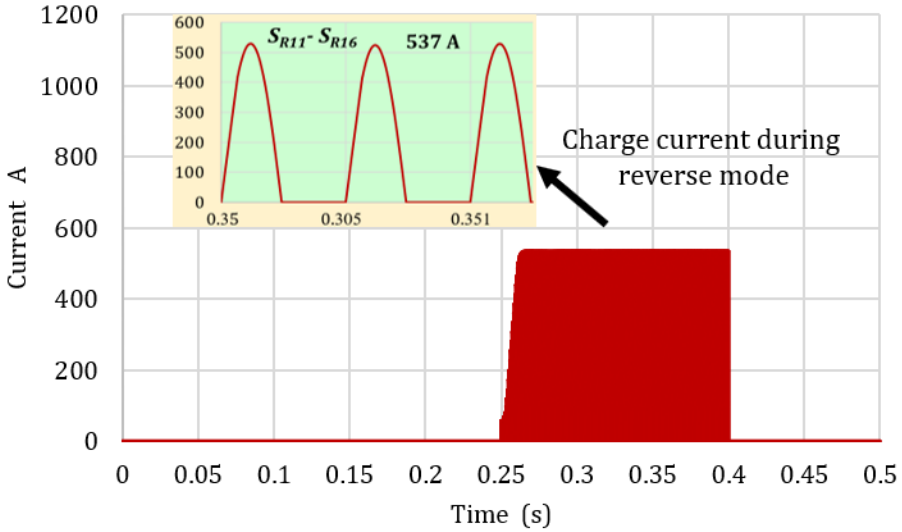


Figure 6.16: Current flows through IGBT during forward mode operation

The parallel discharging current sequentially increases with a peak current of 2.6 kA at 250 µs as shown in Figure 6.17. Its rating current is increased sequentially from the high voltage to the low voltage side by the same value of the first module.

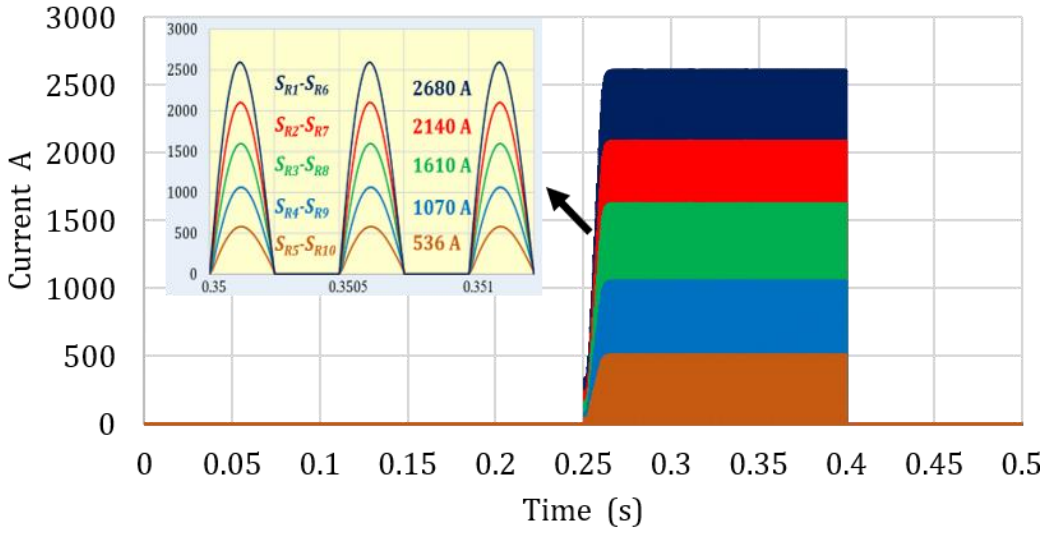


Figure 6.17: Discharging current in parallel through IGBT during reverse mode operating

The voltage stress on the switches *($S_{R11}$ –$S_{R16}$)* is 6 kV during discharge in series and is equal to the $V_H/5$ and the same as in the switches *($S_{F11}$ –$S_{F16}$)*. One can see that the voltage on switches $S_{R1}$ –$S_{R10}$ sequentially decreases in 6 kV steps, the same as in switches $S_{F2}$ –$S_{F10}$ and as illustrated in Figure 6.15 (a). The duty-cycle of both modes of operation is fixed $d$=0.5.

As shown in Figure 6.15(a), the charging voltage of the converter is 6 kV and increases up to 30 kV. However, the switching stress of the devices needs to connect several switches in series to withstand high voltage. The number of IGBT in the cells connected in series is scaled by the nominal voltage rating of the switch. Currently, the high-voltage IGBT with maximum blocking voltage rated up to 6.5 kV/750 A, and the selected high voltage IGBTs and fast recovery diode are 5SNA 1200G450300 and 5SDF 10H6004. The rating of IGBT is 4.5 kV/1200A and diode is 6 kV/ 1100 A. This kind of IGBT and diode are designed by ABB for high power density because it has a high current. The number of strings of IGBTs is different from module to module in the converter because the voltage is not at the same level and as shown in Figure 6.15(a). From left to right in Figure 5.3, the first string consists of two forward IGBTs connected in series and two in reverse because the voltage withstand is 6 kV.

## 6.6 Evaluation of the Dynamic Operation

When offshore wind farms are connected onshore through an HVDC link, it provides increased flexibility for the system. In offshore wind farm applications, there are three main types of fault identified according to their location, such as offshore wind farm faults, DC faults and AC faults (onshore faults). Studies carried out to investigate AC side faults are reported in this section. Generally, a fault on the onshore side reduces the active power flow and increases the voltage on the DC link rapidly. To ensure stability and compliance with the grid code, several control actions, and protective circuits are usually in place and will act during a fault. UK grid codes require the wind farm to ride through an AC fault for 140 ms [117]. The system studied is shown in Figure 6.18.

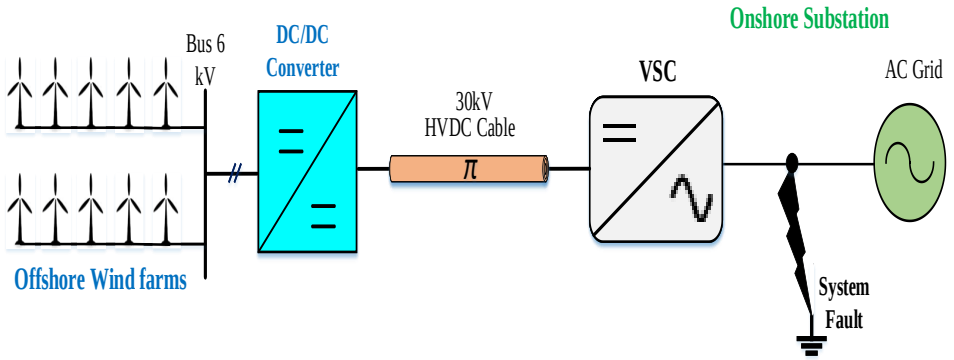


Figure 6.18: A single line diagram of DC-DC converter wind farm connected with the AC system during AC fault (3 Phase to ground)

### 6.6.1 Fault Ride-Through Event Simulation

The capability to ride through a fault in wind turbine generators is one of the most difficult issues. In order to emulate an onshore grid fault, and to test the operation of the bidirectional DC-DC converter at two fixed power levels, the amplitude of the onshore substation AC supply is controlled to follow the voltage-time profile. Figure 6.19 shows a plot reflecting the general shape of voltage tolerance that most grid operators demand, including the variations in time and voltage levels for the grid codes of European countries with large wind energy penetration.

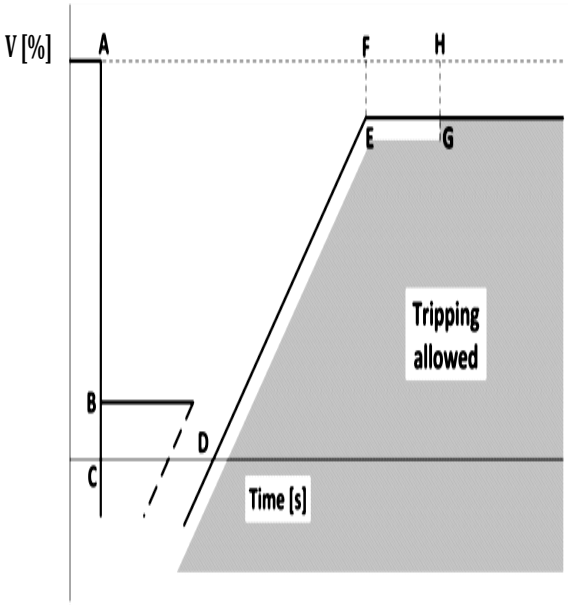


| Grid Code | BC | BD | AF | FE | AH | HG |
|---|---|---|---|---|---|---|
| Denmark | 25% | 0.1 s | 0.75 s | 25% | 10 s | NA |
| Germany (EON)[1] | 0% | 0.15 s | 0.15 s | 30% | 0.7 s | 10% |
| Germany (EON)[2] | 15% | 0.625 s | 3 s | 10% | NA | NA |
| Ireland (EirGrid) | 15% | 0.625 s | 3 s | 10% | NA | NA |
| Spain | 20% | 0.5 s | 1 s | 20% | 15 s | 5% |
| UK (NG) | 0% | 0.14 s | 1.2 s | 20% | 2.5 s | 15% |

[1] For generating unit with large symmetrical short-circuit current component.
[2] For generating unit with low symmetrical short-circuit current component.

Figure 6.19: The typical shape of Fault Ride-Through capability plot [118]

During and after a fault causing a voltage drop with a magnitude and duration above the shaded area, tripping is not allowed. As illustrated in the table in Figure 6.19. United Kingdom tripping is not allowed even with a voltage collapse to 0% for up to 140 ms. While in Denmark, a voltage drop below 25% of the nominal value allows the converter station to trip. To avoid a system trip due to a transient situation and exceeding the voltage operation range, some protection should be provided. A three-phase short circuit ground fault was applied for 200 ms at the AC side. With reference to the Equation (6-6) and Equation (6-7), the short circuit current level in the AC system can be calculated as

$$I_{SC} = \frac{V_{ac}/\sqrt{3}}{z_{SC}} \qquad (6\text{-}16)$$

The simulation results were obtained in Matlab/Simulink Simulation software. The fault was applied at 0.15 ms from the start of the simulation. During a fault in the onshore AC system, the HVDC link voltage increases rapidly. Because the active power of the wind farm has dropped to zero and the reactive power is increased as shown in Figure 6.20.

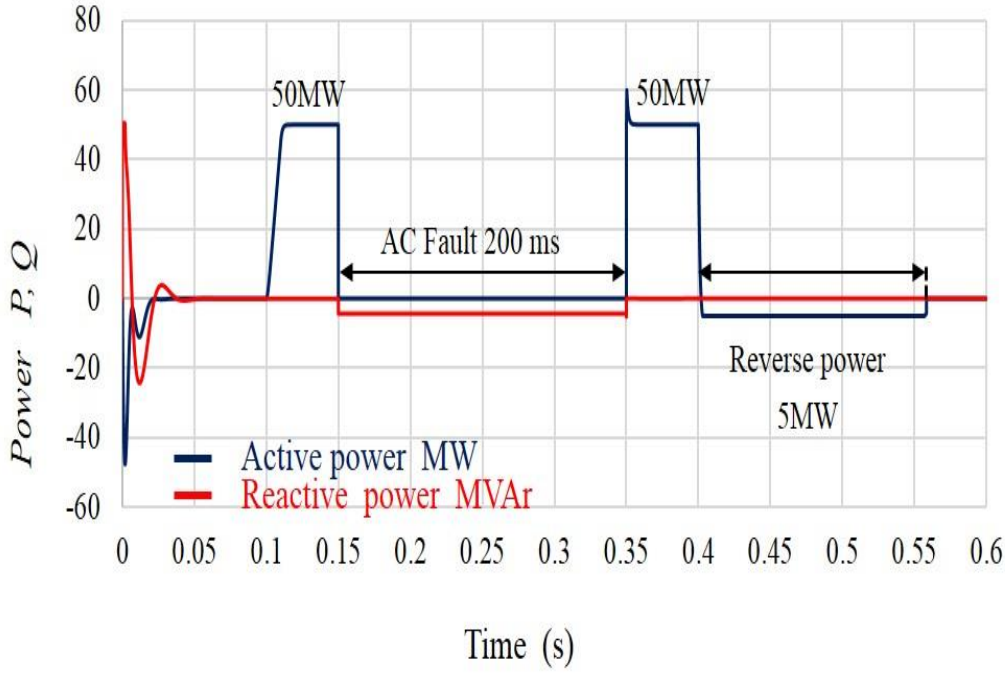


Figure 6.20: Active and reactive power in the AC side

The reason for the active power drop is the voltage drop on the AC side as shown in Figure 6.21. From time 0.1 s to 0.15 s the system is in steady-state and the active power transferred to from offshore wind farm to the AC system is 50 MW. During the fault at 0.15 s the active power is back to zero from time 0.15 s to 0.35 s as illustrated in Figure 6.20. When the fault is cleared the active power returns to transfer with the same value, 50 MW. At time 0.4 s the reverse power transferred from the AC system to the offshore wind farm via HVDC link is 5 MW.

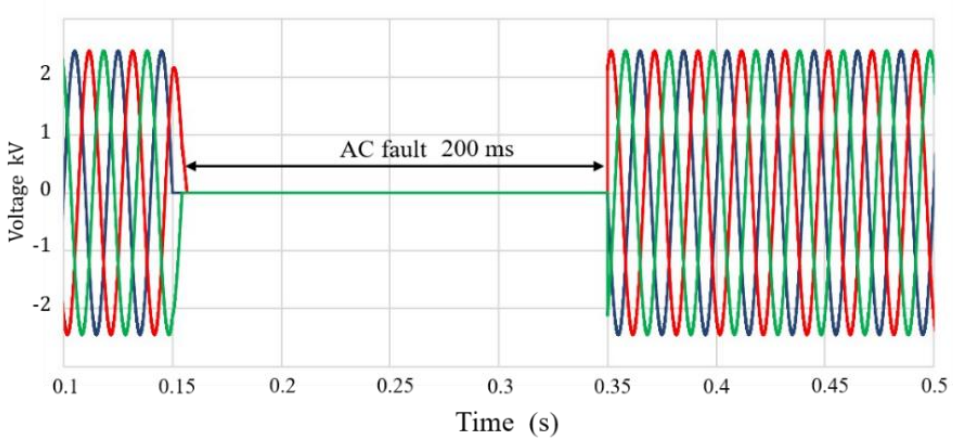


Figure 6.21: Voltage waveforms at fault point

As depicted in Figure 6.21, the duration of the short circuit is 200 ms, in that time the three-phase AC voltage in the onshore substation is zero because the three-phase short circuit has occurred. The wind farm continues to feed the VSC through the DC-DC converter. The HVDC link voltage increases through charging and discharging the capacitors of the DC-DC converter 30 kV to 47 kV in 200 ms as illustrated in Figure 6.22. Once the fault is cleared at 0.35 s, the HVDC link voltage returns to the steady-state level at 29.97 kV as illustrated in Figure 6.22. At time 0.4 s, the VSC sends a signal to the converter demanding a reverse power of 5 MW. Therefore, the voltage steps-down in less than one cycle then returns to the steady-state level of 30 kV as depicted in Figure 6.22. At time 0.55 s, the DC-DC converter is turned 'OFF', by VSC's signal.

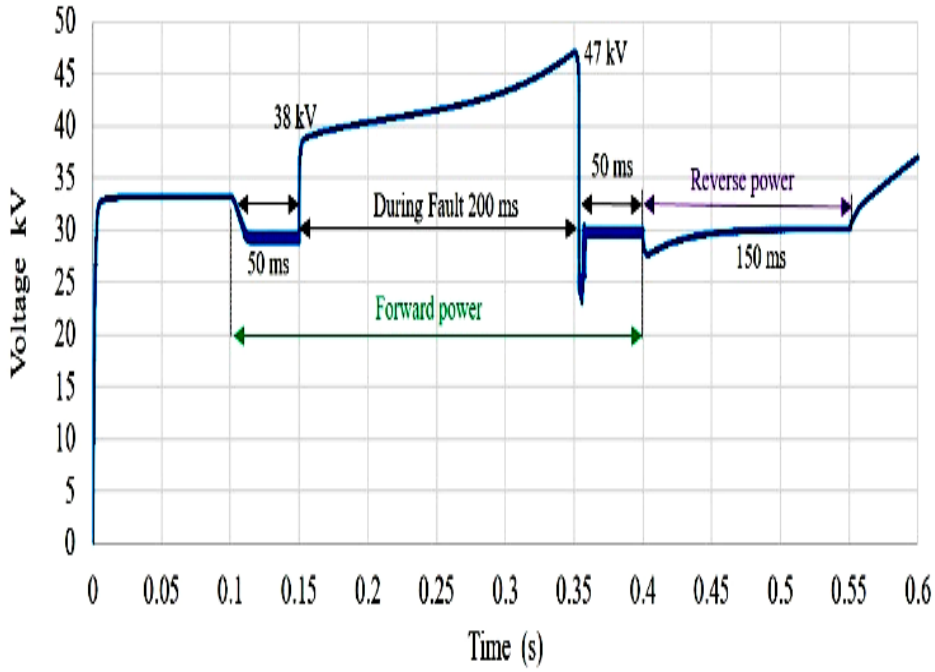


Figure 6.22: HVDC link voltage

### 6.6.2 Device and Component Stresses

As shown in Figure 6.23, from time t = (0~0.1) s, the converter steps-up the voltage but the VSC did not demand the power from offshore wind farm yet. At (t= 0.1 s) VSC demands DC power from offshore wind farm through the converter and the maximum voltage on the switching devices and capacitors is constant and as designed is 24 kV.

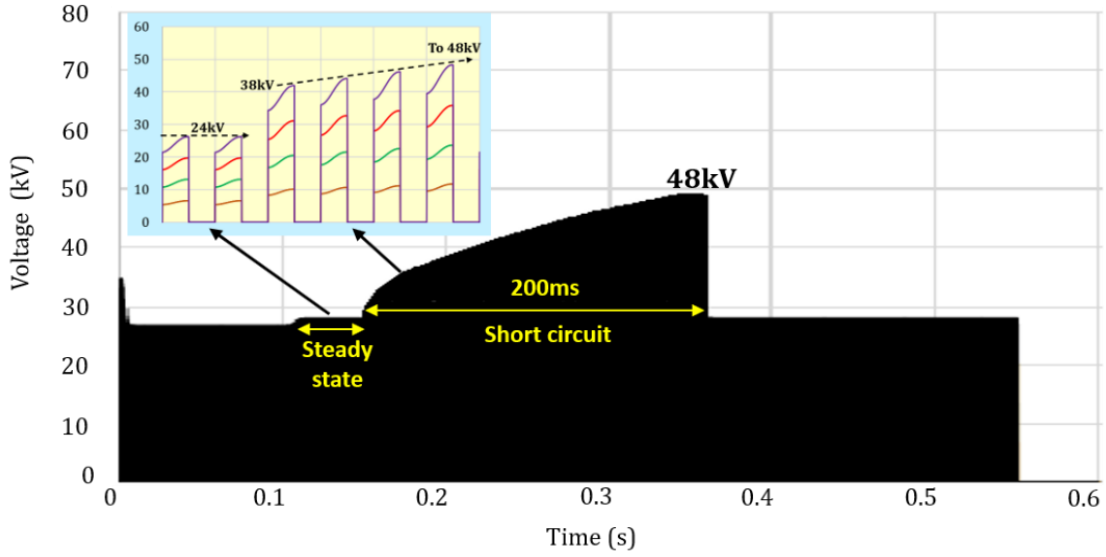


Figure 6.23: IGBT withstand voltage during short circuit

Once the AC fault occurs at t= 0.15 s, the charging voltage in the converter increases rapidly and starts from 38 kV to the maximum voltage at time t=0.35 s is 48 kV. In such a case, if the system is not protected from the increasing high voltage, and not clear the fault, the IGBT will break down.

At time 0.35 s, the AC fault has cleared and the voltage across IGBT switches immediately falls back from 48 kV to the normal voltage level 24 kV. Figure 6.24 shows the currents flow through the IGBTs converter during the AC fault. During forward 50 MW power flows, a reference current step change occurs from steady-state value 27.8 kA to the transient state of 55.3 kA at 0.15 s and it is observable that the current reaches the peak values of up to 79.8 kA at the end of the fault at 0.35 s as shown in Figure 6.24. At this high-value current, and to protect the IGBT from breakdown and damage the IGBT modules should connect in parallel to divide the current through these IGBTs. After 200 ms the fault is cleared, then the current back to the steady-state level of 27.8 kA.

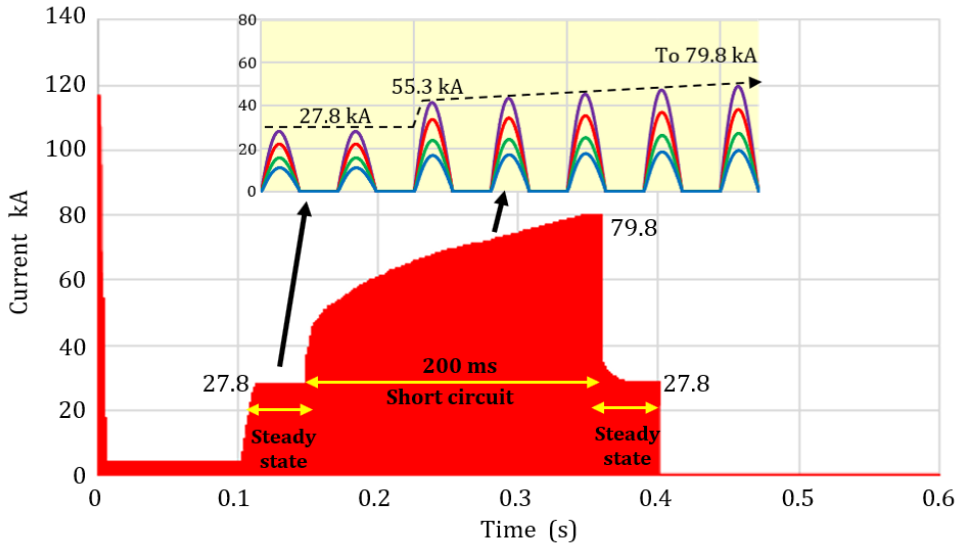


Figure 6.24: Current flows through IGBT Switch during short circuit

In this case, the converter needs protection from the peak currents during the fault. However, the voltage and the power in the DC link back to normal level after the fault cleared as shown in Figure 6.20 and Figure 6.22.

## 6.7 Summary

This chapter addresses DC collection grids for offshore wind farms. A new high-power medium-voltage DC-DC converter provides integration between the offshore wind farm and the AC system. The mathematical analysis which led to the derivation of design equations, which are necessary for the design of such a converter are presented in Chapters 4 and 5. Using the design equations, the fundamental parameters of a 50 MW 6 kV/30 kV DC to DC converter were calculated followed by steady state performance evaluation by simulation. The simulation confirmed the mathematical predictions and operational objectives. The effect of the AC side was investigated which confirmed that the converter can ride through a fault. But in this case, it is necessary to rapidly reduce the upper limit voltage at the HVDC link by using one of the protection methods such as large chopper resistor or de-loading the wind turbine. In addition, the bidirectional modular DC-DC converter has demonstrated its capability to redirect the power flow inside an offshore wind farm scheme.

# Chapter 7

## Conclusions and Future Work

In this final chapter, the conclusions that are drawn from this research work are summarised and a concise description of the main contributions to knowledge are given. An outline of this research study is provided followed by an abridged discussion of potential research directions resulting from the research.

## 7.1 Conclusions

The challenge inherent in a DC collection system requires the development of a high-power DC-DC converter with high voltage transformation ratios, reduced weight, physical size, and DC cables. Different existing DC-DC converter topologies have been reviewed as well as background information regarding other research concerning DC-DC converters.

This thesis are proposed and developed two unidirectional DC-DC converter topologies termed single-stage and multi-stage DC-DC Marx converters. Both are capable of boosting high voltage and transfer unidirectional high power with high rated current. These converters are improved and modified by reducing the number of IGBT switches while maintaining the same power rating as the Veilleux converters. The proposed converters use two IGBTs connected in series to form a high voltage valve. The simulation results show the operation of both proposed converters as expected. The converters' gain is observed for different operating points. Further, variable amplification can be obtained by inserting a step-up converter at the input to have a continuous range of high voltage DC gain or by increasing the number of capacitors in the middle circuit. The two proposed converters have proven successful in achieving gain voltage while naturally reducing the number of active switches, and therefore the cost is low. Both proposed converters' topologies gave acceptable results only in unidirectional power flow. To overcome this drawback, an innovative converter, a bidirectional modular DC-DC converter (BMDC), is proposed and developed with a suitable controller and simulation models for bidirectional power flow. Design methodology and equations for the determination of circuit components and solid-state devices are presented. Its feasibility is assessed through 50MW in boost converter and 5MW in a buck converter simulation. This converter has demonstrated its ability to interface between two different voltages levels.

In addition, the proposed converter is adapted for offshore wind farm application. This converter transmits the power via DC link to the VSC and vice versa, which leads to the system being capable of delivering a good performance under normal conditions. Furthermore, the effect of the AC side was investigated and its behaviour was studied under fault conditions. But in this case, it is necessary to rapidly reduce the upper voltage limit at the HVDC link by using protection methods. Finally, this system avoids the high civil engineering cost of an offshore wind farm capable of supporting heavy AC transformer or high-frequency transformer, which are required for HVDC applications. The main part of the research in this thesis is concerned with the design of a new converter and integrating it into offshore wind farm applications. The overall system is simulated, and each part of this work performs as expected.

## 7.2 Thesis Contributions

The contributions to knowledge achieved by the research described in this thesis are listed below:

- Proposed and developed two modified types of unidirectional DC-DC Marx converter for offshore wind farm, called “a single-stage and modular cascaded Marx converter”. The development includes a reduced count of IGBT, and diode switches compared to the Veilleux converter with the same power rating. The design equations for determining the inductor and capacitor sizes for the converter have been deviced. The two developed and modified types have been proven to be successful in achieving stepping-up to HVDC following the general Marx concept.

- An innovative high power bi-directional modular DC-DC converter (BMDC) has been constructed and adapted for the Marx principle, which is capable of achieving step-up and step-down voltage transformations at kV level and is able to handle MW level power transfers in both directions. Theoretical analysis and simulation results confirmed that the bidirectional modular DC-DC converter is capable of transmitting the

power in both directions and operates between two different voltage levels.

- Inclusion and implementation of the bidirectional Modular DC-DC converter into an offshore wind farm application, including the voltage source converter and the AC system. A power flow control circuit between both of the AC and DC systems is designed. DC transmission has been fully implemented and the transmission distances are greater than 100km. The main drawback with the proposed topology is an uneven voltage level rating of the modules cell which means that the devices in each module receive different voltages causing manufacturing issues and requiring series connection of devices.

- The situation has been studied and investigated regarding electrical network stability during steady-state and dynamic-state operations. Finally, a bidirectional modular DC-DC converter has been proved for offshore wind farm applications.

## 7.3 Recommendations for Future Work

This thesis contributes to the design, development and modification DC-DC converters for offshore wind farms. Based on the results of this research, the author's recommendations for the following research points could be investigated in future:

- Increasing the distance between the DC-DC converter and the AC substation (up to 200 Km) and evaluating the proposed converter under different operating modes and with OWFs three main types of faults.

- Conducting a detailed comparison of losses resulting from DC/DC converters performing similar tasks, and calculating the converter efficiency with different power levels, including quantitative evaluation of bidirectional converter operating losses under different operating modes.

- It is important to validate the obtained simulation results by building an experimental system in the laboratory. The system should involve the proposed converter, AC grid, and DC network of the offshore wind farm. However, the main challenge would be the availability of a high voltage laboratory. Therefore, further investigation of the validating the simulation results proposed converter would be the use of other simulation tools e.g. OPAL RT real-time digital simulator with a CPU that operates at time step of 10 μs.

- Further research in the proposed converter should focus on the development of different control strategies for different types of fault protection as optimising the energy production in both sides is essential to maintain reliable operation and thus support the on shore substation with energy

# References

[1] Bresesti, Paola, Wil L. Kling, Ralph L. Hendriks, and Riccardo Vailati. "*HVDC connection of offshore wind farms to the transmission system.*" IEEE Transactions on energy conversion , Vol. 22, pp. 37-43, Dec 2007.

[2] Rahman, Md Mizanur, Md Fazle Rabbi, Md Khurshedul Islam, and FM Mahafugur Rahman. "*HVDC over HVAC power transmission system: Fault current analysis and effect comparison*." In Electrical Engineering and Information & Communication Technology (ICEEICT), International Conference on, pp. 1-6, 2014.

[3] Wind Europe, "Wind Europe Annual Statistics 2017," *https://windeurope.org/wp-content/uploads/files/about-wind/statistics/WindEurope-Annual-Statistics 2017.pdf*, no. February, pp. 1–12, 2018.

[4] Wind Europe, "Wind Energy in Europe: Scenarios for 2030," *Report-Available at: https://windeurope.org/about-wind/reports/wind-energy-in-europe-scenarios-for-2030/*, Sep 2015.

[5] T. Lüth, "DC / DC converter for high voltage direct current transmission," *PhD diss., Imperial College. London Dep. Electr. Electron. Eng., no.* December, 2014.

[6] Y. A. Kaplan, "Overview of wind energy in the world and assessment of current wind energy policies in Turkey," *Renew. Sustain. Energy Rev.*, vol. 43, pp. 562–568, Sep 2015.

[7] Blaabjerg, Frede, and Ke Ma. "Future on power electronics for wind turbine systems." *IEEE Journal of Emerging and Selected Topics in Power Electronics* 1, no. 3, pp. 139-152, 2013.

[8] R. Perveen, N. Kishor, and S. R. Mohanty, "Off-shore wind farm development: Present status and challenges," *Renew. Sustain. Energy Rev.*, vol. 29, pp. 780–792, 2014.

[9] S. Sawyer, S. Teske, and M. Dyrholm, "The Global Wind Energy Outlook," *Gwec*, 2016. *Available at: https: http://gwec.net/publications/global-wind-energy-outlook/global-wind-energy-outlook*-2016.

[10] Steve Sawyer , Klaus Rave, "Opening up new markets for business," *Gwec* 2015, *Available at: www.gwec.net/ publications/global-wind-energy-*

*outlook/global-wind-energy-outlook*-2015

[11] Henderson, Andrew R., Colin Morgan, Bernie Smith, Hans C. Sørensen, Rebecca J. Barthelmie, and Bart Boesmans. "*Offshore wind energy in Europe—a review of the state-of-the-art*." *Wind Energy: An International Journal for Progress and Applications in Wind Power Conversion Technology* 6, no. 1, pp. 35-52, 2003.

[12] S. Kota, S. B. Bayne, and S. Nimmagadda, "Offshore wind energy: A comparative analysis of UK, USA and India," *Renew. Sustain. Energy Rev.*, vol. 41, no. 5, pp. 685–694, 2015.

[13] Renewable UK. Wind Energy in the UK: State of the Industry Report 2013, (October), 1–40. *Available at: Retrieved from http://www.renewableuk.com/download.cfm/docid/5CE18E20-ECA4-44D2-B2B00E6DE2E3E9F5,* 2013.

[14] I. Erlich, F. Shewarega, C. Feltes, F. W. Koch, and J. Fortmann, "Offshore wind power generation technologies," Proceedings of the IEEE 101, no. 4, pp. 891-905, December, 2013.

[15] Adeuyi, Oluwole Daniel, Nick Jenkins, and Jianzhong Wu. "Topologies of the North Sea supergrid." In *Power Engineering Conference (UPEC), 2013 48th International Universities'*, pp. 1-6. IEEE, 2013.

[16] J. Serrano González, M. Burgos Payán, and J. Riquelme Santos, "Optimum design of transmissions systems for offshore wind farms including decision making under risk," *Renew. Energy*, vol. 59, pp. 115–127, 2013.

[17] Gomis-Bellmunt, Oriol, Jun Liang, Janaka Ekanayake, Rosemary King, and Nicholas Jenkins. "*Topologies of multiterminal HVDC-VSC transmission for large offshore wind farms*." *Electric Power Systems Research* 81, no. 2 , pp. 271-281, 2011.

[18] Y. Fu, S. Member, C. Wang, S. Member, and W. Tian, "Integration of Large-Scale Offshore Wind Energy via VSC-HVDC in Day-Ahead Scheduling," vol. 7, no. 2, pp. 535–545, 2016.

[19] A. Tabassum, M. Premalatha, T. Abbasi, and S. a. Abbasi, "Wind energy: Increasing deployment, rising environmental concerns," *Renew. Sustain. Energy Rev.*, vol. 31, pp. 270–288, 2014.

[20] J. De Decker and A. Woyte, "Review of the various proposals for the European offshore grid," *Renew. Energy*, vol. 49, pp. 58–62, Jan. 2013.

[21] Vrana, T. K., R. E. Torres-Olguin, B. Liu, and T. M. Haileselassie. "The North Sea super grid-A technical perspective, pp. 65-65. 2010.

[22] Dedecca, João Gorenstein, and Rudi A. Hakvoort. "A review of the North Seas offshore grid modeling: Current and future research." Renewable and Sustainable Energy Reviews, pp. 129-143, 2016.

[23] B. V. Yaramasu, B. Wu, P. C. Sen, S. Kouro, and M. Narimani, "High-Power Wind Energy Conversion Systems : State-of-the-Art and Emerging Technologies," vol. 103, no. 5, 2015.

[24] S. H. Qazi and M. W. Mustafa, "Review on active filters and its performance with grid-connected fixed and variable speed wind turbine generator," *Renew. Sustain. Energy Rev.*, vol. 57, pp. 420–438, 2016.

[25] a. Madariaga, J. L. Martín, I. Zamora, I. Martínez De Alegría, and S. Ceballos, "Technological trends in electric topologies for offshore wind power plants," *Renew. Sustain. Energy Rev.*, vol. 24, pp. 32–44, 2013.

[26] C. Meyer, M. Hoing, a. Peterson, and R. W. De Doncker, "Control and Design of DC-Grids for Offshore Wind Farms," *Conf. Rec. IEEE Ind. Appl. Conf. Forty-First IAS Annu. Meet.*, vol. 3, no. 6, pp. 1475–1482, 2006.

[27] I. Erlich, M. Wilch, and C. Feltes, "Reactive Power Generation by DFIG Based Wind Farms with AC Grid Connection Keywords," *Alternatives*, pp. 1–10, 2007.

[28] Feehally, Tom, and Judith M. Apsley. "The doubly fed induction machine as an aero generator." *IEEE Transactions on Industry Applications* 51, no. 4, pp. 3462-3471, 2015.

[29] C. Zhan, C. Smith, a. Crane, a. Bullock, and D. Grieve, "DC transmission and distribution system for a large offshore Wind Farm," *9th IET Int. Conf. AC DC Power Transm. (ACDC 2010)*, pp. O46–O46, 2010.

[30] Machado, João, Mário Ventim Neves, and Paulo Jorge Santos. "*Economic limitations of the HVAC transmission system when applied to offshore wind farms*." In *Compatibility and Power Electronics (CPE), 9th International Conference on*, pp. 69-75. IEEE, 2015.

[31] Ukil, Abhisek. "Theoretical analysis of tuned HVAC line for low loss long distance bulk power transmission." *International Journal of Electrical Power & Energy Systems* 73, pp. 433-437, 2015.

[32] M. M. Rahman, M. F. Rabbi, M. K. Islam, and F. M. M. Rahman, "HVDC over HVAC power transmission system: Fault current analysis and effect comparison," *1st Int. Conf. Electr. Eng. Inf. Commun. Technol. ICEEICT*, 2014.

[33] C. N. Mau, K. Rudion, a. Orths, P. B. Eriksen, H. Abildgaard, and Z. a. Styczynski, "Grid connection of offshore wind farm based DFIG with low-frequency AC transmission system," *IEEE Power Energy Soc. Gen. Meet.*, pp. 1–7, 2012.

[34] Torres-Olguin, Raymundo E., Marta Molinas, and Tore Undeland. "Offshore wind farm grid integration by VSC technology with LCC-based HVDC transmission." *IEEE Transactions on Sustainable Energy* 3, no. 4, pp. 899-907 2012.

[35] Quinonez-Varela, G., G. W. Ault, O. Anaya-Lara, and J. R. McDonald. "Electrical collector system options for large offshore wind farms." *IET Renewable Power Generation* 1, no. 2 , pp. 107-114, 2007.

[36] G. Corbetta, "EWEA: The European offshore wind industry - key trends and statistics 2013," no. January 2014. *Available at:* https://www.ewea.org/.../files/.../statistics/EWEA-European-Offshore-wind farm Statistics-2014.

[37] S. M. Alagab, S. Tennakoon, and C. Gould, "Review of wind farm power collection schemes," *Power Eng. Conf. (UPEC), 50th Int. Universities. pp. 1-5. IEEE.*, vol.–Nov, 2015.

[38] I. M. de Alegría, J. L. Martín, I. Kortabarria, J. Andreu, and P. I. Ereño, "Transmission alternatives for offshore electrical power," *Renew. Sustain. Energy Rev.*, vol. 13, no. 5, pp. 1027–1038, 2009.

[39] Cheng, Ming, and Ying Zhu. "The state of the art of wind energy conversion systems and technologies: A review." *Energy Conversion and Management*, pp. 332-347, 2014.

[40] A. Prof, E. G. Sava, A. Prof, and E. Sorina, "Assessment of collector networks for offshore wind power plants, *Available at: www.agir.ro/buletine/1839.pdf*" no. 3, pp. 225–230, 2013.

[41] P. Lakshmanan, J. Liang, and N. Jenkins, "Assessment of collection systems for HVDC connected offshore wind farms," *Electric Power Systems Research. Res.*, vol. 129, pp. 75–82, December, 2015.

[42] Islam, M. R., S. Mekhilef, and R. Saidur. "Progress and recent trends of wind energy technology." *Renewable and Sustainable Energy Reviews* 21, pp. 456-468, December, 2013.

[43] Xu, Duo, Gang Mu, Hongbo Liu, and Gangui Yan. "Assessment on large-scale offshore wind farm integration." In *Industrial Electronics and Applications (ICIEA), IEEE 9th Conference on*, pp. 556-559, 2014.

[44] R. Perveen, N. Kishor, and S. R. Mohanty, "Off-shore wind farm development: Present status and challenges," *Renew. Sustain. Energy Rev.*, vol. 29, pp. 780–792, 2014.

[45] D. Jovcic and N. Strachan, "Offshore wind farm with centralised power conversion and DC interconnection," *IET Gener. Transm. Distrib.*, vol. 3, no. August 2008, p. 586, 2009.

[46] Bala, J. Pan Sandeep, Magnus C, and Peter Sandeberg. "DC connection of offshore wind power plants without a platform." *In Paper presented at the 13th Wind Integration Workshop*, vol. 11, p. 13. 2014.

[47] W. Chen, A. Q. Huang, C. Li, S. Member, G. Wang, and W. Gu, "Analysis and Comparison of Medium Voltage High Power DC / DC Converters for Offshore Wind Energy Systems," vol. 28, no. 4, pp. 2014–2023, 2014.

[48] M. R. Islam, Y. Guo, and J. Zhu, "A review of offshore wind turbine nacelle: Technical challenges, and research and developmental trends," *Renew. Sustain. Energy Rev.*, vol. 33, pp. 161–176, 2014.

[49] T. Van Nguyen, P. O. Jeannin, E. Vagnon, D. Frey, and J. C. Crebier, "Series connection of IGBTs with self-powering technique and 3-D topology," *IEEE Trans. Ind. Appl.*, vol. 47, no. 4, pp. 1844–1852, 2011.

[50] P. P. W. H. X. Z. J. Z. M. Snook, "IGBT Series Connection under Active Voltage Control with Temporary Clamp," *IECON - 38th Annu. Conf. IEEE Ind. Electron. Soc.*, pp. 465–470, 2012.

[51] M. Rahimo, A. Kopta, R. Schnell, U. Schlapbach, R. Zehringer, and S. Linder, "2.5kV-6.5kV Industry Standard IGBT Modules Setting a New Benchmark in SOA Capability," no. 2, pp. 2–7, 2004.

[52] B. M. Hasaneen and A. a E. Mohammed, "Design and simulation of DC/DC boost converter," *Power Syst. Conf. 2008. MEPCON . 12th Int. Middle-East*, pp. 335–340, December, 2008.

[53] Cuk, Slobodan. "A new zero-ripple switching DC-to-DC converter and integrated magnetics." *IEEE Transactions on Magnetics* 19, no. 2, pp. 57-75, 1983.

[54] F. Ahmad, A. Rasool, E. Ozsoy, A. Sabanovi??, and M. Elit??, "Design of a Robust Cascaded Controller for Cuk Converter," *Proc. - IEEE Int. Power Electron. Motion Control Conf. PEMC*, pp. 80–85, 2016.

[55] L. Approach, "Buck / Boost Converter Control With Fuzzy Logic Approach," *Ind. Electron. Control. Instrumentation, Proc. IECON '93., Int. Conf.*, p. Pages: 1342-1346 vol.2, 1993.

[56] Franquelo, Leopoldo G., Jose Rodriguez, Jose I. Leon, Samir Kouro, Ramon Portillo, and Maria AM Prats. "The age of multilevel converters arrives." *IEEE industrial electronics magazine* 2, no. 2, November, 2008.

[57] A. Parastar, "Multilevel Step-Up DC / DC Converter for MVDC Applications," *30th Power Syst. Conf. (PSC2015), 23-25, Niroo Res. Institute, Tehran, Iran*, no. November, p. Pages: 1342-1346 vol.2, November. 2015.

[58] Meynard, T. A., and Henry Foch. "Multi-level conversion: high voltage choppers and voltage-source inverters." In *Power Electronics Specialists Conference, PESC'92 Record., 23rd Annual IEEE*, pp. 397-403. IEEE, 1992.

[59] Jin, MingGuo, Amir Parastar, and Jul-Ki Seok. "High efficiency multilevel flying-capacitor DC/DC converter for distributed generation applications." In *Energy Conversion Congress and Exposition (ECCE), 2014 IEEE*, pp. 4269-4275. IEEE, 2014.

[60] C. Cheng and L. He, "Flying-Capacitor-Clamped Five-Level Inverter Based on Switched-Capacitor Topology," *IEEE Trans. Ind. Electron.*, vol. 63, no. 12, pp. 7814–7822, 2016.

[61] Parastar, Amir, Ali Gandomkar, and Jul-Ki Seok. "High-efficiency multilevel flying-capacitor DC/DC converter for distributed renewable energy systems." *IEEE Transactions on Industrial Electronics* 62, no. 12, pp. 7620-7630, January, 2015.

[62] L. He, "A Novel Quasi-Resonant Bridge Modular Switched-Capacitor Converter With Enhanced Efficiency and Reduced Output Voltage Ripple," *IEEE Transactions on Power Electronics*. vol. 29, no. 4, pp. 1881–1893, 2014.

[63] Nabae, Akira, Isao Takahashi, and Hirofumi Akagi. "A new neutral-point-

clamped PWM inverter." *IEEE Transactions on industry applications* 5, pp. 518-523, December, 1981.

[64] A. Bendre, G. Venkataramanan, D. Rosene, and V. Srinivasan, "Modeling and design of a neutral-point voltage regulator for a three-level diode-clamped inverter using multiple-carrier modulation," *IEEE Trans. Ind. Electron.*, vol. 53, no. 3, pp. 718–726, 2006.

[65] M. Marchesoni and P. Tenca, "Diode-clamped multilevel converters: A practicable way to balance DC-link voltages," *IEEE Trans. Ind. Electron.*, vol. 49, no. 4, pp. 752–765, 2002.

[66] M. Chaulagain and B. Diong, "Forced redundant states of 5-level single-phase diode-clamped multilevel inverters," *Conf. Proc. - IEEE Southeastcon*, vol. 54–July, 2016.

[67] C. C. Davidson and D. R. Trainer, "Innovative Concepts for Hybrid Multi-Level Converters for HVDC Power Transmission," *9th IET Int. Conf. AC DC Power Transm. (ACDC)*, pp. 1–5, 2010.

[68] G. P. Adam, I. A. Abdelsalam, K. H. Ahmed, and B. W. Williams, "Hybrid multilevel converter with cascaded h-bridge cells for HVDC applications: Operating principle and scalability," *IEEE Trans. Power Electron.*, vol. 30, no. 1, pp. 65–77, 2015.

[69] Ives, Kalle, Luca Bessegato, Lennart Harnefors, Staffan Norrga, and H-P. Nee. "Semi-full-bridge submodule for modular multilevel converters." In *Power Electronics and ECCE Asia (ICPE-ECCE Asia), 9th International Conference on*, pp. 1067-1074. IEEE, 2015.

[70] Lesnicar, Anton, and Rainer Marquardt. "An innovative modular multilevel converter topology suitable for a wide power range." In *Power Tech Conference Proceedings, Bologna*, vol. 3, pp. 6-pp. IEEE, 2003.

[71] Allebrod, Silke, Roman Hamerski, and Rainer Marquardt. "New transformerless, scalable modular multilevel converters for HVDC-transmission." In *Power Electronics Specialists Conference. PESC ,* pp. 174-179. IEEE, 2008.

[72] E. Solas, G. Abad, J. A. Barrena, A. Cárcar, and S. Aurtenetxea, "Modulation of Modular Multilevel Converter for HVDC application," in *Proceedings of EPE-PEMC 14th International Power Electronics and Motion Control Conference*, pp. 84–89, December, 2010.

[73] J. Maneiro, S. Tennakoon, and C. Barker, "Scalable shunt connected HVDC tap using the DC transformer concept," *16th Eur. Conf. Power Electron. Appl. EPE-ECCE Eur. 2014*, pp. 6–8, 2014.

[74] X. Zhang and T. C. Green, "The new family of high step ratio modular multilevel DC-DC converters," *Appl. Power Electron. Conf. Expo.*, vol. 2, pp. 1743–1750, *IEEE* 2015.

[75] G. Kish and P. Lehn, "Modeling Techniques for Dynamic and Steady-State Analysis of Modular Multilevel DC/DC Converters," *IEEE Trans. Power Deliv.*, vol. 1, no. c, pp. 1–1, 2015.

[76] L. Grégoire, S. Member, H. F. Blanchette, and W. Li, "Modular-Multilevel-Converter Dynamic Analysis and Remedial Strategy for Voltage Transients During Blocking," pp. 1–7, 2013.

[77] Parastar, Amir, Yong Cheol Kang, and Jul-Ki Seok. "Multilevel modular DC/DC power converter for high-voltage DC-connected offshore wind energy applications." *IEEE Transactions on Industrial electronics* 62, no. 5, pp. 2879-2890, 2015.

[78] A. Nami, J. Liang, F. Dijkhuizen, and G. D. Demetriades, "Modular multilevel converters for HVDC applications: Review on converter cells and functionalities," *IEEE Trans. Power Electron.*, vol. 30, no. 1, pp. 18–36, 2015.

[79] M. P. Madsen, A. Knott, and M. A. E. Andersen, "Very High Frequency Half-Bridge DC / DC Converter," *Appl. Power Electron. Conf. Expo. (APEC), Twenty-Ninth Annu. IEEE*, pp. 1409–1414, 2014.

[80] Y. Zhou, D. E. Macpherson, W. Blewitt, and D. Jovcic, "Comparison of DC-DC converter topologies for offshore wind-farm application," *6th IET Int. Conf. Power Electron. Mach. Drives PEMD*, pp. A12–A12, 2012.

[81] S. Qiang, Z. Chunming, H. Xiping, and L. Shouzhi, "Application of Sliding Mode Control for Half-Bridge DC / DC Converter," *Int. Conf. E-Product E-Service E-Entertainment*, pp. 1–4, 2010.

[82] P. Range, D. T. Winkler, and S. M. I. Gmbh, "A Method To Achieve ZVS With A DC / DC Half-Bridge Con- verter Working With Constant Frequency In A Wide Output," no. May, pp. 19–21, 2015.

[83] F. Deng, S. Member, Z. Chen, and S. Member, "Control of Improved Full-Bridge Three-Level DC / DC Converter for Wind Turbines in a DC Grid,"

vol. 28, no. 1, pp. 314–324, 2013.

[84] S. Saggini, O. Zambetti, R. Rizzolatti, A. Zafarana, and P. Sacconi, “Isolated resonant full-bridge converter with magnetic integration,” *Conf. Proc. - IEEE Appl. Power Electron. Conf. Expo. - APEC*, pp. 1733–1740, 2017.

[85] M Pahlevani, Majid, Suzan Eren, Alireza Bakhshai, and Praveen Jain. "A series-parallel current-driven full-bridge DC/DC converter." *IEEE Transactions on Power Electronics* 31, no. 2, pp. 1275-1293, 2016.

[86] Lee, Sung-Ho, Chun-Yoon Park, Jung-Min Kwon, and Bong-Hwan Kwon. "Hybrid-type full-bridge DC/DC converter with high efficiency." *IEEE Transactions on Power Electronics* 30, no. 8, pp. 4156-4164, 2015.

[87] Z. Qin, Y. Shen, P. C. Loh, H. Wang, and F. Blaabjerg, “A Dual Active Bridge Converter with an Extended High-Efficiency Range by DC Blocking Capacitor Voltage Control,” *IEEE Trans. Power Electron.*, vol. 8993, no. c, pp. 1–16, 2017.

[88] H. P. System, B. Zhao, S. Member, Q. Song, W. Liu, and Y. Sun, “Overview of Dual-Active-Bridge Isolated Bidirectional DC-DC Converter for,” vol. 29, no. 8, pp. 4091–4106, 2014.

[89] S. P. Engel *et al.*, “Comparison of the Modular Multilevel DC Converter and the Dual-Active Bridge Converter for Power Conversion in HVDC and MVDC Grids,” vol. 30, no. 1, pp. 124–137, 2015.

[90] M. Moonem, C. Pechacek, R. Hernandez, and H. Krishnaswami, “Analysis of a Multilevel Dual Active Bridge (ML-DAB) DC-DC Converter Using Symmetric Modulation,” *Electronics*, vol. 4, no. 2, pp. 239–260, Apr. 2015.

[91] S. P. Engel, M. Stieneker, N. Soltau, S. Rabiee, H. Stagge, and R. W. De Doncker, “Comparison of the modular multilevel DC converter and the dual-active bridge converter for power conversion in HVDC and MVDC grids,” *IEEE Trans. Power Electron.*, vol. 30, no. 1, pp. 124–137, 2015.

[92] Qin, Hengsi, and Jonathan W. Kimball. "Solid-state transformer architecture using AC–AC dual-active-bridge converter." *IEEE Transactions on Industrial Electronics* 60, no. 9, pp. 3720-3730, 2013.

[93] A. Lopez, R. Diez, G. Perilla, and D. Patino, “Analysis and comparison of three topologies of the ladder multilevel DC/DC converter,” *IEEE Trans. Power Electron.*, vol. 27, no. 7, pp. 3119–3127, 2012.

[94] Taghizadeh, H., A. M. Cross, R. Whitehouse, and C. Barker. "Switched capacitor DC-DC converters for HVDC applications", vol. 13, pp. 058-064, 2015.

[95] M. D. Seeman and S. R. Sanders, “Analysis and Optimization of Switched-Capacitor {DC}amp;#x2013;DC Converters,” *IEEE Work. Comput. Power Electron.*, vol. 23, no. 2, pp. 216–224, 2006.

[96] K. Eguchi, S. Hirata, M. Shimoji, and H. Zhu, “Design of a step-up/step-down k (=2,3,...)-Fibonacci DC-DC converter designed by switched-capacitor techniques,” *Proc. - 5th Int. Conf. Intell. Networks Intell. Syst. ICINIS*, pp. 170–173, 2012.

[97] A. Mondzik, Z. Waradzyn, R. Stala, and A. Penczek, “High efficiency switched capacitor voltage doubler with planar core-based resonant choke,” *Proc. - 10th Int. Conf. Compact. Power Electron. Power Eng. CPE-POWERENG*, pp. 402–409, 2016.

[98] Veilleux, Etienne, Boon-Teck Ooi, and Peter W. Lehn. "Marx DC-DC converter for high-power application." *IET Power Electronics* 6, no. 9, pp. 1733-1741, 2013.

[99] Ponniran, Asmarashid, Koji Orikawa, and Jun-ichi Itoh. "Modular multi-stage Marx topology for high boost ratio DC/DC converter in HVDC." In *Telecommunications Energy Conference (INTELEC), IEEE International*, pp. 1-6. IEEE, 2015.

[100] S. M. Alagab, S. B. Tennakoon, and C. A. Gould, “A Compact DC-DC Converter for Offshore Wind Farm Application,” *Renew. Energy Power Qual. J.*, vol. 1, no. 15, pp. 529–533, 2017.

[101] ABB Switzerland Ltd., “Surge currents for IGBT diodes, Application Note 5SYA 2058-02,” 2014.

[102] Veilleux, Etienne. "DC Power Flow Controller and Marx DC-DC Converter for Multiterminal HVDC System." PhD dissertation., McGill University Libraries, 2013.

[103] E. Veilleux and B. T. Ooi, “Marx DC-DC converter for connecting offshore wind farms to multiterminal HVDC,” *IEEE Power Energy Soc. Gen. Meet.*, pp. 1–5, 2013.

[104] S. M. Alagab, S. B. Tennakoon, and C. A. Gould, “High Voltage Cascaded Step-Up DC-DC Marx Converter for Offshore Wind Energy Systems,” *EPE*

*2017 - assigned jointly to Eur. Power Electron. Drives Assoc. Inst. Electr. Electron. Eng.*, no. Mmc, pp. 1–10, 2017.

[105] Alagab, Samir M., S. B. Tennakoon, and C. A. Gould. "A novel bidirectional DC-DC converter for offshore DC collection grid." In *20th European Conference on Power Electronics and Applications (EPE'18 ECCE Europe)*, pp. P-1. IEEE, 2018.

[106] M. Von Hofen, D. Karwatzki, L. Baruschka, and A. Mertens, "Hybrid offshore HVDC converter with diode rectifier and Modular Multilevel Converter," *IEEE 7th Int. Symp. Power Electron. Distrib. Gener. Syst. PEDG*, 2016.

[107] M. H. Johnson, D. C. Aliprantis, and H. Chen, "Offshore wind farm with DC collection system," *IEEE Power Energy Conf. Illinois, (PECI)*, pp. 53–59, 2013.

[108] Y. Lian and S. J. Finney, "DC collection networks for offshore generation," *Wind Energy CDT, United Kingdom 2nd IET Renew. Power Gener. Conf. (RPG 2013), United Kingdom*, pp. 3–6, 2012.

[109] E. Pierri, O. Binder, N. G. A. Hemdan, and M. Kurrat, "Challenges and opportunities for a European HVDC grid," *Renew. Sustain. Energy Rev.*, vol. 70, pp. 427–456, 2017.

[110] Beddard, A., and M. Barnes. "HVDC cable modelling for VSC-HVDC applications." In *PES General Meeting| Conference & Exposition*, pp. 1-5. IEEE, 2014.

[111] "XLPE Submarine Cable Systems Attachment to XLPE Land Cable Systems - User ´ s Guide," *Curr. Available new.abb.com/docs/default-source/ewea.../xlpe-submarine-cable-systems-2gm5007.pdf*.

[112] ABB High Voltage Cable Unit, "XLPE Land Cable Systems - User's Guide," p. 28, 2010.

[113] F. Badrkhani Ajaei and R. Iravani, "Cable Surge Arrester Operation Due to Transient Overvoltages under DC-Side Faults in the MMC-HVDC Link," *IEEE Trans. Power Deliv.*, vol. 31, no. 3, pp. 1213–1222, 2016.

[114] M. Nasr, S. Poshtkouhi, N. Radimov, C. Cojocaru, and O. Trescases, "Fast Average Current Mode Control of Dual-Active-Bridge DC-DC Converter using Cycle-by-Cycle Sensing and Self-Calibrated Digital Feedforward," pp. 1129–1133, 2017.

[115] C. Booth, "A review of control methods for providing frequency response in VSC-HVDC transmission systems," *49th Int. Univ. Power Eng. Conf,* December, 2014.

[116] J. Peralta, H. Saad, S. Dennetiere, and J. Mahseredjian, "Dynamic performance of average-value models for multi-terminal VSC-HVDC systems," *IEEE Power Energy Soc. Gen. Meet.*, pp. 1–8, 2012.

[117] A. G. Endegnanew, S. D'Arco, R. E. Torres-Olguin, J. I. Marvik, and E. Tedeschi, "Collation of European grid codes," *Mar. Rep.*, pp. 1–39, 2013.

[118] Guo, H., K. Rudion, and Z. A. Styczynski. "Integration of large offshore wind farms into the power system." In *Science and Technology, EPU-CRIS International Conference on*, pp. 1-6. *IEEE*, September, 2011.

# Appendix A

## Derivations of Equations for the Single-Stage and Multi-Stage Converters

## A.1 A single Stage and Multi-Stage Converter Deriving Equations

In the first half cycle [$t_0 \le t \le t_1$]

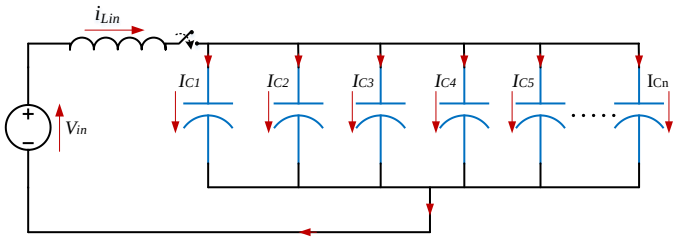


Figure A. 1: Charging capacitors in parallel

As shown in Figure A. 1, the charging capacitor in parallel, and the equivalent capacitance in parallel as:

$$C_{eq(P)} = C_1 + C_2 + C_3 + C_4 + C_5 \ldots + C_n \tag{A.17}$$

And

$$C_{eq(P)} = \sum_{i=1}^{n} C_i \tag{A.18}$$

The general differential equation is

$$V_{in} = \left[ L_{in} \frac{di}{dt} + \left( \frac{i}{C_{eq(P)}} \int_0^t i(t)di \right) \right] \tag{A.19}$$

Then,

$$0 = L_{in} \frac{d^2 i}{dt^2} + \frac{i(t)}{C_{eq\,(P)}} \tag{A.20}$$

$$0 = \frac{d^2 i}{dt^2} + \frac{i(t)}{L_{in} C_{eq\,(P)}} \tag{A.21}$$

The resonant frequency can be calculated as:

$$\omega^2 = \frac{1}{L_{in} C_{eq\,(P)}} \tag{A.22}$$

Compensation equation (A-6) in (A-5)

$$0 = \frac{d^2 i}{dt^2} + \omega^2 \, i(t) \tag{A.23}$$

Solving *i(t)* can be obtained as:

$$i_{Lin}(t) = \frac{V_{in}}{\omega L_{in}} \sin \omega t \tag{A.24}$$

Hence;

$$i_{Lin}(t) = \frac{0.5\Delta V_C}{\omega L_{in}} \sin \omega t \tag{A.25}$$

$$i_{Lin} = \frac{0.5\Delta V_C \, \omega \, L_{in} C}{L_{in}} \sin \omega t \tag{A.26}$$

The current equation of inductor $L_1$ for $(t_0 \leq t \leq t_1)$ is given as

$$i_{Lin} = 0.5 \, C_{eq(P)} \, \omega \, \Delta V_C \sin \omega t \tag{A.27}$$

Substituting $L_{in}$ by $C_{eq}$ and $\omega$, and replacing $V_{in}$ by $0.5\Delta V_c$, where $\Delta V_c$ is the peak to peak capacitor voltage. However, the inductor current can be expressed as:

$$i_{Lin} = \frac{0.5\Delta V_C \, \omega \, L_{in} C_{eq(P)}}{L_{in}} \sin \omega t \tag{A.28}$$

$$i_{Lin}(t) = 0.5\Delta V_C \, C_{eq(P)} \sin \omega t \tag{A.29}$$

The voltage crosses a capacitor can be expressed as:

$$V_C = V_{in} - L \frac{di}{dt} \tag{A-30}$$

$$V_C = V_{in} - L \frac{diL}{dt} \tag{A.31}$$

Substituting for $i_{Lin}$ from equation (A.11) into equation (A.14) and rearranging $V_C$ can be expressed as;

$$V_C = V_{in} - L \frac{di}{dt} \left[ \frac{1}{2} C_{eq(P)} \, \omega \Delta V_C \sin \omega (t - t_0) \right] \tag{A.32}$$

And

$$= V_{in} - \left(0.5\ \omega L\, C_{eq(P)}\, \omega \Delta V_C\, cos\, \omega t\right) \quad \text{(A.33)}$$

$$= V_{in} - \left[0.5\ \left(C_{eq(P)}\, \omega^2\, L\right) \Delta V_C\, cos\, \omega t\right] \quad \text{(A.34)}$$

Then,

$$V_C = V_{in} - 0.5\, \Delta V_C\, cos\, \omega t \quad \text{(A.35)}$$

In the second half cycle: [t0 ≤ t ≤ t2]

As shown in Figure A.2, the discharging capacitor in series, and the equivalent capacitance in series as:

$$\frac{1}{C_{eq(S)}} = \frac{1}{C_1} + \frac{1}{C_2} + \frac{1}{C_3} + \frac{1}{C_4} + \frac{1}{C_5} \ldots + \frac{1}{C_n} \quad \text{(A.36)}$$

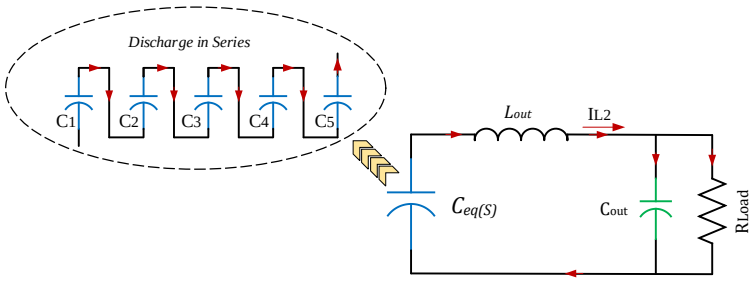


Figure A. 2: Discharging capacitors in series

$$V_{Ceq(s)} = V_{Lout} + V_{Cout} \quad \text{(A.37)}$$

The amount of charge can be calculated as

$$Q = I_{AV} T_S,\ Q = C\, V_C,\ I = \frac{Q}{T} \quad \text{(A.38)}$$

And,

$$i(t) = \frac{dq}{dt} = C \frac{dvc}{dt}\ , \quad \text{(A.39)}$$

From Figure A.2, the inductor current can be given as

$$I_{Lout} = I_{Cout} + I_{Rload} \tag{A.40}$$

$$I_{Lout} = C_{\text{out}} \frac{dv}{dt} + \frac{V_R}{R_{Load}} \tag{A.41}$$

And

$$V_{Ceq} = L_{\text{out}} \frac{di_{Lout}}{dt} + V_R \tag{A.42}$$

Substituting Equation (A.24) into Equation (A.25),

$$V_{Ceq} = L_{\text{out}} \frac{d}{dt}\left[ C_{\text{out}} \frac{dv}{dt} + \frac{V_R}{R_{Load}} \right] + V_R \tag{A.43}$$

$$V_{Ceq}(t) = L_{\text{out}} C_{out} \frac{d^2}{dt^2}(vt) + \frac{L_{\text{out}}}{R_{Load}} \frac{d}{dt}(vt) \tag{A.44}$$

$$V_{Ceq}(t) = L_{\text{out}} C_{out} \frac{d^2 v(t)}{dt^2} + \frac{1}{C_{out} R_{Load}} \frac{d(vt)}{dt} + (vt) \tag{A.45}$$

Assuming no losses within the converters, it can be shown that

$$Q = \frac{P_{rated}}{n V_{in} F_S} \tag{A.46}$$

By using the amount of charge $Q$ and the selected voltage ripple, the capacitance is calculated by using;

$$\Delta V_C = \frac{Q}{C_{eq}} \tag{A.47}$$

Substituting for $Q$ from equation (29) to equation (30) and rearranging;

$$C_{eq} = \frac{P_{rated}}{n V_{in} \Delta V_C F_S} \tag{A.48}$$

The resonant frequency can be calculated as;

$$\omega = \frac{1}{\sqrt{L_{in} C_{eq}}} \tag{A.49}$$

From Equation (29) and Equation (32), the inductor $L_{in}$ can be expressed as

$$\frac{P_{rated}}{Q\,nV_{in}} = \frac{1}{2\pi\sqrt{L_{in}C_{eq}}} \tag{A.50}$$

and

$$L_{in} = \frac{1}{C_{eq}}\left[\frac{Q\,nV_{in}}{2\pi\,P_{rated}}\right]^2 \tag{A.51}$$

In order to ensure soft switching the resonant frequency in the second half-cycle must be made equal to $\omega$. Hence,

$$\omega_2 = \frac{1}{\sqrt{L_{out}(C_{eq} + C_{out})}} \tag{A.52}$$

The switching frequency can be written as;

$$F_S = \frac{1}{2\pi\sqrt{L_{out}C_{eq}}} \tag{A.53}$$

Substituting for $F_S$ from equation (31) into equation (35) and rearranging $L_{out}$ can be expressed as;

$$L_{out} = \frac{1}{(C_{eq} + C_{out})}\left[\frac{Q\,nV_{in}}{2\pi\,P_{rated}}\right]^2 \tag{A.54}$$

As shown in Fig. 2, the total equivalent capacitance of both output capacitor and equivalent capacitance in series can be calculated as;

$$C_{eq} = \frac{(3C_{eq})(C_{out}/2)}{(3C_{eq} + C_{out}/2)} \tag{A.55}$$

Using Equation (29), (30) and (36), the output capacitor value can be calculated using the expression:

$$C_{out} = \frac{(P_{rated}/V_{out})(T_S/2)}{2\pi\,\Delta V_{Cout}} \tag{A.56}$$

## A.2 Calculation of Converter Parameters

For the simulations, the load on the HV side of the DC-DC converter is modelled by the resistor $R_{load}$ where

Resistive load: $$R_{Load} = \frac{V_{out}^2}{P_{rate}}$$

$$= \frac{(30000)^2}{50*10^6} = 18\ \Omega$$

Input voltage = 6 KV, then the output voltage:

$$V_{out} = nV_{input}$$

$$= 5 * 6 = 30\ KV$$

The amount of charge $$Q_{load} = \frac{V_{out}}{R_{Load}} * T_S$$

$$= \frac{30000}{18} * 0.005 = 8.334C$$

The amount of charge (other equation)

$$Q_{load} = \frac{P_{rate}}{MV_{input}} * T_S$$

$$= \frac{50*10^6}{30000} * 0.005 = 8.334C$$

Capacitors $C_n$ $$C_{eq(P)} = \frac{Q_{Load}}{\Delta VC_n}$$

$$= \left(\frac{8.334}{12000}\right)$$

$$C_{eq(P)} = 3472.5\ \mu F$$

$$C_n = \frac{3472.5\ \mu F}{5} = 694.5\ \mu F$$

Capacitors $C_{out}$ $$C_{out} = \frac{(P_{rated}/V_{out})(T_S/2)}{2\pi \Delta V_{Cout}}$$

$$= \left(\frac{\left(50*\frac{10^6}{30}*(30*10^3)\right)(0.005)/2}{2*3.14*4*10^3}\right) = 115\mu F$$

Inductor $L_{in}$ is the same as $L_1$ in the multi-stage converter

$$L_{in} = \frac{1}{C_{eq(P)}} \left( \frac{Q_{Load}\, nV_{in}}{2\pi\, P_{rate}} \right)$$

$$= \frac{1}{3472.5/5} \left( \frac{(30*10^3)*8.334}{2\pi(50*10^6)} \right)$$

$$= 2.53\mu H$$

Inductor $L_{out}$

$$L_{out} = \frac{1}{\left(C_{eq(S)} + C_{out}\right)} \left[ \frac{Q n V_{in}}{2\pi P_{rated}} \right]^2$$

$$= 110\ \mu H$$

Inductors $L_2$, $L_3$ of the multi-stage converter

$$L_2 = \left( \frac{2K^n}{C_{eq(K)}} \right) \left( \frac{C_J}{J^n} \right)^2 = 40\ \mu H$$

$$L_3 = \left( \frac{2L^n}{C_{eq(L)}} \right) \left( \frac{C_K}{K^n} \right)^2 = 400\ \mu H$$

Capacitors $C_J$, $C_K$ and $C_L$ as

$$C_{eq(J)} = \frac{P_{rated}}{N V_{in}\, \Delta V_{C(J)}\, F_S} = 3492.5\ \mu F$$

$$C_K = \frac{C_J}{J + K + L} = 99.21\ \mu F$$

$$C_L = \frac{C_K}{J + K + L} = 14.17\ \mu F$$

# Appendix B

- IGBT Data Sheet
- Fast Recovery Diode

$V_{CE}$ = 4500 V
$I_C$ = 1200 A

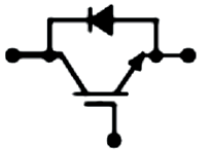

# ABB HiPak

## IGBT Module

# 5SNA 1200G450300

Doc. No. 5SYA 1401-05 03-2016

- Ultra low-loss, rugged SPT⁺ chip-set
- Smooth switching SPT⁺ chip-set for good EMC
- Industry standard package
- High power density
- AlSiC base-plate for high power cycling capability
- AlN substrate for low thermal resistance
- Improved high reliability package
- Recognized under UL1557, File E196689

**Maximum rated values** [1]

| Parameter | Symbol | Conditions | min | max | Unit |
|---|---|---|---|---|---|
| Collector-emitter voltage | $V_{CES}$ | $V_{GE}$ = 0 V | | 4500 | V |
| DC collector current | $I_C$ | $T_c$ = 85 °C | | 1200 | A |
| Peak collector current | $I_{CM}$ | $t_p$ = 1 ms, $T_c$ = 85 °C | | 2400 | A |
| Gate-emitter voltage | $V_{GES}$ | | -20 | 20 | V |
| Total power dissipation | $P_{tot}$ | $T_c$ = 25 °C, per switch (IGBT) | | 10500 | W |
| DC forward current | $I_F$ | | | 1200 | A |
| Peak forward current | $I_{FRM}$ | | | 2400 | A |
| Surge current | $I_{FSM}$ | $V_R$ = 0 V, $T_j$ = 125 °C,<br>$t_p$ = 10 ms, half-sinewave | | 9000 | A |
| IGBT short circuit SOA | $t_{psc}$ | $V_{CC}$ = 3400 V, $V_{CSM CHIP} \leq$ 4500 V<br>$V_{GE} \leq$ 15 V, $T_j \leq$ 125 °C | | 10 | µs |
| Isolation voltage | $V_{isol}$ | 1 min, f = 50 Hz | | 7400 | V |
| Junction temperature | $T_j$ | | | 150 | °C |
| Junction operating temperature | $T_{j(op)}$ | | -50 | 125 | °C |
| Case temperature | $T_c$ | | -50 | 125 | °C |
| Storage temperature | $T_{stg}$ | | -50 | 125 | °C |
| Mounting torques [2] | $M_s$ | Base-heatsink, M6 screws | 4 | 6 | Nm |
| | $M_{t1}$ | Main terminals, M8 screws | 8 | 10 | |
| | $M_{t2}$ | Auxiliary terminals, M4 screws | 2 | 3 | |

[1] Maximum rated values indicate limits beyond which damage to the device may occur per IEC 60747
[2] For detailed mounting instructions refer to ABB Document No. 5SYA2039

**ABB Switzerland Ltd, Semiconductors reserves the right to change specifications without notice.**

## IGBT characteristic values [a]

| Parameter | Symbol | Conditions | | min | typ | max | Unit |
|---|---|---|---|---|---|---|---|
| Collector (-emitter) breakdown voltage | $V_{(BR)CES}$ | $V_{GE}$ = 0 V, $I_C$ = 10 mA, $T_{vj}$ = 25 °C | | 4500 | | | V |
| Collector-emitter [c] saturation voltage | $V_{CE\ sat}$ | $I_C$ = 1200 A, $V_{GE}$ = 15 V | $T_{vj}$ = 25 °C | | 2.6 | 2.9 | V |
| | | | $T_{vj}$ = 125 °C | | 3.55 | 3.9 | V |
| Collector cut-off current | $I_{CES}$ | $V_{CE}$ = 4500 V, $V_{GE}$ = 0 V | $T_{vj}$ = 25 °C | | | 12 | mA |
| | | | $T_{vj}$ = 125 °C | | | 120 | mA |
| Gate leakage current | $I_{GES}$ | $V_{CE}$ = 0 V, $V_{GE}$ = ±20 V, $T_{vj}$ = 125 °C | | -500 | | 500 | nA |
| Gate-emitter threshold voltage | $V_{GE(TO)}$ | $I_C$ = 240 mA, $V_{CE}$ = $V_{GE}$, $T_{vj}$ = 25 °C | | 4.5 | | 6.5 | V |
| Gate charge | $Q_{GE}$ | $I_C$ = 1200 A, $V_{CE}$ = 2800 V, $V_{GE}$ = -15 V .. 15 V | | | 8.86 | | µC |
| Input capacitance | $C_{ies}$ | $V_{CE}$ = 25 V, $V_{GE}$ = 0 V, f = 1 MHz, $T_{vj}$ = 25 °C | | | 120 | | nF |
| Output capacitance | $C_{oes}$ | | | | 6.02 | | |
| Reverse transfer capacitance | $C_{res}$ | | | | 2.58 | | |
| Internal gate resistance | $R_{Gint}$ | | | | 1.2 | | Ω |
| Turn-on delay time | $t_{d(on)}$ | $V_{CC}$ = 2800 V, $I_C$ = 1200 A, $R_G$ = 1.5 Ω, $C_{GE}$ = 220 nF, $V_{GE}$ = ±15 V, $L_\sigma$ = 150 nH, inductive load | $T_{vj}$ = 25 °C | | 740 | | ns |
| | | | $T_{vj}$ = 125 °C | | 750 | | |
| Rise time | $t_r$ | | $T_{vj}$ = 25 °C | | 210 | | ns |
| | | | $T_{vj}$ = 125 °C | | 230 | | |
| Turn-off delay time | $t_{d(off)}$ | $V_{CC}$ = 2800 V, $I_C$ = 1200 A, $R_G$ = 1.5 Ω, $C_{GE}$ = 220 nF, $V_{GE}$ = ±15 V, $L_\sigma$ = 150 nH, inductive load | $T_{vj}$ = 25 °C | | 2260 | | ns |
| | | | $T_{vj}$ = 125 °C | | 2470 | | |
| Fall time | $t_f$ | | $T_{vj}$ = 25 °C | | 600 | | ns |
| | | | $T_{vj}$ = 125 °C | | 660 | | |
| Turn-on switching energy | $E_{on}$ | $V_{CC}$ = 2800 V, $I_C$ = 1200 A, $R_G$ = 1.5 Ω, $C_{GE}$ = 220 nF, $V_{GE}$ = ±15 V, $L_\sigma$ = 150 nH, inductive load | $T_{vj}$ = 25 °C | | 3080 | | mJ |
| | | | $T_{vj}$ = 125 °C | | 4350 | | |
| Turn-off switching energy | $E_{off}$ | $V_{CC}$ = 2800 V, $I_C$ = 1200 A, $R_G$ = 1.5 Ω, $C_{GE}$ = 220 nF, $V_{GE}$ = ±15 V, $L_\sigma$ = 150 nH, inductive load | $T_{vj}$ = 25 °C | | 4960 | | mJ |
| | | | $T_{vj}$ = 125 °C | | 6000 | | |
| Short circuit current | $I_{SC}$ | $t_{psc}$ ≤ 10 µs, $V_{GE}$ = 15 V, $T_{vj}$ = 125 °C, $V_{CC}$ = 3400 V, $V_{CEM\ CHIP}$ ≤ 4500 V | | | 5200 | | A |
| Module stray inductance | $L_{\sigma CE}$ | | | | 18 | | nH |
| Resistance, terminal-chip | $R_{CC'+EE'}$ | | $T_C$ = 25 °C | | 0.07 | | mΩ |
| | | | $T_C$ = 125 °C | | 0.1 | | |

[a] Characteristic values according to IEC 60747 – 9
[c] Collector-emitter saturation voltage is given at chip level

**Electrical configuration**

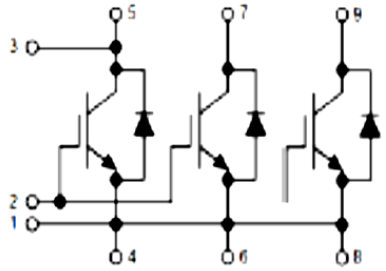


**Outline drawing** [a]

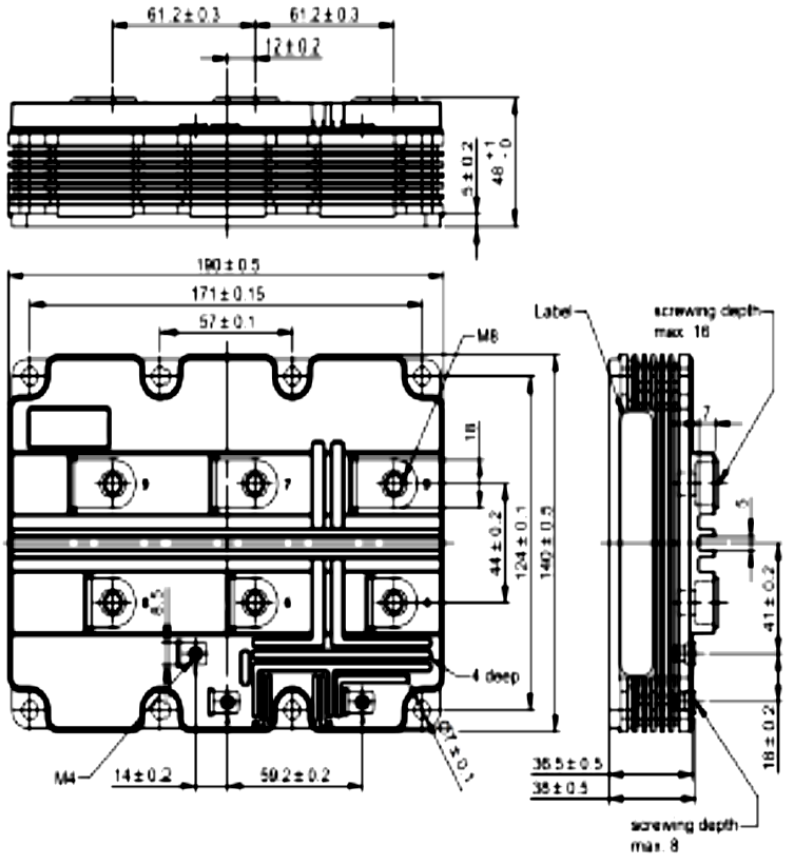


**Note: all dimensions are shown in mm**

[a] For detailed mounting instructions refer to ABB Document No. 5SYA2039

**This is an electrostatic sensitive device, please observe the international standard IEC 60747-1, chap. IX.**

**This product has been designed and qualified for Industrial Level.**

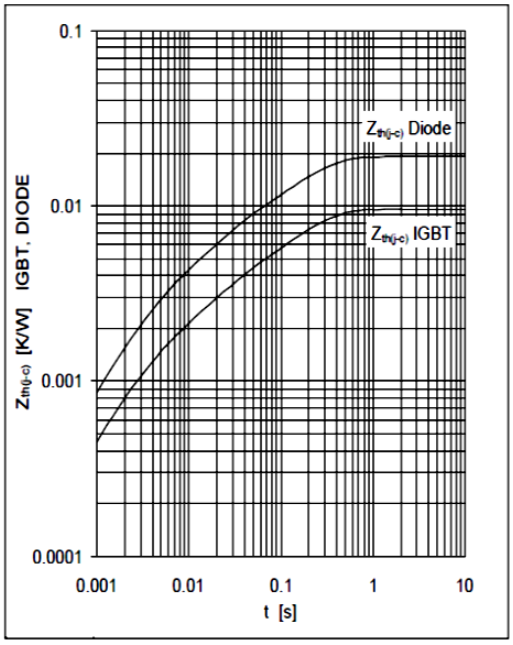


**Fig. 16** Thermal impedance vs time

**Analytical function for transient thermal impedance:**

$$Z_{th\,(j\text{-}c)}(t) = \sum_{i=1}^{n} R_i\,(1 - e^{-t/\tau_i})$$

| | i | 1 | 2 | 3 | 4 | 5 |
|---|---|---|---|---|---|---|
| IGBT | $R_i$(K/kW) | 6.36 | 2.11 | 1.04 | | |
| | $\tau_i$(ms) | 193 | 21.4 | 2.78 | | |
| DIODE | $R_i$(K/kW) | 12.5 | 4.37 | 2.16 | | |
| | $\tau_i$(ms) | 192 | 22.6 | 3.1 | | |

**Related documents:**

5SYA 2042 Failure rates of HiPak modules due to cosmic rays
5SYA 2043 Load - cycle capability of HiPaks
5SYA 2045 Thermal runaway during blocking
5SYA 2053 Applying IGBT
5SYA 2058 Surge currents for IGBT diodes
5SYA 2093 Thermal design of IGBT modules
5SYA 2098 Paralleling of IGBT modules
5SZK 9111 Specification of environmental class for HiPak Storage
5SZK 9112 Specification of environmental class for HiPak Transportation
5SZK 9113 Specification of environmental class for HiPak Operation (Industry)
5SZK 9120 Specification of environmental class for HiPak



**ABB Switzerland Ltd**
**Semiconductors**
Fabrikstrasse 3
CH-5600 Lenzburg, Switzerland

Telephone +41 (0)58 586 1419
Fax +41 (0)58 586 1306
Email abbsem@ch.abb.com
Internet www.abb.com/semiconductors

Doc. No. 5SYA 1401-05 03-2016

| | | |
|---|---|---|
| $V_{RRM}$ | = | 6000 V |
| $I_{F(AV)M}$ | = | 1100 A |
| $I_{FSM}$ | = | $18 \times 10^3$ A |
| $V_{(T0)}$ | = | 1.5 V |
| $r_T$ | = | 0.6 mΩ |
| $V_{DC\text{-}link}$ | = | 3800 V |

# Fast Recovery Diode

# 5SDF 10H6004

Doc. No. 5SYA1109-03 Jan. 10

- **Patented free-floating silicon technology**
- **Low on-state and switching losses**
- **Optimized for use as freewheeling diode in high-voltage GTO converters**
- **Industry standard housing**
- **Cosmic radiation withstand rating**

## Blocking

***Maximum rated values*** [1)]

| Parameter | Symbol | Conditions | Value | Unit |
|---|---|---|---|---|
| Repetitive peak reverse voltage | $V_{RRM}$ | f = 50 Hz, $t_p$ = 10ms, $T_{vj}$ = 125°C | 6000 | V |
| Permanent DC voltage for 100 FIT failure rate | $V_{DC\text{-}link}$ | Ambient cosmic radiation at sea level in open air. (100% Duty) | 3800 | V |

***Characteristic values***

| Parameter | Symbol | Conditions | min | typ | max | Unit |
|---|---|---|---|---|---|---|
| Repetitive peak reverse current | $I_{RRM}$ | $V_R = V_{RRM}$, $T_{vj}$ = 125°C | | | 50 | mA |

## Mechanical data

***Maximum rated values*** [1)]

| Parameter | Symbol | Conditions | min | typ | max | Unit |
|---|---|---|---|---|---|---|
| Mounting force | $F_m$ | | 36 | 40 | 44 | kN |
| Acceleration | a | Device unclamped | | | 50 | $m/s^2$ |
| Acceleration | a | Device clamped | | | 200 | $m/s^2$ |

***Characteristic values***

| Parameter | Symbol | Conditions | min | typ | max | Unit |
|---|---|---|---|---|---|---|
| Weight | m | | | | 0.83 | kg |
| Housing thickness | H | | 26.2 | | 26.6 | mm |
| Surface creepage distance | $D_S$ | | 30 | | | mm |
| Air strike distance | $D_a$ | | 20 | | | mm |

Note 1 Maximum rated values indicate limits beyond which damage to the device may occur

## On-state

***Maximum rated values*** [1)]

| Parameter | Symbol | Conditions | min | typ | max | Unit |
|---|---|---|---|---|---|---|
| Max. average on-state current | $I_{F(AV)M}$ | Half sine wave, $T_C$ = 85 °C | | | 1100 | A |
| Max. RMS on-state current | $I_{F(RMS)}$ | | | | 1700 | A |
| Max. peak non-repetitive surge current | $I_{FSM}$ | $t_p$ = 10 ms, $T_{vj}$ = 125°C, $V_R$ = 0 V | | | $18\times10^3$ | A |
| Limiting load integral | $I^2t$ | | | | $1.62\times10^6$ | $A^2s$ |
| Max. peak non-repetitive surge current | $I_{FSM}$ | $t_p$ = 1 ms, $T_{vj}$ = 125°C, $V_R$ = 0 V | | | $44\times10^3$ | A |
| Limiting load integral | $I^2t$ | | | | $968\times10^3$ | $A^2s$ |

***Characteristic values***

| Parameter | Symbol | Conditions | min | typ | max | Unit |
|---|---|---|---|---|---|---|
| On-state voltage | $V_F$ | $I_F$ = 2500 A, $T_{vj}$ = 125°C | | | 3 | V |
| Threshold voltage | $V_{(T0)}$ | $T_{vj}$ = 125°C<br>$I_F$ = 200...6000 A | | | 1.5 | V |
| Slope resistance | $r_T$ | | | | 0.6 | mΩ |

## Turn-on

***Characteristic values***

| Parameter | Symbol | Conditions | min | typ | max | Unit |
|---|---|---|---|---|---|---|
| Peak forward recovery voltage | $V_{FRM}$ | $dI_F/dt$ = 500 A/µs, $T_{vj}$ = 125°C | | | 150 | V |

## Turn-off

***Characteristic values***

| Parameter | Symbol | Conditions | min | typ | max | Unit |
|---|---|---|---|---|---|---|
| Reverse recovery current | $I_{RM}$ | di/dt = 300 A/µs, $I_{FQ}$ = 1000 A, | | | 1000 | A |
| Reverse recovery charge | $Q_{rr}$ | $T_j$ = 125°C, $V_{RM}$ = 2900 V, | | | 6000 | µC |
| Turn-off energy | $E_{rr}$ | $C_S$ = 3 µF (GTO snubber circuit) | | | 5 | J |

## Thermal

***Maximum rated values*** [1]

| Parameter | Symbol | Conditions | min | typ | max | Unit |
|---|---|---|---|---|---|---|
| Operating junction temperature range | $T_{vj}$ | | -40 | | 125 | °C |
| Storage temperature range | $T_{stg}$ | | -40 | | 125 | °C |

***Characteristic values***

| Parameter | Symbol | Conditions | min | typ | max | Unit |
|---|---|---|---|---|---|---|
| Thermal resistance junction to case | $R_{th(j-c)}$ | Double-side cooled<br>$F_m$ = 36...44 kN | | | 12 | K/kW |
| | $R_{th(j-c)A}$ | Anode-side cooled<br>$F_m$ = 36...44 kN | | | 24 | K/kW |
| | $R_{th(j-c)C}$ | Cathode-side cooled<br>$F_m$ = 36...44 kN | | | 24 | K/kW |
| Thermal resistance case to heatsink | $R_{th(c-h)}$ | Double-side cooled<br>$F_m$ = 36...44 kN | | | 3 | K/kW |
| | $R_{th(c-h)}$ | Single-side cooled<br>$F_m$ = 36...44 kN | | | 6 | K/kW |

**Analytical function for transient thermal impedance:**

$$Z_{th(j-c)}(t) = \sum_{i=1}^{n} R_{th\,i}\left(1 - e^{-t/\tau_i}\right)$$

| i | 1 | 2 | 3 | 4 |
|---|---|---|---|---|
| $R_{th\,i}$ (K/kW) | 7.440 | 2.000 | 1.840 | 0.710 |
| $\tau_i$ (s) | 0.4700 | 0.0910 | 0.0100 | 0.0047 |

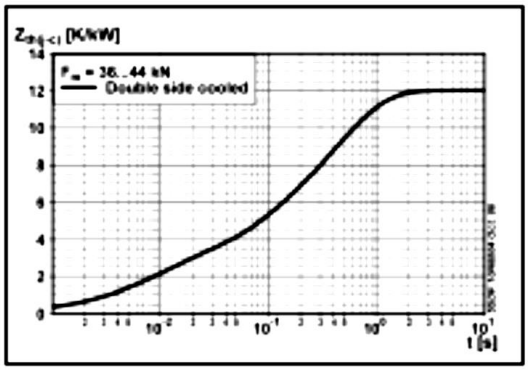


**Fig. 1** Transient thermal impedance junction-to-case

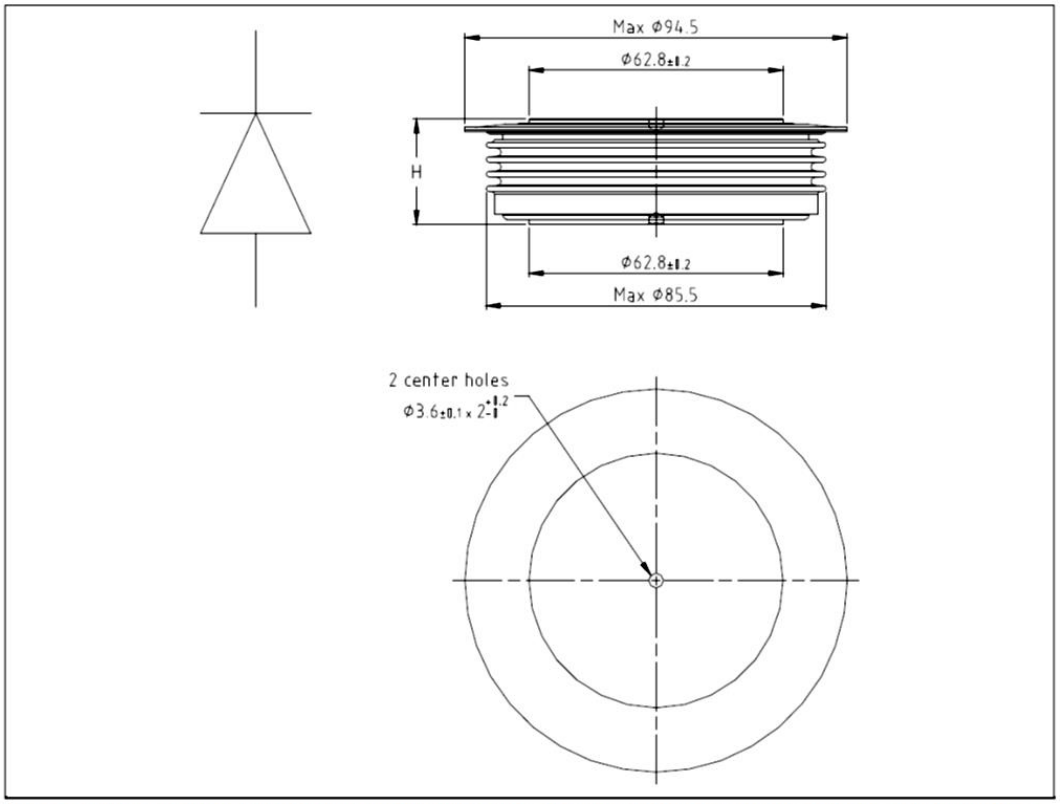


**Fig. 7** Outline drawing, all dimensions are in millimeters and represent nominal values unless stated otherwise

## Related documents:

| Doc. Nr | Titel |
|---|---|
| 5SYA 2036 | Recommendations regarding mechanical clamping of Press Pack High Power Semiconductors |
| 5SZK 9104 | Specification of environmental class for pressure contact diodes, PCTs and GTO, STORAGE available on request, please contact factory |
| 5SZK 9105 | Specification of environmental class for pressure contact diodes, PCTs and GTO, TRANSPORTATION available on request, please contact factory |

Please refer to http://www.abb.com/semiconductors for current version of documents.



**ABB Switzerland Ltd**
**Semiconductors**
Fabrikstrasse 3
CH-5600 Lenzburg, Switzerland

Telephone +41 (0)58 586 1419
Fax +41 (0)58 586 1306
Email abbsem@ch.abb.com
Internet www.abb.com/semiconductors

Doc. No. 5SYA1109-03 Jan. 10

# Appendix C

## Details of Matlab/Simulink Simulation Models

- A single-stage converter circuit
- Multi-stage converter circuit
- Bidirectional converter circuit
- System parameters in Matlab functions

---

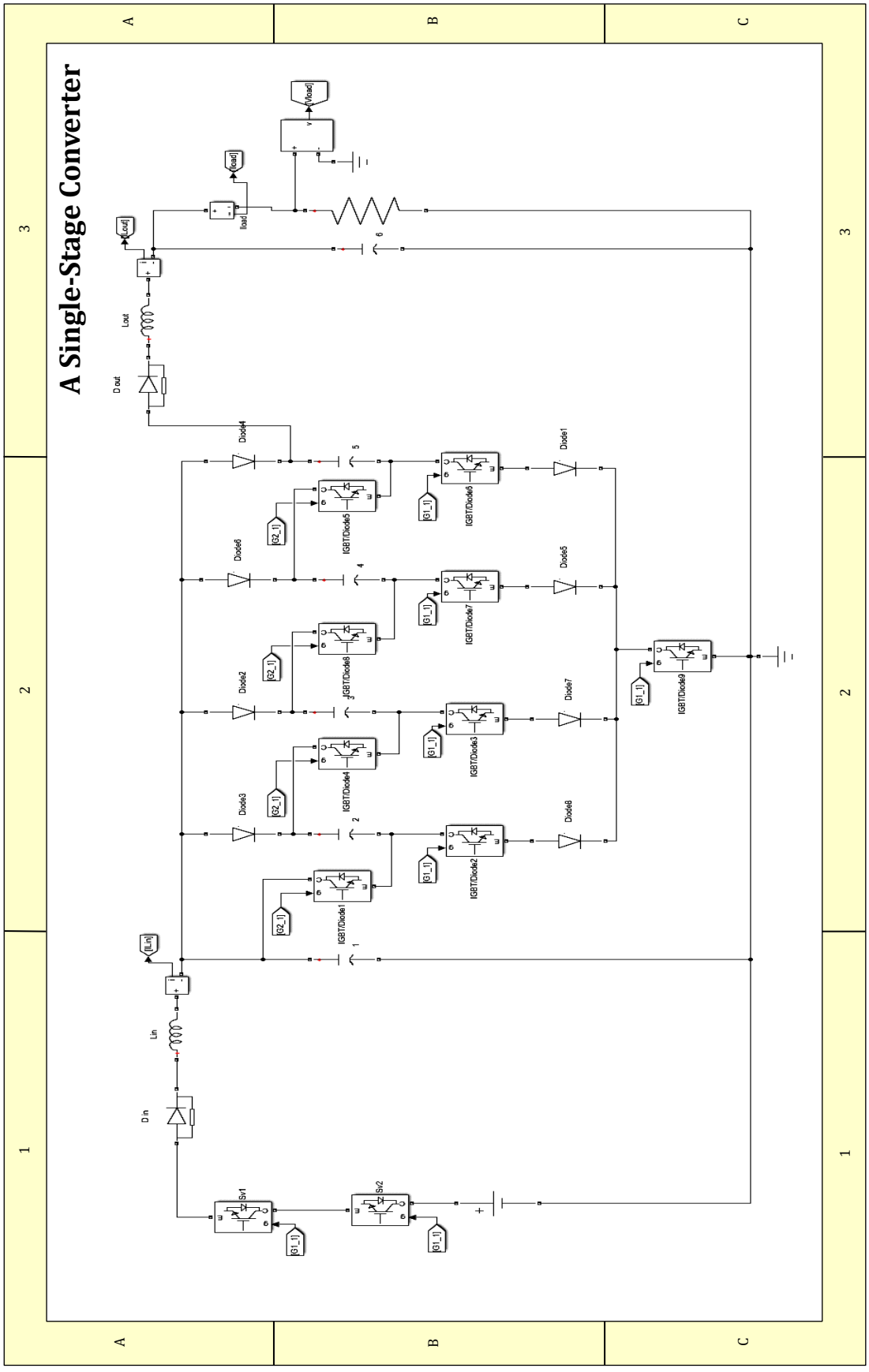
A Single-Stage Converter
A
B
C
1
2
3
Vload
Iload
Iout
Lout
D out
Diode4
Diode6
Diode2
Diode3
Diode1
Diode5
Diode7
Diode8
IGBTDiode5
IGBTDiode7
IGBTDiode8
IGBTDiode4
IGBTDiode1
IGBTDiode3
IGBTDiode2
IGBTDiode9
G2_1
G1_1
Iin
Lin
D in
Sv1
Sv2

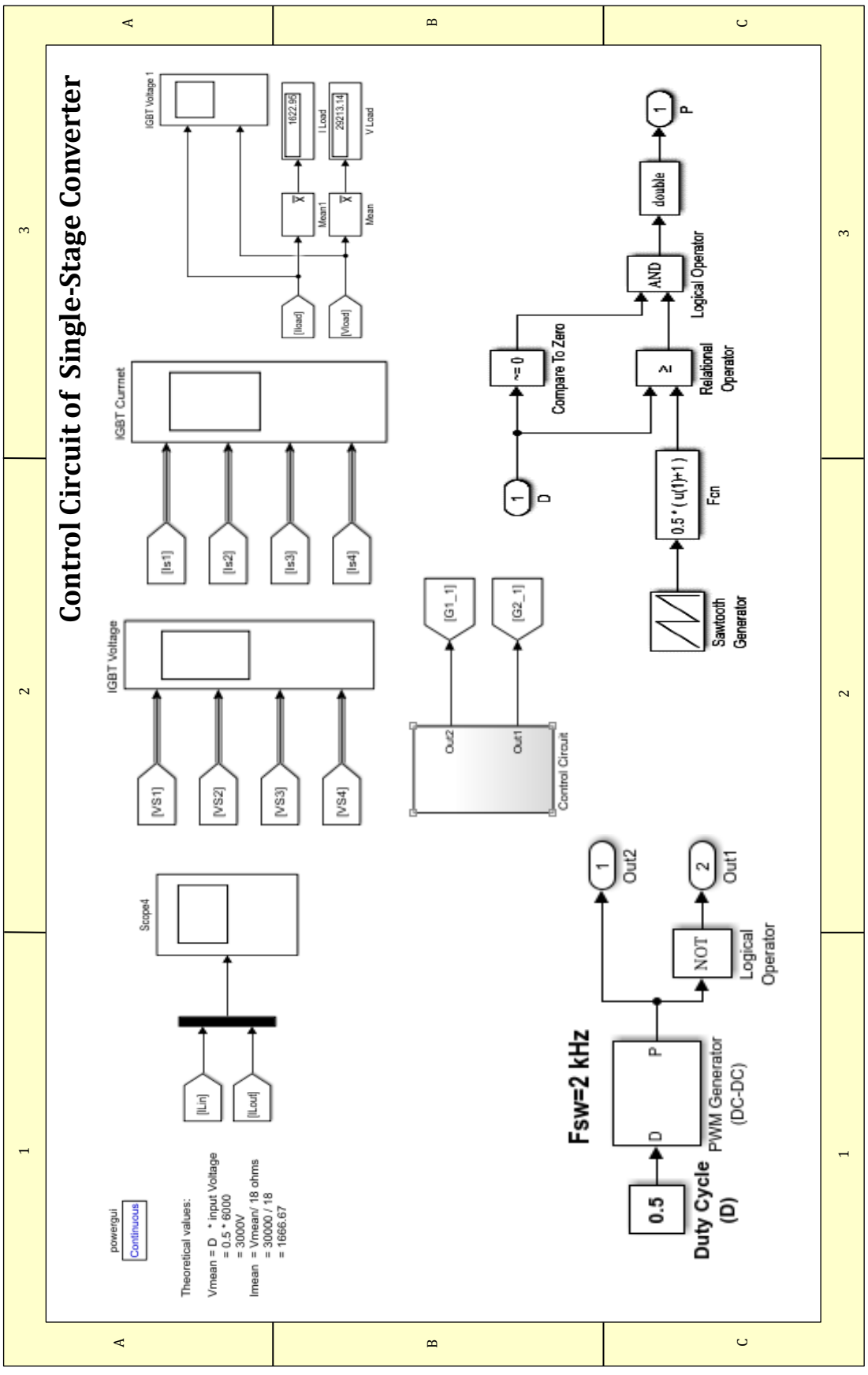
Control Circuit of Single-Stage Converter
IGBT Voltage 1
1822.95
I Load
29213.14
V Load
Mean1
Mean
[Iload]
[Vload]
IGBT Current
[Is1]
[Is2]
[Is3]
[Is4]
IGBT Voltage
[VS1]
[VS2]
[VS3]
[VS4]
[G1_1]
[G2_1]
Out2
Out1
Control Circuit
~= 0
Compare To Zero
D
AND
Logical Operator
double
P
≥
Relational Operator
0.5 * ( u(1)+1 )
Fcn
Sawtooth Generator
Scope4
[ILin]
[ILout]
powergui
Continuous
Theoretical values:
Vmean = D * input Voltage
= 0.5 * 6000
= 3000V
Imean = Vmean/ 18 ohms
= 30000 / 18
= 1666.67
Fsw=2 kHz
0.5
Duty Cycle (D)
D
P
PWM Generator (DC-DC)
NOT
Logical Operator
Out2
Out1

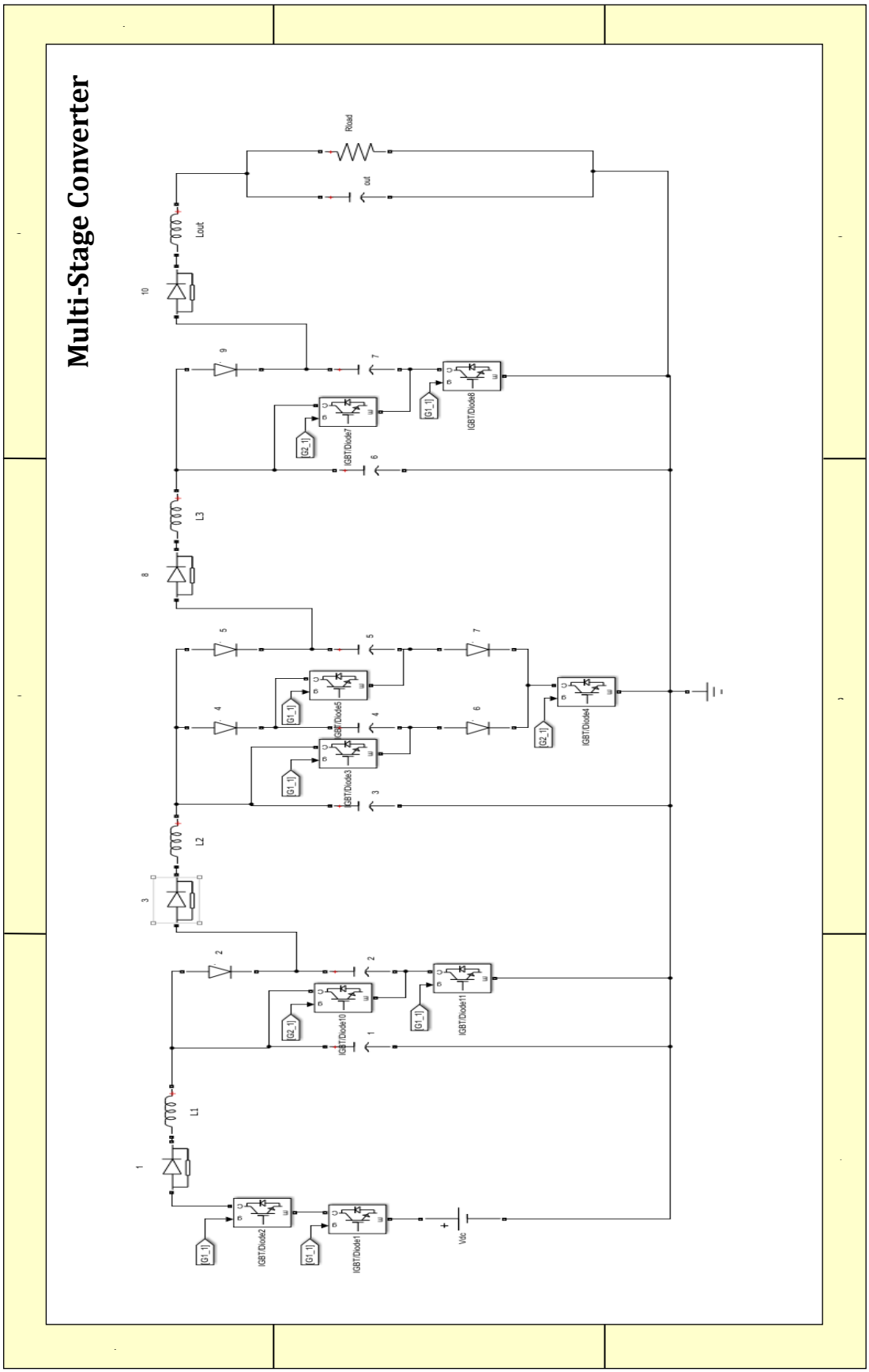
Multi-Stage Converter
Rload
out
Lout
L3
L2
L1
Vdc
IGBT/Diode1
IGBT/Diode2
IGBT/Diode3
IGBT/Diode4
IGBT/Diode5
IGBT/Diode6
IGBT/Diode7
IGBT/Diode10
IGBT/Diode11
G1_1
G2_1

**Bidirectional Modular Converter**

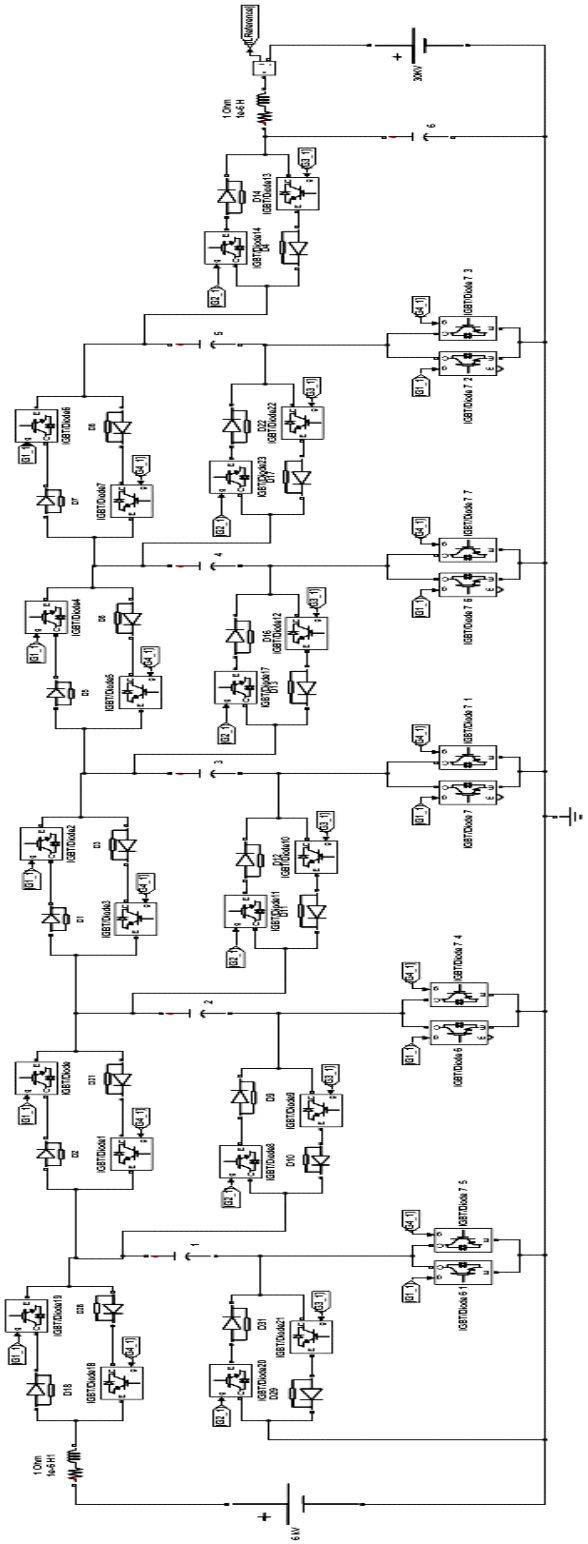

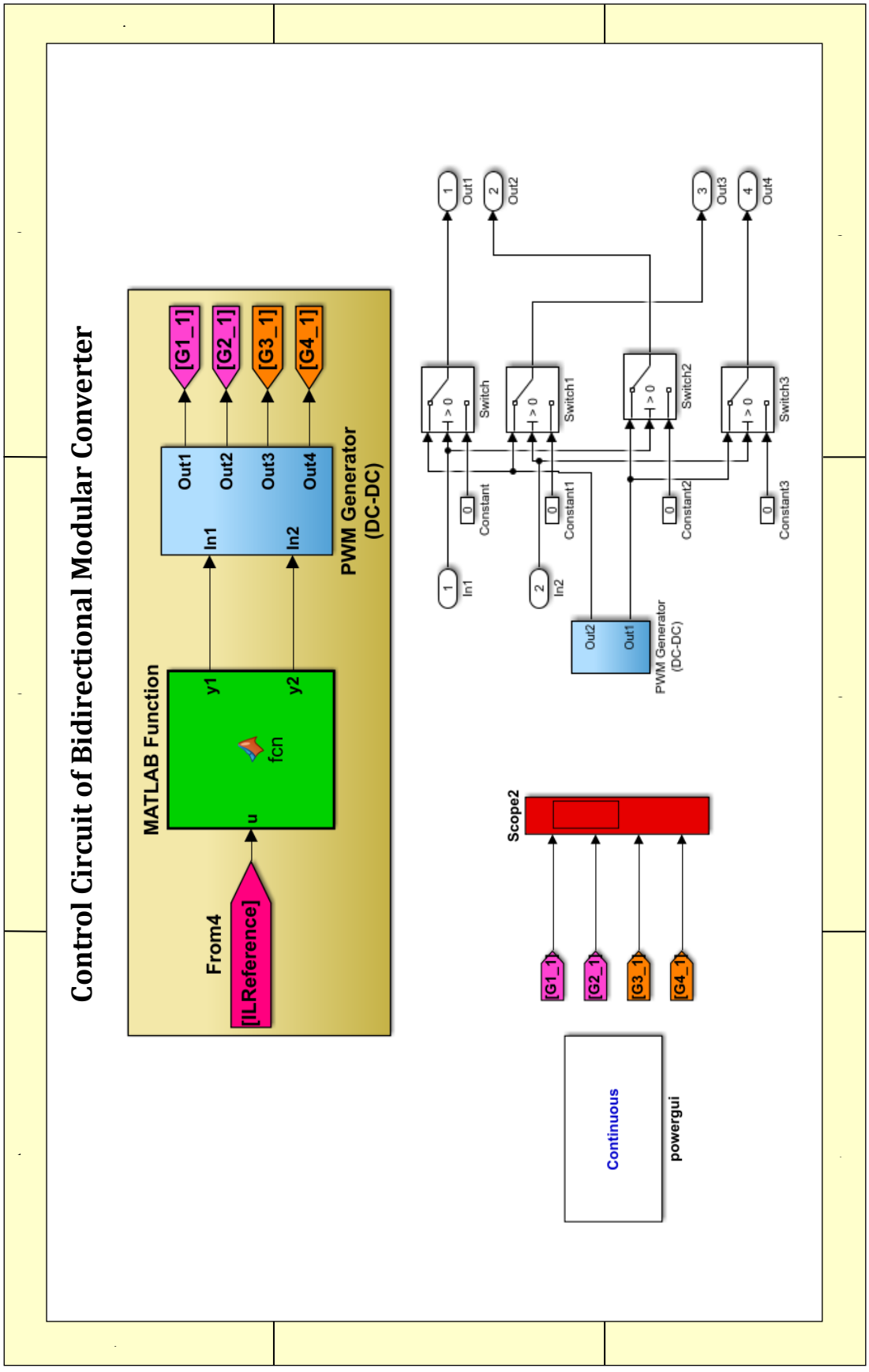
Control Circuit of Bidirectional Modular Converter
PWM Generator (DC-DC)
Out1
Out2
Out3
Out4
In1
In2
[G1_1]
[G2_1]
[G3_1]
[G4_1]
MATLAB Function
y1
y2
u
fcn
From4
[ILReference]
Switch
Switch1
Switch2
Switch3
Constant
Constant1
Constant2
Constant3
In1
In2
Out1
Out2
Out3
Out4
PWM Generator (DC-DC)
Scope2
Continuous
powergui

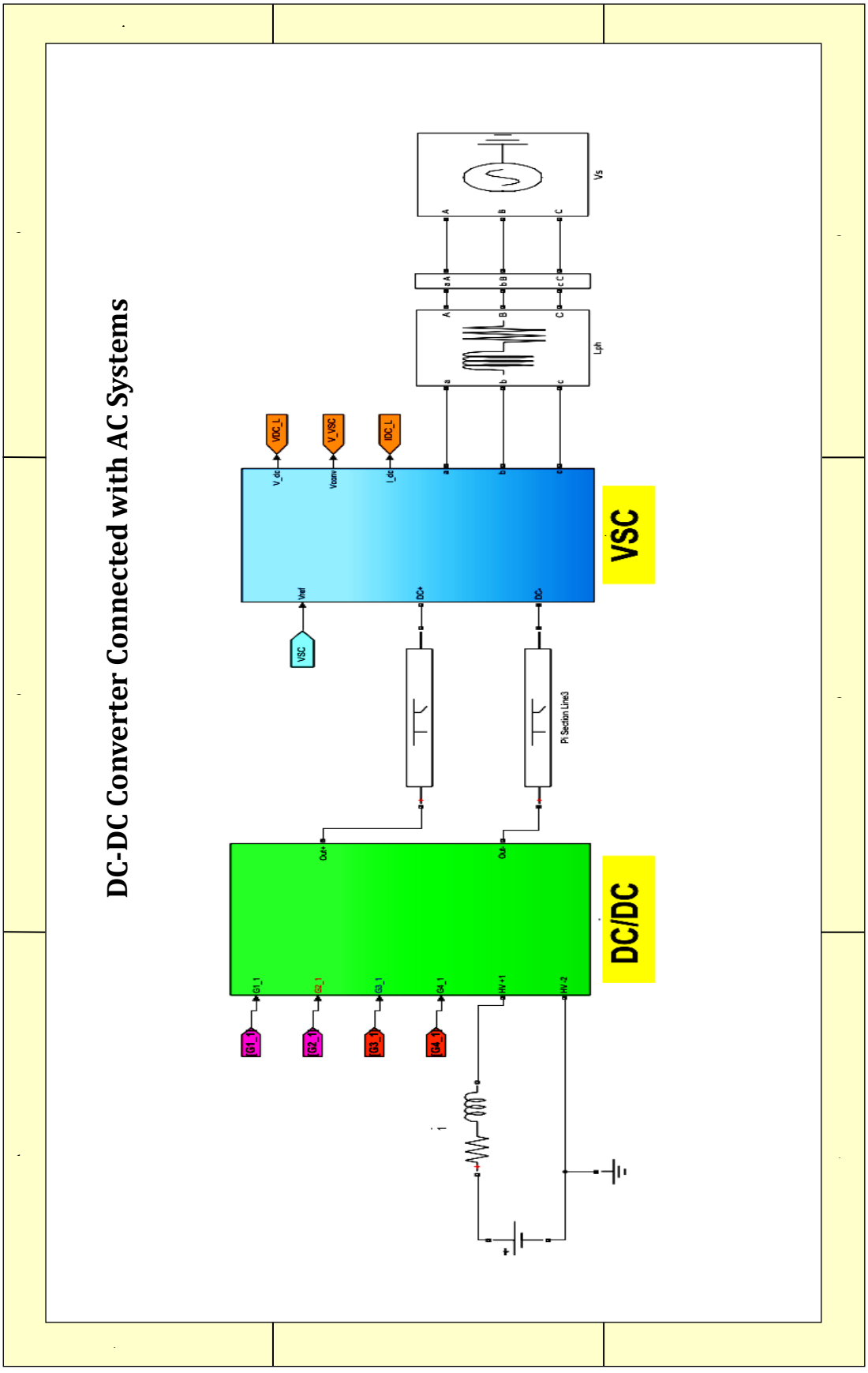
DC-DC Converter Connected with AC Systems
Vs
Lph
VDC_L
V_VSC
IDC_L
V_dc
Vconv
I_dc
VSC
Vref
IDC+
IDC-
Pi Section Line3
Out+
Out-
DC/DC
G1_1
G2_1
G3_1
G4_1
HV +1
HV -2
G1_1
G2_1
G3_1
G4_1

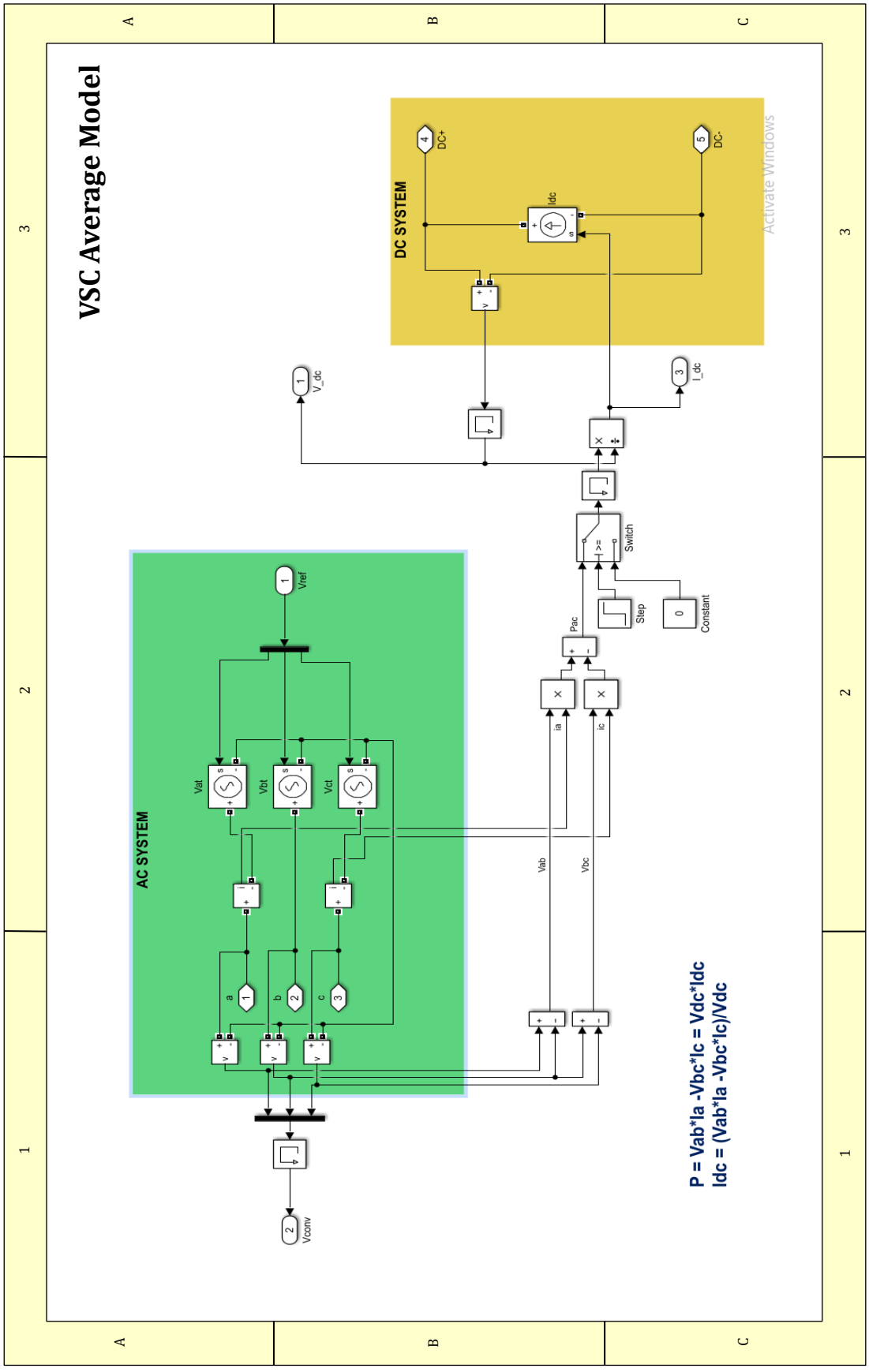
VSC Average Model
DC SYSTEM
DC+
DC-
Idc
V_dc
I_dc
Switch
Step
Constant
Pac
ia
ic
Vab
Vbc
AC SYSTEM
Vref
Vat
Vbt
Vct
a
b
c
Vconv
P = Vab*Ia -Vbc*Ic = Vdc*Idc
Idc = (Vab*Ia -Vbc*Ic)/Vdc
Activate Windows

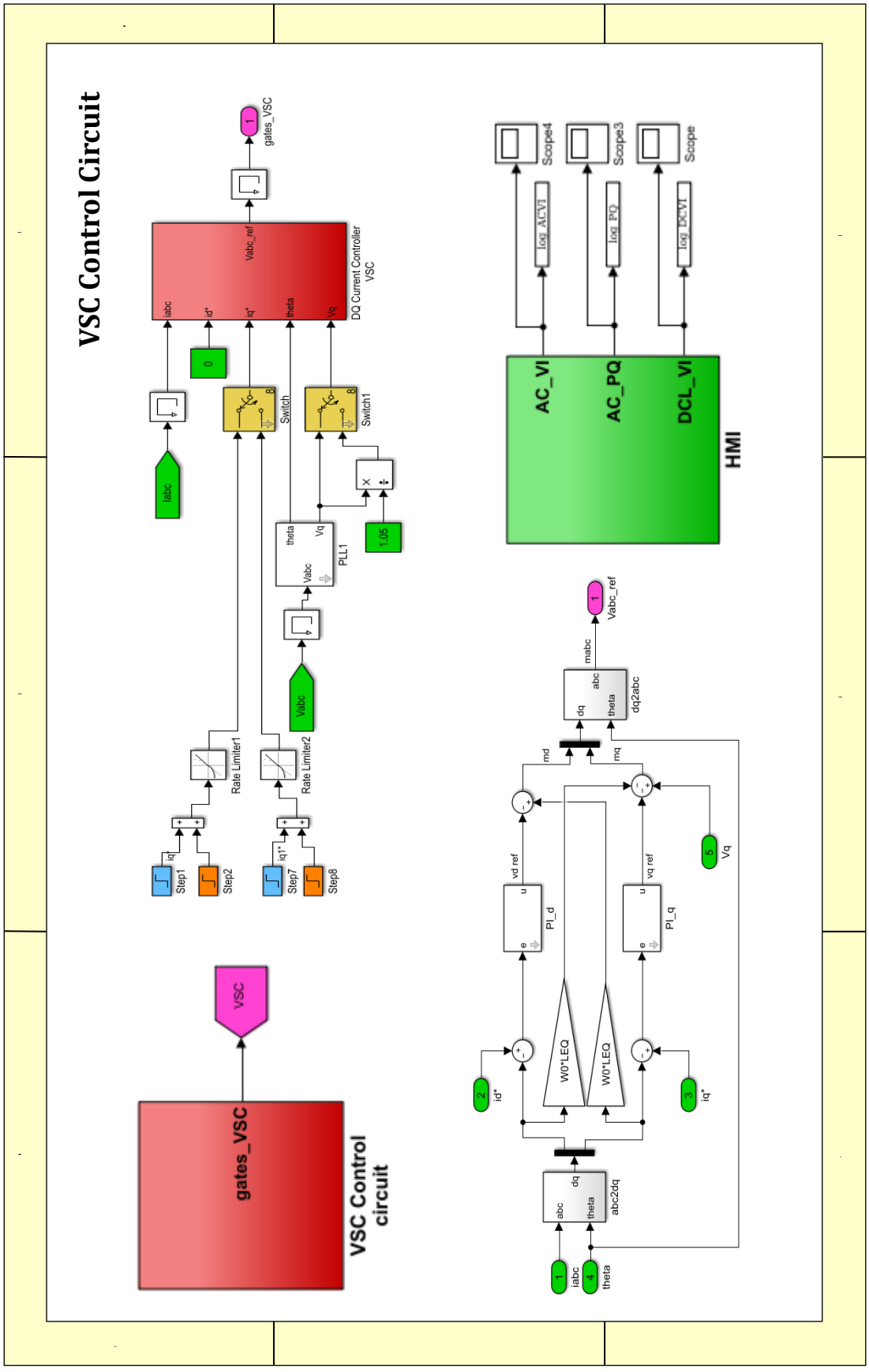
VSC Control Circuit
gates_VSC
DQ Current Controller VSC
Switch
Switch1
PLL1
Rate Limiter1
Rate Limiter2
Step1
Step2
Step7
Step8
Scope4
Scope3
Scope
log_ACVI
log_PQ
log_DCVI
AC_VI
AC_PQ
DCL_VI
HMI
dq2abc
abc2dq
PI_d
PI_q
W0*LEQ
W0*LEQ
Vq
VSC Control circuit

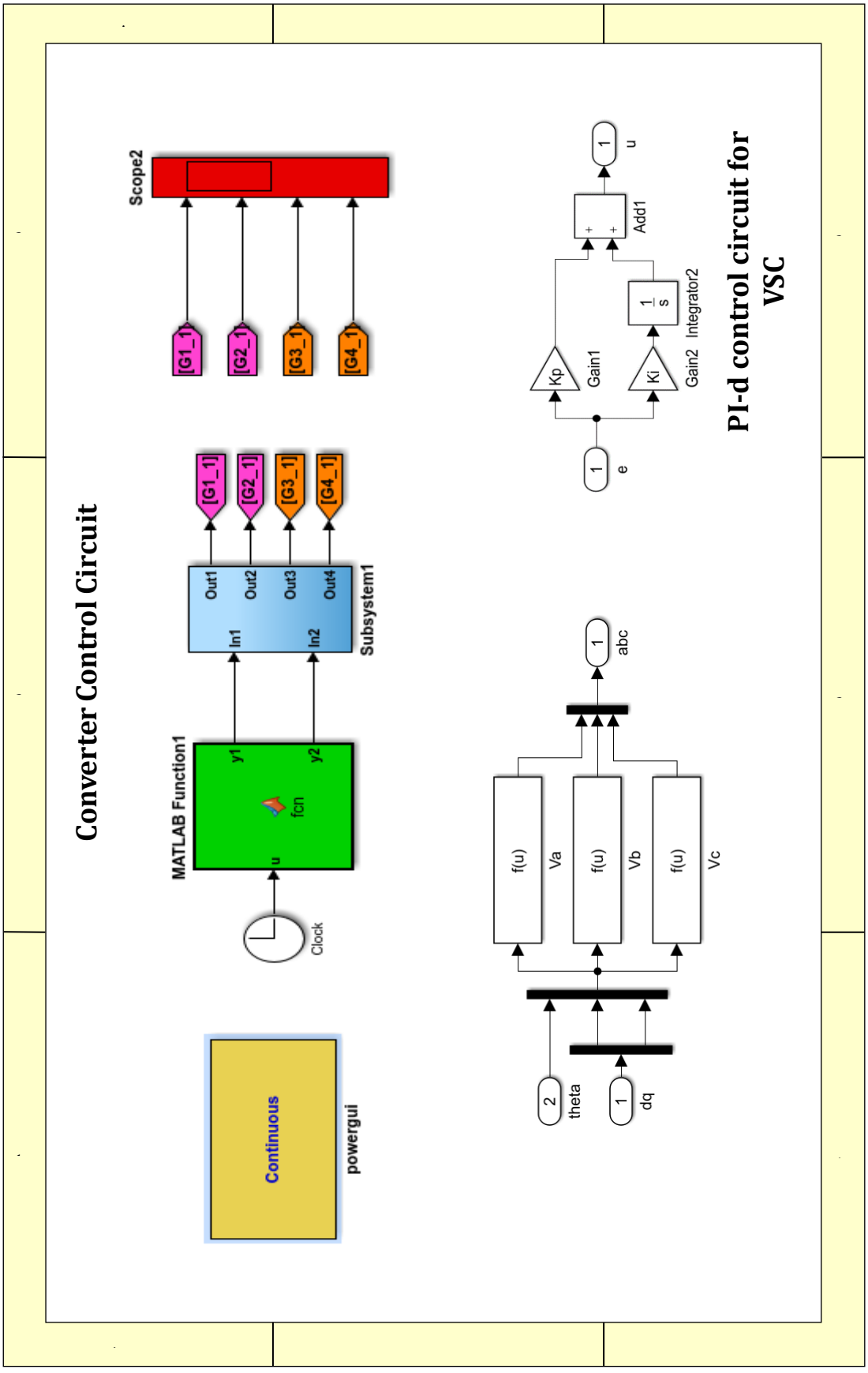
Converter Control Circuit
Scope2
[G1_1]
[G2_1]
[G3_1]
[G4_1]
Out1
Out2
Out3
Out4
In1
In2
Subsystem1
MATLAB Function1
y1
y2
fcn
u
Clock
Continuous
powergui
PI-d control circuit for VSC
1
u
Add1
Kp
Gain1
Ki
Gain2
1/s
Integrator2
1
e
1
abc
f(u)
Va
f(u)
Vb
f(u)
Vc
2
theta
1
dq

# System model parameters in MATLAB functions

```
%-------------------------------------
       AC PARAMETERS
%-------------------------------------
F0=50; % Nominal system frequency (Hz)
W0=F0*2*pi;
VAC=25000;
VDC=6000;
LEQ=25e-4;
REQ=150e-6;
Pn=49e6;
PN=4.5e6;
%-------------------------------------
%       VSC PARAMETERS
%-------------------------------------
Iq_ref=-Pn/1.5/(sqrt(2)/sqrt(3)*VAC);
Rs=0.00123;
Iq_ref1=PN/1.5/(sqrt(2)/sqrt(3)*VAC);
Ls=0.0000001337e-9;
psi_pll=0.7;
Tpll=2*psi_pll/W0;
Cs=0.0000001e-12;
Kpll=2*psi_pll*W0/VAC/sqrt(2);
Ti=0.001;
KPI1=LEQ/Ti;
KII1=REQ/Ti;

%-------------------------------------
%       HV DC CABLE PARAMETERS
%-------------------------------------
R=11e-3;
L=2.615e-3;
C=0.198e-6;
Le=116;
Ps=8;

%-------------------------------------
%       DC-DC CONVERTER PARAMETERS
%-------------------------------------
RL=0.01e-3;
LL=2.53e-6;
CL=83e-6;
Cn=496.5e-6;
LH=110e-6;
CH=116e-6;
Ts=5e-3;
Fs=2e3;
%-------------------------------------
```

```
Function [y1,y2] = fcn(u)
if (u>0 && u <=0.4)
    y1=1;
    y2=0;
elseif (u>0.4 && u<=0.55)
    y2=1;
    y1=0;
else
    y1=0;
    y2=0;
end;
end

Function y1  = fcn(u)
if (u>0.15 && u <=0.35)
    y1=1;
elseif (u>0.35 && u<=0.4)
    y1=0;
else
    y1=0;
end;
end
```

# Appendix D

## Selected Publications

The Journal of Engineering

The 9th International Conference on Power Electronics, Machines and Drives (PEMD 2018)

IET Journals
The Institution of Engineering and Technology

# Bidirectional marx DC–DC converter for offshore wind farm application

eISSN 2051-3305
Received on 25th June 2018
Accepted on 31st July 2018
E-First on 14th May 2019
doi: 10.1049/joe.2018.8222
www.ietdl.org

Samir Milad Alagab[1] ✉, Sarath Tennakoon[1], Chris Gould[1]
[1]School of Creative Arts and Engineering, Staffordshire University, Stoke on Trent, United Kingdom
✉ E-mail: Samir.alagab@research.staffs.ac.uk

**Abstract:** The bidirectional DC–DC converter explained here is based on the Marx principle and is capable of achieving step-up and step-down voltage transformations at kV level and is able to handle MW-level power transfers in both directions. The main features of this topology are the absence of a high-frequency transformer, reduced weight, volume, and soft switching to reduce the switching losses. In the boost mode, five capacitors are charged in parallel and discharged in series to achieve the step-up action, and in the buck mode, the converse action takes place. The operating principle is explained, and the steady-state analysis of the converter is given. Matlab/Simulink simulation of a 50 MW converter, interfacing 6 kV, and 30 kV systems supports and validates the theoretical analysis, enables positive supporting the conclusions to be made.

## 1 Introduction

A high-voltage direct current (HVDC) grid is a natural extension of the grid integration of large offshore wind farms using voltage source converter (VSC)-based HVDC systems. Such systems would require the interconnection of sections operating at different DC-voltage levels through DC–DC converters [1]. The power flow through the DC–DC converter needs to be in both directions. During normal generation, the power flow is from the wind farm to the grid. However, when the wind farm is not generating, the auxiliaries in the wind farm require a small amount of power which must be drawn from the grid. Therefore, the DC–DC converter needs to be bidirectional.

This paper is organised as follows: in Section 2, a number of bidirectional DC–DC converter topologies found in literature are explained. A new bidirectional converter and its steady-state analysis is presented in Sections 3 and 4, respectively. In Section 5, a simulation study in the forward and reverse mode has been presented. Finally, conclusions are drawn in Section 6.

## 2 Bidirectional DC–DC converter topologies

Dual active bridge (DAB) converter [2–5] shown in Fig. 1*a* typically operates at a high switching frequency in order to reduce the size of the transformer. Although these topologies use soft switching to reduce switching losses, their magnetic core losses are still high and have high ripple currents and large leakage inductances. These converters also require complex control.

Thomas [5] has presented three types of DAB converter, which require complex control. Xing [6] presented a modular bidirectional buck/boost DC/DC converter for HVDC grid as illustrated in Fig. 1*b*. It uses small sub-module capacitors when compared to the modular multilevel converter, which will significantly reduce the converter volume and weight, but the drawback of this converter is the variable duty cycle and large inductance.

In Fig. 1*c*, Pires [7] presented a bi-directional buck/boost converter for electrochemical storage devices. The voltage ratio of this converter is high, but has a variable duty cycle in both forward and reverse operation. The switching frequency is high, leading to high switching losses and hence is impractical in high power converters.

Dragan [8] proposed a high-power DC converter without a transformer which uses thyristors as switching devices as shown in Fig. 1*d*. It can transfer the power in both directions and has an ability to isolate faults. However, the Dragan's converter has eight inductors and requires several switches in series to withstand the high voltage.

LCL bidirectional DC–DC converter [9, 10] shown in Fig. 1*e* uses IGBTs unlike the Dragan converter [8]. The advantage of this converter is the ability to achieve current regulation, even under extreme external DC faults and soft switching to reduce the switching losses. The disadvantage of this converter is the large size of inductor requires to reduce the current ripple and requires series connection of devices. In addition, Kolparambath presented

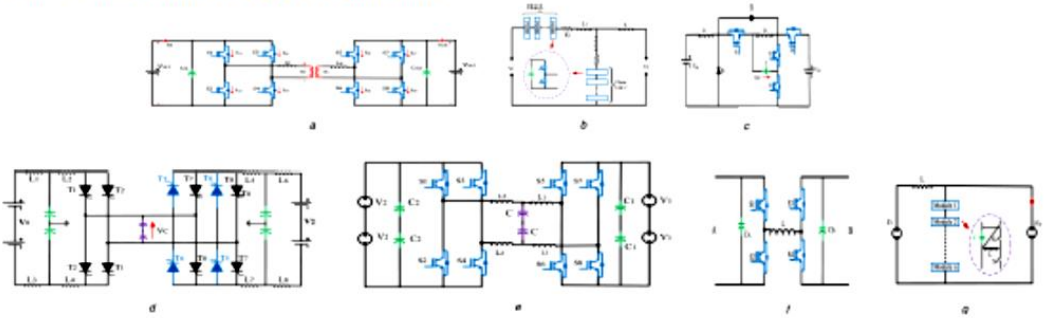

**Fig. 1** *Common bidirectional DC-DC converter topologies*
*(a)* DAB, *(b)* Modular buck/boost, *(c)* buck/boost quadratic, *(d)* Thyristor converter, *(e)* IGBT converter, *(f)* Four quadrant converter, and *(g)* MMC converter

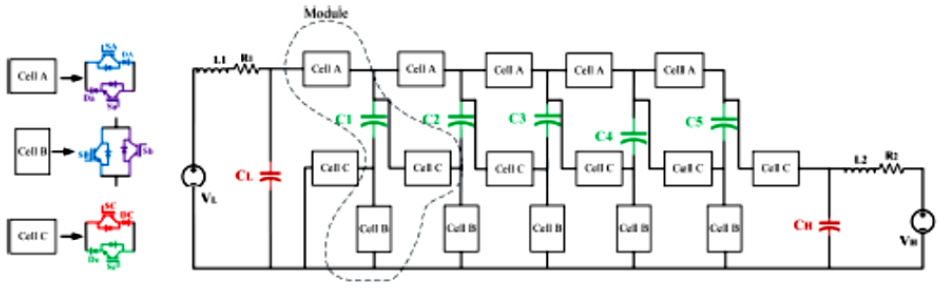


**Fig. 2** *Bidirectional DC-DC converter*

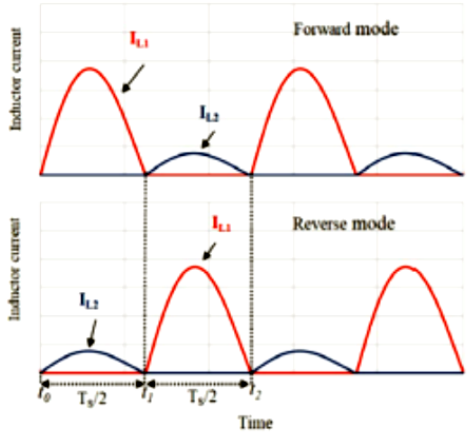


**Fig. 3** *Inductor current waveforms during both modes*

an LCL bidirectional DC–DC converter in multi-terminal direct-current MTDC systems [11] as depicted in Fig. 1*f*. This converter has one inductor which is an advantage, high-voltage ratio, and a low switching frequency. However, the inductor is large and requires many switches in series to withstand the high voltage. This converter uses hard switching, which leads to high switching losses.

Filsoof [12] developed a bidirectional modular multilevel DC–DC converter of the triangular structure as illustrated in Fig. 1*g*. This converter has a significant reduction in the output voltage ripple and input current. However, this topology suffers from high switching frequency and has a two-level structure with only one boost inductor. This leads to design difficulties for HVDC application.

## 3 Bidirectional DC–DC marx converter

### 3.1 Circuit configuration

The main circuit of the bidirectional DC–DC Marx converter is illustrated in Fig. 2. It consists of three circuits. The first circuit is comprised of inductor $L_1$ and capacitor $C_L$ connected in series with DC voltage $V_L$.

There are five identical modules in the second circuit. Each module is composed of three cells: A, B, and C; cells A and C have two anti-parallel IGBT switches with diodes connected in series and a capacitor for holding the cell voltage. Cell B has two anti-parallel IGBT switches only. The converter can transfer the power in both directions and scale the voltage up or down the transformation ratio by changing the number of modules. The third circuit is similar to the first consisting of the inductor $L_2$ and the capacitor $C_H$ connected in series with the DC voltage $V_H$

### 3.2 Operating principle

The operation of the converter is based on the Marx generator concept. Five modules are used to achieve a voltage ratio of 1:5. In this study, a range of power levels up to 50 MW in the forward direction and up to 5 MW in reverse direction are considered.

All the IGBTs are switched at zero current to reduce the switching losses. In addition, all the switches must be capable of bidirectional blocking and forward conducting. The converter operation can be divided into two modes of operation: forward mode (FM) and reverse mode (RM).

*3.2.1 Forward mode:* In this mode, the energy flows from the low-voltage side to the high-voltage side. FM can also be divided into two sub-commutations. In the first sub-commutation ($t_0$–$t_1$) as shown in Fig. 3, the charging current flows through five capacitors ($C_1$–$C_5$) in parallel by switching ON switches ($S_A$–$S_B$), while all the other switches are turned OFF, as shown in Fig. 4. The diodes ($D_A$) block the reverse current flow.

In the second sub-commutation ($t_1$–$t_2$), the capacitors that were charged during the first sub-commutation are discharged in series to create the high voltage on the HV side by switching ON switches (SC), while diodes (DC) block the reverse current flow during capacitor discharge.

In this case, as there are five modules and the voltage gain is 5 and the electric charges is transferred from the five series-connected capacitors $C_1$, $C_2$, $C_3$, $C_4$ and $C_5$ to the capacitor $C_H$ as depicted in Fig. 5.

*3.2.2 Reverse mode:* As shown in Fig. 6, the current flows from high-voltage $V_H$ to the low-voltage $V_L$. In the first sub-commutation, inductor current $I_{L2}$ charges the five capacitors ($C_1$–

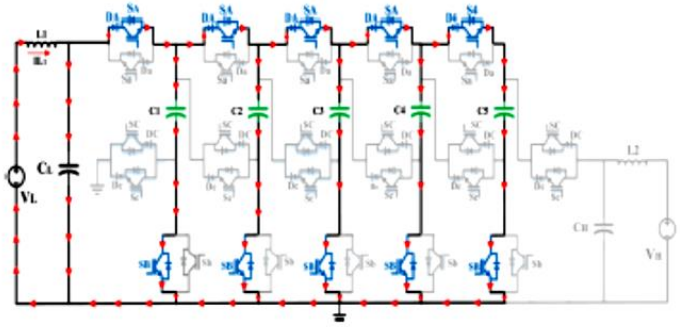

**Fig. 4** *Switching and corresponding current flow directions of charging capacitors in parallel in forward mode*

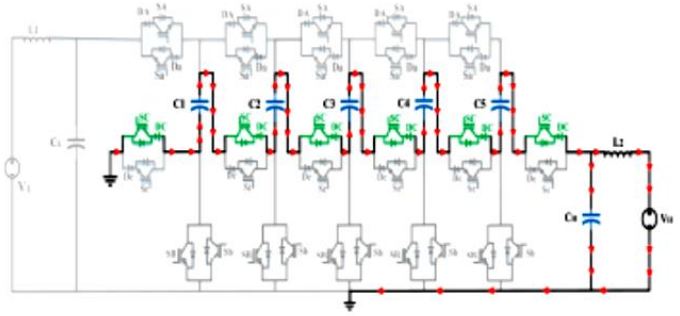

**Fig. 5** *Switching and corresponding current flow directions of discharging capacitors in series in FM*

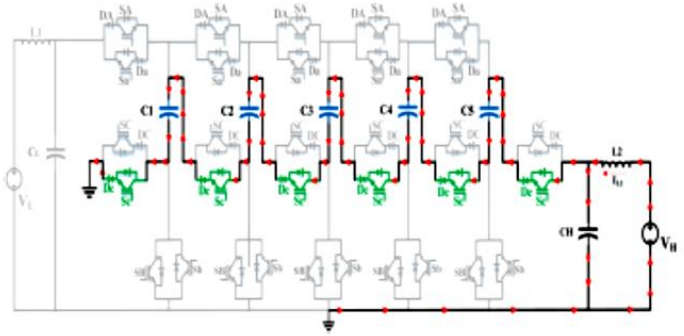

**Fig. 6** *Switching and corresponding current flow direction of charging capacitors in series in reverse mode*

$C_5$) in series in time interval ($t_0$–$t_1$), as shown in Fig. 3, by switching ON switches ($S_C$) and diodes ($D_C$), are connected in series with switches ($S_C$) to ensure unidirectional transfer of charge from the voltage source VH, to series-connected capacitors and which are forward biased, while all the other switches are turned OFF.

In the second sub-commutation, the switches ($S_a$, $S_b$) are turned ON, and the capacitors are discharged in parallel in time interval ($t_1$–$t_2$) to the low-voltage $V_L$ through inductor $L_1$ as depicted in Fig. 3, while the other switches are turned OFF as shown in Fig. 7.

## 4 Steady-state analysis

It is assumed that the converter has reached the steady-state condition. The converter voltage gain is the same as the number of capacitors 'n' and hence

$$n = \frac{V_H}{V_L} \tag{1}$$

where $V_L$ and $V_H$ are the low side and high side voltages, respectively. The equivalent capacitance in forward mode at the first sub-commutation is

$$C_{eq} = \sum_{k=1}^{k} C_i \tag{2}$$

where $C_i$ is the capacitance, and $C_{eq}$ is the equivalent capacitance of parallel connected capacitors in the first sub- commutation. However, in the first-commutation, the inductor $L_1$ and the equivalent capacitance $C_{eq\,(1)}$ forms an oscillatory $L$–$C$ circuit and hence the current in the first sub-commutation is given by

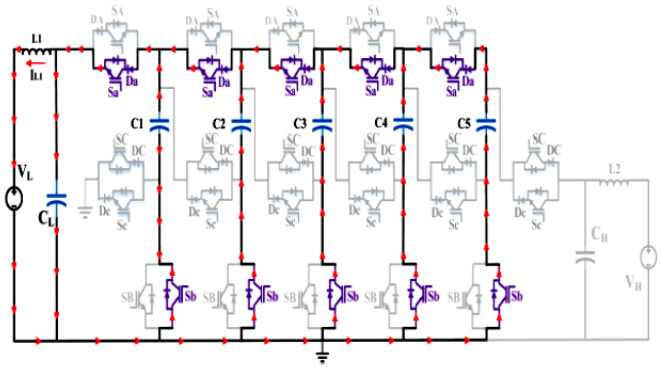


**Fig. 7** *Discharging capacitors in parallel in reverse mode*

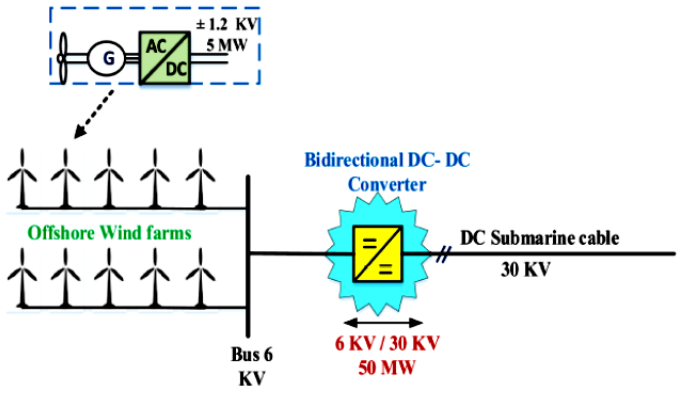


**Fig. 8** *DC collection topology system of wind farm*

$$i_{L1} = i_{ceq} = \frac{V_L}{\omega L_1}\sin(\omega t) \tag{3}$$

and

$$\omega = \frac{1}{\sqrt{L_1 C_{eq}}} \tag{4}$$

Based on the designed power rating of the bidirectional converter and the charge transfer, the inductor $L_1$ can be given as

$$L_1 = \frac{1}{C_{eq}}\left[\frac{QnV_L}{2\pi P_{rate}}\right]^2 \tag{5}$$

where $P_{rate}$ is the rating power of the converter and $Q$ is the amount of charge during charging in parallel. The value of inductor $L_2$ depends on the peak-to-peak of output current $\Delta I_{L2}$ and can be expressed as

$$L_2 = \left[\frac{nV_L T_S}{\Delta I_{L2}}\right]^2 \tag{6}$$

The determination of the capacitance value $C_{eq}$, is based on the capacitor voltage ripple and the amount of charge in the cycle.

$$C_{eq} = \frac{Q}{\Delta V C} \tag{7}$$

The value of high side-voltage capacitor $C_H$ depends on the relationship between the amount of charge to output converter voltage $V_2$ at the half period ($T_S$ /2) and the voltage ripple on the capacitor $C_H$. Hence

$$C_H = \frac{(P_{rate}/V_2)(T_S/2)}{2\pi\Delta V C_H} \tag{8}$$

Similarly, the value of low side-voltage capacitor $C_L$ can be expressed as

$$C_L = \frac{(P_{rate}/V_1)(T_S/2)}{2\pi\Delta V C_L} \tag{9}$$

## 5 Simulation studies

The location of the converter studied here is shown within the blue star in Fig. 8. The total power is 50 MW, and the voltages are 6 and 30 kV. The wind farm cluster is formed by two parallel lines of wind turbines, each containing five wind turbines in series. Hence, there is a total of 10 wind turbines; each rated at 5 MW, 1.2 kV [13–15]. The DC–DC Converter is required to transfer the power in both directions and is connected to the collection bus tie interconnect at the 6 kV side to the 30 kV side. The forward and reverse powers are 50 and 5 MW. Using the equations derived in Section 4, the parameters of the DC–DC converter used for the simulation were calculated and are listed in Table 1.

As the interest is on the converter operation, the system shown in Fig. 8 was reduced to the circuit shown in Fig. 9. The two systems on either side of the converter are represented by two voltage sources behind equivalent resistances and inductances. In practice, the power flow is controlled by the VSC at the onshore substation. However, for the simulation, the power flow was

**Table 1** Converter Parameters used for circuit simulation

| Parameters | | value | |
|---|---|---|---|
| number of modules | | 5 | |
| low voltage | $V_L$ | 6 | kV |
| high voltage | $V_H$ | 30 | kV |
| inductor | $L_1$ | 2.53 | μH |
| inductor | $L_2$ | 110 | μH |
| capacitor in the middle circuit Cn | | 694.5 | μF |
| capacitor | $C_L$ | 83 | μF |
| capacitor | $C_H$ | 116 | μF |
| rated power | $P_{rate}$ | +50, −5 | MW |
| frequency | $F_S$ | 2 | kHz |

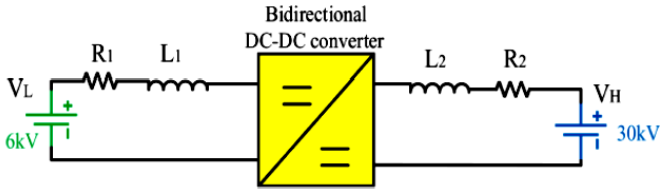


**Fig. 9** *Simulation circuit diagram*

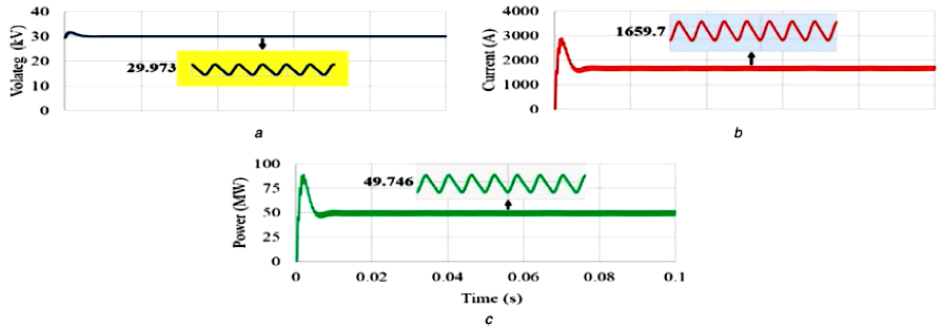


**Fig. 10** *Simulation waveforms of the forward mode operation*
***(a)*** Load voltage, ***(b)*** Load current, ***(c)*** Load power

controlled by varying the resistance values $R_1$ and $R_2$ on both sides.

The switching frequency $F_S$ of the converter is determined by the LC resonances in the circuit and is 2 kHz, and the fixed duty cycle of $d = 50\%$ was used. The converter is simulated in Matlab/ Simulink, using the SimPowerSystem toolbox. The waveforms of the voltage, current, and power during forward mode are depicted in Fig. 10.

The DC gain obtained by the simulation is 4.9, which is very close to the design value of 5. The output voltage, current, and power of the converter in forward mode operation should be 30 KV/ 1667 A, 50 MW as designed. However, the output voltage of the proposed converter is 29.97 KV and the current is 1659 A. In addition, the load power is 49.7 MW as shown in Fig. 10.

As illustrated in Figs. 11*a* and *b*, IGBT and diode currents in modules 1, 2, 3, 4, 5 increases, peaking at 18.6 kA in 250 μs in the last module. IGBTs capable of this duty are commercially available. An example is the IGBT 5SNA 1200G450300 [16].

During discharging the capacitors in series, the voltage across the IGBT switches SC is 6 kV as shown in Fig. 11*c*. However, the voltages across switches $S_B$ increase by 6 kV from left to right reaching a maximum of 24 kV on the shunt IGBT switch at the HV side as shown in Fig. 11*d*. This means that the devices in each module sees different voltages causing manufacturing issues and requiring series connection of devices. In addition, a reverse voltage of 6 kV appears across switches SA as illustrated in Fig. 11*e*.

Waveforms of voltage, current, and power during reverse mode are shown in Fig. 12. The voltage gain obtained by the simulation (0.204) is very close to the theoretical value of 0.2. The output voltage, current, and power of converter in reverse mode operation is also close to the theoretical values.

As illustrated in Fig. 13*b*, the voltage stress on the switch $S_b$ is 6 kV during discharge in series is equal to the $V_H/5$. The charging current in series is the same as through the IGBT switches (ISc = 536 A) as shown in Fig. 13*c*. One can see that the voltage on switches $S_b$ sequentially decreases in 6 kV steps as illustrated in Fig. 13*d*.

## 6 Conclusions

A new bidirectional DC–DC Marx converter is presented here. Full mathematical analysis led to the design methodology to determine the component values and ratings including solid-state devices. The mathematical equations are validated by simulation. The simulation demonstrated the ability of the converter to interface a 6 kV system with a 30 kV system leading to a gain of 5. The gain can be increased for application to higher voltages by increasing the number of modules. Therefore, the converter is easily scaled up or down. The resonances between the inductors and capacitors are

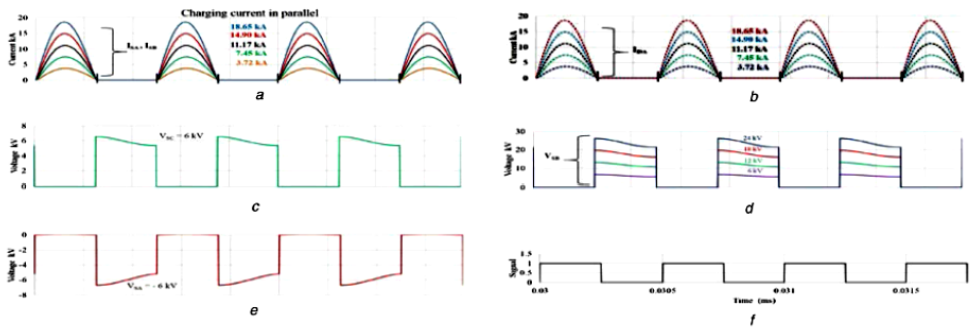


**Fig. 11** *IGBT and diode switch simulation waveforms of forward mode operation*
***(a)*** Charging current through IGBTs, ***(b)*** Charging current through diodes, ***(c)*** Voltage across cells C, ***(d)*** Voltage across cells B, ***(e)*** Voltage across cells A, and ***(f)*** Switching pattern

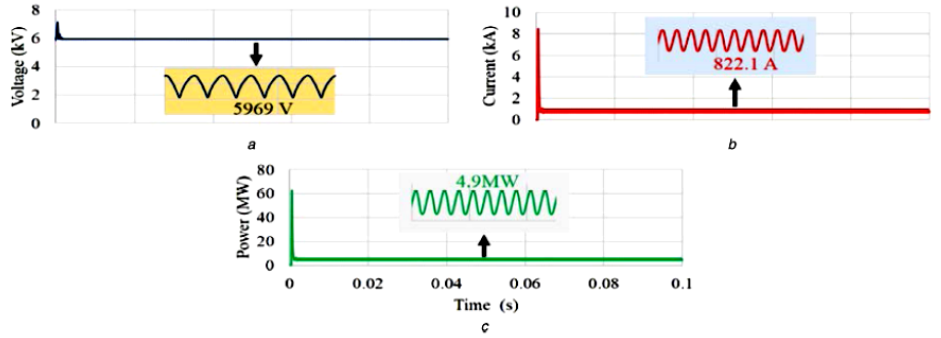


**Fig. 12** *Simulation waveforms of the forward mode operation*
***(a)*** Load voltage, ***(b)*** Load current, ***(c)*** Load power

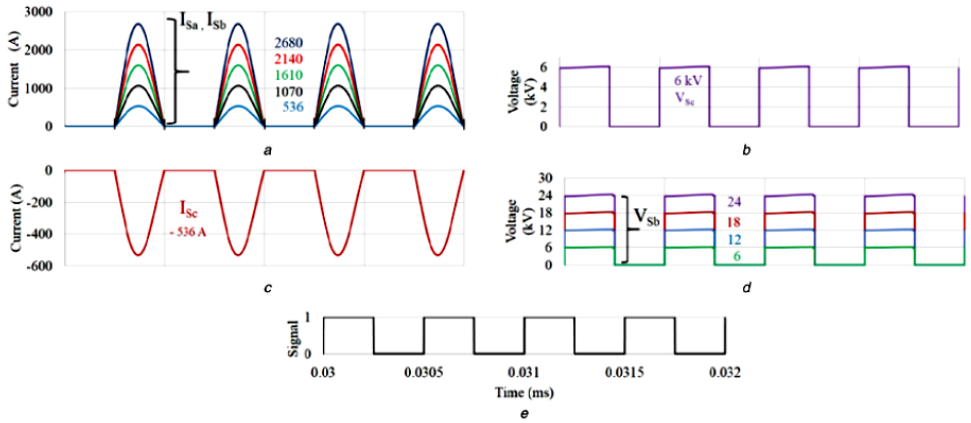


**Fig. 13** *IGBT and diode switches simulation waveforms of reverse mode operation*
***(a)*** Currents through cells A and B, ***(b)*** Stress voltage on cells C, ***(c)*** Charging current in series in cells A, and ***(d)*** Step voltage on cells B

used to determine the switching frequency enabling soft switching to reduce the losses.

## 7 Acknowledgments

The authors would like to thank the Higher Institute of Science and Technology, Alkhums, Libya, and Staffordshire University, Staffordshire, United Kingdom, for funding Mr Samir Milad Alagab PhD.

## 8 References

[1] Alagab, S.M., Tennakoon, S., Gould, C.: 'Review of wind farm power collection schemes'. 50th Int. Universities Power Engineering Conf. (UPEC), Stoke-on-Trent, UK, 2015, pp. 1–5
[2] Carrizosa, M.J., Benchaib, A., Alou, P., *et al.*: 'DC transformer for DC/DC connection in HVDC network'. 2013 15th European Conf. on Power Electronics and Applications (EPE 2013), Lille, France, 2013
[3] Qin, Z., Shen, Y., Loh, P.C., *et al.*: 'A dual active bridge converter with an extended high-efficiency range by DC blocking capacitor voltage control', *IEEE Trans. Power Electron.*, 2017, **8993**, (c), pp. 1–16
[4] Todor, T., Bauer, P., Ferreira, J.A.: 'Bidirectional modular multilevel DC-DC converter control and efficiency improvements through separate module control method', 2013, pp. 2038–2043

[5] Lagier, T., Ladoux, P.: 'A comparison of insulated DC-DC converters for HVDC off-shore wind farms'. 5th Int. Conf. on Clean Electrical Power Renew. Energy Resour. Impact (ICCEP 2015), Taormina, Italy, 2015, pp. 33–39

[6] Xing, Z., Ruan, X., Xie, H., *et al.*: 'A modular bidirectional buck/boost dc/dc converter suitable for interconnecting HVDC grids'. 2016 IEEE 8th Int. Power Electronics and Motion Control Conf. (IPEMC- ECCE Asia 2016), Hefei, China, 2016, pp. 3348–3354

[7] Pires Fernao, C.A., Foito, D.: 'Bidirectional boost/buck quadratic converter for distributed generation systems with electrochemical storage system'. 5th IET Int. Conf. on Renewable Energy Research and Applications (ICRERA 2016), 2016, vol. 5, pp. 5–10

[8] Jovcic, D.: 'Bidirectional, high-power DC transformer', *IEEE Trans. Power Deliv.*, 2009, **24**, (4), pp. 2276–2283

[9] Jovcic, D., Member, S., Zhang, L., *et al.*: 'LCL DC / DC converter for DC grids', *IEEE Trans. Power Delivery*, 2013, **28**, (4), pp. 2071–2079

[10] Jahromi, M.G., Mirzaeva, G.: 'Design of a high power low losses DC-DC converter for mining applications', 2016, pp. 1–8

[11] Kolparambath, S.K., Suul, J.A.: 'Analysis of DC/DC converters in multiterminal HVDC systems for large offshore wind farms'. Power Energy (TAP), Kollam, India, 2015, pp. 415–420

[12] Filsoof, K., Lehn, P.W.: 'A bidirectional modular multilevel DC-DC converter of triangular structure', *IEEE Trans. Power Electron.*, 2015, **30**, (1), pp. 54–64

[13] Lakshmanan, P., Liang, J., Jenkins, N.: 'Assessment of collection systems for HVDC connected offshore wind farms', *Electr. Power Syst. Res.*, 2015, **129**, pp. 75–82

[14] Alagab, S.M., Tennakoon, S.B., Gould, C.A.: 'A compact DC-DC converter for offshore wind farm application', *Renew. Energy Power Qual. J.*, 2017, **1**, (15), pp. 529–533

[15] Alagab, S.M., Tennakoon, S.B., Gould, C.A.: 'High voltage cascaded step-Up DC-DC marx converter for offshore wind energy systems'. EPE 2017 - assigned jointly to Eur. Power Electron. Drives Assoc. Inst. Electr. Electron. Eng., no. Mmc, 2017, pp. 1–10

[16] ABB Switzerland Ltd.: 'Surge currents for IGBT diodes, application note 5SYA 2058-02', 2014

International Conference on Renewable Energies and Power Quality (ICREPQ'17)
Malaga (Spain), 4th to 6th April, 2017
Renewable Energy and Power Quality Journal (RE&PQJ)
ISSN 2172-038 X, No.15 April 2017

# A Compact DC-DC Converter for Offshore Wind Farm Application

S. M. Alagab[1], S.B. Tennakoon[1] and C.A. Gould[1]

[1] School of Creative Arts and Engineering, Staffordshire University

College Road – Stoke on Trent, ST4 2DE (United Kingdom)
Phone number: +441782294861
E-mail: samir.alagab@research.staffs.ac.uk, S.B.Tennakoon@staffs.ac.uk, C.A.Gould@staffs.ac.uk

**Abstract.** A DC-DC converter suitable for the grid integration of windfarms through a DC grid is presented. The operation is based on the Marx principle where charged capacitors are connected in series and parallel in turn to achieve the voltage transformation. The two inductors at the two ends of the converter are designed to resonate with the capacitors to create resonance forcing current zeros to enable zero current switching thereby reducing switching losses. The design of a 50 MW, 6kV/30kV DC-DC converter was carried out by analysis and simulation.

**Key words**
DC–DC converter, IGBT, offshore windfarm

## 1. Introduction

Due to the increasing distances of renewable and embedded generation in transmission and distribution systems, it is expected that the use of High Voltage Direct Current HVDC transmission and Medium Voltage Direct Current (MVDC) distribution systems for the grid integration of windfarms will grow worldwide [1]. One of the key components in such systems is the DC-DC converter, required to act as the interface between the generation, transmission and distribution voltage levels. Well established DC to DC converters based on pulse width modulated (PWM) converters which require high frequency switching are not suitable. Application to high voltage, high power systems mean series connection of devices and high power losses. Hence such converters are not technically and economically feasible. In order to combat these issues a new breed of DC-DC converters based on the age old concept of switching capacitors is being developed. Such converters are referred to as Switched Capacitor DC-DC Converters (SW-DC-DC) [2-6].

The structure of this paper is organized as follows: In Section 2 a number of DC-DC converter topologies are explained. From these Veilleux Converter is explained in section 3. An improved converter based on the Veilleux topology and the principle of operation are explained in Section 4 followed by the mathematical analysis in Section 5. In section 6 simulation results are presented and a comparison of both topologies is given in Section 7. Finally, the conclusion drawn in section 8.

## 2. DC-DC converter topologies

A number of DC to DC converters suitable for high voltage applications are currently in research but none are not yet commercially available [5-8]. Non modular multi-level converters such as Flying Capacitor [9,10] and Diode Clamped [12] are not considered in this paper due to their complexity and difficulty of implementation. The modular, switched capacitor (SC) topologies explained in this paper are (a) Fibonacci, (b) Ladder (c) Interleaved (d) Doubler (e) Modular multilevel (MMC) and (f) Parallel-Series.

In all topologies the operation is based on charging and discharging of module capacitors in a particular sequence. In some cases, soft switching is used in order to reduce the switching losses enabling a higher frequency operation. If hard switching is used, switching frequencies above the power frequency becomes impractical due to unacceptably high losses. Topologies (a) to (d) are switched at high frequency and the literature does not indicate whether switching at low frequencies is feasible [2-4]. The Fibonacci topology has a high number of switches as depicted in Fig. 1(a) [2].

One module of the ladder converter as illustrated in Fig. 1(b), consists of two capacitors and four IGBTs switches leading to a complex structure and , the efficiency is low compared with the other topologies [3]. The interleaved topology requires the parallel connection of several two level converters at the input side as shown in fig. 1(c), and the multistage connection of capacitors at the output side with an interleaved switching scheme leads to a complex structure [4].

High switching frequency, low efficiency and the high number of components are also major issues. As shown in

Fig. 1(d), the Doubler is similar to the Fibonacci topology and the same issues apply [2,4].

MMC converter presented in [5,12] is proposed for HVDC connected offshore wind farm. However, the number of IGBTs switches is high for HVDC application as illustrated in Fig. 1(e), which is expected. The series-parallel DC-DC converter, is based on the Marx principle where, the capacitors are charged in parallel connected to the LV side voltage, and discharged in series to produce high voltage on the HV side as depicted in Fig. 1(f). This principle was used by Maneiro [9] to produce a DC to DC converter to tap power from a DC transmission line which can be used to power a remote area. Also the principle was used by Veilleux *et al*. to produce a DC-DC converter for off shore wind applications [7].

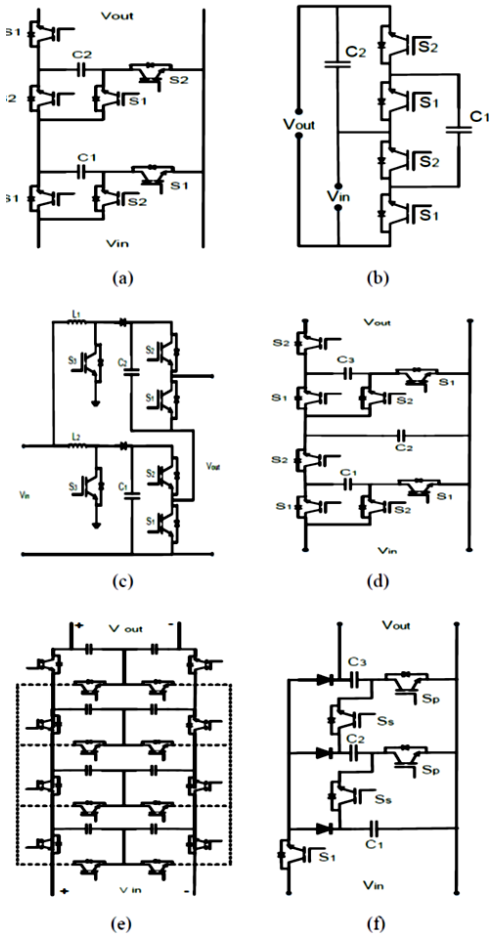


Fig. 1. Common switching DC-DC converter topologies: (a) Fibonacci, (b) The ladder, (c) interleaved boost, (d) Doubler, (e) multilevel modular MMC and (f) Parallel / Series Converter

## 3. Veilleux Converter

Fig. 1. Shows the Veilleux [7] converter with 5 submodule capacitors to achieve a voltage ratio of 1:5 and is based on the MARX principle. In addition, there are two capacitors at the two terminals to provide smoothing. The switching components are IGBTs and diodes. The operation can be divided into two sub periods. In the first sub period, the capacitors $C_n$= (1, 5) are charged in parallel from the LV source by switching the IGBTs $S_{pj}$(j=1-4). The IGBTs $S_k$(k =1-4) are switched off and hence the charging currents flow through $S_{in}$, $D_{in}$, diodes $D_n$ (n=1-5) and the IGBTs $S_{pj}$(j=1-4). In the second sub period, IGBTs $S_{sk}$ are switched on and IGBTs $S_{Pj}$ (j =1-4) are switched off to connect the capacitors in series to create a high voltage equal to 5 times the LV across the converter HV output.

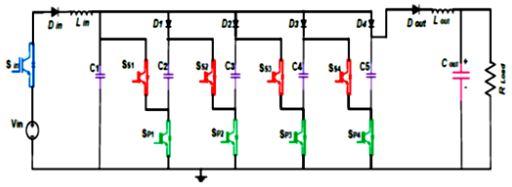

Fig. 2. Veilleux DC-DC Converter

A disadvantage of this topology is the number of IGBTs switches in the charging state $S_P$ is high and the increasing voltage stresses in the IGBTS in successive stages. The number of IGBTs can be reduced from 23 to 13 by combining function of 4 IGBTs ($S_{P1}$-$S_{P4}$) to be performed by 4 diodes and 1 IGBT ($S_{valve}$) as shown in next section (proposed topology).

## 4. Proposed topology

### a. *Circuit Configuration*

The structure of the converter as depicted in Fig. 2, can be broken down into three circuits; input circuit, middle circuit and the output circuit. The converter is aimed at application to a power collection system in an offshore windfarm grid connection system. A possible configuration showing the position of the DC to DC converter is shown in Figure 6. Where the specifications shown are used in the design.

Therefore the input circuit consists of an input DC voltage source of magnitude $V_{in}$ = 6 KV, input HV valve ($S_{valve}$), and an input inductor $L_{in}$ connected in series with an input diode $D_{in}$. Depending on the voltages in a particular application, and IGBT ratings a number of IGBTs in series are needed to form the High voltage valve ($S_{valve}$).

The middle circuit comprises a number of IGBT switches, capacitors, and diodes $D_{(1-8)}$. The number of capacitors denoted by "n" is set to 5 to create a voltage amplification of 5. The capacitances in the 5 sub-modules are indicated by $C_n$, where n= (1, 5). The switching

components are IGBTs $S_{(1-4)}$, IGBT valve switches $S_{valve}$, and diodes $D_{(1-8)}$.

The output circuit consists of an output diode $D_{out}$ connected in series with the output inductor $L_{out}$, and one output capacitor $C_{out.}$. The load, modelled by a pure resistor $R_{load}$, is connected in parallel.

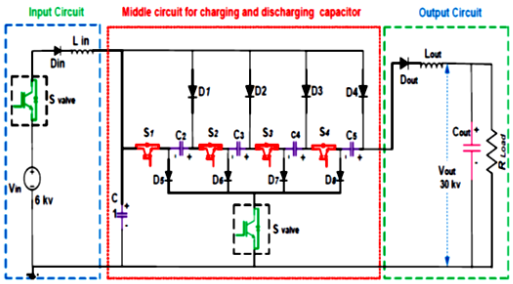


Fig. 3. Improved Veilleux DC-DC converter

*b. Operating Principle*

The operation of the converter can be divided into two equal sub-periods. During the first sub period all the cell capacitors $C_n$, (n =1, 5) in the middle circuit are connected in parallel across the input low voltage (LV). The total charging current flows through the valve ($S_{valve}$), diode $D_{in}$, input inductor $L_{in}$, and diodes $D_n$ where n=1, 8 and through the valve $S_{valve}$ . Energy from the LV DC source transfers to the cell capacitors as illustrated in Fig. 4(a).

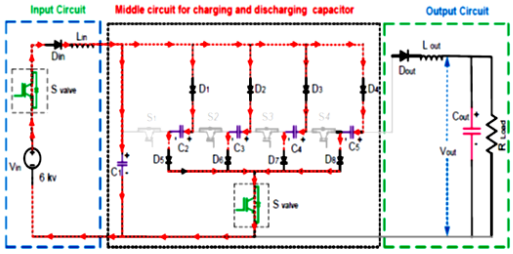


(a)

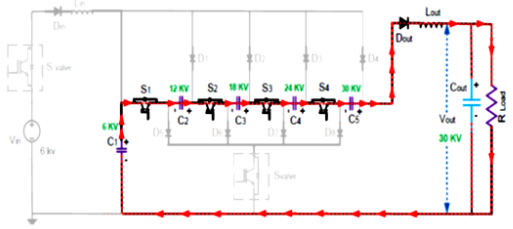


(b)

a) Connected the Capacitors in parallel during charging
b) Connected the Capacitors in Series during discharging

Fig. 4. Operation states of Improved Veilleux DC-DC converter

During the second sub-period of time, the cell capacitors are connected in series through IGBT switches n= 1, 4 to produce the higher voltage as shown in Fig. 4(b). Energy transfers from the cell capacitors to the output capacitor $C_{out}$. The inductor and capacitor combination must be designed so that the resonance frequency is less than switching frequency. This is used to implement soft switching to reduce the switching losses.

## 5. Mathematical analysis

The analysis of the improved Veilleux converter resulted in the following equations which can be used to determine the component values, optimise the switching frequency and determine the ratings of the IGBTs and diodes. The voltage transformation ratio is the same as the number of capacitors "n" and hence

$$n = \frac{V_{out}}{V_{in}} \qquad (1)$$

The output load ($R_{load}$) is dependent on the power rating of the converter and hence

$$R_{load} = \frac{V_{out}^2}{P} \qquad (2)$$

Where P is the power rating of the converter.
The input inductance $L_{in}$ is given by,

$$L_{in} = \frac{V_{out}}{5} \cdot \left(\frac{I_{Lin}}{\Delta I_L}\right) \cdot \frac{T_s}{2} \qquad (3)$$

Where $\Delta I_L$ is the inductor current peak to peak ripple, $I_{Lin}$ is the input inductor current and $T_S$ is the switching time. The current of input inductor $L_{in}$ is a positive half sine wave during the first sub-period, charging the capacitors in $T_S$ /2 given as

$$i_{Lin}(t) = I_{Lin}^P \sin(\omega t) \qquad (4)$$

Where $I_{Lin}^P$ is the peak inductor current. The capacitance value $C_n$ is given by

$$C_n = \frac{(P/nV_{in}) \cdot (1/F_S)}{\Delta Vc_n} \qquad (5)$$

Where $\Delta V_c$ is the capacitor voltage ripple. The value of output inductance can be found as

$$L_{out} = \frac{V_{out} \cdot (T_S/2)}{F_S \cdot \Delta L_{out}} \qquad (6)$$

The output capacitance value is given by,

$$C_{out} = \frac{(P/nV_{in}) \cdot (T_S/2)}{2\pi \Delta Vc_{out}} \qquad (7)$$

Where $\Delta V_{out}$ is the peak to peak voltage ripple on the output capacitor voltage. A fixed frequency-switching pattern is applied to the circuit cells. Meanwhile, the equation (8) shows the resonant frequency $F_{res}$ for two stages.

$$F_{res} = \frac{1}{2\pi\sqrt{LC}} \qquad (8)$$

## 6. Simulation studies

The arrangement shown in Fig. 5, forms the basis for the simulation study. In this topology, the cluster is formed by two parallel lines of wind turbine, each containing 5 wind turbines in series. Hence, there is a total of 10 wind turbines; each rated at 5 MW, 1.2 KV [14]. Therefore, the total value of wind turbine cluster bus voltage is 6 KV and 50 MW. Hence the DC-DC converter input voltage is 6kV.

The DC – DC Converter is connected to the collection bus to step up the voltage to 30kV for MV Transmission using the equations derived in section 5 the parameters of the DC – DC converter were calculated which are given in Table.1.

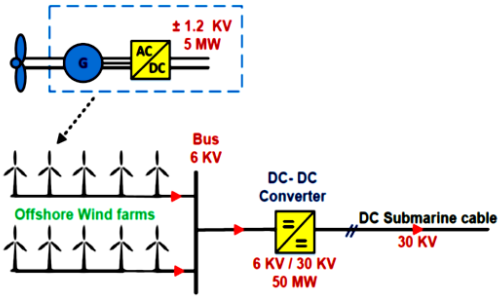


Fig. 5. DC collection topology system of wind farm

A switching frequency of $F_S$ = 2 KHz is used with fixed duty cycle of $d$ = 0.5. The load resistance was calculated using the 50 MW power and the output voltage of 30kV.

Table 1. System Parameters used for DCMC circuit simulation

| Parameter | Symbol | value |
|---|---|---|
| Input Voltage | $V_{in}$ | 6 KV |
| Output Voltage | $V_{out}$ | 30kV |
| Load current | $I_{load}$ | 1.667 KA |
| Rated power | $P_{rate}$ | 50 MW |
| Switching frequency | $F_S$ | 2 KHz |
| Number of sub module capacitors | $C_n$ | 5 |
| Sub module Capacitance | $C_1$-$C_5$ | 694.5 µF |
| Output capacitance | $C_{out}$ | 115 µF |
| Input inductance | $L_{in}$ | 2.53µH |
| Output inductance | $L_{out}$ | 110µH |
| Load resistance | $R_{load}$ | 18 Ω |

The converter is simulated in Matlab/Simulink software package. The waveforms of input and output inductor currents, and the load voltage are depicted in Fig. 6(c) shows that the resonating inductor current increases to a peak around 26 KA in 250 µs, which also flows through the IGBT. Inspection of the characteristics of the IGBT 5SNA 1200G450300 [15], shows that this is feasible. As the current begins to reverse in direction, the diode $D_{out}$ blocks the current flow. The DC gain is 4.98 compared with the theoretical gain of 5. To the output voltage is 29.93 KV which is very close to the design specification of 30kV. The peak load current pf 1.662kA is very close to the design value of 1.667.

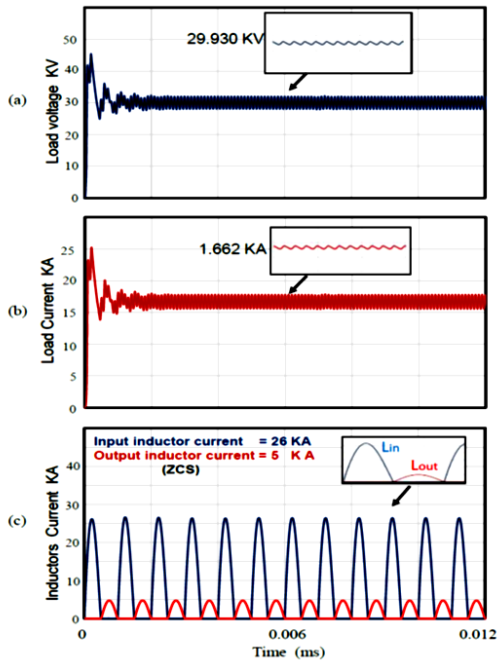


a) Output load voltage, b) Output load current and c) Inductor currents (ZCS)

Fig. 6. Simulation waveforms of the improved converter

## 7. Comparison with the Veilleux converter

A quantitative comparison was carried out using data from the output results by Matlab/ Simulink simulation, and the proposed configuration is evaluated and compared with Veilleux converters in terms of the power device count to highlight its advantages for high-voltage applications.

Both topologies, are operating with the same DC-DC Marx converter principle; hence, the comparison is made for the same three gains, same input voltage, same power rating, same load, same soft witching technique, and same switching frequency.

The output voltage and current of both topologies should be 30 KV/ 1667A as designed. However, the output voltage of Veilleux topology is 29.59 KV, and the proposed topology is 29.93 KV. In addition, the load current of Veilleux topology is 1644 A, and a proposed topology is 1662 A. numbers of IGBTs switches in gain (1:5) are 11 only in a proposed topology, but in a Veilleux topology are 20 as depicted in Fig. 8.

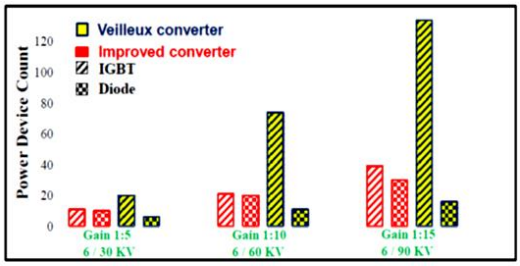


Fig. 7. Power device count comparison

## 8. Conclusion

The improved converter achieves the required gain of 5 with reduced components. Soft switching can be implemented and a method for calculating the resonant component values and the switching frequency is given. Also a design methodology for the determination of the circuit components and solid state devices is given.

## References


[1] S. M. Alagab and C. Gould, "Review of wind farm power collection schemes," In Power Engineering Conference (UPEC), 50th International Universities 2015.

[2] J. C. Mayo-maldonado, S. Member, J. C. Rosas-caro, and P. Rapisarda, "Modeling Approaches for DC – DC Converters With Switched Capacitors," vol. 62, no. 2, pp. 953–959, 2015.

[3] H. Taghizadeh, A. M. Cross, R. Whitehouse, and C. Barker, "Switched Capacitor DC-DC Converters for HVDC Applications," pp. 1–9.

[4] A. Ponniran, K. Orikawa, and J. Itoh, "Interleaved High Boost Ratio Marx Topology DC-DC Converter."

[5] M. D. Seeman and S. R. Sanders, "Analysis and Optimization of Switched-Capacitor {DC}amp;#x2013;DC Converters," *2006 IEEE Work. Comput. Power Electron.*, vol. 23, no. 2, pp. 216–224, 2006.

[6] X. Zhang and T. C. Green, "The Modular Multilevel Converter for High Step-Up Ratio DC-DC Conversion," *Ind. Electron. IEEE Trans.*, vol. 62, no. 8, pp. 4925–4936, 2015.

[7] P. W. Lehn, B.-T. Ooi, and E. Veilleux, "Marx dc–dc converter for high-power application," *IET Power Electron.*, vol. 6, no. April, pp. 1733–1741, 2013.

[8] A. Parastar, "High-Power Multilevel Step-Up DC / DC Converter for Offshore Wind Energy Systems," vol. 0046, no. c, pp. 4781–4788, 2015.

[9] S. Tennakoon, "Scalable Shunt Connected HVDC Tap Using the DC Transformer Concept," pp. 6–8.

[10] C. Cheng and L. He, "Flying-Capacitor-Clamped Five-Level Inverter Based on Switched-Capacitor Topology," vol. 0046, no. c, 2016.

[11] A. Parastar, A. Gandomkar, and J. Seok, "High-Efficiency Multilevel Flying-Capacitor Renewable Energy Systems," vol. 62, no. 12, pp. 7620–7630, 2015.

[12] J. Zhao, Y. Han, X. He, C. Tan, J. Cheng, and R. Zhao, "Multilevel circuit topologies based on the switched-capacitor converter and diode-clamped converter," *IEEE Trans. Power Electron.*, vol. 26, no. 8, pp. 2127–2136, 2011.

[13] H. D. Offshore, "Multilevel Modular DC / DC Power Converter for Wind Energy Applications," vol. 62, no. 5, pp. 2879–2890, 2015.

[14] P. Lakshmanan, J. Liang, and N. Jenkins, "Assessment of collection systems for HVDC connected offshore wind farms," *Electr. Power Syst. Res.*, vol. 129, pp. 75–82, Dec. 2015.

[15] ABB, "Surge currents for IGBT diodes," 2014.


## Biography

**Samir Milad Alagab** (Ph.D Researcher) was born in Tripoli Libya. He obtained his HND (Eng) Degree and MSc degree in Electrical Eng. from higher institute for preparing trainers- Zliten- Libya in 1996 and Staffordshire University, United Kingdom, in 2009, respectively. He worked as Electrical Engineer in Power Operation Department, High Line Division, Sirte Oil Company for Production, Manufacturing of Oil & Gas, Libya and he worked as a lecturer assistant in the Department of Electrical Engineering at high professional institute for comprehensive professions, Khoms- Libya. Presently, he is working on his Ph.D. degree at Staffordshire University, Stoke-on-Trent, U.K. His research interest include renewable energy technologies, DC/DC converter for power collection in offshore wind farm.

**Sarath Tennakoon** (M'87) received the B.Sc. degree in electrical engineering from the University of Moratuwa, Sri Lanka, the M.Sc. degree from the University of Aston, Birmingham, U.K., and the Ph.D. degree in Electrical Engineering and Electronics from the University of Central Lancashire, Lancashire, U.K. Currently, he is a Professor of power electronic systems and the Director of Centre for Energy Efficient Systems, Staffordshire University, Stoke-on-Trent, U.K. His research interests are DC grids and HVDC, power system protection, and power electronics and harmonics.

**Dr. Chris Gould** received the BEng (Hons) Degree in Engineering from Coventry University in 1996, Masters in Business Administration (MBA) from the University of Hertfordshire in 2006, and a PhD in Electrical and Electronic Engineering in the field of thermoelectricity from Staffordshire University in 2014. Chris is currently the Senior Lecturer in Electrical and Electronic Engineering, and the Award Leader for the BEng/MEng Electrical Engineering Award at Staffordshire University in the United Kingdom. Research interests include thermoelectricity, energy harvesting, energy storage, and semiconductor device modelling and simulation.

# Review of wind farm power collection schemes

Samir Milad Alagab
Staffordshire University, UK
Au004497@student.staffs.ac.uk

Sarath Tennakoon
Staffordshire University, UK
S.B.Tennakoon@staffs.ac.uk

Chris Gould
Staffordshire University, UK
C.A.Gould@staffs.ac.uk

***Abstract*- The main development trend of wind power generation systems is large offshore wind farms (OWFs) with grid connection. However offshore wind farms have grown rapidly due to much better wind conditions. Hence, several large scale offshore wind farms are planned to be built and installed at distances greater than 100 km from the coast. Traditionally, an AC collector scheme collects energy from the wind farm and step up the voltages by power transformers and transmit power via AC submarine cables to the onshore substation. However, this is suitable for shorter distances about 50 km. When the distances are greater the AC transmission of bulk power from the wind farm to the onshore grid via undersea cables is not viable due the reactive power issues. Therefore HVDC transmission is now being considered for the grid connection of wind farms. However as wind farms constitute weak systems Line commutated converter (LCC) based HVDC is not viable and newer Modular Multilevel Converter (MMC) based Voltage Source Converters(VSC) are needed for AC-DC conversion. Opting for dc systems for both power collection and transmission pose a number of technical challenges in terms of developing HVDC breakers and DC –DC converters.**

***Index Terms*-- *Offshore wind farm, onshore wind farm, HVAC, HVDC transmission and collection.***

## I. INTRODUCTION

WIND power has emerged as one of the most dominant renewable sources of energy with immense growth potential across the globe [1]. In fact the global wind energy capacity has increased rapidly and has become the fastest developing renewable energy technology [2]. With the rapid development of wind energy, the wind energy conversion systems have been developed by researchers and manufacturers [3]-[4].

Offshore wind farms have many advantages over onshore wind farms. Some of those are strong less turbulent wind, the availability of large sea areas and the reduced visual and noise impact from offshore structures. These advantages lead to an increase in energy production and also to a reduction of fatigue on the blades and the structural components of the wind turbines [5]. The target for installed capacity in Europe is 40 GW by the end of 2020 [6].

The offshore technology has a number of issues in terms of modest efficiency, high weight, and size of the offshore installation, cost of transportation, installation and maintenance [7]. Presently, there are two solutions to integrate offshore electrical power transmission: HVAC and HVDC VSC [8]. HVAC has the advantage of a simpler system structure and the lower cost. However, the transmission distances are getting longer, and the capacities of offshore wind farms are increasing, leading to the following problems [5]:

- The stability of the system decreases with the increase of transmission distance.
- Dynamic reactive power compensation must be provided, in particular under AC faults.
- Cost increases with the increase of transmission distance.

These problems can be overcome by using HVDC VSC which has the following advantages:

- Maximum capture of wind energy by frequency control
- Black-start capability.
- Independent control of real and reactive power.

The paper is divided into four sections. In Section I, a general introduction is given. In Section II, a summary of general wind power generation is given followed by explanations of, HVAC and HVDC transmission system topologies based on VSC- HVDC transmission systems. In section III different methods of wind power collection schemes are also explained. Finally, in Section IV, conclusions are drawn.

## II. WIND POWER GENERATION

Wind energy has the potential to be the cheapest power source in Europe [8]. EU targets will require a significant change in renewable energy development over a relatively short period of time [8]. According to the Commission's Renewable Energy Roadmap, 34% of all electricity consumption in 2020 is expected to be met by renewable sources, and around 12% could be generated by wind power alone [9]-[10].

The Global cumulative wind power capacity from 1999 to 2020 shows that the wind power has grown quickly to a capacity of 283 GW with 45 GW installed in 2012, and this number is expected to achieve 760 GW in 2020 based on a moderate growth scenario [10]. Wind energy grows more rapidly than any other renewable energy source and is becoming a major player in the modern energy mix. For example, Denmark has a high penetration of wind power and today more than 30% of the electrical energy is supplied by wind [10]. The ambition of Denmark is to achieve 100% non-fossil based power generation by 2050 [10]-[11]. In the United Kingdom renewable energy target is to achieve 20% of energy by 2020. However, it is expected that wind energy will form a large proportion of the renewable energy increase [11]-[12]. Wind farms can either be on shore or off shore.

### *A. Onshore Wind farms (OWF's)*

Onshore wind already plays a leading role in the generation of renewable electricity in the UK [13]-[14]. In 2010, it generated around 7TWh which is more than a quarter of the electricity provided by British renewables at that time and onshore wind is expected to generate up to 30TWh.

The UK's first commercial wind farm was built in Delabole, Cornwall in 1991. Since then, onshore wind energy has

978-1-4673-9682-0/15/$31.00 ©2015 IEEE

established itself as a mature, clean and productive technology. It is now the UK's largest source of renewable energy. [14]. In the UK, there are numerous onshore wind projects, ranging from single turbines to larger, multi-turbine schemes. Projects are developed by an increasingly diverse range of people, from large energy companies and independent developers, to community groups or small businesses and farms [15]. Tallentire was also one of the very first operational wind farms to receive the RES' Local Electricity Discount Scheme. Tallentire onshore wind farm, which was completed in June 2013, is made up of six wind turbines located on Tallentire Hill near Cockermouth, Cumbria [16].

### B. *Offshore Wind farms (OWF's)*

The concept of offshore wind power is the extension of onshore wind power, and the main differences between offshore wind farms and the traditional onshore wind farms are as follows:

- High wind speed, large available areas
- Less restriction. Due to the less noise limit, higher speed turbines can be used
- Difficulties of offshore wind power transmission and integration to the grid [9].
- High cost of construction and maintenance. Structures need to resist huge disturbance, such as slat-spray and sea-waves, the initial investment is higher than that on the shore [17].

Over the past 20 years, offshore wind farms developed rapidly, with the transmission distances ranging from 3 km to 56 km and the capacities increasing from 5 MW to 504 MW [8]. The worldwide capacity will reach 75 GW by the end of 2020 [18]. The offshore wind energy potential in the seas of the European Union with water depths of up to 50 m, and is several times larger than the total European electricity consumption [18]. Consequently, in addition to the current large number of onshore sites, many offshore sites are in the planning or implementation stages.

Offshore wind farm capacity in the North Sea and the Baltic Sea (off the northern coast of Europe) alone is expected to rise to 20–25 GW by 2030 [16]-[18]. Many offshore wind farms will be installed at distances greater than 100 km from the coast. It is a great technical challenge to integrate such a large amount of wind power through long distance transmission systems [18].

The UK has done more than any other country to support the development of a sustainable and ambitious offshore wind industry. During 2013, Government has been working in partnership with industry to develop the UK's offshore wind industry, provide the tools necessary to support large scale investment in the UK supply chain and raise awareness of the commercial opportunities in the UK and overseas, to deliver the innovation and competition needed to bring down costs the innovation and competition needed to bring down costs for consumers [16].

Furthermore, the world's largest offshore wind farm, London Array was opened in July 2013. London Array has a 630 MW capacity and produces enough electricity for nearly half a million homes which is equivalent to two thirds of the homes in Kent [19].

## III. GRID CONNECTION SCHEMES

The Future offshore wind farms (OWF's) will be mostly located far away from the shore, and have to be connected to the grid point of common coupling (PCC) via undersea cables over long distances [20]. The wind farm electrical system consists of wind turbine clusters, undersea power collection and transmission cables, platform substation, transformers and onshore substation [21]. The key criteria that offshore wind farm connection design must consider are the trade-offs between the initial capital investment, power losses and availability due to scheduled maintenance or wind turbine failure and other system faults [22].

The availability and reliability issue is particularly important as the repairing process is very difficult in the marine environment [20]-[22]. The mature transmission technology is High Voltage Alternating Current (HVAC). However the problems arising from reactive power flow has led to the consideration of High Voltage Direct Current (HVDC) technology, particularly, for windfarms considerably away from the shore.

The electrical system of a wind farm can be considered as several distinct subsystems. As shown in Fig 1, the electrical system of OWF typically consists of five sub-systems.

- Wind farm (generation)
- Power collection
- Voltage step up
- Transmission system
- AC grid


Fig. 1. The different components on OWF's electrical system

### A. *Alternating Current transmission (AC)*

Most of the existing offshore wind farm transmission systems use HVAC for the transport of electrical power between mainland and stations located on (or under) the sea [23]. It is a well-established technology, and HVAC system contains the following main components:

1) AC collection system.
2) Offshore transforming substation with transformers and reactive power compensation.
3) Three-phase submarine cable
4) Onshore substation with transformers and reactive power compensation.

The electrical system depends on the distance and the windfarm capacity. For short distances if the connection voltage is at distribution level. High voltage transmission may not be necessary and hence the number of voltage transformations can be reduced. If the transmission distance is long, the number of cables and the losses are too high and a raise in the transmission voltage is necessary. Horns Rev Wind Farm in Denmark, with a power of 160 MW and a

transmission distance of 21 km, is first offshore wind farm using HVAC [23].
The distributed capacitance in submarine cables is much higher than the capacitance in overhead lines [23]. Therefore, due to economic and technical reasons the practical transmission length is short for marine applications. Reactive power increases with voltage and length of the cable and long-transmission distances require large reactive compensation equipment at both ends of the line [23]-[24]. Therefore for longer transmission lengths DC is the only option.

*B. High Voltage Direct Current transmission (HVDC)*

As offshore wind farms become larger and more distant from shore, the justification of using HVDC to transmit the power to the onshore network becomes easier, particularly at power levels of *500* MW or more, and at a distance of 60-80 km for offshore submarine transmission [25]. The costs of the converter stations, offshore and onshore, are significant in themselves, but when put in the context of the complete project cost, including the cables and the wind turbine generators, they feature less prominently.
Two types of converters are available, the Line-Commutated Converter (LCC) and the more recently introduced Voltage-Sourced Converter (VSC). For offshore wind power LCC converter is not suitable, because the LCC requires a strong network voltage to commutate, and wind farms usually have weaker grids that cannot supply such a strong voltage. In addition, the capability to energize the system from shore (black start) is a challenge [26]. These issues can be alleviated by combining the LCC-interface for an offshore wind farm with some auxiliary source of reactive power. The LCC produces considerable AC side current harmonics that require filter banks [25]-[26].
High power IGBT (Insulator Gate Bipolar Transistor) development allows the use of VSCs in HVDC systems with much lower harmonic distortion than HVDC LCC systems although with higher power losses [23]. The VSC is able to control active and reactive power independently and generates a voltage on the AC side. It is therefore able to operate in weak networks [26]. A VSC connected wind farm requires a tailored control system. The main drawback of the VSC is its lower current capability. Even for very short durations, over currents cause thermal stresses that degrade or cause permanent damage to the switching elements [23][26].

*C. Wind farm power collection system*

The wind farm collection system gathers the wind turbine's power production and brings it to a central collection point (CCP), which then ties in to the main grid through the transmission system (TS) [22]. This section presents the state of the art MVAC collector systems and MVDC collector systems.

1) MVAC collector systems

There are a number of possible turbine arrangements in wind farm MVAC collector systems but three of them are being currently considered: namely radial layout, star connection and double-sided ring collector systems [22].
A radial collect system (CS), also known as string, is that in which a number of OWTs are connected to a single cable feeder within a string. Such a system is used in Barrow, Lillgrund, Thorntonbank-1 and Belwind-1 [22].
The number of wind turbines on each string feeder is determined by the capacity of the generators and the maximum rating of the MVAC submarine cable within the string. Its advantages are the simplicity of its control and the smaller total cable length.
Its major drawback is its poor reliability, as cable or switchgear faults at the hub end of the string can prevent all downstream turbines from exporting power.
The main purpose of the star connection is to reduce cable ratings and to provide a high level of security for the entire wind farm. Voltage regulation along the cables between wind turbines is also likely to be better in this design [24]-[26]. However, there are additional expenses due to the longer diagonal cable runs and some short sections of higher-rated cabling; but these expenses are not likely to be significant.
The more complex switchgear requirement at the wind turbine is the major cost implication [26]-[27]. The main advantages of star topology are better voltage regulation and reliability.
Double-sided ring design is a way to lower losses through high voltage collection, and provide greater security; however this kind of connection requires much more expensive high voltage cables [16]. This layout has higher reliability compared to the radial layout. In case of fault, the radial connection (in normal operation) can be reconfigured and the energy produced is not lost [28]. Because of higher cable sections, higher cable length (connections between collector groups), more complex system (depending on location and number of reconfiguration switches), this solution implies higher investing costs [28]-[29].

2) MVDC collector systems

Conceptually, MVDC collector systems are those linking turbines with DC output and a HVDC transmission link to shore. In a general sense, the arrangement of these collector systems (CSs) can be one of those previously commented on for MVAC collector systems.
In general, the DC grid consists of several clusters, which are connected either in parallel or in series [12]-[30]. Since the difference between the output power of each turbine and the total power transferred to the shore is huge, several voltage steps are needed [30]. Consequently, a DC/DC converter system is needed for stepping up the voltage [12]-[30]. Three possible DC collection schemes for offshore wind farms as discussed below.

*a) AC Collection – DC Transmission*

As shown in Fig. 2, wind turbines are arranged in clusters and the wind generator produces variable frequency variable magnitude voltage AC voltage, which needs to be processed as the grid voltage is at fixed frequency and voltage [7].
This process is carried out by a DC link converter-comprising a generator side rectifier and a grid side inverter. Then this

voltage, which is 690V in UK, is stepped up to the level required by the medium voltage collection bus. This medium voltage is then stepped up to the transmission level and fed to a HVDC converter for dc transmission. At the onshore substation the DC power is converted back to AC for connecting to the grid. This arrangement requires a large number of conversion stages [8].

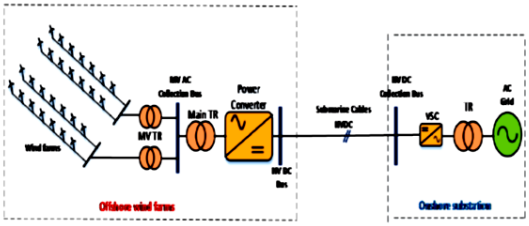


Fig. 2. AC collection - DC transmission

*b) DC Collection – DC Transmission: one cluster step-up*

The second solution is shown in Fig. 3 (a) where the power is collected first and then a DC-DC converter steps up the voltage to the transmission level. Since the number of converters is lower and the transformers are eliminated, this design is better [30]-[31]. However, only two voltage levels are used and consequently the distribution level strongly depends on the generator voltage. The advantage of this collection is that it leads to the lowest losses because of the short distances within the wind farm [30]-[32]. However the required voltage transformation may not be achievable with one stage of dc-dc conversion.

*c) DC Collection – DC Transmission (two step-ups)*

In this method as shown in Fig. 3 (b), two DC/DC converters are used; one steps up the voltage after each turbine up to the medium-voltage level. Afterward the power is collected and stepped up a second time to the transmission level.

The use of high power DC-DC converters may lead to significant reduction in the overall system size and weight as well as the construction and installation cost of the wind turbines and substation platform [12]-[31].

An advantage of this configuration is the direct step-up of the voltage after the turbine, which leads to reduced cable losses at the distribution level. Furthermore, the voltage can be controlled individually, but there is one drawback of this configuration method is the additional DC-DC converter, leading to extra losses, investment cost and low efficiency.

*c) DC Collection – DC Transmission (turbine step-up)*

The final HVDC collection, only use single DC/DC converters are connected directly to each turbine as shown in Fig. 3 (c). Hence, only two levels are used and the losses at the distribution level are reduced, because of the high voltage [30]. Nevertheless, the output rectifier of the DC-DC converter needs to be designed for the transmission voltage with quite a low power level e.g. 160 kV at 5 MW, which could reduce the efficiency of these converters [31]-[32].

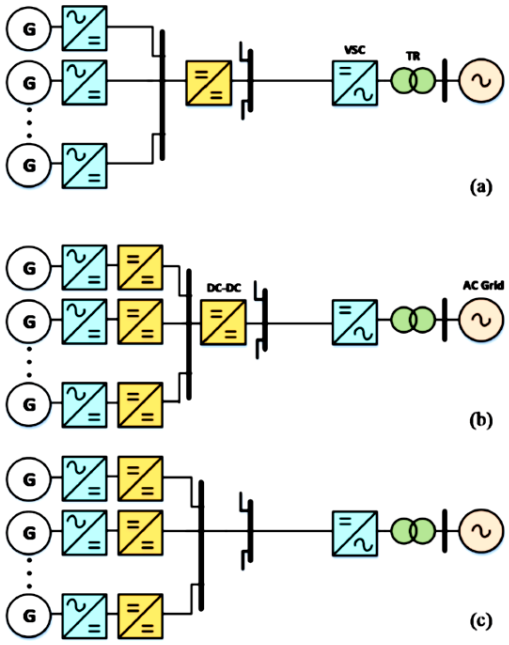


Fig. 3. Different configurations for the dc grid. (a) One cluster step-up. (b) Two step-ups. (c) Turbine step-up [30].

## IV. CONCLUSIONS

Offshore wind farm technology has experienced a major transformation in terms of both the level of installed capacity and the technological maturity. All indications are that there is a further significant growth potential in the years ahead. This paper has highlighted the main features of HVDC systems. It has made a comparison with HVAC systems and shown that HVDC systems have good characteristics interms of electrical, economic and environmental considerations.

VSC-based HVDC system is a viable transmission connection for large offshore wind farms, especially when long distances are involved. HVDC and HVAC connection systems for offshore wind power plants have been proposed, which HVDC would offer lower cost, higher efficiency, and enhanced grid support in comparison with AC solutions.

By eliminating the offshore substation and having grid interface converters at the onshore substation, the overall system maintainability and availability would be greatly improved. This design concept may become attractive as wind farms move into deeper water and offshore platforms potentially become even more expensive.

There is no available high power MV DC-DC converter for offshore wind farm energy system at present, but a number of different topologies have been studied recently. The specification requirements of high power MV DC-DC converters, because the offshore wind farm with MVDC-grid

collection does not exist today, but is a promising alternative, specification analysis of high power MV DC-DC converter is necessary.

## REFERENCES


[1] Y. A. Kaplan, "Overview of wind energy in the world and assessment of current wind energy policies in Turkey," *Renew. Sustain. Energy Rev.*, vol. 43, pp. 562–568, 2015.

[2] K. Dai, A. Bergot, C. Liang, W.-N. Xiang, and Z. Huang, "Environmental issues associated with wind energy – A review," *Renew. Energy*, vol. 75, pp. 911–921, 2015.

[3] S. K. Chaudhary, R. Teodorescu, and P. Rodriguez, "Wind Farm Grid Integration Using VSC Based HVDC Transmission - An Overview," *2008 IEEE Energy 2030 Conf.*, 2008.

[4] a. Tabassum, M. Premalatha, T. Abbasi, and S. a. Abbasi, "Wind energy: Increasing deployment, rising environmental concerns," *Renew. Sustain. Energy Rev.*, vol. 31, pp. 270–288, 2014.

[5] J. Serrano González, M. Burgos Payán, and J. Riquelme Santos, "Optimum design of transmissions systems for offshore wind farms including decision making under risk," *Renew. Energy*, vol. 59, pp. 115–127, 2013.

[6] D. Xu, G. Mu, H. Liu, and G. Yan, "Assessment on large-scale offshore wind farm integration," no. 59937150, pp. 556–559, 2014.

[7] C. N. Mau, K. Rudion, a. Orths, P. B. Eriksen, H. Abildgaard, and Z. a. Styczynski, "Grid connection of offshore wind farm based DFIG with low frequency AC transmission system," *IEEE Power Energy Soc. Gen. Meet.*, pp. 1–7, 2012.

[8] J.-G. Lee, U. A. Khan, S.-W. Lim, W. Shin, I.-J. Seo, and B.-W. Lee, "Comparative Study of Superconducting Fault Current Limiter both for LCC-HVDC and VSC-HVDC Systems," *Phys. C Supercond. its Appl.*, 2015.

[9] "Onshore Wind Cost Reduction Taskforce Report," no. April, 2015.

[10] F. Blaabjerg, "Future on Power Electronics for Wind," vol. 1, no. 3, pp. 139–152, 2013.

[11] Y. Zhou, D. E. Macpherson, W. Blewitt, and D. Jovcic, "Comparison of DC-DC converter topologies for offshore wind-farm application," *6th IET Int. Conf. Power Electron. Mach. Drives (PEMD 2012)*, pp. A12–A12, 2012.

[12] W. Chen, a Q. Huang, C. Li, G. Wang, and W. Gu, "Analysis and Comparison of Medium Voltage High Power DC/DC Converters for Offshore Wind Energy Systems," *Power Electron. IEEE Trans.*, vol. 28, no. 4, pp. 2014–2023, 2013.

[13] S. M. Muyeen, R. Takahashi, and J. Tamura, "Operation and Control of HVDC-Connected Offshore Wind Farm," *IEEE Trans. Sustain. Energy*, vol. 1, no. 1, pp. 30–37, 2010.

[14] M. Cheng and Y. Zhu, "The state of the art of wind energy conversion systems and technologies : A review," *Energy Convers. Manag.*, vol. 88, pp. 332–347, 2014.

[15] B. K. Sahu, M. Hiloidhari, and D. C. Baruah, "Global trend in wind power with special focus on the top five wind power producing countries," *Renew. Sustain. Energy Rev.*, vol. 19, pp. 348–359, 2013.

[16] C. Feltes, S. M. Ieee, F. W. Koch, J. Fortmann, and M. Ieee, "Offshore Wind Power Generation Technologies," 2013.

[17] S. J. Shao and V. G. Agelidis, "Review of DC System Technologies for Large Scale Integration of Wind Energy Systems with Electricity Grids," *Energies*, vol. 3, no. 6, pp. 1303–1319, 2010.

[18] Decc, "UK Renewable Energy Roadmap," *Carbon N. Y.*, vol. 5, no. November, pp. 293–298, 2011.

[19] O. H. Germany and D. Infi, "Wind Energy," *Wind Energy*, 2001.

[20] H. Guo, K. Rudion, and Z. a. Styczynski, "Integration of large offshore wind farms into the power system," *2011 EPU-CRIS Int. Conf. Sci. Technol.*, pp. 1–6, 2011.

[21] C. Zhan, C. Smith, a. Crane, a. Bullock, and D. Grieve, "DC transmission and distribution system for a large offshore Wind Farm," *9th IET Int. Conf. AC DC Power Transm. (ACDC 2010)*, pp. O46–O46, 2010.

[22] a. Madariaga, J. L. Martin, I. Zamora, I. Martínez De Alegría, and S. Ceballos, "Technological trends in electric topologies for offshore wind power plants," *Renew. Sustain. Energy Rev.*, vol. 24, pp. 32–44, 2013.

[23] I. M. de Alegría, J. L. Martín, I. Kortabarria, J. Andreu, and P. I. Ereño, "Transmission alternatives for offshore electrical power," *Renew. Sustain. Energy Rev.*, vol. 13, no. 5, pp. 1027–1038, 2009.

[24] D. Velasco, C. L. Trujillo, and R. a. Peña, "Power transmission in direct current. Future expectations for Colombia," *Renew. Sustain. Energy Rev.*, vol. 15, no. 1, pp. 759–765, 2011.

[25] M. R. Islam, S. Mekhilef, and R. Saidur, "Progress and recent trends of wind energy technology," *Renew. Sustain. Energy Rev.*, vol. 21, pp. 456–468, 2013.

[26] G. Corbetta, "EWEA: The European offshore wind industry - key trends and statistics 2013," no. January, 2014.

[27] P. Bresesti, W. L. Kling, R. L. Hendriks, and R. Vailati, "HVDC connection of offshore wind farms to the transmission system," *IEEE Trans. Energy Convers.*, vol. 22, no. 1, pp. 37–43, 2007.

[28] A. Prof, E. G. Sava, A. Prof, and E. Sorina, "Assessment of collector networks For offshore wind power plants assessment of collector collec tor networks for offshore wind power," no. 3, pp. 225–230, 2013.

[29] K. Sano and M. Takasaki, "A boost conversion system consisting of multiple DC-DC converter modules for interfacing wind farms and HVDC transmission," *2013 IEEE Energy Convers. Congr. Expo. ECCE 2013*, pp. 2613–2618, 2013.

[30] C. Meyer, M. Hoing, a. Peterson, and R. W. De Doncker, "Control and Design of DC-Grids for Offshore Wind Farms," *Conf. Rec. 2006 IEEE Ind. Appl. Conf. Forty-First IAS Annu. Meet.*, vol. 3, no. 6, pp. 1475–1482, 2006.

[31] J. Pan, S. Bala, M. Callavik, and P. Sandeberg, "DC Connection of Offshore Wind Power Plants without Platform," no. November, pp. 11–13, 2014.

[32] M. Rahman, F. Rabbi, K. Islam, and F. M. M. Rahman, "HVDC over HVAC Power Transmission System : Fault Current Analysis and Effect Comparison," 2014.

# High Voltage Cascaded Step-Up DC-DC Marx Converter for Offshore Wind Energy Systems

S. M. Alagab[1], S.B. Tennakoon[1] and C.A. Gould[1]
[1]SCHOOL OF CREATIVE ARTS AND ENGINEERING, STAFFORDSHIRE UNIVERSITY
College Road – Stoke on Trent, ST4 2DE
United Kingdom
Tel.: +447440012994
E-mail: samir.alagab@research.staffs.ac.uk, S.B.Tennakoon@staffs.ac.uk, C.A.Gould@staffs.ac.uk
URL: http://www.Staffs.ac.uk

## Keywords

«Emerging technology», «Wind Energy», «Converter circuit», «HVDC», « Multilevel converters », «Soft switching».

## Abstract

This paper presents an improved cascaded DC-DC resonant converter for offshore windfarms. The improvements are reduced losses and the number of components. The topology is based on the Marx principle where charged capacitors are charged in parallel and discharged in series to achieve the voltage transformation. The four inductors of the converter are designed to resonate with the capacitors to create resonance forcing current zeros to enable zero current switching thereby reducing switching losses. The operating principles and design considerations of the proposed converter are discussed and the design equations are presented. In order to evaluate the operation of 50 MW converter aimed at connecting a 30 kV DC Busbar in a wind power collection system to a 360 kV high voltage DC bus for transmission to the onshore grid was simulated and the results are presented.

## Introduction

Due to the increased distances to off shore windfarms from the shore, it is expected that the use of High Voltage Direct Current (HVDC) transmission and Medium Voltage Direct Current (MVDC) distribution systems for the grid integration of windfarms will grow worldwide. One of the key components in such systems is the DC-DC converter, required to act as the interface between the generation, transmission and distribution voltage levels [1]. Well-established DC-to-DC converters based on pulse width modulated (PWM) converters, which require high frequency switching, are not suitable. Application to high voltage, high power systems mean series connection of devices and high power losses [2]. Hence, such converters are not technically and economically feasible.

Some converter topologies, which are suitable for high-voltage operation, have been proposed in the literature. Laird [3] and Alagab [1] have proposed suitable step-up converters. The drawback of these converters is the limited voltage gain. The coupled inductor boost converter and cascaded boost converter presented by Hu [4] and Noui [5] has the advantage of low input current ripple, but its efficiency decreases with increasing power and its switching frequency is high.

Siwakoti, [6], has presented a high step-up DC–DC converter based on a switched coupled inductor arrangement. The converter draws a continuous current from the source, and its voltage gain is controlled by the duty-cycle. A step up resonant converter was introduced by Parastar [7]; the drawback of this converter is the high voltage across the passive components and large power device conduction losses. Modular multilevel converters (MMC) [8]-[9] are proposed for HVDC connected offshore wind

farms. However, the number of IGBT switches is high. The MMC requires a complex capacitor voltage balancing control scheme.

Recently, the common types of Switched Capacitor Converters (SCC) based on the Marx principle have been considered as an alternative topology. The Marx principle allows the realization of a high voltage gain by connecting the capacitors that are charged in parallel and reconnected in series to discharge. Maneiro [10] presented a shunt HVDC tap using a step down DC to DC converter. This arrangement rquires a large number of IGBT switches.

Veilleux [11,12] DC-DC resonant converter topologies based on the Marx principle, although performs well, the conduction losses are relatively high due to the large number of IGBTs. Improvements were made to reduce the number of IGBTS through a multistage arrangement

## Etienne Veilleux Cascaded topology

As depicted in Fig. 1, there are multi stages of the Marx modules connected in cascade comprising three main sections of input, middle and output section. The middle section consists of three stages, stage 1, stage 2, and stage 3. Stage 1 and stage 3 are identical but the size of the components are different and every stage consists of two capacitors, three switches, two diodes and an inductor. Stage 2 has three capacitors, four switches and three diodes. The overall DC voltage gain is 2x3x2= 12, (1:12). In addition, there is an output capacitor at the output stage to smoot the load voltage. The operation can be divided into two sub-commutations.

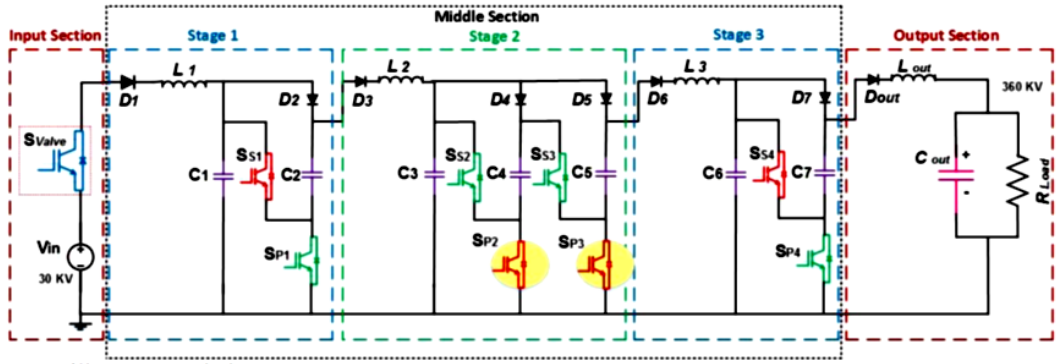


Fig. 1: Veilleux Cascaded Marx DC-DC converter

The charging currents flow through $L_1$ and $L_3$. There are no currents in $L_2$ and $L_{out}$. In the second sub-commutation, capacitors in stages 1 and 3 are connected in series and discharge to stage 2 and the output section respectively. Stage 2 capacitors are connected in parallel during this period. The charging currents flow through $L_2$ and $L_{out}$. There is no current flow in $L_1$ and $L_3$.

The process is repeated periodically transferring the electric charges from the input voltage $V_{in}$ to the load $R_{load}$ via stages 1, 2, and 3. A disadvantage of this topology is the high number of IGBT switches in stage 2, and the increasing voltage stress in the IGBTs in successive stages.

## Proposed topology

### Structure of Cascaded Converter

The structure of the proposed Cascaded DC-DC converter as depicted in Fig. 2 is derived from the Etienne Veilleux converter by modifying the middle section. The advantage is that the number of components are reduced as shown later in the document and the flexibility for increasing the number of stages in the middle section for increasing the gain. The ratings and the component values used for this study are determined for application to the HV converter in a typical wind energy system [Fig. 6]. Fig. 2 shows the equivalent circuit. The input section consists of an input DC voltage source of magnitude $V_{in}$ = 30 kV and HV valve ($S_{valve}$) comprising series connected IGBTs. The middle section is composed of three stages; stage 1, stage 2 and stage 3. The number of capacitors in stages 1, 2 and 3 are set to 2,

3, and 2 respectively to create a voltage amplification of 2x3x2= 12. However, in general, the number of capacitors can be J, K and L respectively and hence; $C_J$, $C_K$ and $C_L$ indicate the capacitances in the stages 1, 2, and 3 respectively.

The switching components in the middle section denoted by Ssi (i=1-4) are used to connect the capacitors in series. The IGBT switches denoted by $S_{Pi}$ (i=1-3) are used to connect the capacitors in parallel. The diodes are used to trap the charges in the capacitors and to ensure that they discharge in the correct direction. The output section consists of an output diode $D_{out}$ connected in series with the output inductor $L_{out}$, and one output capacitor $C_{out}$. The load is modeled by a pure resistor $R_{load}$.

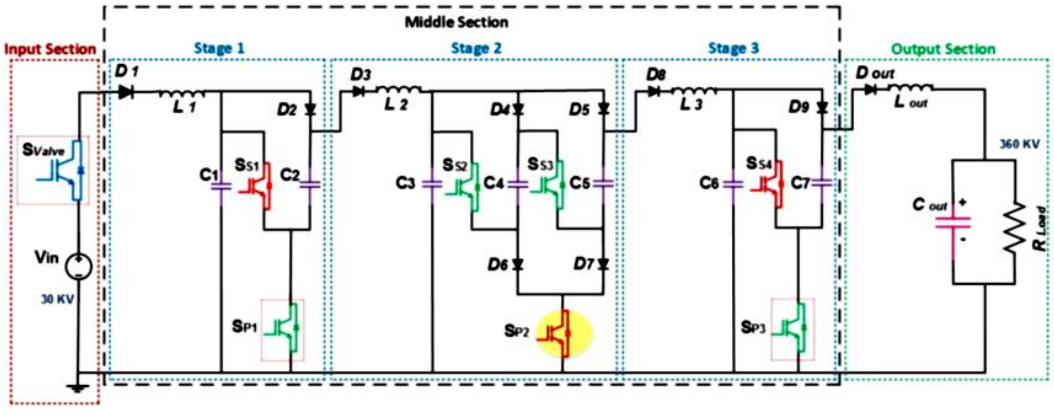


Fig. 2: Improved Cascaded Marx DC-DC Converter

## Steady State Operation

The steady state operation can be explained in terms of two sub-commutations. In simple terms, the IGBTs are switched so that the charges in capacitors are pumped from left to right sequentially resulting in a high voltage at the converter output. The switching of the devices are summarised in Table I. The corresponding sub-circuits are shown in Fig 3 and Fig 4, respectively where the ON and OFF devices are shown in green and light grey, respectively. During the first sub-commutation, capacitors in stages 1 and 3 are connected in parallel and are being charged through the inductors $L_1$ and $L_3$. The capacitors in Stage 2, which have been charged in the previous cycle are in series and discharges into stage 3 capacitors. Diodes $D_1$, $D_2$, $D_8$ and $D_9$ conduct.

**Table I: IGBT switching logic for the improved converter**

| Switches | $S_{Vlave}$ | $S_{P1}$ | $S_{P2}$ | $S_{P3}$ | $S_{S1}$ | $S_{S2}$ | $S_{S3}$ | $S_{S4}$ | $D_1$ | $D_2$ | $D_3$ | $D_4$ | $D_5$ | $D_6$ | $D_7$ | $D_8$ | $D_9$ | $D_{out}$ |
|---|---|---|---|---|---|---|---|---|---|---|---|---|---|---|---|---|---|---|
| First sub commutation | 1 | 1 | 0 | 1 | 0 | 1 | 1 | 0 | 1 | 1 | 0 | 0 | 0 | 0 | 0 | 1 | 1 | 0 |
| Second sub commutation | 0 | 0 | 1 | 0 | 1 | 0 | 0 | 1 | 0 | 0 | 1 | 1 | 1 | 1 | 1 | 0 | 0 | 1 |

In the second sub commutation the devices are switched so that capacitors in stage 1and 3 and stage 2 are in parallel and series respectively. Hence, capacitors in stages 1 and 3 and 2 are charged and discharged respectively. Repeated switching results in continuous transfer of charge from input side to the output side resulting in a voltage gain of 12, which is equal to the product of number of capacitors (2x3x2) in each stage. The corresponding voltage and current waveforms are given in Fig. 5

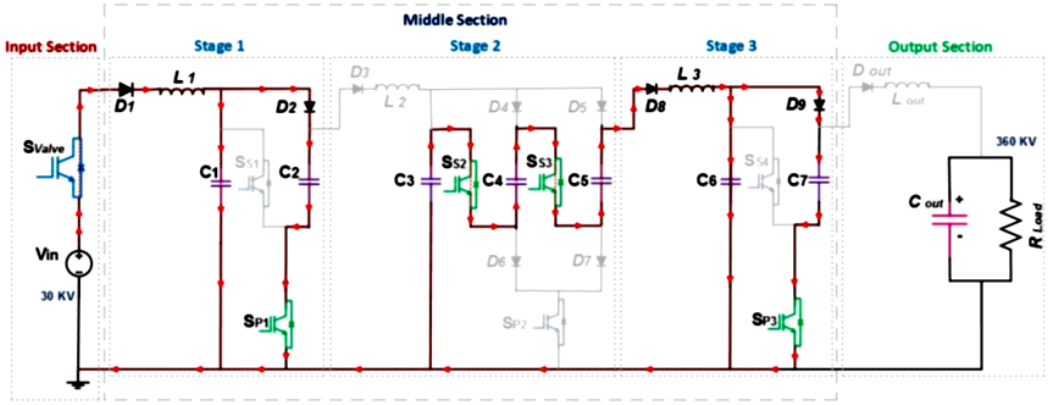


Fig. 3: First sub-commutation configuration

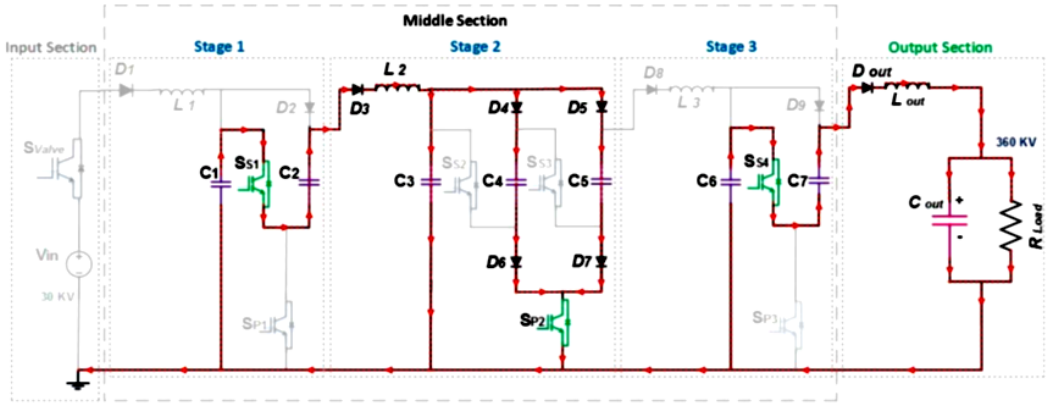


Fig. 4: Second sub-commutation configuration

## Generalised analysis of the steady state operation

It is assumed that the cascaded DC-DC converter has already reached steady state. The gain of the converter is depended on the number of capacitance cells in stage 1 (J), stage 2 (K), stage 3 (L). The voltage transformation ratio N is given as;

$$N = \frac{V_{out}}{V_{in}} = J\,K\,L \tag{1}$$

where $V_{out}$ and $V_{in}$ are the output and input voltages, respectively. The equivalent capacitance in stage 1 is

$$C_{eq(J)} = \sum_{J=1}^{J} C_j \tag{2}$$

where $C_J$ is the capacitance, and $C_{eq(J)}$ is the equivalent capacitance of parallel connected capacitors in stage 1. During the first-commutation, the inductor $L_1$ and the equivalent capacitance $C_{eq\,(J)}$ forms an oscillatory L-C circuit and hence the current in the stage 1 is given by,

$$i_{L1} = i_{Ceq\,(J)} = \frac{V_{in}}{\omega L_1} \sin(\omega t) \tag{3}$$

and

$$\omega = \frac{1}{\sqrt{L_1 C_{eq(J)}}} \tag{4}$$

where $i_{Ceq\,(J)}$ is the current in $C_{eq\,(J)}$. As shown in Fig. 5(a), the peak current in the inductor $I_{L1}^{P}$ can be deduced form the equation (3);

$$I_{L1}^{P} = V_{in}\sqrt{\frac{Ceq\,(J)}{L_1}} \tag{5}$$

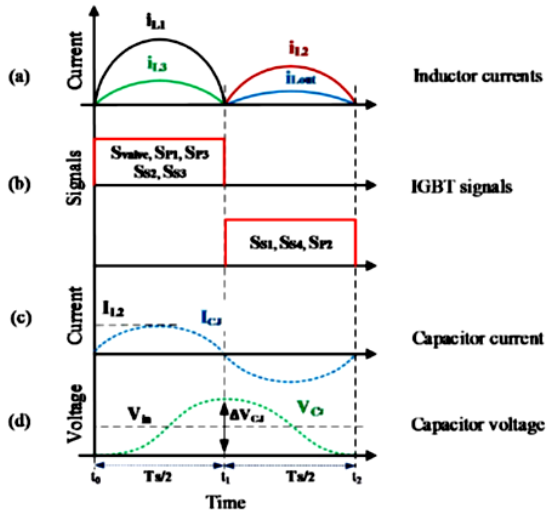


Fig. 5: Ideal steady state waveforms

In order to achieve soft switching, the IGBTs must be switched at the resonant frequency of the inductor current waveform. Therefore, the switching frequency can be written as;

$$F_S = \frac{1}{2\pi\sqrt{L_1 C_{eq\,(J)}}} \tag{6}$$

**Determination of stage 1 parameters**

The charge transferred to the capacitors in stage 1 can be expressed as;

$$Q = I_{AV}\, T_S \tag{7}$$

where $I_{AV}$ is the average of current in inductor $L_1$ and $T_S$ is the switching period. Assuming no losses within the converters, it can be shown that

$$Q = \frac{P_{rated}}{NV_{in}}\, T_S \tag{8}$$

where $P_{rated}$ is the rated power, Q is the amount of charge in the switching period and $T_S = (1/F_S)$. Hence,

$$Q = \frac{P_{rated}}{NV_{in}\, F_S} \tag{9}$$

From Fig. 5(d), the charge transferred to stage 1capacitors results in a voltage change of $\Delta V_{CJ}$, which is given by;

$$\Delta V_{C(J)} = \frac{Q}{C_{eq\,(J)}} \tag{10}$$

Substituting for Q from equation (9) to equation (10) and rearranging;

$$C_{eq\,(J)} = \left(\frac{P_{rated}}{NV_{in}\ \Delta V_{C(J)}\ F_S}\right) \tag{11}$$

Hence,

$$C_J|_{j=1,J} = \left(\frac{P_{rated}}{NV_{in}\ \Delta V_{C(J)}\ F_S}\right)\ \frac{1}{J} \tag{12}$$

Substituting for $F_S$ from equation (6) into equation (9) and rearranging $L_1$ can be expressed as;

$$L_1 = \frac{1}{C_{eq\,(J)}}\ \left[\ \frac{Q\,NV_{in}}{2\pi\,P_{rated}}\ \right]^2 \tag{13}$$

**Determination of stage 2 parameters**

Capacitance values in stage 1, 2 and 3 are chosen so that percent ripple on all the capacitors are the same. This means:

$$C_K = \frac{C_J}{J+K+L} \tag{14}$$

In order to ensure soft switching the resonant frequency in the second sub-commutation must be made equal to ω. Hence,

$$\omega = \frac{1}{\sqrt{L_2\left[C_{eq\,(J)} + C_{eq\,(K)}\right]}} \tag{15}$$

where ω is the resonant Frequency of the converter and $C_{eq\,(K)}$ is the equivalent capacitance of both stages $C_J$ in series and $C_K$ in parallel. As shown in Fig.4, the number of capacitors in stage 2, (K) are connected and charged by the number of series capacitors in stage 1 (J). Therefore, the equivalent capacitance of this state is given as;

$$C_{eq} = \frac{(C_J/2)(3C_K)}{(C_J/2)+(3C_K)} \tag{16}$$

By combining Equation (15) and (16), equation (17) can be written as:

$$L_2 = \left(\frac{2K^n}{C_{eq(K)}}\right)\left(\frac{C_J}{J^n}\right)^2 \tag{17}$$

**Determination of stage 3 parameters**

The capacitors in stage 3 is given by equation (19), and in the same way of inductor $L_2$ was derived, Inductor $L_3$ can be obtained as;

$$L_3 = \left(\frac{2L^n}{C_{eq(L)}}\right)\left(\frac{C_K}{K^n}\right)^2 \tag{18}$$

and

$$C_L = \frac{C_K}{J+K+L} \tag{19}$$

Although, two capacitors are shown in Fig. 2. In general, there can be J capacitors. Therefore, capacitance in the stage 1 is denoted by $C_J$. Similarly, number of capacitor in the stage 2 and stage 3 are denoted by $C_K$ and $C_L$, respectively.

The relationship between ripple voltage and capacitor voltage in the first stage is the same in stages 2 and 3, and can be shown as:

$$\frac{\Delta VC_J}{VC_J} = \frac{\Delta VC_K}{VC_K} = \frac{\Delta VC_L}{VC_L} \tag{20}$$

**Determination of output section parameters**

As illustrated in Fig. 4, the output stage is charged from ($t_0$-$t_1$), and the electric charge in stage 3 is transferred in series to the output capacitor $C_{out}$ through an output inductor $L_{out}$ and an output diode $D_{out}$. The size of the output inductor depends on the output voltage and the amount of charges that needs to be transferred. The value of output inductor depends on the peak-to-peak of output current $\Delta I_{Lout}$ can therefore be expressed as;

$$L_{out} = \left(\frac{NV_{in}\, T_s}{\Delta I_{Lout}}\right) \tag{21}$$

The output voltage waveform is not similar to the other voltage capacitor waveforms in the middle stage. Nevertheless, the value of the output capacitor depends on the relation between the amount of charge to the load at half period of time $T_S/2$ and the voltage ripple on the output capacitor. Furthermore, the output capacitor works as charge storage for continuous delivery to the load. The equation can be written as:

$$C_{out} = \frac{\left(P_{rated}/V_{out}\right)\left(T_S/2\right)}{2\pi\, \Delta VC_{out}} \tag{22}$$

## Simulation studies

The arrangement and location of the proposed converter is shown in Fig. 6, which forms the basis for the simulation study. In this topology, the cluster is formed by two parallel lines of wind turbines, each containing 5 wind turbines in series. Hence, there is a total of 10 wind turbines; each rated at 5 MW, 1.2 kV [13],[14]. Therefore, the cluster bus voltage is 6 kV and the rated power is 50 MW. The medium voltage (MV) DC-DC converter boosts the voltage from 6 kV to 30 kV. A submarine cable is used to connect the MV converter platform to the main bus of the HV converter.

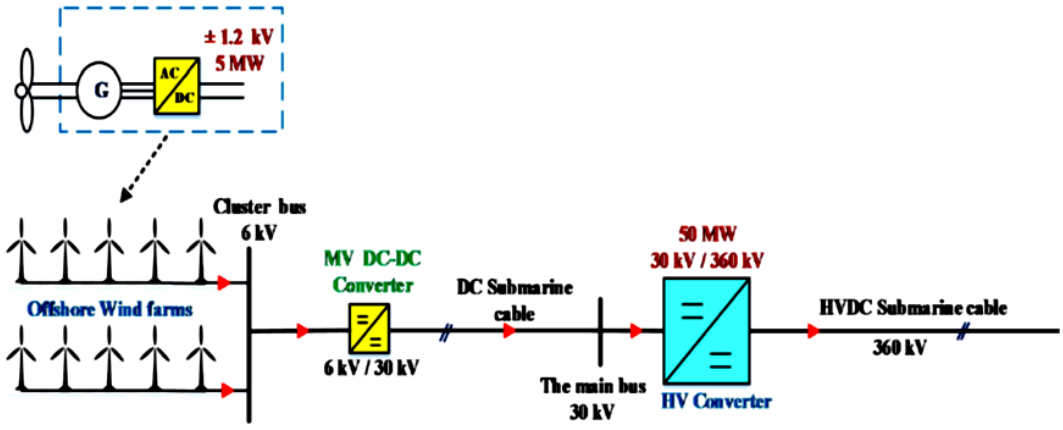


Fig. 6: Electrical system for the Grid Connection of a Windfarm

The HV converter, whose equivalent circuit is shown in Fig. 2, was simulated by Matlab/Simulink software package. The converter parameters (Table II) were calculated using the design equations derived in the previous section.

**Table II: Parameters used for cascaded DC-DC converter simulation**

| Parameter | | | Value/ model |
|---|---|---|---|
| Number of stages | n | | 3 |
| Number of capacitors in each stage | J K L | | 2, 3, 2 |
| Input Voltage | $V_{in}$ | | 30 kV |
| Output Voltage | $V_{out}$ | | 360 kV |
| Load Current | $L_{out}$ | | 138.89 A |
| Rated power | $P_{rated}$ | | 50 MW |
| Switching Frequency | $F_S$ | | 2 kHz |
| Output Load Resistance | $R_{Load}$ | | 2592 Ω |
| IGBT | | | 5SNA 1200G450300 |
| Fast recovery diode | | | 5SDF13H4501 |
| Capacitors | | Inductors | |
| $C_J$ | 694.5 µF | $L_1$ | 5.3 µH |
| $C_K$ | 99.21 µF | $L_2$ | 40 µH |
| $C_L$ | 14.17 µF | $L_3$ | 400 µH |
| $C_{out}$ | 300 µF | $L_{out}$ | 2.2 mH |

Current waveforms in Fig. 7(a) shows the resonant nature of the currents through inductors and IGBTs allowing soft switching at current zeros leading to a reduction in switching losses. Figure 7(b) shows the switching signals clearly indicating soft switching at a frequency of 2 kHz.

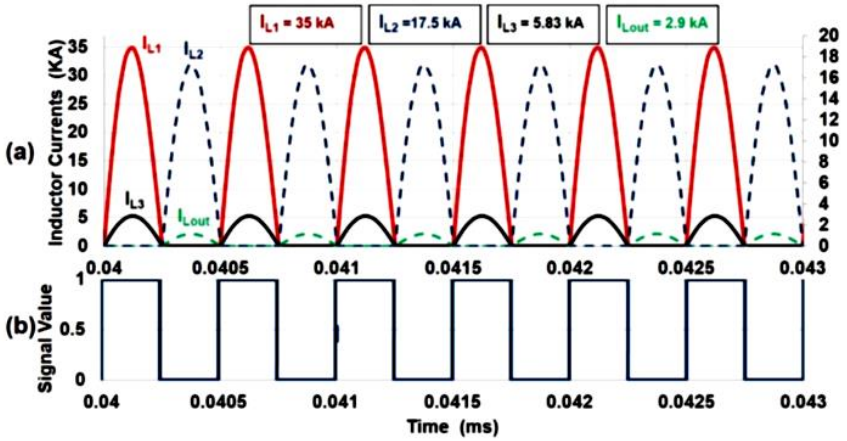


Fig. 7: Matlab / Simulink Simulation results. a) Inductor current waveforms (ZCS), b) switching pattern

Fig. 8 shows the load voltage and current waveforms confirming that the design specifications are met. The DC amplification gain of the simulation is 11.96, which is very close to the design value of 12. The resonating inductor current, which flows through the IGBT increases to a peak $I_{L1}$= 35 KA in 250 µs, which is within the capability of modern IGBTs [15]. As seen from Fig. 7, the respective peak inductor currents in consequent stages decrease according to the number of capacitors in the previous stage. The effect can be generalised as shown in Table III. The proposed cascaded configuration is evaluated and compared with Veilleux converter in terms of the power device count to highlight its advantages in high-voltage applications. The high voltage with a maximum blocking voltage rated up the ratings of the IGBT considered for this study are 4.5 kV and 1200 A. The total number of IGBTs

can be reduced from 52 to 38 by combining the function of 2 IGBT switches ($S_{P2}$-$S_{P3}$) to be performed by 2 diodes and 1 IGBT (Svalve) as illustrated in the yellow circle in Fig.2.

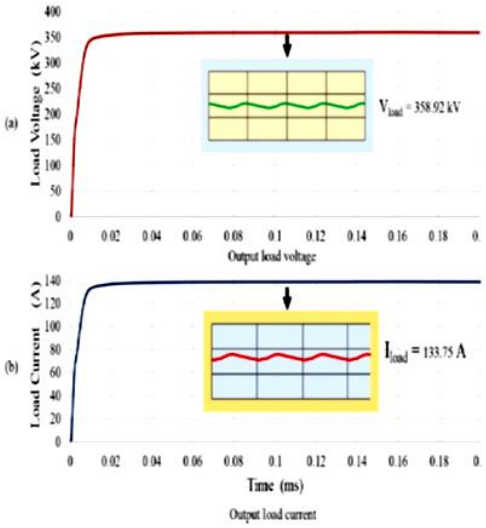


Fig. 8: Simulation waveforms of the improved topology

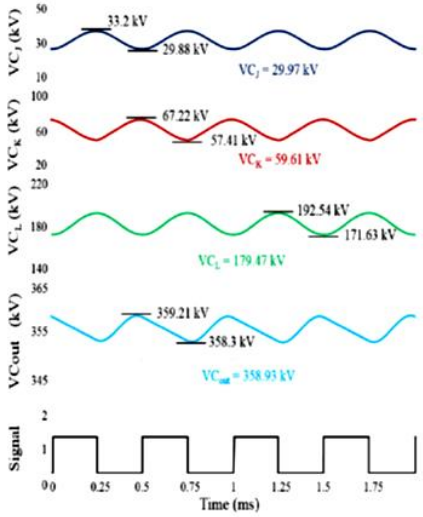


Fig. 9: Simulation results Capacitor voltage waveforms

**Table III: shows the peak inductor currents and voltage across capacitors**

| Parameters | Stage 1 | Stage 2 | Stage 3 | Output section |
|---|---|---|---|---|
| Number of capacitors | *2* | *3* | *2* | *1* |
| Peak inductor currents relation | $I_{L1}$ | $I_{L2} = I_{L1}/2$ | $I_{L3} = I_{L2}/3$ | $I_{Lout} = I_{L3}/2$ |
| Number of stages | *J* | *K* | *L* | $L_{out}$ |
| Peak inductor currents | $I_{L1}^{P}$ | $I_{L2}^{P} = I_{L1}^{P}/J$ | $I_{L3}^{P} = I_{L2}^{P}/K$ | $I_{out}^{P} = I_{L3}^{P}/L$ |
| Voltage cross capacitors | $V_{C1}=V_{C2}=V_{in}$ | $V_{C3}=V_{C4}=V_{C5}=JV_{in}$ | $V_{C6}=V_{C7}=JKV_{in}$ | $V_{out}= JKLV_{in}$ |

As shown in Fig. 9, the average DC voltages a cross capacitors increase and their values depend of the number of capacitors in each stage as depicted in the Table III. Capacitor voltage in stage 1, stage 2, and stage 3 is charging by 29.97 kV, 59.69 kV and 179.47 kV, respectively. The discrepancy between design charging voltage and simulation results is mainly due to small resistance of the IGBT switches and diodes, which have been omitted in the mathematical analysis equations but it is included in the simulation.

Fig. 10 shows that the output voltage in the improved converter is higher than that of Veilleux converter, but both topologies perform equally well. Several HV DC-DC topologies that have a high gain ration, but not always with reduced number of semiconductor component as one of the major goals. Therefore, the improved topology concentrated on reducing the number of devices.

The total number of devices for varying voltage gains are shown in Fig. 11 that shows the device count comparison with different gains between the Veilleux Cascaded converter and the improved cascaded converter. For both configuration, IGBT switches are comprised of several series connected power devices to withstand the rated voltage.

Fig. 11 shows the comparison of designs to give voltage gains of 1:12, 1:27, and 1:36. The number of reduces by 27%, 30% and 37% as the gain increases by 12, 27, and 36, respectively. However, the diode count increases by a small margin. However, diodes are cheaper and easy to connect in series.

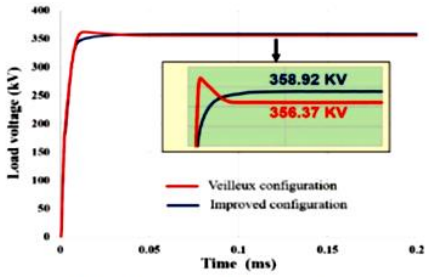


Fig. 10: Load voltage comparisons between Veilleux converter and improved converter

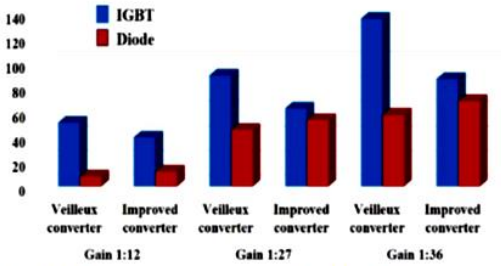


Fig. 11: Components count for DC-DC converter topologies comparisons between Veilleux converter and improved converter

## Conclusions

In this paper, the analysis, design and simulation of a high voltage cascaded DC-DC converter using a multi-stage topology suitable for HVDC offshore wind farm applications is presented. This converter can achieves gain with reduced components. The reduction increases with the increase in voltage gain. Soft switching can be implemented and a method for calculating the resonant component values and the switching frequency is given. A design methodology and equations for the determination of the circuit components and solid-state devices is presented. The theoretical predictions have been confirmed by the simulations.

## References

[1] S. M. Alagab, S. Tennakoon, and C. Gould.: Review of wind farm power collection schemes, staffordshire University. Power Eng. UPEC Conf., vol. 2015–Novem, 2015.

[2] M. H. Johnson, D. C. Aliprantis, and H. Chen.: Offshore wind farm with DC collection system, 2013 IEEE Power Energy Conf. Illinois, PECI 2013, pp. 53–59, 2013.

[3] I. Laird and D. D. C. Lu.: High step-up DC/DC topology and MPPT algorithm for use with a thermoelectric generator, IEEE Trans. Power Electron., vol. 28, no. 7, pp. 3147–3157, 2013.

[4] Xuefeng Hu and Chunying Gong.: A High Voltage Gain DC-DC Converter Integrating Coupled-Inductor and Diode& IEEE Trans. Power Electron., vol. 29, no. 2, pp. 789–800, 2014.

[5] T. Nouri, S. H. Hosseini, E. Babaei, and J. Ebrahimi.: A non-isolated three-phase high step-up DC-DC converter suitable for renewable energy systems, Electr. Power Syst. Res., vol. 140, pp. 209–224, 2016.

[6] Y. P. Siwakoti, F. Blaabjerg, and P. C. Loh.: High Step-Up Trans-Inverse (Tx −1 ) DC–DC Converter for the Distributed Generation System, IEEE Trans. Ind. Electron., vol. 63, no. 7, pp. 4278–4291, 2016.

[7] A. Parastar.: High Power Step-up Modular Resonant Converter , pp. 3341–3348, 2014.

[8] J. A. Ferreira.: The multilevel modular DC converter, IEEE Trans. vol. 28, no. 10, pp. 4460–4465, 2013.

[9] X. Zhang and T. C. Green.: The New Family of High Step Ratio Modular Multilevel DC-DC Converters, vol. 2, pp. 1743–1750, 2015.

[10] J. Maneiro, S. Tennakoon, and C. Barker.: Scalable shunt connected HVDC tap using the DC transformer concept, 2014 16th Eur. Conf. Power Electron. Appl. EPE-ECCE Eur. 2014, pp. 6–8, 2014.

[11] P. W. Lehn, B.-T. Ooi, and E. Veilleux.: Marx dc–dc converter for high-power application, IET Power Electron., vol. 6, no. April, pp. 1733–1741, 2013.

[12] E. Veilleux and B. T. Ooi.: Marx-dc-dc converter for connecting offshore wind farms to multiterminal HVDC, IEEE Power Energy Soc. Gen. Meet., pp. 1–5, 2013.

[13] P. Lakshmanan, J. Liang, and N. Jenkins.: Assessment of collection systems for HVDC connected offshore wind farms, Electr. Power Syst. Res., vol. 129, pp. 75–82, Dec. 2015.

[14] S. M. Alagab, S. B. Tennakoon, and C. A. Gould.: A Compact DC-DC Converter for Offshore Wind Farm Application, Renew. Energy Power Qual. J., vol. 1, no. 15, pp. 529–533, 2017.

[15] ABB.: Surge currents for IGBT diodes, 2014.

# A novel bidirectional DC-DC converter for offshore DC collection grid

Samir. M. Alagab[1], S. B. Tennakoon[1,2] and C. A. Gould[1]
[1]SCHOOL OF CREATIVE ARTS AND ENGINEERING, STAFFORDSHIRE UNIVERSITY
College Road – Stoke on Trent, ST4 2DE
United Kingdom
Tel.: +447822924000
[2]CARNEGIE MELLON UNIVERSITY AFRICA
Kigali, Rwanda
E-mail: samir.alagab@research.staffs.ac.uk, S.B.Tennakoon@staffs.ac.uk, C.A.Gould@staffs.ac.uk

## Keywords

«Wind Energy », «Emerging topology », «DC collector network», «High voltage power converter»

## Abstract

In this paper, a new bidirectional DC-DC converter based on the Marx principle for offshore windfarms is presented. The proposed topology is named "Bidirectional Modular DC-DC converter" (BMDC). The operating principle and the theoretical analysis of the converter under both boost and buck modes are presented, and demonstrate that a high step-up and step-down voltage gain can be achieved with an appropriate fixed duty ratio. The two inductors of the converter are designed to resonate with the capacitors to create resonance, forcing current zeros to enable zero current switching, and thereby reducing switching losses during both modes of operation. Simulation of a 50 MW, 6 kV/ 30 kV converter with a switching frequency of 2kHz is explained, and the results are presented and discussed.

## Introduction

In Europe, offshore wind farms expect a generation of about 150 TWh by the year 2035, and a further increase to a capacity of 309 TWh by 2050 is expected [1-2]. Researchers are working towards developing the technologies required for realizing a European DC Grid for integrating offshore wind generation in Europe, and the solar generation in North Africa, to the European Grid. As HVDC links at different voltage levels need to be interconnected, bidirectional high power high voltage DC-DC conversion systems are required [3]. A number of DC-DC converter topologies have been presented by a number of researchers. Some of those are briefly highlighted below focusing on their salient features. Isolated bidirectional DC-DC converter topologies [4], [5], [6], [7] need a high-frequency transformer in order to keep the weight and size low. This requires high-frequency switching in the converter leading to high switching losses.

Recently, a class of non-isolated topologies, referred to as Switched Capacitor (SC) topologies, based on the Marx generator principle has been receiving much attention. Maneiro [8] presented a non-isolated DC-DC converter for tapping a proportion of power from an HVDC line which requires a large number of IGBT switches.

In existing non-isolated Marx DC-DC converter topologies [9],[10],[11],[12],[13] power flow is from the wind farm to the onshore substation. However, a proportion of the rated power is needed to be drawn from the onshore substation to the wind farm, because during doldrums (light and calm winds) and for maintenance work, it is necessary to supply the offshore wind farm with auxiliary power. This means the DC-DC converter must be capable of bidirectional power flow. The converter explained by Xing [15] contains a large number of passive components and has a variable duty cycle with hard switching, resulting in high switching losses.

EPE'18 ECCE Europe ISBN: 978 - 9 - 0758 - 1528 - 3 - IEEE catalog number: CFP18850-ART P.1
Assigned jointly to the European Power Electronics and Drives Association & the Institute of Electrical and Electronics Engineers (IEEE)

In this paper, a novel converter topology developed by the authors is presented. The converter, based on the Marx principle is suitable for windfarm application and uses a soft switching technique to minimise the switching losses. Also, it does not require a transformer, thus, reducing volume and weight.

## Bidirectional Modular DC-DC converter

### Converter structure

As shown in Fig 1, the bidirectional DC-DC converter is modular and comprises three circuits. The first circuit consists of an inductor $L_1$ connected in series with the DC input voltage $V_1$ and a capacitor $C_L$ connected in parallel with the input DC voltage.

The second circuit consists of five identical modules. Each module comprises three cells; each cell has two anti-parallel IGBT switches with series diodes and a capacitor for holding the cell voltage as shown in Fig. 1. The converter can be scaled up or down and the voltage transformation ratio can be altered by changing the number of modules. The third circuit consists of an inductor $L_2$ and a capacitor $C_H$.

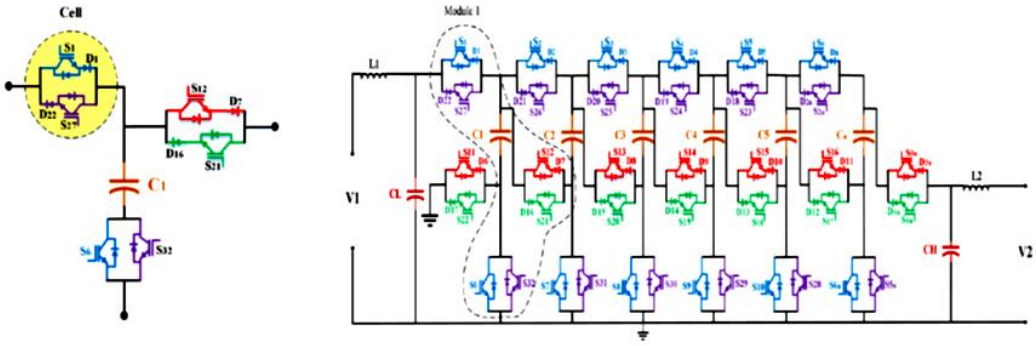


*a)* Module 1 *b)* Converter circuit

Fig. 1: Bidirectional DC-DC converter

### Operating principle

In the studies reported in this paper five modules were used to transform a voltage from 6 kV to 30 kV and vice versa, giving a ratio of 1:5 and applicable to a wide range of power levels up to 50 MW, which is of the order of a bidirectional DC-DC converter required for power collection in a typical wind farm. All the active switches must be capable of bidirectional blocking and forward conducting. The operation of the bidirectional DC-DC converter has two modes of operation; forward and reverse mode.

#### *a) Forward Mode*

The energy flow is from the low voltage $V_1$ to the high voltage $V_2$. In the first half-cycle, the capacitors are charged in parallel as shown in Fig. 2(a). In the second half-cycle, the capacitors are discharged in series in order to boost the voltage. Ideal voltage and current waveforms applicable to the forward operation are shown in Fig. 4.

In the first half cycle $[t_0\text{-}t_1]$ switches $(S_1\text{-}S_{10})$, and $(S_n, S_{6n})$ are turned ON to charge the capacitors $C_1$ to $C_n$; all other IGBT switches are turned OFF. The diodes $D_1$ to $D_n$ blocks reverse current flow ensuring unidirectional transfer of charge.

In the second half cycle $[t_1\text{-}t_2]$ the capacitors that were charged during the first half cycle are discharged in series to create the high voltage on the HV side. In this case, as there are 5 modules the voltage gain is 5. The second cycle is initiated by switching IGBTs $S_{11}$ to $S_{3n}$ 'ON' and switching the devices $S_1$ to $S_{6n}$ 'OFF'. Diodes $(D_6$ to $D_{3n})$ are forward bias and blocks reverse current flow through discharge of the

capacitors in series. The electric charges are transferred from the five series-connected capacitors $C_1$, $C_2$, $C_3$, $C_4$, and $C_5$ to $C_H$ as shown in Fig. 2(b).

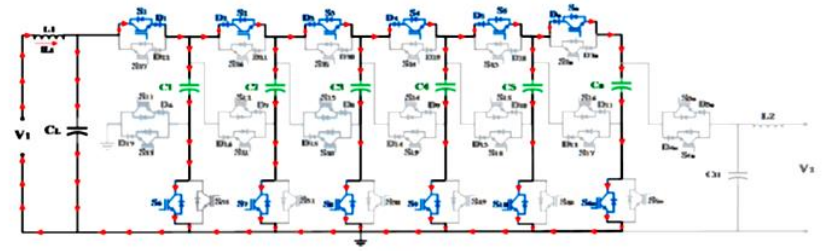

*a) Charging the capacitors in parallel*

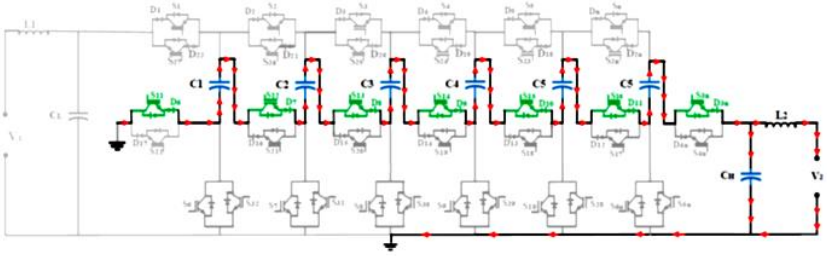

*b) Discharging the capacitors in series*

Fig. 2: Forward mode of operation converter states

### *b) Reverse Mode*

In this mode, the energy flow is from the high voltage $V_2$ to the low voltage $V_1$. In this case, the capacitors are charged in series in the time interval $[t_1\text{-}t_2]$. The switches $S_{4n}$ to $S_{22}$ are turned 'ON'; diodes $D_{4n}$ to $D_{17}$ are forward biased and all of the other IGBT switches are turned 'OFF'. Inductor current $I_{L2}$ flows from high voltage source $V_2$ through the switches $(S_{4n} - S_{22})$ and charges the capacitors $C_1$, $C_2$, $C_3$, $C_4$, $C_5$ and $C_n$ in series. Meanwhile, the diodes $(D_{4n}–D_{17})$ are connected in series with the switches $(S_{4n} - S_{22})$ to ensure unidirectional transfer of charges from the voltage source $V_2$ to series-connected capacitors.

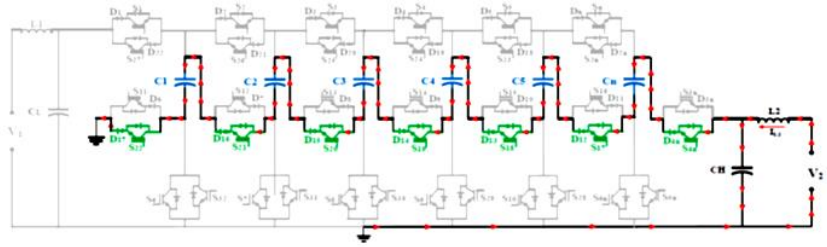

*a) Charging the capacitors in series*

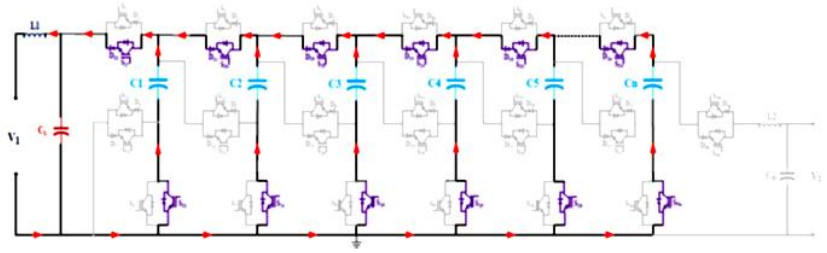

*b) Discharging the capacitors in parallel*

Fig. 3: Reverse mode of operation converter states

The capacitors are discharged in the time interval $[t_2 - t_3]$, where the switches $(S_{2n}, S_{5n})$ and $(S_{23}\text{-}S_{32})$ are turned 'ON', while the switches $(S_{4n} - S_{22})$ and the other switches are turned 'OFF'. The capacitors $C_1$ to $C_n$ are discharged in parallel through the switches $(S_{2n}, S_{5n})$ and $(S_{23}\text{-}S_{32})$ to the input voltage source $V_1$ through the inductor $L_1$. The waveforms are identical to those in Fig. 4 between $t_0$ and $t_1$.

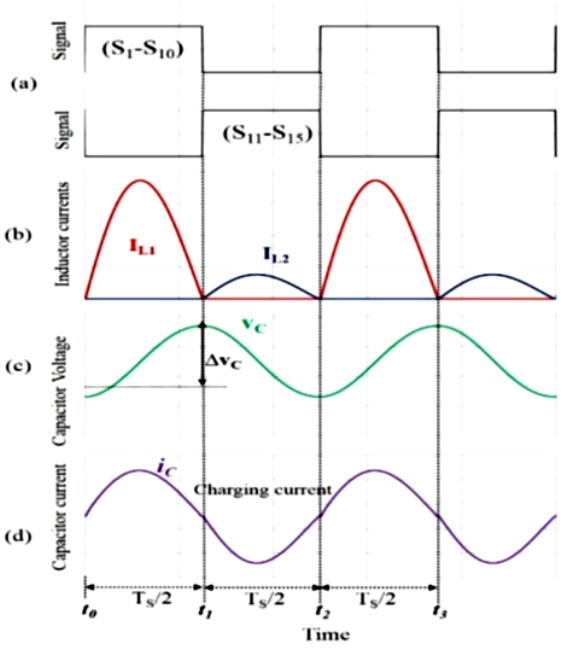


Fig. 4: Ideal steady-state waveforms

## General Analysis

It is assumed that the system has reached the steady-state condition. The converter voltage gain is the same as the number of capacitors "$n$" and hence;

$$n = \frac{V_2}{V_1} \tag{1}$$

when the capacitors are in parallel the equivalent capacitance $C_{eq}$ is given by,

$$C_{eq(P)} = \sum_{i=1}^{n} C_i \tag{2}$$

where $C_i$ is the capacitance of the $i^{th}$ capacitor. The inductor $L_1$ and the equivalent capacitance $C_{eq(P)}$ forms an oscillatory L-C circuit and hence the current in the inductor $L_1$ is a positive half sine wave during the first half cycle, as depicted in Fig. 4(b).

$$i_{L1} = i_{eq(P)} = \frac{V_1}{\omega L_1} \sin \omega (t - t_0) \tag{3}$$

where $\omega$ is the resonance frequency. Hence,

$$\omega = \frac{1}{\sqrt{L_1 C_{eq(P)}}} \tag{4}$$

Considering the rated power of the converter and the charge transfer the inductance $L_1$ can be expressed as:

$$L_1 = \frac{1}{C_{eq(P)}}\left[\frac{Q\,nV_1}{2\pi\,P_{rate}}\right]^2 \tag{5}$$

where $P_{rated}$ is the rating power of the converter. From Fig. 2(c), the charge $Q$ transferred to the capacitor $C_H$ results in a voltage change of $\Delta V_C$, which is given by;

$$\Delta V_C = Q\,C_{eq(P)} \tag{6}$$

Where $\Delta V_C$ is the capacitor voltage ripple and $C_{eq(P)}$ is the equivalent capacitance of parallel-connected capacitors. Hence, the capacitor value is based on the desired capacitor voltage ripple and the amount of charge, therefore, the equivalent parallel capacitance can be calculated as

$$C_{eq(P)} = \frac{\Delta V_C}{Q} \tag{7}$$

Equation (2) gives $C_{eq(P)}$ in terms of individual capacitances. However, individual capacitances have the same value and hence;

$$C_i = \frac{C_{eq(P)}}{n} \tag{8}$$

The value of inductor $L_2$ depends on the peak-to-peak of output current $\Delta I_{LH}$ and can be expressed as;

$$L_2 = \frac{(nV_1 - V_2)}{\Delta I_{LH}} \tag{9}$$

The value of the capacitor $C_H$ depends on the relationship between the amount of charge to output converter voltage $V_2$ at half-period $T_S/2$ and the voltage ripple on the capacitor $C_H$. Hence,

$$C_H = \frac{(P_{rate}/V_2)(T_S/2)}{2\pi\,\Delta V_{CH}} \tag{10}$$

Similarly,

$$C_L = \frac{(P_{rate}/V_1)(T_S/2)}{2\pi\,\Delta V_{CL}} \tag{11}$$

where $C_L$ is the capacitor in the low voltage side $V_1$, and $\Delta V_{CL}$ is the voltage ripple on the capacitor $C_L$

## Grid Connection

The number of conversion stages can be reduced, and transformers can be avoided by using a DC collector network instead of an AC collection system in an offshore wind farm. A possible DC collection and transmission system is shown in Fig. 5, where the cluster is formed by two parallel lines of wind turbines, each containing 5 wind turbines in series [16] and [3]. Hence, there is a total of 10 wind turbines each rated at 5 MW, 1.2 kV [16],[9]. Therefore, the cluster bus voltage is 6 kV and the rated power is 50 MW. The medium voltage (MV) DC-DC converter boosts the voltage from 6 kV to 30 kV. A submarine cable is used to connect the MV converter platform to the main bus of the HV converter.

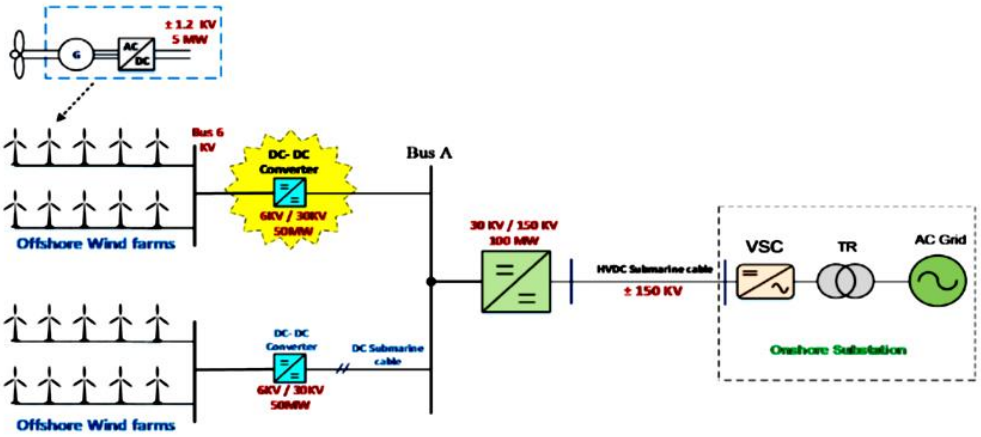


Fig. 5: Electrical system for the Grid Connection of a Windfarm

The location of the new converter studied in this paper is shown within the yellow star in Fig. 5. The proposed converter is used to step-up the low DC voltage from the wind turbine converters, via a DC cable of 116km, to the onshore substation, and step down the high DC voltage form VSC in the onshore station to the wind farm. The DC cable parameters are based on [17],[18]. The system to the right of the Bus A is modelled by referring the parameters of the DC submarine cable and VSC for ease of simulation, as the focus is on the performance of the power collection converter. The resulting simulation model is shown in Fig. 6.

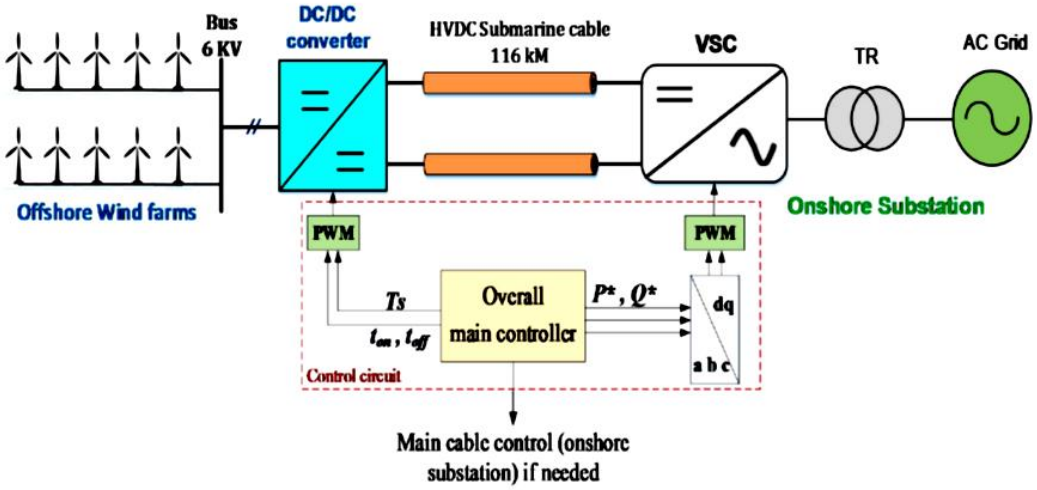


Fig. 6: The model of the DC-DC converter connected to the AC system for simulation

## Power control circuits

### VSC control circuit

In the simulation, the simple 2-level averaged VSC model (Fig. 7) based on direct quadrature *(d-q)* synchronous reference frame is used [5], [19]. The converter controls the exchange of both the active power *P* and the reactive power *Q* between the HVDC system and the local AC grid.

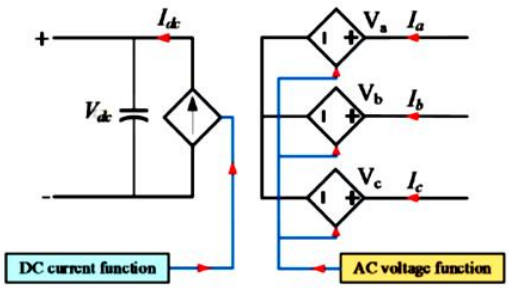


Fig. 7. Averaged model of the VSC

The AC side of the VSC in the phase (*a, b, c*) reference frame is composed of three voltage-controlled sources [19],[20] as;

$$V_j = \frac{1}{2} V_{dc} m_j \quad , \quad j = a,b,c \tag{12}$$

where $m_j$ corresponds to the modulation function and is obtained from the *dq0-abc* transformation of the reference voltage $V^*_{abc}$. The DC side of the VSC is derived using the principle of power conservation, meaning the power on the AC side must be equal to the power on the DC side plus the converter losses. Neglecting converter losses, The DC side can be also computed on the *dq0* reference frame and can be expressed as;

$$I_{dc} = \frac{3}{2V_{dc}} \left( V_d I_d + V_q I_q \right) \tag{13}$$

The main control blocks of the VSC are inner current control and outer *P, Q* and $V_{dc}$ control which include a Phase-Locked Loop (PLL) to adjust the grid angle as shown in Fig. 8(a). The inner control loop controls the d-q axis parameters of the VSC's reference voltage. The current reference in the inner current control $i^*_d$, $i^*_q$ to get the desired reactive and active power $(Q^*, P^*)$ is as shown in Fig. 8(b).

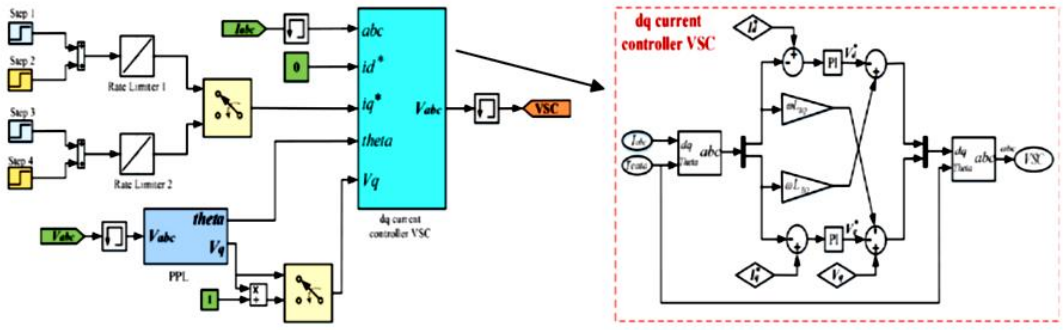


a) VSC control circuit b) dq inner control circuit

Fig. 8. The main control circuit of VSC

### DC-DC converter control circuit

A fixed frequency switching pattern is applied to the circuit cells, as can be shown in Fig 4(a). Meanwhile, the control circuit is controlled by the signal received from the VSC. There are two signals, one for boost (forward) converter switching, and the other for buck (reverse) converter switching as shown in Fig. 9. In order to avoid high switching losses in the semiconductors, ZCS is implemented, making use of the two L-C resonant circuits established in the DC-DC Marx converter during the two main commutation subintervals ($t_{on}$ and $t_{off}$) for both modes.

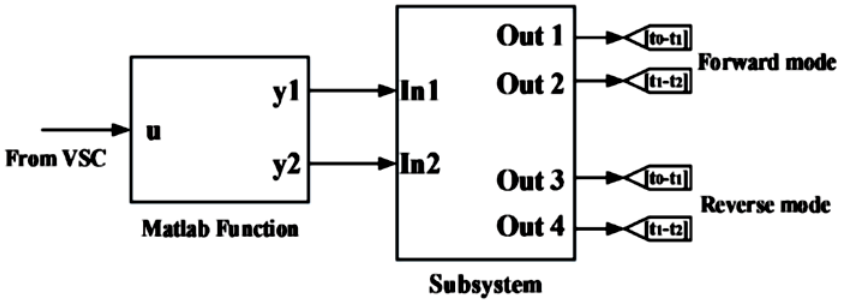


Fig. 9. Control circuit of the DC-DC converter

## Investigation of the steady-state performance

The operation of the system shown in Fig. 6 was investigated by digital simulations using Matlab/Simulink software package. The parameters of the system were calculated using the equations derived and the parameter values are given in Table 1. Once the steady state is reached the VSC demands 50MW at 100ms as shown in Fig. 11. Corresponding voltage and current waveforms are shown in Fig. 10 and Fig. 13.

**Table I: System Parameters used for simulation**

| DC-DC converter | | Value | |
|---|---|---|---|
| Number of modules | | 5 | |
| Input Voltage | $V_1$ | 6 | kV |
| Output Voltage | $V_2$ | 30 | kV |
| Inductor | $L_1$ | 2.53 | µH |
| Inductor | $L_2$ | 110 | µH |
| Capacitor | Cn | 694.5 | µF |
| Capacitor | $C_L$ | 83 | µF |
| Capacitor | $C_H$ | 116 | µF |
| Rated power | $P_{rate}$ | +50, -5 | MW |
| frequency | $F_S$ | 2 | kHz |
| DC cable | | | |
| R | | 0.011 | Ω/kM |
| L | | 2.615 | mH/kM |
| C | | 0.1908 | µF/kM |
| Length | | 116 | kM |

Fig. 10. Shows the initial no-load voltage of 33kV which drops to the rated voltage of 30kV at 100ms when the VSC demands the rated power of 50MW. At 250ms, the VSC signals the converter demanding reverse power of 5MW. The power flows from the AC system via the VSC, the DC link and the DC-DC converter to the wind farm. At 400ms the DC-DC converter is turned OFF. In this simulation, the VSC still sends power towards the windfarm, raising the DC-DC converter terminal voltage as seen in Fig. 10.

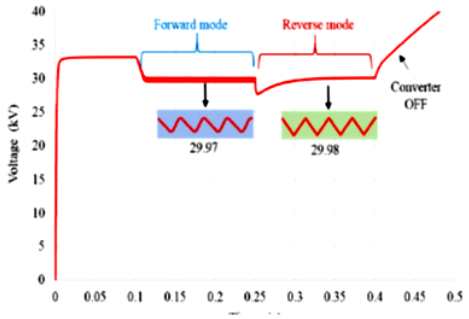


Fig. 10: DC Voltage waveform in both modes

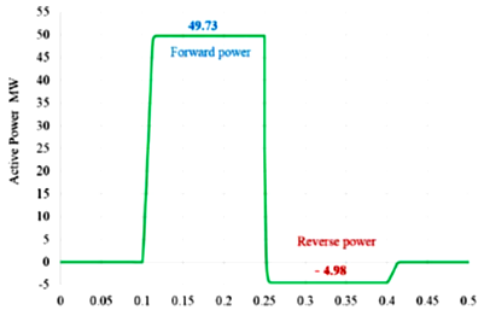


Fig. 11: Power flows in the DC link in both modes

The VSC model can reflect the active power exchange between the AC side and the DC side. Fig. 12 displays the variable AC current flow and the DC current reference in the VSC. During the simulation, the reactive power demand is kept at zero by keeping the quadrature axis current $I_q$ at zero. The notch in the voltage waveform at 250ms is due to the charge mismatch is the capacitor $C_H$ when the current flow changes. The settling time is less than 5 ms. The voltage ripple is illustrated in Fig. 10. As shown in Fig. 13, the forward and reverse currents are 1661.7 A and 165.3 A respectively.

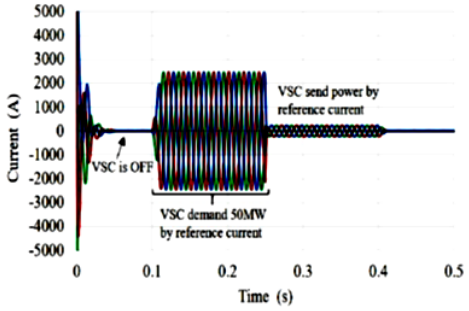


Fig. 12: DC Voltage waveform in both modes

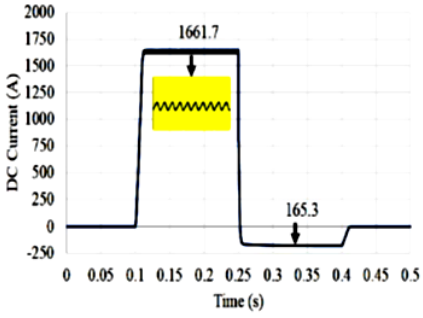


Fig. 13: Current DC link in both modes

## Conclusions

A novel high-power, medium-voltage, DC-DC converter suitable for application to power collection systems in an offshore wind farm has been investigated. The proposed converter is based on the Marx operation concept, and avoids the use of a transformer, adopting a Marx converter IGBT switch topology. The performance evaluation of a bidirectional Marx dc-dc converter using the soft-switching technique for DC collection has been explained. A design methodology for the determination of the circuit components and solid-state devices has also been presented. The operating principle of the proposed DC-DC Marx converter is confirmed by simulation using Matlab/Simulink software. From the simulation results, it is easy to see that the proposed converter has several advantages, such as a simple structure, flexible operation, fast dynamic response, and a capability of bidirectional power flow. Future study will include a dynamic-state and involve the addition of a wind turbine model to the system.

## References

[1] T. Traber, H. Koduvere, and M. Koivisto, "Impacts of offshore grid developments in the North Sea region on market values by 2050: How will offshore wind farms and transmission lines pay?," *Int. Conf. Eur. Energy Mark. EEM*, pp. 1–6, 2015.

[2] Wind Europe, "Wind Energy in Europe: Scenarios for 2030," *Report- Available at: https://windeurope.org/about-wind/reports/wind-energy-in-europe-scenarios-for-2030/*, no. September, 2015.

[3] S. M. Alagab, S. Tennakoon, and C. Gould, "Review of wind farm power collection schemes," *Power Eng. Conf. (UPEC), 2015 50th Int. Univ. pp. 1-5. IEEE, 2015.*, vol. 2015.

[4] M. Pahlevani, S. Eren, A. Bakhshai, and P. Jain, "A Series – Parallel Current-Driven Full-Bridge," vol. 31, no. 2, pp. 1275–1293, 2016.

[5] K. Filsoof and P. W. Lehn, "A bidirectional multiple-input multiple-output modular multilevel DC-DC converter and its control design," *IEEE Trans. Power Electron.*, vol. 31, no. 4, pp. 2767–2779, 2016.

[6] U. Karaagac, J. Mahseredjian, L. Cai, and H. Saad, "Offshore Wind Farm Modeling Accuracy and Efficiency in MMC-Based Multiterminal HVDC Connection MT," vol. 32, no. 2, pp. 617–627, 2017.

[7] M. Nasr, S. Poshtkouhi, N. Radimov, C. Cojocaru, and O. Trescases, "Fast Average Current Mode Control of Dual-Active-Bridge DC-DC Converter using Cycle-by-Cycle Sensing and Self-Calibrated Digital Feedforward," pp. 1129–1133, 2017.

[8] J. Maneiro, S. Tennakoon, and C. Barker, "Scalable shunt connected HVDC tap using the DC transformer concept," *2014 16th Eur. Conf. Power Electron. Appl. EPE-ECCE Eur. 2014*, pp. 6–8, 2014.

[9] S. M. Alagab, S. B. Tennakoon, and C. A. Gould, "A Compact DC-DC Converter for Offshore Wind Farm Application," *Renew. Energy Power Qual. J.*, vol. 1, no. 15, pp. 529–533, 2017.

[10] E. Veilleux and B. T. Ooi, "Marx-dc-dc converter for connecting offshore wind farms to multiterminal HVDC," *IEEE Power Energy Soc. Gen. Meet.*, pp. 1–5, 2013.

[11] A. Ponniran, K. Orikawa, and J. Itoh, "Modular Multi-stage Marx Topology for High Boost Ratio DC / DC Converter in HVDC," pp. 58–63, 2015.

[12] A. Parastar, A. Gandomkar, M. Jin, and J. K. Seok, "High power solid-state step-up resonant Marx modulator with continuous output current for offshore wind energy systems," *2013 IEEE Energy Convers. Congr. Expo. ECCE 2013*, pp. 1709–1716, 2013.

[13] S. M. Alagab, S. B. Tennakoon, and C. A. Gould, "High Voltage Cascaded Step-Up DC-DC Marx Converter for Offshore Wind Energy Systems," *EPE 2017 - assigned jointly to Eur. Power Electron. Drives Assoc. Inst. Electr. Electron. Eng.*, no. Mmc, pp. 1–10, 2017.

[14] D. V. A. N. Hertem, O. Gomis-bellmunt, and J. U. N. Liang, "HVDC grids: for offshore and supergrid of the future," p. 528, 2016.

[15] Z. Xing, X. Ruan, H. Xie, and X. Wang, "A modular bidirectional buck/boost dc/dc converter suitable for interconnecting HVDC grids," *2016 IEEE 8th Int. Power Electron. Motion Control Conf. IPEMC-ECCE Asia 2016*, pp. 3348–3354, 2016.

[16] P. Lakshmanan, J. Liang, and N. Jenkins, "Assessment of collection systems for HVDC connected offshore wind farms," *Electr. Power Syst. Res.*, vol. 129, pp. 75–82, Dec. 2015.

[17] "XLPE Submarine Cable Systems Attachment to XLPE Land Cable Systems - User ′ s Guide," *Curr. Available new.abb.com/docs/default-source/ewea.../xlpe-submarine-cable-systems-2gm5007.pdf.*

[18] F. Badrkhani Ajaei and R. Iravani, "Cable Surge Arrester Operation Due to Transient Overvoltages under DC-Side Faults in the MMC-HVDC Link," *IEEE Trans. Power Deliv.*, vol. 31, no. 3, pp. 1213–1222, 2016.

[19] C. Booth, "A review of control methods for providing frequency response in VSC-HVDC transmission systems," no. June 2016, 2014.

[20] J. Peralta, H. Saad, S. Dennetiere, and J. Mahseredjian, "Dynamic performance of average-value models for multi-terminal VSC-HVDC systems," *IEEE Power Energy Soc. Gen. Meet.*, pp. 1–8, 2012.

# Comparison of Single-stage and Multi-stage Marx DC-DC converters for HVDC application

Samir Milad Alagab
*School of Creative Arts and Engineering*
*Staffordshire University, Stoke on Trent*
*United kingdom*
Samir.alagab@research.staffs.ac.uk

Sarath Tennakoon
*Carnegie Mellon University Africa*
*Kigali, Rwanda*
*Staffordshire University, Stoke on Trent*
*United Kingdom*
S.B.Tennakoon@staffs.ac.uk

Chris Gould
*School of Creative Arts and Engineering*
*Staffordshire University, Stoke on Trent*
*United kingdom*
C.A.Gould@staffs.ac.uk

***Abstract*— A high voltage DC-DC converter is a key component of future HVDC grids. This paper presents a comparison of a single-stage and multi-stage converter. Both topologies are based on the Marx principle where charged capacitors are charged in parallel and discharged in series to achieve the voltage transformation. Detailed models of both converter topologies at 50 MW, 6kV/72kV are designed and simulated using Matlab/Simulink package software.**

***Keywords*— DC-DC converter, HVDC, IGBT, soft switching.**

## I. INTRODUCTION

DC-DC converters with high power and high voltage ratio are required for High Voltage Direct Current HVDC, and to act as interfaces between the generation, transmission, and distribution voltage levels [1]. There are several topologies that have been proposed in literature for HVDC DC-DC converters [2],[3],[4],[5],[6]. Most of these topologies propose to use a high-frequency transformer. However, the weight of the heavy electrical components, such as the transformer, and their physical volume, create serious issues for HVDC and are important factors in offshore wind farms. Intuitively, the Marx converter will be the most attractive and suitable configuration for HVDC applications because it avoids the use of transformers, and is lower in weight and size than alternative converter topologies.

Parastar and Gandomkar [12],[13] presented a multilevel DC-DC converter to achieve a high-gain ratio for offshore wind farms. The presence of this converter topology increases the number of conversion stages, resulting in a large number of passive components and active switches, which adds up to the system power losses and cost. Consequently, transformer less-based systems have been targeted in order to improve the wind turbine construction and maintenance requirements. Switched capacitor (SC) converters based on the Marx principle are considered as an attractive topology. Converters based on the Marx principle are capable of a realizing a high voltage gain and is a suitable for HVDC application [9],[10],[11]. Maneiro and Birkel [7],[8] presented shunt HVDC tap, using this method for stepping down the transmission voltage to a lower voltage for supplying a load, such as a remote area, where there is no existing grid. However, this topology requires a large number of IGBT switches. In this paper, a comparison of the steady-state performance of two Marx converter topologies suitable for high voltage application is presented. Single stage and multistage converters developed by the authors [14, 15] are compared, and to ensure meaningful comparison, the two converters were designed for the same voltage and current ratings. Single-stage and multi-stage structures and principles of operation are explained in Section II. A comparative performance evaluation is presented in Section III. Finally, the conclusions are drawn in section IV.

## II. SINGLE STAGE AND MULTI-STAGE CONVERTERS

Both Marx converter topologies are compared in terms of rated voltage and power. It is assumed that a single-stage DC-DC converter and multi-stage DC-DC Marx converter have already reached their steady-state. For a single stage converter, the duty cycle of both converters is fixed at 50%. The IGBT switches of both converters are operated using the soft switching technique, and the switching frequency is given.

### *A. Single-stage DC-DC Marx Converter*

- *Structure configuration*

As shown in Fig. 1, the structure of the converter can be divided into three sections; the input section; middle section; and the output section. The input section consists of a DC voltage source $V_{in}$, two HV valve switches and an input diode $D_{in}$ connected in series with an input inductor $L_{in}$. The middle section comprises of '$n$' number of capacitors which is set to 12 in Fig. 1, which gives a voltage transformation ratio of 1:12, diodes $D_{(1\text{-}23)}$ and a number of IGBT switches $(S_1\text{-}S_{22})$, $(S_{valve2}\text{-}\ S_{valve3})$. Depending on the voltage level in the application a number of IGBTs are required to be connected in series to form high voltage switches. The 12 capacitances in the middle section are indicated by $C_n$, where $n = (1, 12)$.

The output section consists of three components; the output inductor $L_{out}$; the diode $D_{out}$; the output capacitor $C_{out}$; and the load modelled by a resistor denoted by $R_{Load}$. The voltage transformation is done in one stage and hence the name Single Stage Converter.

- *Operating Principle*

Under steady-state one cycle of operation can be explained by considering two half-cycles. In the first half cycle, 12 capacitors in the middle section are charged in parallel by the

978-1-5386-2910-9/18/$31.00 ©2018 IEEE

input voltage $V_{in}$. In Fig. 2, the charging current path through the 12 capacitors, the valve switches ($S_{valve1}$- $S_{valve5}$), diodes $D_{in}$, ($D_1$-$D_{23}$) and input inductor $L_{in}$ are illustrated.

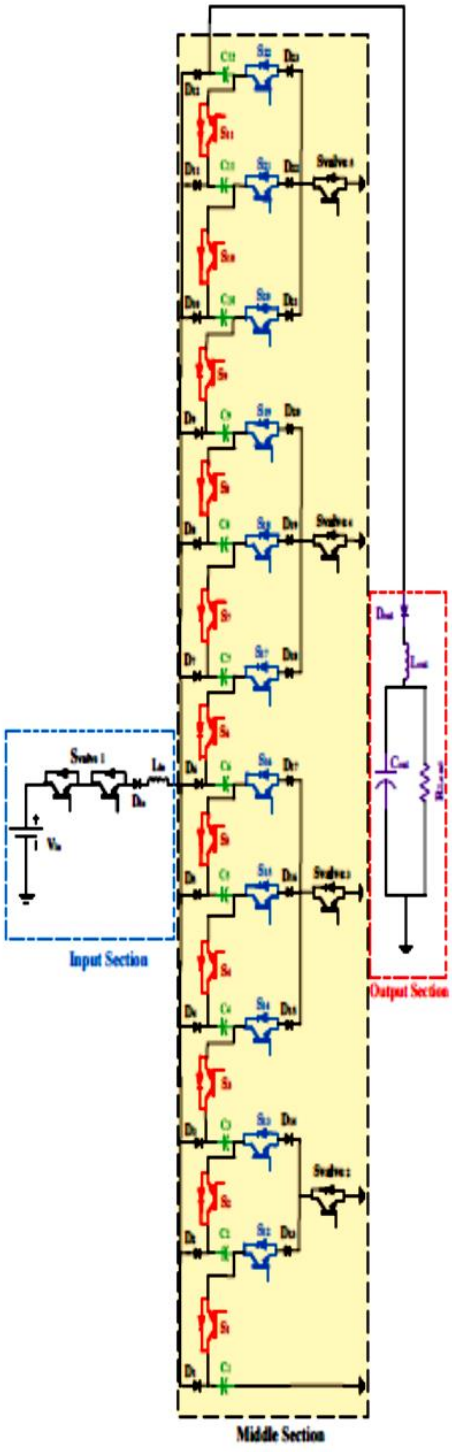


Fig. 1: Single-stage Marx converter

During the second half cycle, the 12 capacitors are discharged in series through the switches ($S_1$-$S_{11}$) to create the high voltage as depicted in Fig. 3.

The current is transferred from the middle section capacitors $C_n$ in series to the output capacitor $C_{out}$, and load $R_{Load}$ through output diode $D_{out}$ and output inductor $L_{out}$. The resonance frequency of the converter is chosen to line up with the switching frequency to enable soft switching.

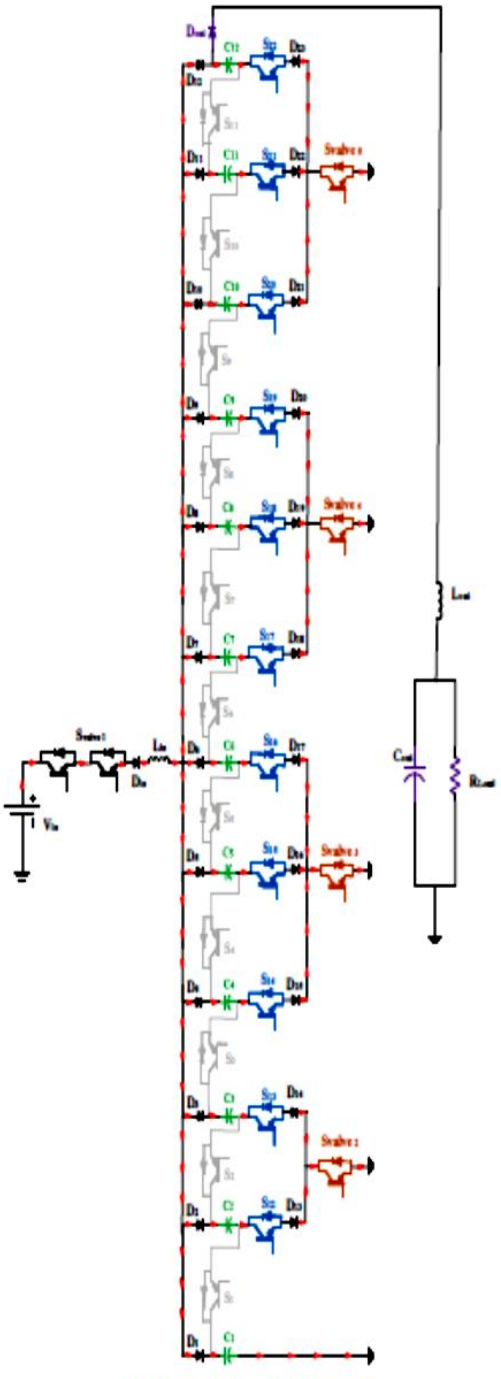

Fig. 2: First half-cycle configuration

### B. *Multi-stage DC-DC Marx Converter*

- *Structure*

This converter shown in Fig. 4 comprises three sections. The input and the output sections are identical to those in the

single stage converter. The middle section consists of three stages rather than one stage. The number of capacitors in stages 1,2 and 3 are set to 2, 3 and 2 respectively to create the voltage gain of 2x3x2=12 as shown in Fig. 4.

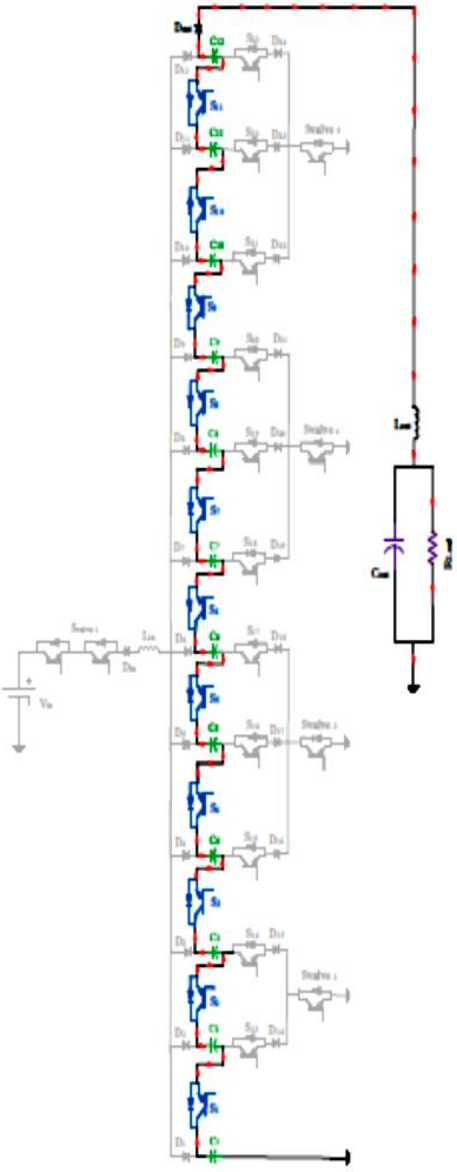

Fig. 3: Second half cycle configuration

- *Operating Principle*

Basically, the IGBTs are switched so that the charges in capacitors are pumped from the first stage to the second stage and to the third stage sequentially, resulting in a high voltage at the converter output. The switching of the multi-stage converter is listed in Table I.

Steady state operation is considered and therefore in order to aid the explanation, it is assumed that the capacitors $C_3$, $C_4$, and $C_5$ in the middle stage are each charged to $2V_{in}$.

During the first half-cycle, the switch $S_{switch1}$ is ON and the capacitors in stage 1 are charged in parallel by input voltage $V_{in}$, and through diode $D_1$, and inductor $L_1$. The charge on the capacitors in stage 2 discharge in series into the capacitors in stage 3 in parallel, and through inductor $L_3$ and diode $D_7$ as shown in Fig. 5.

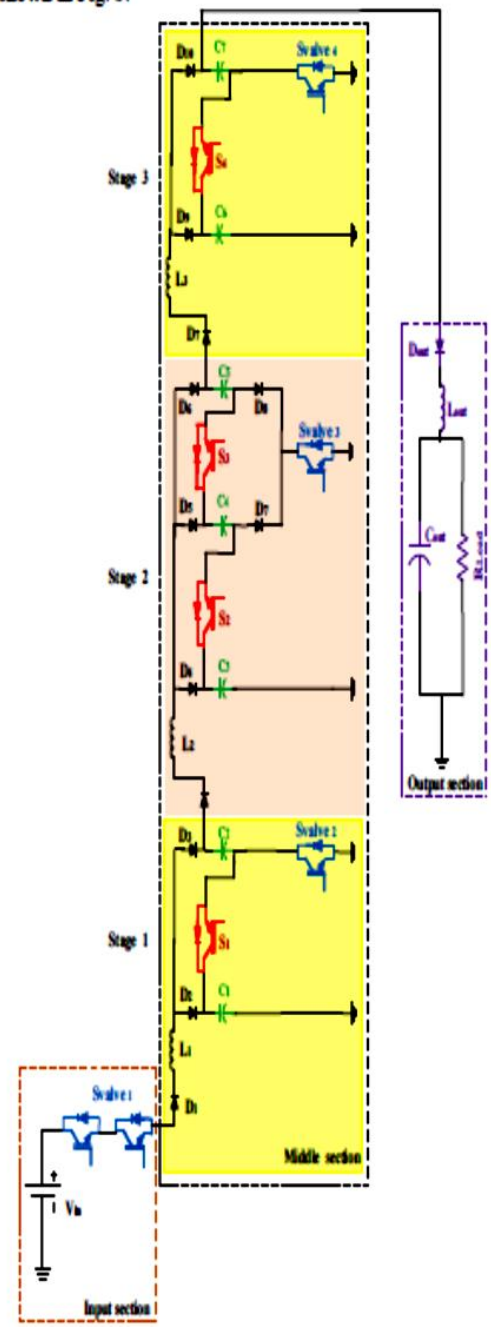


Fig. 4: Multi-stage Marx converter

TABLE I. IGBT SWITCHING LOGIC FOR THE MULTI-STAGE CONVERTER

| Switches | $S_{Switch\ 1}$ | $S_{Switch\ 2}$ | $S_{Switch\ 3}$ | $S_{Switch\ 4}$ | $S_1$ | $S_2$ | $S_3$ | $S_4$ |
|---|---|---|---|---|---|---|---|---|
| First half-cycle | 1 | 1 | 0 | 1 | 0 | 1 | 1 | 0 |
| Second half-cycle | 0 | 0 | 1 | 0 | 1 | 0 | 0 | 1 |

Fig. 5: First half-cycle configuration

In the second half-cycle, the device switching is the complement of the switching in the first half-cycle as depicted in Table I. The capacitors in stages 1 and 3 are in series, and the capacitors in stage 2 are in parallel, as shown in Fig. 6. The charging currents flow through inductor $L_2$ in stage 2 and $L_{out}$ in the output section. Meanwhile, there is no current in the inductors $L_1$ and $L_3$. Hence, the capacitors in the middle section in stage 1 and 3 are discharged, and the capacitors in stage 2 are charged.

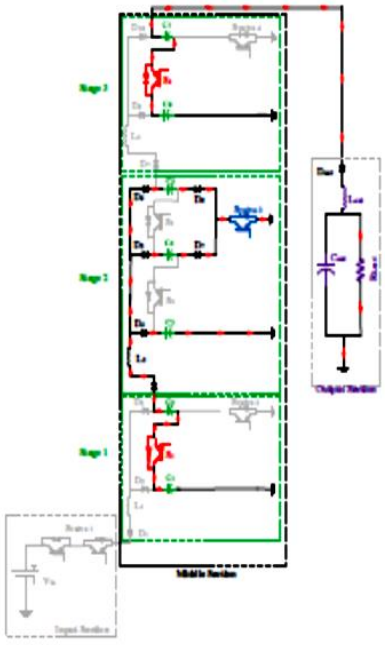

Fig. 6: Second half-cycle configuration

Continuous charging and discharging by repeated switching causes transfer of charge from the input section to the output section to supply the load $R_{Load}$, resulting in a voltage gain of 12. The diodes $(D_1$-$D_{10})$ which are in series with the capacitors and inductors ensure unidirectional current transfer. The output capacitor in the output section $C_{out}$ serves as a charge storage for continuous delivery, and this capacitor has to be designed for a ripple voltage in the load.

## III. Comparative Performance Evaluation

The voltage and power ratings of the converters are set to 6kV/72kV, 50MW. The switching frequency $F_S$ = 2kHz is used with a fixed duty cycle of 50%. The load resistance was calculated using the power rating of 50 MW and the output voltage of 72kV. Both converters are simulated in the Matlab/Simulink software package. The waveforms of input and output inductor currents of both converters are shown in Fig. 7. The resonant inductor current in a single stage converter increases to a peak current of 42.3 kA.

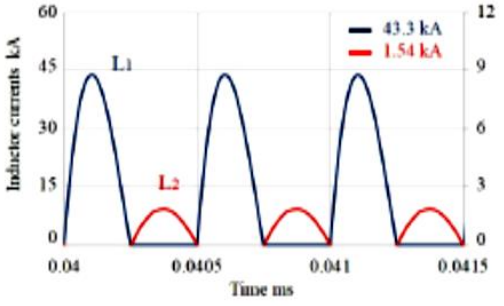


a)

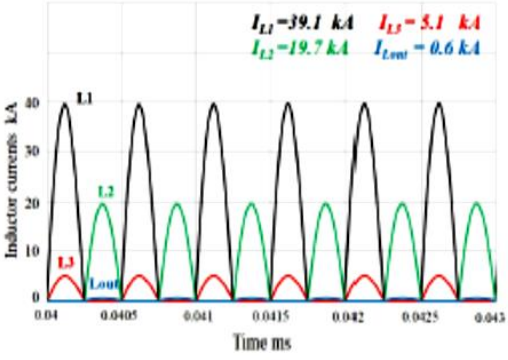


b)

Fig. 7: Inductor current waveforms: a) A single stage converter, b) Multi-stage converter

Fig. 7 clearly shows the effect of soft-witching, where current zeros resulting from the L-C oscillations lead to a reduction in switching losses. The resonating inductor current of the multi-stage converter increases to a peak of around 39kA in 250µs, while the resonant inductor current of the single stage converter increases to a peak of around 43.3kA. As shown in [16], the surge current capability of the ABB IGBT switch 5SNA 1200G450300 is 80kA in 100 µs, and 14kA in 10ms.

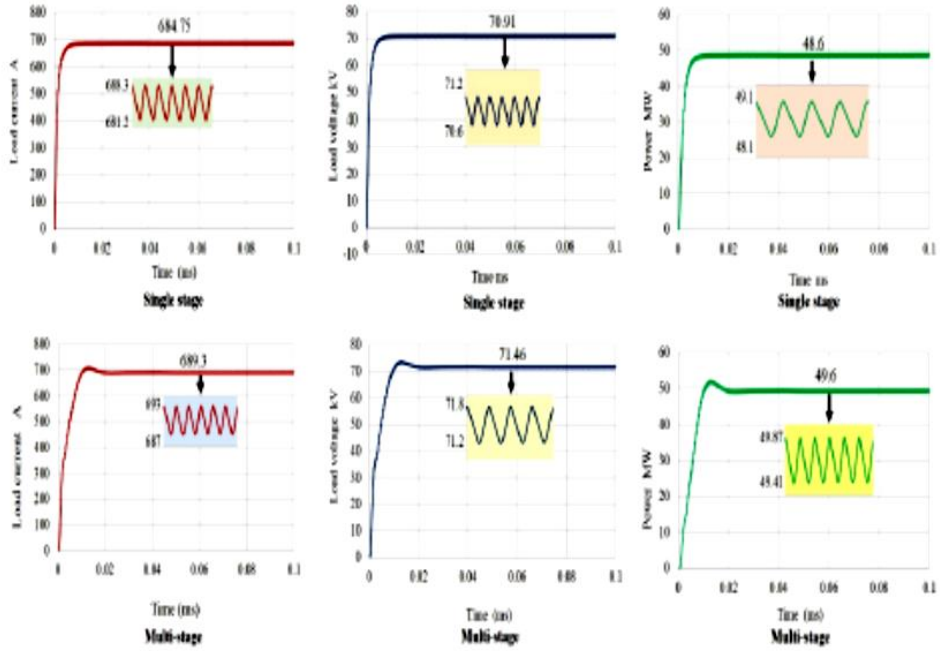


Fig. 8: Load voltage, Load current and load power waveforms both of converters

A quantitative comparison was carried out using data from the output results by Matlab/Simulink simulation. Both single-stage and multi-stage converters are evaluated and compared in terms of the power device count, to highlight its advantages for high-voltage applications. As mentioned before, both converter topologies operate under the same DC-DC Marx converter principle; hence, the comparison is made for the same voltage gain, same input voltage, same power rating, same load, same soft switching technique, and same switching frequency. Fig. 8, shows the simulation results of a single stage and a multi-stage converter. The DC gain of a single stage and multi-stage converter is 11.81 and 11.92 respectively, and have been compared with the theoretical gain of 12.

The output voltage, current, and power of the converter should be 72KV/ 694.5 A, 50MW as designed. It can be seen that both circuit output voltages are 70.91kV and 71.46kV respectively, which is very close to the design specification of 72kV. Fig. 8 shows that the output voltage in the multi-stage converter is higher than that of the single-stage converter, but both topologies perform equally well. Comparing with other HV DC-DC topologies that have a high gain ratio, they do not demonstrate a similar reduction in semiconductor components in the same application, perhaps because this has not been a focus area for the designer. Also, the peak load current of both converters is 684.75 A and 689.3 A, which is very close to the design value of 694.5 A. In addition, the load power of both converters as shown in Fig. 8 is 48.6MW and 49.6MW.

For both configurations, IGBT switches are comprised of several series-connected power devices to withstand the rated voltage.

Fig. 9 shows the active and passive component count comparison with a different gain voltage between both of the converter topologies. For both configurations, IGBT switches and diodes are comprised of several series-connected power switches to withstand the rated voltage. Currently, the high voltage has a maximum blocking voltage rated up to 6.5 kV 600A, but the ratings of the IGBT considered for this study is 4.5 kV and 1200 A. An inspection of the characteristics of the IGBT 5SNA 1200G450300, shows that this is feasible [16]. The required number of IGBT switches and diodes is mainly determined by peak current and peak voltage. The number of capacitors is calculated based on the required voltage rating and capacitance. The input and output sections of both converter topologies require the same number of active switches.

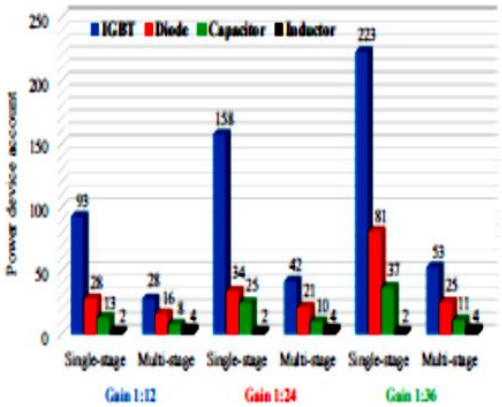


Fig. 9: Components count for DC-DC converter topologies comparisons between single-stage and multi-stage converters

As shown in Fig. 9, the comparison of designs includes three different voltage gains of 1:12, 1:24, and 1:36. The number of IGBT switches and capacitors in multi-stages is reduced when compared with a single-stage component, except for the inductor count which increases by a fixed small margin of only 2, and can be increased and depends on the number of stages in the middle section of the multi-stage converter.

In the multi-stage topology, the increase of the active switches (24%) depends on the voltage gain, while in the single stage topology there is a large increase of the active and passive components of 69%. The reduction in the component count in the multi-stage converter leads to a reduction of weight, cost, and complexity.

## IV. CONCLUSIONS

In this paper, two DC-DC converters based on the Marx principal for HVDC applications are compared with each other. The principles of operation of both DC-DC converter concepts are described and validated by computer simulations. The simulation findings show that the single-stage converter requires a large number of switching devices and passive components when compared with the multi-stage converter. Therefore, the physical volume and weight of a single-stage converter is higher than a multi-stage converter. Although both topologies achieve the required voltage gain of 12, the simulation results demonstrate that the voltage drop in a single-stage converter is more than the voltage drop in the multi-stage converter. Finally, it can be concluded that both single-stage and multi-stage converters are suitable and recommended for HVDC application.

## REFERENCES


[1] S. M. Alagab, S. Tennakoon, and C. Gould, "Review of wind farm power collection schemes," *Proc. Univ. Power Eng. Conf.*, vol. 2015–Novem, 2015.

[2] M. Barrenetxea, I. Baraia, I. Larrazabal, and I. Zubimendi, "Design of a Novel Modular Energy Conversion Scheme for DC Offshore Wind Farms," 2015.

[3] M. Moonem, C. Pechacek, R. Hernandez, and H. Krishnaswami, "Analysis of a Multilevel Dual Active Bridge (ML-DAB) DC-DC Converter Using Symmetric Modulation," *Electronics*, vol. 4, no. 2, pp. 239–260, Apr. 2015.

[4] S. Liu, L. Shi, and Z. Chen, "Improved zero-voltage-switching pulse width modulation full bridge converter with self-regulating auxiliary current," *IET Power Electron.*, vol. 6, no. 2, pp. 287–296, 2013.

[5] Zakis, Janis, Dmitri Vinnikov, and Ivars Rankis. "Steady state analysis of the galvanically isolated DC/DC converter with a commutating LC filter." Industrial Technology (ICIT), *2012 IEEE International Conference on. IEEE, 2012.*

[6] Y. A. N. Zhou, Y. Lian, G. P. Adam, and S. J. Finney, " DC / DC Converter for Offshore Dc Collection Grid," pp. 7–11.

[7] J. Manseiro, S. Tennakoon, and C. Barker, "Scalable shunt connected HVDC tap using the DC transformer concept," *2014 16th Eur. Conf. Power Electron. Appl. EPE-ECCE Eur. 2014*, pp. 6–8, 2014.

[8] A. Birkel and M. M. Bakran, "Comparison of shunt connected tapping concepts in HVDC transmission systems," *2016 18th Eur. Conf. Power Electron. Appl. EPE 2016 ECCE Eur.*, 2016.

[9] A. Parastar, A. Gandomkar, M. Jin, and J. K. Seok, "High power solid-state step-up resonant Marx modulator with continuous output current for offshore wind energy systems," *2013 IEEE Energy Convers. Congr. Expo. ECCE 2013*, pp. 1709–1716, 2013.

[10] P. W. Lehn, B.-T. Ooi, and E. Veilleux, "Marx dc–dc converter for high-power application," *IET Power Electron.*, vol. 6, no. April, pp. 1733–1741, 2013.

[11] E. Veilleux and B. T. Ooi, "Marx-dc-dc converter for connecting offshore wind farms to multiterminal HVDC," *IEEE Power Energy Soc. Gen. Meet.*, pp. 1–5, 2013.

[12] A. Parastar, A. Gandomkar, and J. Seok, "High-Efficiency Multilevel Flying-Capacitor Renewable Energy Systems," vol. 62, no. 12, pp. 7620–7630, 2015.

[13] A. Gandomkar, S. Member, A. Parastar, S. Member, J. Seok, and S. Member, "High-Power Multilevel Step-Up DC / DC Converter for Offshore Wind Energy Systems," vol. 46, no. c, 2016.

[14] S. M. Alagab, S. B. Tennakoon, and C. A. Gould, "A Compact DC-DC Converter for Offshore Wind Farm Application," *Renew. Energy Power Qual. J.*, vol. 1, no. 15, pp. 529–533, 2017.

[15] S. M. Alagab, S. B. Tennakoon, and C. A. Gould, "High Voltage Cascaded Step-Up DC-DC Marx Converter for Offshore Wind Energy Systems," *EPE 2017 - assigned jointly to Eur. Power Electron. Drives Assoc. Inst. Electr. Electron. Eng.*, no. Mmc, pp. 1–10, 2017.

[16] ABB Switzerland Ltd., "Surge currents for IGBT diodes, Application Note 5SYA 2058-02," 2014.